

**Bangor University**

## **DOCTOR OF PHILOSOPHY**

### **Fingerprinting ice-rafted detritus ice stream sources in the northeast Atlantic during the Last Glacial Stage**

Purcell, Catriona

*Award date:*  
2018

*Awarding institution:*  
Bangor University

[Link to publication](#)

#### **General rights**

Copyright and moral rights for the publications made accessible in the public portal are retained by the authors and/or other copyright owners and it is a condition of accessing publications that users recognise and abide by the legal requirements associated with these rights.

- Users may download and print one copy of any publication from the public portal for the purpose of private study or research.
- You may not further distribute the material or use it for any profit-making activity or commercial gain
- You may freely distribute the URL identifying the publication in the public portal ?

#### **Take down policy**

If you believe that this document breaches copyright please contact us providing details, and we will remove access to the work immediately and investigate your claim.

# Fingerprinting ice-rafted detritus ice stream sources in the northeast Atlantic during the Last Glacial Stage

Catriona Purcell



PRIFYSGOL  
**BANGOR**  
UNIVERSITY

Thesis submitted for the degree of Doctor of Philosophy

School of Ocean Sciences

Bangor University

September 2017



## Declaration

I hereby declare that this thesis is the results of my own investigations, except where otherwise stated. All other sources are acknowledged by bibliographic references. This work has not previously been accepted in substance for any degree and is not being concurrently submitted in candidature for any degree unless, as agreed by the University, for approved dual awards.

-----

Yr wyf drwy hyn yn datgan mai canlyniad fy ymchwil fy hun yw'r thesis hwn, ac eithrio lle nodir yn wahanol. Caiff ffynonellau eraill eu cydnabod gan droednodiadau yn rhoi cyfeiriadau eglur. Nid yw sylwedd y gwaith hwn wedi cael ei dderbyn o'r blaen ar gyfer unrhyw radd, ac nid yw'n cael ei gyflwyno ar yr un pryd mewn ymgeisiaeth am unrhyw radd oni bai ei fod, fel y cytunwyd gan y Brifysgol, am gymwysterau deuol cymeradwy.





## **Abstract**

Ice-rafted detritus (IRD) across the North Atlantic provides an important archive for reconstructing the dynamics of adjacent ice margins during the Last Glacial Maximum (LGM). The complex relationship between ice sheet mass balance and IRD flux is still unclear; an increase in IRD could indicate both a positive or a negative mass balance. To address these uncertainties, the source of the IRD needs to be established. Determining the source of IRD for the British Irish Ice Sheet (BIIS) hitherto has only identified broad lithospheric provenances. This study aimed to link IRD within three adjacent deep ocean cores to individual ice streams draining the former BIIS using X-ray Fluorescence (XRF) core scanning to define elemental geochemical provinces. Principal Component Analysis was used to establish five glacigenic ice stream end members from the former BIIS: 1) Irish Sea; 2) Celtic Sea; 3) Donegal; 4) Malin Sea and 5) Minch. These end members were then used to geochemically link the IRD in the deep ocean to ice stream source. All three deep ocean cores record BIIS IRD flux; contribution of IRD from the ice streams is governed by the presence of a marine-terminating margin and the direction of the surface currents which are shown to be variable during deglaciation. Significant BIIS IRD contribution to the deep ocean occurs between 31-20 kyr BP. Analyses suggests a marine-terminating BIIS pre-Heinrich event 4 and provides offshore evidence for a smaller regionalised marine terminating margin ~14 kyr BP and during the Younger Dryas stadial. The data highlight shifts in the timing of ice stream vs. ice lobe contribution from adjacent sources (Hebrides Ice Stream vs. Donegal Bay ice lobe) and that IRD source in the Rosemary Bank has stronger affinities with the Hebrides Ice Stream than with the adjacent Minch Ice Stream, indicating northward iceberg drift along the NW sector of the margin during and following the Last Glacial Maximum.



## **Acknowledgments**

Firstly, I would like to offer my sincere thanks to my supervisor Prof James Scourse for his guidance and support throughout this PhD. I would also like to thank Prof Richard Chiverrell for his invaluable support and advice in generating the XRF data.

I would like to acknowledge numerous people at the University of Liverpool whose input greatly helped this project. These include Dr John Boyle, Mike O'Connor, Jennifer Bradley and Joshua Hicks.

A special thank you to the BRITICE-CHRONO consortium, which has been an invaluable source of data and discussion about the collapse of the BIIS. Particular thanks to Prof Colm Ó Cofaigh, Prof Grant Bigg, Dr Katrien Van Landeghem, Dr Margot Saher, Dr Louise Callard and Kevin Schiele.

I wish to express my gratitude to Dr Fiona Hibbert for allowing me to include the MD04-2822 dataset within my research and to Prof William Austin for granting me permission to delve in to the cold store and subsample MD04-2822 at the University of St Andrews.

Thank you to Prof Jaap van der Meer who helped me with my first dissertation on LGM ice sheet limits and whose enthusiasm for teaching and fieldwork has had a lasting effect.

I have been very lucky to be part of such a friendly postgraduate community in Menai Bridge. I did not know what to expect when I first arrived on Anglesey Sept 2013, it has been a wonderful place to live and study.

Finally, a big thank you to my parents, family and my boyfriend Alex for their endless encouragement, patience and understanding throughout this process. I really couldn't have got to where I am today without them by my side.



# Contents

Title page .....	i
Declaration .....	iii
Abstract .....	v
Acknowledgements .....	vii
Contents .....	ix
List of figures .....	xiii
List of tables .....	xxxi

<b>1 Introduction.....</b>	<b>1</b>
1.1 Rationale.....	1
1.2 Project Aims .....	3
1.3 Thesis structure.....	4
1.4 Fingerprinting ice-rafted detritus.....	5
1.5 Western margin of the British Irish Ice Sheet.....	7
1.5.1 Irish Sea Ice Stream.....	7
1.5.2 Western Ireland and the Hebrides Ice Stream .....	9
1.5.3 Minch Ice Stream.....	10
1.6 Geology .....	11
1.7 Palaeo-hydrography .....	12
1.8 Conclusions .....	12
<b>2 Materials and Methodology .....</b>	<b>15</b>
2.1 Introduction .....	15
2.2 Fingerprinting ice-rafted detritus.....	19

2.2.1 Geochemical signature of the shelf end members .....	20
2.2.2 Fingerprinting the ice-rafted detritus record in the deep ocean.....	22
2.2.3 Multivariate analysis.....	23
2.2.4 Grain size .....	23
<b>3 Methodological considerations .....</b>	<b>25</b>
3.1 Quality control .....	25
3.2 Artifacts in micro XRF scan data .....	26
3.3 Correlation matrices .....	27
3.4 Adjusting for water content.....	29
<b>4 Irish Sea Ice Stream sector.....</b>	<b>45</b>
4.1 Irish Sea Ice Stream continental shelf cores .....	46
4.1.1 Lithostratigraphy .....	46
4.2 XRF geochemistry of the continental shelf cores .....	50
4.3 MD04-2820CQ .....	57
4.3.1 Lithostratigraphy .....	57
4.4 XRF geochemistry of MD04-2820CQ .....	57
4.5 Integration of the shelf end members and MD04-2820CQ XRF data .....	62
<b>5 Hebrides Ice Stream and Donegal Bay sector .....</b>	<b>69</b>
5.1 Hebrides Ice Stream and Donegal Bay continental shelf cores .....	71
5.1.1 Lithostratigraphy .....	71
5.2 XRF geochemistry of the continental shelf cores .....	74
5.3 MD04-2822 .....	78
5.3.1 Lithostratigraphy .....	78
5.4 XRF geochemistry of MD04-2822.....	78
5.5 Integration of the shelf end members and MD04-2822 XRF data .....	81
<b>6 Minch Ice Stream sector.....</b>	<b>87</b>
6.1 Minch Ice Stream continental shelf cores .....	88
6.1.1 Lithostratigraphy .....	88
6.2 XRF geochemistry of the continental shelf cores .....	90
6.3 MD04-2829CQ .....	95
6.3.1 Lithostratigraphy .....	95
6.4 XRF geochemistry of MD04-2829CQ .....	95

6.5 Integration of the shelf end members and MD04-2829CQ XRF data .....	98
<b>7 Discussion.....</b>	<b>103</b>
7.1 Geochemical signature of the Irish Sea Ice Stream sector .....	104
7.1.1 Establishing Irish Sea Ice Stream end members.....	104
7.1.2 Geochemical signature of MD04-2820CQ.....	113
7.1.3 Exploring the geochemical relationship between MD04-2820CQ and the Irish Sea Ice Stream end members.....	115
7.2 Geochemical signature of the Hebrides Ice Stream and Donegal Bay sector .....	119
7.2.1 Establishing Hebrides Ice Stream and Donegal Bay end members.....	119
7.2.2 Geochemical signature of MD04-2822 .....	125
7.2.3 Exploring the geochemical relationship between MD04-2822 and the Hebrides Ice Stream and Donegal Bay end members.....	126
7.3 Geochemical signature of the Minch Ice Stream sector .....	133
7.3.1 Establishing Minch Ice Stream end members .....	133
7.3.2 Geochemical signature of MD04-2829CQ.....	138
7.3.3 Exploring the geochemical relationship between MD04-2829CQ and the Minch sediment cores .....	139
7.4 Integration of all ice stream XRF data.....	144
7.5 Integration of the XRF data from the three deep ocean cores .....	146
7.6 Synthesis.....	147
7.6.1 MD04-2820CQ and the Hebrides Ice Stream and Donegal Bay end members ....	148
7.6.2 MD04-2820CQ and the Minch Ice Stream end members .....	150
7.6.3 MD04-2822 and the Irish Sea Ice Stream end members .....	152
7.6.4 MD04-2822 and the Minch Ice Stream end members.....	153
7.6.5 MD04-2829CQ and the Irish Sea Ice Stream end members .....	155
7.6.6 MD04-2829CQ and the Hebrides Ice Stream and Donegal Bay end members ....	157
7.7 Summary.....	159
<b>8 Conclusion .....</b>	<b>167</b>
8.1 The indicative meaning of the ice-rafted detritus record in the deep ocean .....	167
8.2 Iceberg trajectories.....	168
8.3 Ice-rafted detritus record and implications for the dynamics and collapse of the British-Irish Ice Sheet .....	168



8.4 Geochemical signature of Heinrich events .....	170
8.5 Future work.....	170
8.6 Implications for BRITICE-CHRONO.....	172
<b>References .....</b>	<b>174</b>
<b>Appendices .....</b>	<b>189</b>

## **List of figures**

- Figure 1.1 Photograph of MD04-2820CQ alongside a synthetic stratigraphy for the 15-38 kyr interval. The colours relate to the hypothetical shelf end members and represent the position of the ice stream's calving margin. Source of bathymetry: EMODnet Bathymetry Consortium (2016): EMODnet Digital Bathymetry (DTM). Source of land DEM: SRTM 90m DEM, NASA shuttle, version 2.1. All subsequent maps use the same bathymetry and land DEM and therefore the same source..... 4
- Figure 1.2 Map depicting conflicting models of maximum extent of the last BIIS as mentioned in the text; Smedley *et al.* 2017 (Blue line); Praeg *et al.* 2015 (Yellow line); Peters *et al.* 2015 (Green line); Sejrup *et al.* 2005; Scourse *et al.* 2009; Clark *et al.* 2012 (Black line); Small *et al.* 2016 (Red line) and Bradwell and Stoker 2015 (Purple line). Major ice streams are also included 1) Irish Sea Ice Stream 2) Hebrides Ice Stream and 3) Minch Ice Stream; and trough mouth fans BF: Barra Fan; SF: Sula Sgeir..... 8
- Figure 1.3 Various retreat margins of the Irish Sea Ice Stream showing the location of geochronological sites used for the Bayesian modelling and modelled ages for retreat (From Chiverrell *et al.* 2013)..... 9
- Figure 2.1 Location map showing the locations of the deep ocean cores MD04-2820CQ, MD04-2822 and MD04-2829CQ; and the continental shelf cores analysed within this study. The continental shelf cores are divided into three areas: the Irish Sea Ice Stream (Red circles); the Hebrides Ice Stream and Donegal Bay ice lobe (purple circles) and the Minch Ice Stream (pink circles). .... 17
- Figure 3.1 Ti, Zr peaks and Zr/Rb, Ca/Fe ratios vs lithostratigraphic core log JC106-068VC. Core log produced by Margot Saher..... 28
- Figure 3.2 Ca, Ti peaks and Zr/Rb, Fe/Rb ratios vs lithostratigraphic core log JC106-084VC. Core log produced by Margot Saher..... 30
- Figure 3.3 Zr/Rb ratio vs lithostratigraphic core log JC106-063VC. Core log produced by Margot Saher..... 31
- Figure 3.4 Correlations for the element concentrations of Ti, Mn, Cu, Zn, Rb, Sr, Y and Zr for the JC106, JC123 and MD04-2829CQ cores. Wet scan data measured by the Olympus

DELTA (ppm) and dry subsamples measured by the SPECTRO XEPOS (ppm). The intercept has been set through zero.....	33
Figure 3.5 Correlations for the element concentrations of Pb, K, Ca, Fe, Al and Si for the JC106, JC123 and MD04-2829CQ cores. Wet scan data measured by the Olympus DELTA (ppm) and dry subsamples measured by the SPECTRO XEPOS (ppm). The intercept has been set through zero excluding Pb and Si.....	34
Figure 3.6 Correlations for the element concentrations of Mn, Zn, Sr, Pb and Ca for the JC106, JC123 and MD04-2829CQ cores. Wet scan data measured by the Olympus DELTA (ppm) and dry subsamples measured by the SPECTRO XEPOS (ppm). Red data points are the deleted outliers. These points have been classified as outliers because they exceed the boundary of $(IQR*3) + Q3$ for each element. The intercept has been set through zero excluding Pb.....	35
Figure 3.7 Correlations for the element concentrations of Ti, Mn, Cu, Zn, Rb, Sr, Zr and Pb for MD04-2820CQ core. Wet scan data measured by ITRAX (cps) and dry subsamples measured by the SPECTRO XEPOS (ppm). The intercept has been set through zero...	36
Figure 3.8 Correlations for the element concentrations of Al, Si, K, Ca and Fe for MD04-2820CQ core. Wet scan data measured by ITRAX (cps) and dry subsamples measured by the SPECTRO XEPOS (ppm). The intercept has been set through zero excluding Al. ....	37
Figure 3.9 Correlations for the element concentrations of Ti, Mn, Zn, Rb, Sr, Zr, Si and K for MD04-2822 core. Wet scan data measured by ITRAX (cps) and dry subsamples measured by the SPECTRO XEPOS (ppm). The intercept has been set through zero....	38
Figure 3.10 Correlations for the element concentrations of Ca and Fe for MD04-2822 core. Wet scan data measured by ITRAX (cps) and dry subsamples measured by the SPECTRO XEPOS (ppm). The intercept has been set through zero.....	39
Figure 3.11 Element concentration data for JC106, JC123 and MD04-2829CQ cores. Green line represents Olympus DELTA uncorrected data. Blue line reflects the SPECTRO XEPOS subsample data. Red line represents the Olympus DELTA data corrected by regression on wet Olympus Delta data.....	40

Figure 3.12 Element concentration data for MD04-2820CQ core. Green line represents ITRAX uncorrected data. Blue line reflects the SPECTRO XEPOS subsample data. Red line represents the ITRAX data corrected by regression on wet ITRAX data.....	41
Figure 3.13 Element concentration data for MD04-2822 core. Green line represents ITRAX uncorrected data. Blue line reflects the SPECTRO XEPOS subsample data. Red line represents the ITRAX data corrected by regression on wet ITRAX data.....	42
Figure 3.14 Scattering of primary rhodium X-rays as a function of sediment water content. The 38% water content sediment is from JC106-087VC (2.5 m depth) and the 7% water content sediment is from JC123-012VC (2.49 m depth). The wetter sample has a greater proportion of Compton scattering.....	43
Figure 3.15 Rayleigh/Compton scattering ratio measured by the Olympus DELTA for the corresponding depths for the subsamples from JC106-087VC, the XRF inferred dry matter content for these subsamples and the measured subsample dry matter content...	44
Figure 3.16 Relationship between measured subsample water content and the XRF inferred water content derived using the Rayleigh/Compton scattering ratio measured by the Olympus DELTA for the corresponding depths for the subsamples from JC106-087VC. ....	44
Figure 4.1 Location map of the 18 JC106 cores analysed for the former Irish Sea Ice Stream and adjacent deep ocean core MD04-2820CQ.....	46
Figure 4.2 Lithostratigraphy for six cores from the Celtic Sea region of the former Irish Sea Ice Stream. Core logs, x-ray imagery, core image, shear strength, radiocarbon dates ( $\Delta R=0$ ) and lithostratigraphy key. Black outline boxes highlight the sediment analysed for this study. Core logs were produced by Margot Saher.....	47
Figure 4.3 Lithostratigraphy for seven cores from the Irish Sea region of the former Irish Sea Ice Stream. Core log, x-ray imagery, core image, shear strength and radiocarbon dates ( $\Delta R=0$ ). Black outline boxes highlight the sediment analysed for this study. Core logs were produced by Margot Saher.....	48
Figure 4.4 Lithostratigraphy for six cores from the Irish Sea region of the former Irish Sea Ice Stream. Core log, x-ray imagery, core image, shear strength and radiocarbon dates ( $\Delta R=0$ ). Black outline boxes highlight the sediment analysed for this study. Core logs were produced by Margot Saher.....	49

- Figure 4.5 PCA biplot for the Irish Sea Ice Stream sediment cores. PC 1 summarises 72% of the total variance in the dataset and PC 2 13%. Each core has been colour coded..... 51
- Figure 4.6 PCA biplot for the Irish Sea Ice Stream sediment cores divided into regions. PC 1 summarises 72% of the total variance in the dataset and PC 2 13%. Each core and region has been colour coded. Ellipses represent 0.95 confidence level. Henceforth all figures which include ellipses will be at 0.95 confidence level..... 51
- Figure 4.7 Boxplot displaying Fe concentrations of the 18 sediment cores from the former Irish Sea Ice Stream. The cores have been colour coded by region. The lower and upper hinges correspond to the 25<sup>th</sup> and 75<sup>th</sup> percentiles. The upper whisker extends from the hinge to the largest value no further than 1.5\* inter quartile range ( $IQR(IQR=UQ-LQ)$ ) from the hinge. The lower whisker extends from the hinge to the smallest value at most 1.5\* IQR of the hinge. Data beyond the whiskers are plotted individually and called ‘outliers’. The black lines in the middle of the boxes are median values..... 52
- Figure 4.8 PCA biplot for the Irish Sea Ice Stream sediment cores focusing on grain size A) Each core has been colour coded and symbols display the grain size of each data point. B) Every data point has been colour coded by grain size..... 53
- Figure 4.9 PCA biplot displaying internal elemental concentration and grain size variability for two Celtic Sea cores as a function of stratigraphy. A) JC106-012VC B) JC106-018VC. Blue data points are proximal sediments transitioning to distal sediments (red data points). The remaining Irish Sea Ice Stream cores are shown by the yellow data points. .... 54
- Figure 4.10 PCA biplot displaying internal elemental concentration and grain size variability for one Celtic Sea core as a function of stratigraphy JC106-033VC. Blue data points are proximal sediments transitioning to distal sediments (red data points). The remaining Irish Sea Ice Stream cores are shown by the yellow data points..... 55
- Figure 4.11 PCA biplot displaying internal elemental concentration and grain size variability for one Irish Sea core as a function of stratigraphy JC106-063VC. Blue data points are proximal sediments transitioning to distal sediments (red data points)..... 55
- Figure 4.12 PCA biplot displaying internal elemental concentration and grain size variability for two Irish Sea cores as a function of stratigraphy. A) JC106-069VC B) JC106-073VC.

Blue data points are proximal sediments transitioning to distal sediments (red data points).....	56
Figure 4.13 Lithological log for MD04-2820CQ produced by Cooke, 2008.....	58
Figure 4.14 Lithostratigraphic core log for MD04-2820CQ. Heinrich events and the ambient clay silt lithofacies have been colour coded. H1-Red, H2- Blue, H3- Green and H4 Purple. Post H1-Orange, Post H2- Yellow, Pre-H2- Pink, Post H4-Brown and Pre-H4 Grey. These same colours will be used in subsequent analysis.....	59
Figure 4.15 PCA biplot for MD04-2820CQ. A) PC 1 summarises 45% of the total variance in the dataset and PC 2 16%. Heinrich events and the ambient clay silt lithofacies have been colour coded. H1-Red, H2- Blue, H3-Green and H4-Purple. Post H1-Orange, Post H2- Yellow, Pre-H2-Pink, Post H4-Brown and Pre-H4 Grey. B) PCA biplot for MD04-2820CQ excluding Heinrich events, the ambient lithofacies have been colour coded. PC 1 accounts for 38% of the variance and PC 2 20%. The PC 2 scores have flipped from Figure 4.15A, so what was negative is now positive and vice versa.....	60
Figure 4.16 Lithostratigraphic core log for MD04-2820CQ. H1-Red, H2-Blue, H3-Green and H4-Purple. Post H1-Orange, Post H2-Yellow, Pre-H2-Pink, Post H4-Brown and Pre-H4 Grey. Arrows correspond to the stratigraphic position of the ambient samples that occur along the main SW Heinrich vector of the PCA in Figure 4.15A, and NW vector of Figure 4.15B.....	61
Figure 4.17 Lithostratigraphic core log for MD04-2820CQ. H1-Red, H2- Blue, H3- Green and H4 Purple. Post H1-Orange, Post H2- Yellow, Pre-H2- Pink, Post H4-Brown and Pre-H4 Grey. Arrows correspond to the stratigraphic position of the ambient samples that occur along the NW arm of the PCA in Figure 4.15A and SW arm of the PCA in Figure 4.15B. ....	62
Figure 4.18 Biplots illustrating the PCA results obtained by integrating the shelf end members and MD04-2820CQ XRF data. PC 1 explains 47% of the variance and PC 2 24%. A) MD04-2820CQ has been colour coded by its lithofacies and the Irish end members are black. B) MD04-2820CQ is black and the Irish end members are colour coded by core.....	63

- Figure 4.19 Biplot displaying the results of a PCA analysing both the shelf end members and H2 samples from MD04-2820CQ. H2 sediments are black and the Irish Sea end members are colour coded by core. PC 1 explains 59% of the total variance, PC 2 25%..... 64
- Figure 4.20 Biplots of the PCA results of the ambient MD04-2820CQ lithofacies and the ISIS end members. PC summarises 50% of the total variance and PC 2 23%. A) MD04-2820CQ ambient lithofacies have been colour coded and the Irish end members are black. B) MD04-2820CQ ambient lithofacies are black and the ISIS end members have been colour coded by core..... 65
- Figure 4.21 Biplots of the PCA results of the ambient MD04-2820CQ lithofacies and the ISIS end members. PC summarises 50% of the total variance and PC 2 23%. A) MD04-2820CQ ambient lithofacies have been colour coded, the ISIS end members are black and have been categorised by region. B) MD04-2820CQ ambient lithofacies are black and the ISIS end members have been colour coded by core and categorised by region..... 66
- Figure 4.22 Biplots of the PCA results of the ambient MD04-2820CQ lithofacies and two sediment cores from the former ISIS. A) JC106-019VC and MD04-2820CQ ambient lithofacies. PC 1 summarises 38% of the variance, PC 2 21%. B) JC106-054VC and MD04-2820CQ ambient lithofacies. PC 1 accounts for 38% of the variance and PC 2 20%..... 67
- Figure 4.23 Biplot of the PCA results of the ambient MD04-2820CQ lithofacies and one sediment cores from the former ISIS. JC105-073 and MD04-2820CQ ambient lithofacies. PC 1 summarises 37% of the total variance and PC 2 21%..... 68
- Figure 5.1 Location map of the nine JC106 cores analysed for the Hebrides Ice Stream, Donegal Bay ice lobe and adjacent deep ocean core MD04-2822.....70
- Figure 5.2 Lithostratigraphy for three cores from the former Donegal Bay ice lobe. Core logs, x-ray imagery, core image, shear strength, radiocarbon dates ( $\Delta R=0$ ) and lithostratigraphy key. Black outline boxes highlight the sediment analysed for this study. Core logs from Ó Cofaigh *et al.* (in press) and Schiele (pers. comm. 2017)..... 72
- Figure 5.3 Lithostratigraphy for six cores from the former Hebrides Ice Stream. Core logs, x-ray imagery, core image, shear strength, radiocarbon dates ( $\Delta R=0$ ) and lithostratigraphy key. Black outline boxes highlight the sediment analysed for this study. Core logs produced by Louise Callard..... 73

Figure 5.4 PCA biplot for the Hebrides Ice Stream and Donegal Bay sediment cores. PC 1 summarises 52% of the total variance in the dataset and PC 2 17%. Each core has been colour coded.....	74
Figure 5.5 PCA biplot for the Hebrides Ice Stream and Donegal Bay sediment cores divided into regions. PC 1 summarises 52% of the total variance in the dataset and PC 2 17%. Each core and region has been colour coded.....	75
Figure 5.6 Boxplot displaying Fe concentrations of the nine sediment cores from the former Hebrides Ice Stream and Donegal Bay ice lobe. The cores have been colour coded by region. The lower and upper hinges correspond to the 25 <sup>th</sup> and 75 <sup>th</sup> percentiles. The upper whisker extends from the hinge to the largest value no further than 1.5* inter quartile range (IQR(IQR=UQ-LQ)) from the hinge. The lower whisker extends from the hinge to the smallest value at most 1.5* IQR of the hinge. Data beyond the whiskers are plotted individually and called ‘outliers’. The black lines in the middle of the boxes are median values.....	75
Figure 5.7 PCA biplot for the Hebrides Ice Stream and Donegal Bay sediment cores focusing on grain size. Each core has been colour coded and symbols display the grain size of each data point.....	76
Figure 5.8 PCA biplot for the Hebrides Ice Stream and Donegal Bay sediment cores focusing on grain size. Every data point has been colour coded by grain size.....	76
Figure 5.9 PCA biplot displaying internal elemental concentration and grain size variability for JC106-102VC as function of stratigraphy. Blue data points are proximal sediments transitioning to distal sediments (red data points).....	77
Figure 5.10 PCA biplot displaying internal elemental concentration and grain size variability for JC106-146VC as function of stratigraphy. Blue data points are proximal sediments grading to distal sediments (red data points).....	78
Figure 5.11 Lithostratigraphic core log and key for MD04-2822. The section of interest for this study is 3.83-18.55 m (~14-31 kyr BP). Edited from Hibbert (pers. comm. 2016).....	79
Figure 5.12 PCA biplot for MD04-2822. PC 1 summarises 33% of the total variance in the dataset and PC 2 30%. The core has been subdivided into age intervals which are colour coded.....	80



- Figure 5.13 PCA biplot for MD04-2822. PC 1 summarises 33% of the total variance in the dataset and PC 2 30%. The core has been colour coded by age intervals and further grouped into broader age intervals (14-24 kyr BP and 24-31 kyr BP)..... 80
- Figure 5.14 Biplot illustrating the PCA results obtained by integrating the shelf end members and MD04-2822 XRF data. PC 1 explains 49% of the variance and PC 2 22%. MD04-2822 has been colour coded by its age intervals and the Hebrides Ice Stream and Donegal Bay end members are black..... 81
- Figure 5.15 Biplot of the PCA results of MD04-2822 and Hebrides Ice Stream (HIS) and Donegal Bay end members. PC 1 summarises 49% and PC 2 22%. The age intervals of MD04-2822 have been colour coded, the Hebrides Ice Stream and Donegal Bay end members are black and each core is shown by an ellipse... .. 82
- Figure 5.16 Biplot of the PCA results of MD04-2822 and Hebrides Ice Stream and Donegal Bay end members. PC 1 summarises 49% and PC 2 22%. Each core is shown by an ellipse and has been colour coded..... 82
- Figure 5.17 Biplot of the PCA results of MD04-2822 and Hebrides Ice Stream (HIS) and Donegal Bay end members. PC 1 summarises 49% and PC 2 22%. The cores have been colour coded and further grouped by ellipses into broader age intervals and Hebrides Ice Stream and Donegal Bay sediments..... 83
- Figure 5.18 Biplot of the PCA results of MD04-2822 and Hebrides Ice Stream (HIS) and Donegal Bay end members. PC 1 summarises 49% and PC 2 22%. The cores have been colour coded and further grouped by ellipses into regional areas and MD04-2822..... 84
- Figure 5.19 Biplot of the PCA results of MD04-2822 and JC106-096VC. PC 1 summarises 38% and PC 2 28%. The age intervals of the MD04-2822 have been colour coded and JC106-096VC is black..... 84
- Figure 5.20 Biplot of the PCA results of MD04-2822 and JC106-112VC. PC 1 summarises 38% and PC 2 28%. The age intervals of the MD04-2822 have been colour coded and JC106-112VC is black..... 85
- Figure 5.21 Biplot of the PCA results of MD04-2822 and JC106-149VC. PC 1 summarises 36% and PC 2 28%. The age intervals of the MD04-2822 have been colour coded and JC106-149VC is black..... 85

Figure 6.1 Location map of the eight JC123 cores analysed for the former Minch Ice Stream and adjacent deep ocean core MD04-2829CQ.....	88
Figure 6.2 Lithostratigraphy for eight cores from the former Minch Ice Stream. Core logs, x-ray imagery, core image, shear strength, radiocarbon dates ( $\Delta R=0$ ) and lithostratigraphy key. Black outline boxes highlight the sediment analysed for this study. Core logs were produced by Margot Saher.....	89
Figure 6.3 PCA biplot for the Minch Ice Stream sediment cores. PC 1 summarises 58% of the total variance of the dataset and PC 2 21%. Each core has been colour coded.....	91
Figure 6.4 PCA biplot for the Minch Ice Stream sediment cores divided into regions. PC 1 summarises 58% of the total variance in the dataset and PC 2 21%. Each core and region has been colour coded.....	91
Figure 6.5 Boxplot displaying Fe concentrations of the eight sediment cores from the former Minch Ice Stream. The cores have been colour coded by region. The lower and upper hinges correspond to the 25 <sup>th</sup> and 75 <sup>th</sup> percentiles. The upper whisker extends from the hinge to the largest value no further than 1.5* inter quartile range ( $IQR(IQR=UQ-LQ)$ ) from the hinge. The lower whisker extends from the hinge to the smallest value at most 1.5* IQR of the hinge. Data beyond the whiskers are plotted individually and defined as ‘outliers’. The black lines in the middle of the boxes are median values....	92
Figure 6.6 PCA biplots for the Minch Ice Stream sediment cores focusing on grain size. A) Each core has been colour coded and symbols display the grain size of each data point; B) Every data point has been colour coded by grain size.....	93
Figure 6.7 PCA biplot displaying internal elemental concentration and grain size variability for JC123-015VC as a function of stratigraphy. Blue data points are proximal sediments transitioning to distal sediments (red data points).....	94
Figure 6.8 PCA biplot displaying internal elemental concentration and grain size variability for JC123-039VC as a function of stratigraphy. Blue data points are proximal sediments grading to distal sediments (red data points).....	94
Figure 6.9 PCA biplot displaying internal elemental concentration and grain size variability for JC123-049VC as a function of stratigraphy. Blue data points are proximal sediments grading to distal sediments (red data points).....	95

Figure 6.10 Lithostratigraphic core log and key for MD04-2829CQ. The section of interest for this study is 3.13-8.08 m (~18-30 kyr BP). Edited from MD141 Alienor shipboard log (Hall pers. comm. 2017).....	96
Figure 6.11 PCA biplot for MD04-2829CQ. PC 1 summarises 33% of the total variance in the dataset and PC 2 20%. The core has been subdivided into age intervals which are colour coded.....	97
Figure 6.12 PCA biplot for MD04-2829CQ. PC 1 summarises 33% of the total variance in the dataset and PC 2 20%. The core has been colour coded by age intervals and further grouped into broader age intervals (18-22 kyr BP, 22-26 kyr BP and 26-30 kyr BP)....	97
Figure 6.13 Biplot illustrating the PCA results obtained by integrating the shelf end members and MD04-2829CQ XRF data. PC 1 explains 60% of the variance and PC 2 18%. MD04-2829CQ has been colour coded by its age intervals and the Minch Ice Stream end members are shown in black.....	98
Figure 6.14 Biplot of the PCA results of MD04-2829CQ and Minch end members. PC 1 explains 60% of the variance and PC 2 18%. Each core has been colour coded.....	98
Figure 6.15 Biplot of the PCA results of MD04-2829CQ and Minch end members. PC 1 explains 60% and PC 2 18% of the variance. The age intervals of MD04-2829CQ have been colour coded; the Hebrides Ice Stream and Donegal Bay end members are shown in black and each core is shown by an ellipse.....	99
Figure 6.16 Biplot of the PCA results of MD04-2829CQ and Minch end members. PC 1 explains 60% and PC 2 18% of the variance. Each core is shown by an ellipse and has been colour coded.....	99
Figure 6.17 Biplot of the PCA results of MD04-2829CQ and Minch end members. PC 1 explains 60% and PC 2 18% of the variance. The cores have been colour coded and further grouped by ellipses into broader age intervals (MD04-2829CQ) and Minch Ice Stream sediments.....	100
Figure 6.18 Biplot of the PCA results of MD04-2829CQ and Minch end members. PC 1 explains 60% and PC 2 18% of the variance. The cores have been colour coded and further grouped by ellipses into regional areas and MD04-2829CQ.....	101

Figure 6.19 Biplot of the PCA results of MD04-2829CQ and JC123-018VC. PC 1 explains 33% and PC 2 20% of the variance. The age intervals of the MD04-2829CQ have been colour coded and JC123-018VC is shown in black.....	101
Figure 6.20 Biplot of the PCA results of MD04-2829CQ and JC123-039VC. PC 1 explains 42% and PC 2 17% of the variance. The age intervals of the MD04-2829CQ have been colour coded and JC123-039VC is shown in black.....	102
Figure 6.21 Biplot of the PCA results of MD04-2829CQ and JC123-049VC. PC 1 explains 58% and PC 2 15% of the variance. The age intervals of the MD04-2829CQ have been colour coded and JC123-049VC is shown in black.....	102
Figure 7.1 Element concentration profiles A) JC106-051PC, Ca and Sr B) JC106-051PC, Ca and Fe C) JC123-031PC, Ca and Sr D) JC123-031PC, Ca and Fe.....	105
Figure 7.2 PCA biplots displaying internal elemental concentration and grain size variability for two Irish Sea Ice Stream cores as a function of stratigraphy. A) JC106-012VC B) JC106-018VC. Blue data points are proximal sediments transitioning to distal sediments (red data points). The remaining Irish Sea Ice Stream cores are shown by the yellow data points.....	107
Figure 7.3 PCA biplots displaying internal elemental concentration and grain size variability for two Irish Sea Ice Stream cores as a function of stratigraphy. A) JC106-033VC B) JC106-063VC. Blue data points are proximal sediments transitioning to distal sediments (red data points). The remaining Irish Sea Ice Stream cores are shown by the yellow data points.....	108
Figure 7.4 PCA biplots displaying internal elemental concentration and grain size variability for two Irish Sea Ice Stream cores as a function of stratigraphy. A) JC106-069VC B) JC106-073VC. Blue data points are proximal sediments transitioning to distal sediments (red data points). The remaining Irish Sea Ice Stream cores are shown by the yellow data points.....	109
Figure 7.5 PCA biplot for the Irish Sea Ice Stream sediment cores divided into regions. PC 1 explains 72% of the total variance in the dataset and PC 2 13%. Each core and region has been colour coded.....	110

Figure 7.6 Elemental concentrations for the Celtic Sea sediment cores have been integrated. The plots show the downcore variation of Ca and Sr for the six sediment cores.....	110
Figure 7.7 Elemental concentrations for the Celtic Sea sediment cores have been integrated. The plots show the downcore variation of Ca and Fe for the six sediment cores.....	111
Figure 7.8 Geological map of the Celtic Sea region. The key illustrates the main formations present (British Geological Survey, 2008).....	111
Figure 7.9 Boxplot displaying Fe concentrations of the 17 sediment cores from the former Irish Sea Ice Stream. The cores have been colour coded by region.....	112
Figure 7.10 Geological map of the Irish Sea region. The key illustrates the main formations present (British Geological Survey, 2008).....	113
Figure 7.11 PCA biplot for the Irish Sea Ice Stream sediment cores colour coded by grain size.....	113
Figure 7.12 PCA biplot for MD04-2820CQ. PC 1 summarises 45% of the total variance in the dataset and PC 2 16%. Heinrich events and the ambient clay-silt lithofacies have been colour coded. H1-Red, H2- Blue, H3- Green and H4 Purple. Post H1-Orange, Post H2- Yellow, Pre-H2- Pink, Post H4-Brown and Pre-H4 Grey.....	114
Figure 7.13 Lithostratigraphic core log for MD04-2820CQ. H1-Red, H2- Blue, H3- Green and H4 Purple. Post H1-Orange, Post H2- Yellow, Pre-H2- Pink, Post H4-Brown and Pre-H4 Grey. A) Arrows correspond to the stratigraphic position of the ambient samples that occur along the main SW Heinrich vector of the PCA in Figure 7.12. B) Arrows correspond to the stratigraphic position of the ambient samples that occur along the NW arm of the PCA in Figure 7.12.....	115
Figure 7.14 Biplots illustrating the PCA results obtained by integrating the shelf end members and MD04-2820CQ XRF data. MD04-2820CQ has been colour coded by its lithofacies and the Irish Sea Ice Stream end members are black and have been grouped into regions.....	117
Figure 7.15 Biplot displaying the results of a PCA analysing both the shelf end members and H2 samples from MD04-2820CQ. H2 sediments are black and the Irish Sea Ice Stream end members are colour coded by core. PC 1 explains 59% of the total variance, PC 2 25%.....	118

Figure 7.16 PCA for MD04-2820CQ and JC106-033VC, showing the nearest neighbour approach. Whichever depths within MD04-2820CQ plot most closely to JC106-033VC data points are assigned a JC106-033VC affinity. These are then plotted stratigraphically in Figure 7.17.....	118
Figure 7.17 Schematic diagram displaying the location of the cores analysed and the colour that has been assigned to individual cores. Using the nearest neighbour approach, it has been possible to fingerprint depths within MD04-2820CQ to geochemically similar shelf end members.....	119
Figure 7.18 PCA biplot displaying internal elemental concentration and grain size variability for one Donegal Bay ice lobe core as a function of stratigraphy JC106-102VC.....	120
Figure 7.19 PCA biplot displaying internal elemental concentration and grain size variability for one Hebrides Ice Stream core as a function of stratigraphy JC106-146VC.....	121
Figure 7.20 PCA biplot for the Hebrides Ice Stream and Donegal Bay sediment cores divided into regions. Each core and region has been colour coded.....	121
Figure 7.21 Geology of the northwestern margin of the BIIS. The key illustrates the main formations present. From Knutz <i>et al.</i> (2001).....	122
Figure 7.22 Boxplot displaying Fe concentrations of the nine sediment cores from the former Hebrides Ice Stream and Donegal Bay ice lobe. The cores have been colour coded by region.....	123
Figure 7.23 Geological map of the Malin Sea region. The key illustrates the main formations present (British Geological Survey, 2008).....	123
Figure 7.24 PCA biplot for the Hebrides Ice Stream and Donegal Bay sediment cores colour coded by grain size.....	124
Figure 7.25 PCA biplot for MD04-2822. The core has been colour coded by age intervals and further grouped into broader age intervals (14-24 kyr BP and 24-31 kyr BP).....	126
Figure 7.26 Biplot of the PCA results of MD04-2822 and Hebrides Ice Stream and Donegal Bay end members. Each core is shown by an ellipse and has been colour coded.....	127

Figure 7.27 Schematic diagram displaying the location of the cores analysed and the colour that has been assigned to individual cores. Using the nearest neighbour approach, it has been possible to fingerprint depths within MD04-2822 to geochemically similar shelf end members.....	128
Figure 7.28 Location map of Skye and northwest Scotland showing locations mentioned in text. LS-Loch Scavaig, WRR- Wester Ross Readvance limits. Arrows show generalized ice flow directions of the Minch Ice Stream, (MIS) and the Hebrides Ice Stream (BDIS) From Small <i>et al.</i> (2016).....	130
Figure 7.29 Location of sites with observations of relative sea-level change in Scotland from Shennan <i>et al.</i> (2006). Sites 11 (Arisaig) and 12 (Kentra) are referred to in text.....	131
Figure 7.30 PCA biplots displaying internal elemental concentration and grain size variability for two Minch Ice Stream cores as a function of stratigraphy. A) JC123-015VC B) JC123-039VC Blue data points are proximal sediments transitioning to distal sediments (red data points). The remaining Minch Ice Stream cores are shown by the yellow data points..	134
Figure 7.31 PCA biplot displaying internal elemental concentration and grain size variability of one Minch Ice Stream core as a function of stratigraphy JC123-049. Blue data points are proximal sediments transitioning to distal sediments (red data points). The remaining Minch Ice Stream cores are shown by the yellow data points.....	135
Figure 7.32 PCA biplot for the Minch Ice Stream sediment cores divided into regions. Each core and region has been colour coded.....	136
Figure 7.33 Boxplot displaying Fe concentrations of the seven sediment cores from the former Minch Ice Stream. The cores have been colour coded by region.....	136
Figure 7.34 Geological map of the Minch and the Hebrides Shelf. The key illustrates the main formations present (British Geological Survey, 2008).....	137
Figure 7.35 Sediment thickness map of the Minch and the Hebrides Shelf and the two main over-deepened basins (North Lewis Basin and North Minch Basin (Bradwell and Stoker, 2015).....	137
Figure 7.36 PCA biplot for the Minch Ice Stream sediment cores colour coded by grain size. ....	138

Figure 7.37 PCA biplot for MD04-2829CQ. PC 1 summarises 33% of the total variance in the dataset and PC 2 20%. The core has been colour coded by age intervals and further grouped into broader age intervals (18-22 kyr BP, 22-26 kyr BP and 26-30 kyr BP).	139
Figure 7.38 Biplot of the PCA results of MD04-2829CQ and Minch end members. PC 1 summarises 60% and PC 2 18%. The cores have been colour coded and further grouped by ellipses into broader age intervals (MD04-2829CQ) and Minch Ice Stream sediments.	140
Figure 7.39 Schematic diagram displaying the location of the cores analysed and the colour that has been assigned to individual cores. Using the nearest neighbour approach, it has been possible to fingerprint depths within MD04-2829CQ to geochemically similar shelf end members.	141
Figure 7.40 Reconstruction of the confluent British (BIS) and Fennoscandian Ice Sheets (FIS) at LGM (30–25 ka BP), with hypothesised flow lines from Bradwell <i>et al.</i> 2008. RB-Rosemary Bank; MIS-Minch Ice Stream; SS-Sula Sgeir Fan; R-Rona Wedge; F-Foula Wedge; NSF-North Sea Fan; FICIS-Fair Isle Channel Ice Stream.	142
Figure 7.41 Biplot illustrating the PCA results obtained by integrating XRF data from each ice stream. PC 1 explains 64% of the variance and PC 2 17%. Each ice stream has been colour coded.	145
Figure 7.42 Biplot illustrating the PCA results obtained by integrating XRF data from each ice stream. PC 1 explains 64% of the variance and PC 2 17%. Each ice stream has been subdivided into end members. These end members have been colour coded.	145
Figure 7.43 Biplot illustrating the PCA results obtained by integrating the XRF data from the three deep ocean cores excluding the Heinrich events in MD04-2820CQ. PC 1 summarises 34% of the variance and PC 2 22%. Each core has been colour coded.	147
Figure 7.44 Schematic diagram displaying the location of the cores analysed and the colour that has been assigned to individual cores. Using the nearest neighbour approach, it has been possible to fingerprint depths within MD04-2820CQ to geochemically similar shelf end members from the Hebrides Ice Stream and Donegal Bay.	148



Figure 7.45 Annual mean surface currents for level 1 (~15 m depth). Note the currents and land masses have been interpolated onto a regular latitude-longitude grid for ease of presentation (Bigg 2017, pers. comm.).....	151
Figure 7.46 Annual mean surface currents for level 2 (~45 m depth). Note the currents and land masses have been interpolated onto a regular latitude-longitude grid for ease of presentation and the additional almost exposed land compared to Figure 7.45 is Rockall Bank (Bigg 2017, pers. comm.).....	151
Figure 7.47 Schematic diagram displaying the location of the cores analysed and the colour that has been assigned to individual cores. Using the nearest neighbour approach, it has been possible to fingerprint depths within MD04-2820CQ to geochemically similar shelf end members from the Minch Ice Stream.....	152
Figure 7.48 Schematic diagram displaying the location of the cores analysed and the colour that has been assigned to individual cores. Using the nearest neighbour approach, it has been possible to fingerprint depths within MD04-2822 to geochemically similar shelf end members from the ISIS.....	153
Figure 7.49 Schematic diagram displaying the location of the cores analysed and the colour that has been assigned to individual cores. Using the nearest neighbour approach, it has been possible to fingerprint depths within MD04-2822 to geochemically similar shelf end members from the Minch Ice Stream.....	154
Figure 7.50 Schematic diagram displaying the location of the cores analysed and the colour that has been assigned to individual cores. Using the nearest neighbour approach, it has been possible to fingerprint depths within MD04-2829CQ to geochemically similar shelf end members from the ISIS.....	156
Figure 7.51 Reconstruction of ice-sheet extent and configuration for the Late Weichselian glacial maximum (MIS 3-2), in the North Sea Basin from Graham <i>et al.</i> 2011. The location of the Norwegian Channel Ice Stream is shown. This diagram separates the Moray Firth Ice Stream and the Witch Ground Basin Ice Stream, whereas this thesis refers to these ice streams collectively as the Fair Isle Channel Ice Stream.....	157
Figure 7.52 Schematic diagram displaying the location of the cores analysed and the colour that has been assigned to individual cores. Using the nearest neighbour approach, it has	

been possible to fingerprint depths within MD04-2829CQ to geochemically similar shelf end members from the Hebrides Ice Stream and Donegal Bay..... 158

Figure 7.53 Schematic diagram summarising the trajectories and fates of icebergs/IRD from the five end members. A) Pre-H4; B) H4-31 kyr BP. The figure displays the location of three deep ocean cores analysed and the five end members colour coded (Green-Irish Sea, Beige-Celtic Sea, Purple-Donegal Bay, Red-Malin Sea and Blue-Minch Ice Stream). Dashed lines-minor input, solid lines-significant input, question marks-possible/questionable trajectories..... 161

Figure 7.54 Schematic diagram summarising the trajectories and fates of icebergs/IRD from the five end members; 31-27 kyr BP. The figure displays the location of three deep ocean cores analysed and the five end members colour coded (Green-Irish Sea, Beige-Celtic Sea, Purple-Donegal Bay, Red-Malin Sea and Blue-Minch Ice Stream). Dashed lines-minor input, solid lines-significant input, question marks-possible/questionable trajectories..... 162

Figure 7.55 Schematic diagram summarising the trajectories and fates of icebergs/IRD from the five end members; 27-24 kyr BP. The figure displays the location of three deep ocean cores analysed and the five end members colour coded (Green-Irish Sea, Beige-Celtic Sea, Purple-Donegal Bay, Red-Malin Sea and Blue-Minch Ice Stream). Dashed lines-minor input, solid lines-significant input, question marks-possible/questionable trajectories..... 163

Figure 7.56 Schematic diagram summarising the trajectories and fates of icebergs/IRD from the five end members; 24-20 kyr BP. The figure displays the location of three deep ocean cores analysed and the five end members colour coded (Green-Irish Sea, Beige-Celtic Sea, Purple-Donegal Bay, Red-Malin Sea and Blue-Minch Ice Stream). Dashed lines-minor input, solid lines-significant input, question marks-possible/questionable trajectories..... 164

Figure 7.57 Schematic diagram summarising the trajectories and fates of icebergs/IRD from the five end members; 20-15 kyr BP. The figure displays the location of three deep ocean cores analysed and the five end members colour coded (Green-Irish Sea, Beige-Celtic Sea, Purple-Donegal Bay, Red-Malin Sea and Blue-Minch Ice Stream). Dashed lines-minor input, solid lines-significant input, question marks-possible/questionable trajectories..... 165

Figure 7.58 Schematic diagram summarising the trajectories and fates of icebergs/IRD from the five end members;15-14 kyr BP. The figure displays the location of three deep ocean cores analysed and the five end members colour coded (Green-Irish Sea, Beige-Celtic Sea, Purple-Donegal Bay, Red-Malin Sea and Blue-Minch Ice Stream). Dashed lines-minor input, solid lines-significant input, question marks-possible/questionable trajectories..... 166

## **List of tables**

Table 1. Summary table of core details..... 18

Table 2. Summary table of the average standard deviation of repeat measurements on certified reference materials analysed by the SPECTRO XEPOS XRF. Number of certified reference materials used, *N*. Reference material used: Stream73373, LGC6139, GBW7604, Rock73302, Tibet70317, Stream73309, GBW7602, Tibet70314, SJQNIST2709, GBW7605, NIST1632b, GBW7603, Carb70309, CRM7002, Rock73301, Carb70302, Tibet70319..... 26



# 1 Introduction

## 1.1 Rationale

The present ablation and dynamic thinning of contemporary ice sheets is occurring at rates much higher than expected (Rignot *et al.* 2011). Significant mass loss is taking place on both the Greenland and Antarctic ice sheets, which are impacting on future ice sheet extent and thickness (Mouginot *et al.* 2015; Joughin *et al.* 2014). The West Antarctic Ice Sheet (WAIS) is of particular concern due to its buttressed marine-terminating margin and inherent sensitivity to climate perturbations (Joughin and Alley 2011). However, due to the short duration of observational datasets, the ability to accurately predict the fate of these ice sheets and the ramifications on future sea-level change is limited (Bamber and Aspinall 2013). Crucial to interpreting these changes is a need for a better understanding of ocean-atmosphere-cryosphere interactions over millennial timescales to put these present-day observations into context. Reconstructing palaeo-ice sheets grants the opportunity to better understand global climate change over longer time scales and improve current ice sheet models (Stokes *et al.* 2015).

The former British-Irish Ice Sheet (BIIS) is known to have had a large marine-terminating margin and was comprised of several major ice streams (Bradwell *et al.* 2007; Dunlop *et al.* 2010; Clark *et al.* 2012; Chiverrell *et al.* 2013). These ice streams operated as fast flowing conduits draining the ice sheet. The mass balance of an ice sheet is fundamentally determined by these high flux corridors with repercussions for the overall stability of the ice sheet (Stokes *et al.* 2015). A greater understanding of palaeo-ice streams will improve our understanding of present-day ice-sheet behaviour (Stokes and Clark 2001) considering that more than 90 % of mass lost from the WAIS is through ice streams (Payne *et al.* 2004).

The ice-rafted detritus (IRD) record from the deep ocean has been used as palaeoclimatic proxy since the 1960s and has been instrumental in understanding the interactions involved in ocean-atmosphere-cryosphere linkages (e.g. Heinrich events) (Heinrich 1988; Bond *et al.* 1993; Broecker 1994). However, significant uncertainty remains over the glaciodynamic processes that result in IRD flux to the sea bed. This uncertainty has been highlighted by Scourse *et al.* (2009) whereby an increase in IRD flux could be the result of ice sheet growth (positive mass balance) or, conversely it could be the result of ice sheet collapse (negative mass balance). The indicative meaning of the IRD record is thus unclear. Scourse *et al.* (2009) propose a hybrid model in which IRD can be a function of both ice sheet growth or collapse, however this hypothetical model requires verification through field testing.

This PhD contributes to the NERC-funded BRITICE-CHRONO project. BRITICE-CHRONO aims to reconstruct the retreat stages of the BIIS from its maximum extent during the Last Glacial Maximum (LGM) until it backstepped onto land. Marine geophysics, sediment coring and an extensive dating programme have been used to explore the decay of the BIIS. With this extensive dataset, it will be possible to link the IRD flux record from the adjacent deep ocean cores to the detailed retreat stages of individual ice streams draining the BIIS. To date, IRD fingerprinting techniques have been unable to identify specific ice streams within the BIIS, only an ambient BIIS signal with the exception of the Irish Sea Ice Stream (ISIS) in which Cretaceous chalk is used as a diagnostic fingerprint (Scourse *et al.* 2009).

## **1.2 Project Aims**

This PhD thesis has one main aim: (1) to determine the indicative meaning of the IRD record in the deep ocean. This aim will be addressed by studying a collection of cores from both the continental shelf of the UK and Ireland and the deep ocean adjacent to the BIIS. The objectives of the project are summarised as follows:

To address Aim (1):

1. Use  $\mu$ XRF to determine the geochemical signature of the glacial sediments across the UK and Irish continental shelves;
2. Demonstrate the geochemical variations in the glacial end members within and between ice streams;
3. Use  $\mu$ XRF to determine the geochemical variability of adjacent deep ocean cores
4. Determine whether the offshore IRD record can be linked to the shelf glacial end members.

To address the aim, this study will test the hypothesis ‘IRD is a function of ice sheet growth or ice sheet collapse, or both’. To test this hypothesis, this study will build upon the premise of Farmer *et al.* (2003) whereby IRD reflects the local geology of a calving margin. Using this as a basis, this study proposes a hypothetical synthetic stratigraphy (Figure 1.1) and will explore the notion that if we can determine the geochemical signature of the shelf end members, they will be mirrored in the deep ocean cores (Figure 1.1). These end members will represent the position of the ice sheet’s calving margin and its growth and decay.



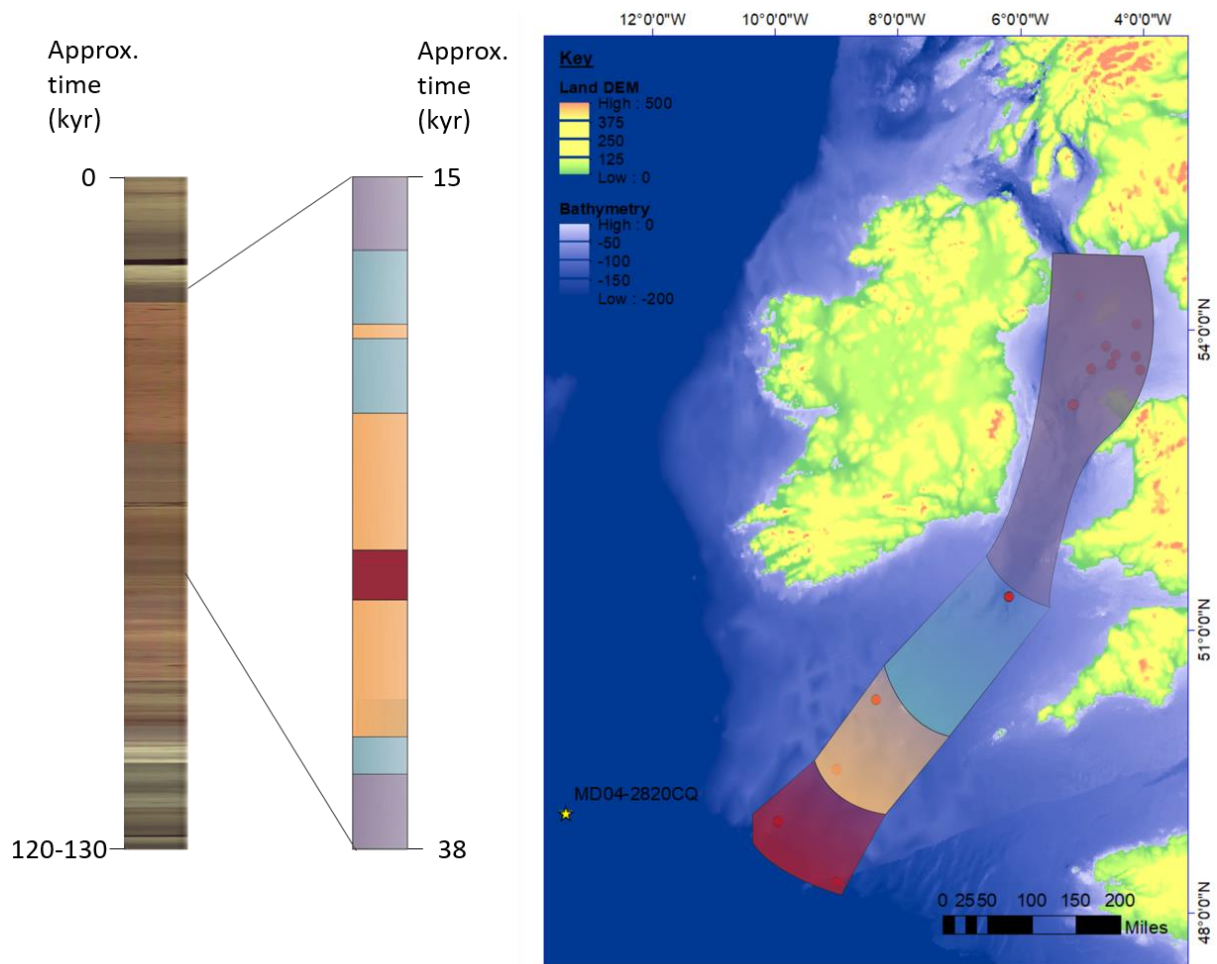


Figure 1.1 Photograph of MD04-2820CQ alongside a synthetic stratigraphy for the 15-38 kyr interval. The colours relate to the hypothetical shelf end members and represent the position of the ice stream's calving margin. Source of bathymetry: EMODnet Bathymetry Consortium (2016): EMODnet Digital Bathymetry (DTM). Source of land DEM: SRTM 90m DEM, NASA shuttle, version 2.1. All subsequent maps use the same bathymetry and land DEM and therefore the same source.

### **1.3 Thesis structure**

The principal findings of this study are structured in to four chapters (Chapters 4, 5 and 6). Chapters 4, 5 and 6 address Aim (1). Chapter 7 will interpret and discuss the results of Chapters 4, 5 and 6. While Chapter 8 will conclude the main scientific findings.

**Chapter 1** introduces the topics discussed in the subsequent chapters. This includes a review of IRD provenance analysis; the growth and decay of the BIIS; and an overview of the geology and palaeo-hydrography of the study area.

**Chapter 2** provides an overview of the materials and methods employed and the multivariate analysis performed.

**Chapter 3** presents the methodological considerations that need to be understood when analysing  $\mu$ XRF data. This chapter also presents the calibration of the  $\mu$ XRF scan data to dry mass concentration.

**Chapter 4** presents the results for the Irish Sea Ice Stream sector. These include: core logs; radiocarbon dates; geochemical data collected from both continental shelf cores and deep ocean core; and the statistical analysis performed.

**Chapter 5** presents the results from the Hebrides Ice Stream and Donegal Bay sector. These include: core logs; radiocarbon dates; geochemical data collected from both continental shelf cores and deep ocean core; and the statistical analysis performed.

**Chapter 6** presents the results from the Minch Ice Stream sector. These include: core logs; radiocarbon dates; geochemical data collected from both continental shelf cores and deep ocean core; and the statistical analysis performed.

**Chapter 7** interprets the results and discusses the findings in relation to the retreat/demise of the BIIS.

**Chapter 8** concludes the thesis and presents proposals for future work.

#### **1.4 Fingerprinting ice-rafted detritus**

IRD is not synonymous with just Heinrich events and the destabilisation of the Laurentide Ice Sheet but also the behaviour of the marine-terminating ice margins circum-North Atlantic (Peak *et al.* 2007). IRD located within the Ruddiman belt could originate from a variety of marine ice sheet margins and therefore one crucial element of analysis is to determine the source of the IRD and what the IRD flux indicates. Scourse *et al.* (2009) proposed a hybrid model whereby an increase in IRD flux could equally indicate an advancing or a collapsing ice margin. To verify this hypothetical model detailed provenance analysis must be undertaken to fingerprint IRD to its source area.

IRD is the sediment that is transported by icebergs and settles on the seafloor when the ice melts. IRD consists of all grain sizes, not limited to the  $>150\ \mu\text{m}$  fraction (Andrews 2000). The most important sources are ice stream termini. IRD is produced by the erosion and comminution of bedrock that gets subglacially entrained and transported by an ice sheet and then transported by icebergs when they calve off the margin (Farmer *et al.* 2003). Farmer *et al.* (2003) stated that deposits from glacial erosion correlate to the rock type located within 50-100 km of an ice margin and therefore, icebergs rafting from an ice sheet should thus carry predominantly 'local' material.

Studies analysing IRD provenance commonly use a light microscope to pick, count and identify IRD grain types however this method is very time consuming (Scourse *et al.* 2000; Knutz *et al.* 2001; Haapaniemi *et al.* 2010). Scourse *et al.* (2009) highlight the problems of solely relying on this approach when identifying IRD provenance in more distal areas; whereby a single lithic species could derive from a multitude of localities and is therefore not solely diagnostic of a particular ice stream. The authors discuss the importance of using additional fingerprinting techniques to help confirm provenance allocation. Additional methods for fingerprinting IRD include: radiogenic isotopes (e.g: Sm-Nd; Rb-Sr; Pb; and K/Ar) (Hemming 2004); magnetic properties (Peters *et al.* 2008; Walden *et al.* 2007) and X-ray diffraction (Andrews *et al.* 2011); these methods are also time consuming and can be destructive.

High resolution non-destructive  $\mu$ X-ray fluorescence ( $\mu$ XRF) core scanning is a fast and effective tool for palaeoclimate research. The variation in elements along a core profile can indicate environmental change, sedimentological change, pollution inputs and can also assist in core correlation.  $\mu$ XRF core scanners have become increasingly popular over the last decade due to rapidity of analysis and high stratigraphic resolution. This technique can be applied to a range of sediments from a multitude of different sedimentary environments.  $\mu$ XRF core scanning has been used to identify IRD within sediment cores by spikes in elements such as Ca, Fe, Sr, Ti/K (Prins *et al.* 2001; Peck *et al.* 2007; Van Rooij *et al.* 2007; Hodell *et al.* 2008; Jonkers *et al.* 2010; Mao *et al.* 2014; Plaza-Morlote *et al.* 2017), however it has not been previously used as a method for determining the provenance of IRD other than broad geographical regions e.g. continentally derived IRD (Jonkers *et al.* 2010).

$\mu$ XRF scan data has been increasingly used for determining the provenance of marine sediment such as turbidites (Rothwell *et al.* 2006), glacial debris-flows (Pope *et al.* 2016), or the origin of glacial deposits in lake settings (Wittmeier *et al.* 2015). This study aims to use  $\mu$ XRF to determine the provenance of IRD in the deep ocean and to fingerprint its geochemical signature to the individual ice streams draining the BIIS. IRD in the adjacent deep ocean cores to the BIIS have been analysed extensively (Scourse *et al.* 2000; Knutz *et al.* 2001; Peck *et al.* 2006; Peck *et al.* 2007; Walden *et al.* 2007; Peters *et al.* 2008., Hibbert *et al.* 2010; Scourse *et al.* 2009; Haapaniemi *et al.* 2010), but to date the geochemical compositional data does not allow the identification of specific ice stream sources (excluding the identification of ISIS by the presence of Cretaceous chalk by Scourse *et al.* 2009). Through using  $\mu$ XRF this study aims to determine the indicative meaning of the IRD record in the deep ocean and to improve our understanding of the collapse of the BIIS.

## **1.5 Western margin of the British Irish Ice Sheet**

Clark *et al.* (2012) highlighted that our knowledge of the offshore and marine sectors of the ice sheet margins for the BIIS are spatially incomplete and fragmentary. Considering that two thirds of the BIIS was marine based this is inhibiting for ice sheet reconstruction. The following sections aim to summarise our understanding of positions of the western ice margins of the BIIS at its last maximum extent and its subsequent retreat until it back stepped onto land (Figure 1.2).

### **1.5.1 Irish Sea Ice Stream**

The Irish Sea Ice Stream was the largest ice stream that drained the BIIS and therefore, its dynamism would have had internal repercussions for the BIIS as a whole (Patton *et al.* 2013). The ice stream was grounded but largely had a marine-terminating margin. The ice stream was fed by ice from the Scottish Highlands, the Lake District and Ireland (Chiverrell *et al.* 2013). The ice flowed south across the Irish Sea Basin and into the Celtic Sea, the southernmost extension of the BIIS (Scourse *et al.* 1990). The extent of this advance has been contested by the presence of glacial material across the shelf even at the shelf break. It has been proposed that during the LGM the ice sheet had a grounding-line position across the mid-shelf (Figure 1.2, blue line) and in this scenario glacial material at the shelf edge could derive from iceberg turbates and glacial marine deposits (Scourse *et al.* 1990; Scourse 1991). However, Praeg *et al.* (2015) have identified stratified diamicts at the shelf edge that are over consolidated and on this basis they propose that the ice stream reached the shelf edge (Figure 1.2, yellow line). A date from a single mollusc valve from glacial marine sediments indicates retreat by 24.3 kyr BP. Bayesian modelling (Figure 1.3) shows that the ice stream advanced into the Celtic Sea between 25.3-24.5 kyr BP (Chiverrell *et al.* 2013). This is supported by new geochronological data presented by Smedley *et al.* (2017) which demonstrates ice advancing to a limit across the northern Isles of Scilly at ~26 kyr BP. The timing of maximum extent coincides with the increase in IRD in the deep ocean (Scourse *et al.* 2009; Happoniemi *et al.* 2010) and the subsequent rapid collapse occurs after Heinrich event 2. The exact position of the ice margin is unknown (mid-shelf or shelf break position), however from the Bayesian modelling they infer the retreat was initially rapid, ~550 m a<sup>-1</sup>, but became progressively slower as the ice stream retreated between southern Ireland and Wales. However, in the northern Irish Sea Basin rates of retreat increased and the area was ice free by 23.7-22.9 kyr BP (Chiverrell *et al.* 2013).

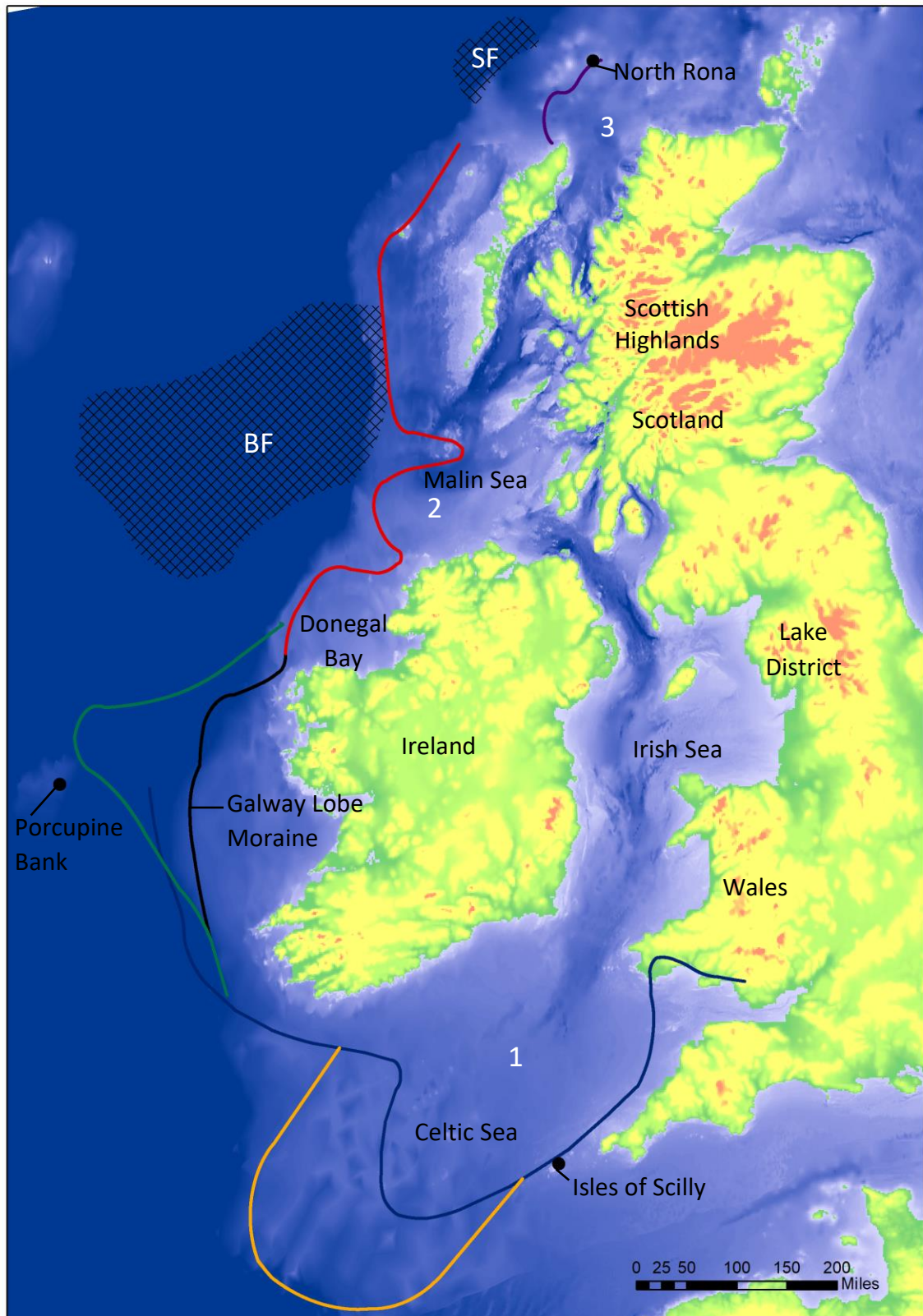


Figure 1.2 Map depicting conflicting models of maximum extent of the last BIIS as mentioned in the text; Smedley *et al.* 2017 (Blue line); Praeg *et al.* 2015 (Yellow line); Peters *et al.* 2015 (Green line); Sejrup *et al.* 2005; Scourse *et al.* 2009; Clark *et al.* 2012 (Black line); Small *et al.* 2016 (Red line) and Bradwell and Stoker 2015 (Purple line). Major ice streams are also included 1) Irish Sea Ice Stream 2) Hebrides Ice Stream and 3) Minch Ice Stream; and trough mouth fans BF: Barra Fan; SF: Sula Sgeir.



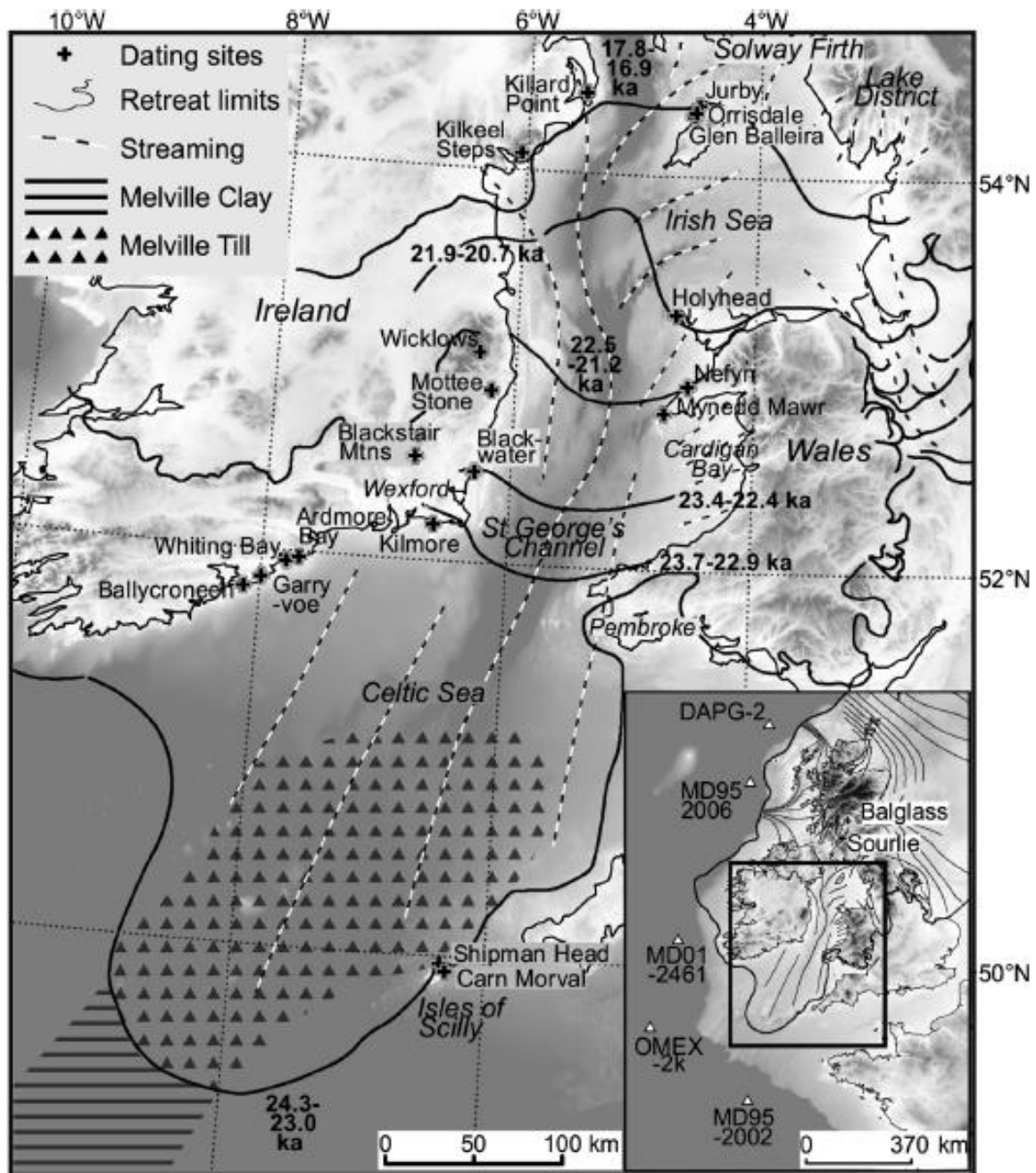


Figure 1.3 Various retreat margins of the Irish Sea Ice Stream showing the location of geochronological sites used for the Bayesian modelling and modelled ages for retreat (From Chiverrell *et al.* 2013).

### 1.5.2 Western Ireland and the Hebrides Ice Stream

Offshore western Ireland large moraine complexes span the continental shelf providing evidence for a grounded ice sheet. Previous reconstructions have placed the western ice sheet limit at the Galway Lobe Moraine (Sejrup *et al.* 2005; Scourse *et al.* 2009; Clark *et al.* 2012) (Figure 1.2, black line), however Peters *et al.* (2015) positioned the limit ~ 80 km further west (Figure 1.2, green line). A radiocarbon date from a highly consolidated till indicates the ice sheet advanced across the Porcupine Bank after 24.7 kyr BP and was deglaciating by 19.2 kyr BP. Estimated retreat of the ice across the shelf range from ~70 to 180 m a<sup>-1</sup> (Peters *et al.* 2015).

Further north, Ó Cofaigh *et al.* (2012) identified a suite of nested arcuate ridges offshore Donegal Bay and interpreted them as moraines. Analysis of these moraines indicate that the BIIS reached the shelf break in this region (Figure 1.2, red line) and retreat from the shelf edge occurred before 23 kyr BP (Purcell 2014). Rates of retreat were initially rapid and associated with iceberg calving as recorded by the iceberg ploughmarks distal to the outermost moraine (Ó Cofaigh *et al.* 2012). Retreat across the shelf was slow and punctuated by still stands as indicated by the presence of nested moraines and thick beds of laminated glacimarine sediments (Ó Cofaigh *et al.* 2012; Purcell 2014).

The Hebrides Ice Stream was grounded to the shelf break in the Malin Sea (Dunlop *et al.* 2010) (Figure 1.2, red line). Direct evidence from the glacial geomorphology across the shelf indicates the area was a zone of confluence for Irish and Scottish ice (Dunlop *et al.* 2010). IRD recovered from the Barra Fan (Figure 1.2) records major growth of the ice stream at around 29 kyr BP and a shelf break position by 27 kyr BP (Wilson and Austin 2002; Scourse *et al.* 2009). Iceberg furrows on the outer shelf indicate initial retreat was associated with iceberg calving (Dunlop *et al.* 2010). Evidence suggests deglaciation from the shelf edge at ~ 25 kyr BP with the ice attaining the present-day coastline position by 17-16 kyr BP (Clark *et al.* 2012; Hughes *et al.* 2016; Small *et al.* 2017). Geomorphological evidence indicates that initial retreat was rapid, followed by a slow punctuated retreat around bedrock obstacles (Dove *et al.* 2015; Small *et al.* 2016).

### **1.5.3 Minch Ice Stream**

The continental shelf offshore NW Scotland exhibits well preserved glacial sediment and landform assemblages interpreted to record the extension of the BIIS (Bradwell and Stoker 2015). The landforms indicate that the Minch Ice Stream flowed across the shelf depositing sediment in a large trough-mouth fan (Sula Sgeir Fan, Figure 1.2). Moraines across the shelf indicate past ice stream terminus positions. Bradwell and Stoker (2015) propose that the ice stream reached at least a mid-shelf position during the LGM (Figure 1.2, purple line), with outermost moraines from pre-MIS 2-3. Cosmogenic exposure ages from North Rona indicate that BIIS retreated from the mid-shelf area ~25 kyr BP (Everest *et al.* 2013). Radiocarbon dates from marine macro- and micro-fauna indicate open cold water conditions in the Minch at 15 kyr BP (Bradwell and Stoker 2015). The retreat across the central Minch may have been rapid as indicated by the absence of moraines. Bradwell and Stoker (2015) predict that the majority of the ice stream margin was floating during deglaciation, with significant calving occurring.

However, the large complex of moraines in coastal waters suggests a long-lived stillstand by a stable grounded marine-terminating ice sheet margin most likely between 16-22 kyr BP.

## **1.6 Geology**

The bedrock composition of the study area determines the geochemical composition of the glacial sediments across the continental shelf (Sheldon *et al.* 2016) and the IRD which calved from the BIIS (Farmer *et al.* 2003). It is therefore important to have a firm appreciation of the bedrock geology of the study area(s).

The Irish Sea Ice Stream basin can be divided into two sectors: The Celtic Sea and the Irish Sea. The geology of the Celtic Sea is characterised by Miocene mudstone and siltstone. There are also outcrops of Devonian and Carboniferous mudstones and sandstones, the Early Permian Haig Fras granite and Upper Cretaceous Chalk (Edwards *et al.* 1991; British Geological Survey, 2008). The Irish Sea can be subdivided into the Irish Sea Basin and the northern Irish Sea. The Irish Sea Basin is characterised largely by Cenozoic, Permo-Triassic and Jurassic mudstone and sandstone. The Northern Irish Sea is comprised of Cenozoic mudstone, sandstone and conglomerate and Carboniferous to Jurassic mudstone, sandstone, limestone, siltstone, halite, volcanics and slate. There are also outcrops of coal and to the east of Anglesey, the Monian supergroup (British Geological Survey, 2008).

The Malin Sea is comprised mainly of Lewisian gneiss and Permian to Paleogene mudstone, sandstone, siltstone, limestone and argillaceous rocks and the Dalradian supergroup. The Torridon group occurs in the northern sector of the Malin Sea alongside many igneous intrusions and lava formations (British Geological Survey, 2008). The bedrock geology of Donegal Bay is not documented however, the onshore geology of the region is predominantly Carboniferous limestone, sandstone and siltstone and Pre-Cambrian schist and gneiss with quartzite (Geological Survey of Ireland, 2014). There are also igneous intrusions of Ordovician to Devonian granite along the northwest coast of County Donegal (Geological Survey of Ireland, 2014).

The geology of the Minch can be divided into five regions. The Hebrides shelf is characterised by Permo-Triassic conglomerate, sandstone, siltstone and mudstone, Jurassic argillaceous rocks with subordinate sandstone and limestone and Lewisian gneiss. Whereas the continental shelf break is dominated by Eocene to Pliocene argillaceous rocks and sandstone. The Minch is mainly Jurassic argillaceous rocks with subordinate sandstone, limestone and mudstone with outcrops of Torridon group sandstone and igneous intrusions. The Torridon group extends along the coastline of the Eastern Minch and there are outcrops of Scourian



gneiss. The coastline of Cape Wrath is characterised by Precambrian to Ordovician rocks (British Geological Survey, 2008).

### **1.7 Palaeo-hydrography**

Proxy reconstructions suggest that North Atlantic Ocean circulation was different during the LGM in comparison to contemporary circulation (Hebbeln *et al.* 1998; Bauch *et al.* 2001). The Atlantic Meridional Overturning Circulation (AMOC) is an important element of the climate system because it is associated with a net northward transport of heat (Lynch-Stieglitz *et al.* 2007). The AMOC comprises the Gulf Stream and the North Atlantic Current which transports warm water northwards which then cools and sinks and forms the North Atlantic Deep water (NADW). The NADW is the southward-flowing cold nutrient-poor water (Buckley and Marshall 2016). During the LGM it has been documented that the NADW was displaced upwards into shallower, intermediate waters by nutrient rich waters from the Southern Ocean forming the Glacial North Atlantic Intermediate Water (GNAIW) (Marchitto and Broecker 2006), however the LGM strength of the AMOC is still contested as discussed by Lippold *et al.* (2012). Some studies argue for a weaker AMOC (Hesse *et al.* 2011), whilst others argue for a similar, or even stronger, formation rate than the present day (Hewitt *et al.* 2003). Lynch-Stieglitz *et al.* (2007) contests these notions stating that the AMOC was neither completely sluggish nor stronger than the present day. However, because IRD flux is conditioned by iceberg trajectories and determined by ocean currents, the focus here will be on the strength and direction of surface currents during the LGM (Bigg *et al.* 1997). These surface currents transport icebergs across the ocean to zones of melting or grounding (Watkins *et al.* 2007). Using patterns of IRD deposition across the North Atlantic, Ruddiman (1977) and Grousset *et al.* (1993) determined that an anti-clockwise surface gyre was active during the LGM. For the purpose of this study, this suggests icebergs calving from the BIIS will predominantly travel northwards along the margin, thus there will be a dilution of source material in the deep ocean cores by other southerly ice streams such as the Irish Sea Ice Stream.

### **1.8 Conclusions**

The BIIS was a relatively small but dynamic ice sheet with 2/3 of the ice sheet marine based, it is an important example of how marine influenced ice sheets deglaciates. Reconstructing the behaviour of palaeo-ice streams operating in marine based sectors (such as the ISIS, the Hebrides Ice Stream and the Minch Ice Stream) will greatly inform our understanding of present-day ice sheet behaviour. Analysing marine sediment cores provides a means of

developing a greater understanding of the collapse of the BIIS. Using  $\mu$ XRF to fingerprint IRD to the individual ice streams draining the BIIS will help to determine the indicative meaning of the IRD record and how it relates to the collapse of the BIIS. These techniques will be discussed in the following chapter.



## 2 Materials and Methodology

### **2.1 Introduction**

The data collected during this study involved a dataset of thirty five continental shelf cores and three deep ocean cores from UK and Irish waters. This chapter describes the core locations, the techniques used to fingerprint the IRD flux in the deep ocean including methods of multivariate analysis.

### **SEQUOIA programme**

The three deep ocean cores analysed for this study (MD04-2820CQ, MD04-2822 and MD04-2829CQ, Figure 2.1, Table 1) were recovered by the R.V. *Marion Dufresne* in 2004. This cruise was organised as part of the SEQUOIA (Sequencing Ocean-Ice Interaction) programme. The aim of the cruise was to investigate the ice-ocean-climate interaction in the NE Atlantic over the last 60 kyr BP. The cruise focused on the interaction between the thermohaline-circulation, ice sheet behaviour and climate. The NE Atlantic is a prime setting for reconstructing past ice-ocean-climate interactions because of its proximity to the gulf stream and it is the location of large swathes of IRD from both the Laurentide Ice Sheet and the British Irish Ice Sheet (Stewart, 2004).

A total of twenty one cores were extracted from around the UK and Ireland using either a CALYPSO II corer or a CASQ giant box coring device. MD04-2820CQ (a giant box core) was extracted from the lower continental slope region of the Goban Spur (49° 04.18'N 13°

24.77°W). The core is 10.04 m in length and was taken at a water depth of 3633 m. The record extends to Marine Isotope Stage 6 (Scourse *et al.* 2009). The core was split and logged on board the research vessel. MD04-2822 (a giant piston core) was extracted from the Rockall Trough, along the distal margin of the Barra-Donegal Fan (56° 50.54' N, 11° 22.96' W). The core is 37.7 m in length and was taken at a water depth of 2344 m (Hibbert *et al.* 2010; Channell *et al.* 2016). The record extends to 195 kyr BP. MD04-2829CQ (a giant box core) was extracted from Rosemary bank (58° 56.93' N, 9° 34.30' W). The core is 10.08 m in length, extending to ~41.1 kyr BP and was taken at a water depth of 1743 m.

### **BRITICE-CHRONO**

The thirty five continental shelf sediment cores analysed for this study were recovered on the RRS James Cook (JC106/JC123) in 2014/2015 (BRITICE-CHRONO cruise report 2014/2015) (Figure 2.1; Table 1). These two cruises were organised as part of the BRITICE-CHRONO consortium to fulfil the marine component of the fieldwork. The aim of the cruises was to collect and date material to constrain the timing and rates of change of the BIIS. During JC106 geophysical data were collected from a Kongsberg SBP-120 sub-bottom profiler and multibeam echo sounder systems EM120 and EM710. A total of two hundred and twenty three cores were recovered using a British Geological Survey (BGS) 6 m long vibrocorer system and National Marine Facilities Sea Systems (NMFSS) 12 m piston corer. During JC123 geophysical data were collected from a Kongsberg SBP-120 sub-bottom profiler and an EM710 multibeam echo sounder system. A total of one hundred and seventy nine cores were recovered using a BGS 6 m long vibrocorer and NMFSS 9-15 m piston corer.

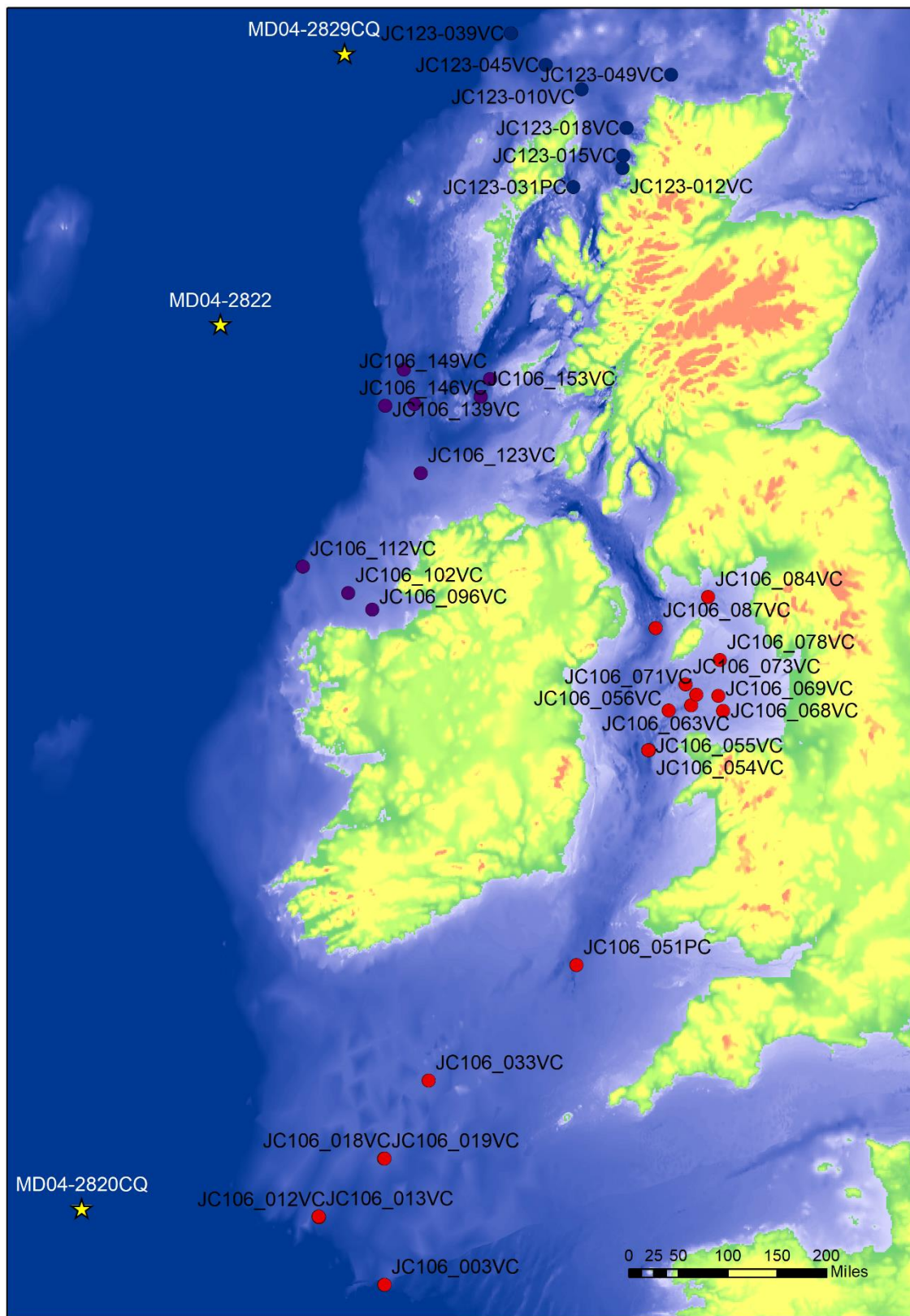


Figure 2.1 Location map showing the locations of the deep ocean cores MD04-2820CQ, MD04-2822 and MD04-2829CQ; and the continental shelf cores analysed within this study. The continental shelf cores are divided into three areas: the Irish Sea Ice Stream (Red circles); the Hebrides Ice Stream and Donegal Bay ice lobe (purple circles) and the Minch Ice Stream (pink circles).

Table 1. Summary table of core details.

Study area	Core name	Latitude	Longitude	Water depth	Length of core (m)	Coring technique
Continental shelf cores						
Irish Sea Ice Stream	JC106-003VC	48.32403	-8.99061	211	1.65	Vibro core
Irish Sea Ice Stream	JC106-012VC	48.97906	-9.94756	170	1.59	Vibro core
Irish Sea Ice Stream	JC106-013VC	48.98537	-9.95148	168	3.3	Vibro core
Irish Sea Ice Stream	JC106-018VC	49.54034	-8.99374	146	1.86	Vibro core
Irish Sea Ice Stream	JC106-019VC	49.53904	-8.99170	145	1.62	Vibro core
Irish Sea Ice Stream	JC106-033VC	50.27430	-8.34522	132	1.82	Vibro core
Irish Sea Ice Stream	JC106-051PC	51.34570	-6.18485	116	6.29	Piston core
Irish Sea Ice Stream	JC106-054VC	53.26616	-5.12741	146	3.19	Vibro core
Irish Sea Ice Stream	JC106-055VC	53.26718	-5.13792	160	1.31	Vibro core
Irish Sea Ice Stream	JC106-056VC	53.61575	-4.83919	65	5.50	Vibro core
Irish Sea Ice Stream	JC106-063VC	53.65871	-4.50771	91	5.77	Vibro core
Irish Sea Ice Stream	JC106-068VC	53.61113	-4.04128	49	3.05	Vibro core
Irish Sea Ice Stream	JC106-069VC	53.74102	-4.11442	47	0.71	Vibro core
Irish Sea Ice Stream	JC106-071VC	53.75242	-4.43444	61	4.84	Vibro core
Irish Sea Ice Stream	JC106-073VC	53.84030	-4.59079	67	4.04	Vibro core
Irish Sea Ice Stream	JC106-078VC	54.04859	-4.09088	41	0.74	Vibro core
Irish Sea Ice Stream	JC106-084VC	54.58745	-4.26520	63	4.48	Vibro core
Irish Sea Ice Stream	JC106-087VC	54.32303	-5.03023	133	5.20	Vibro core
Donegal Bay	JC106-096VC	54.48188	-9.16968	75	3.06	Vibro core
Donegal Bay	JC106-102VC	54.62345	-9.51890	90.5	2.52	Vibro core
Donegal Bay	JC106-112VC	54.84513	-10.18137	125	1	Vibro core
Hebrides Ice Stream	JC106-123VC	55.62552	-8.46130	91	1.435	Vibro core

Hebrides Ice Stream	JC106-129VC	56.18944	-8.55304	130	1.33	Vibro core
Hebrides Ice Stream	JC106-139VC	56.17709	-8.97967	148.8	3.67	Vibro core
Hebrides Ice Stream	JC106-146VC	56.47296	-8.70696	150	4.14	Vibro core
Hebrides Ice Stream	JC106-149VC	56.39728	-7.44881	136	4.5	Vibro core
Hebrides Ice Stream	JC106-153VC	56.25168	-7.58738	113.5	3.35	Vibro core
Minch Ice Stream	JC123-010VC	58.66957	-6.10917	123.5	5.36	Vibro core
Minch Ice Stream	JC123-012VC	58.06561	-5.5139	68.1	2.55	Vibro core
Minch Ice Stream	JC123-015VC	58.16218	-5.50133	119.5	3.86	Vibro core
Minch Ice Stream	JC123-018VC	58.37602	-5.45453	113	5.24	Vibro core
Minch Ice Stream	JC123-031PC	57.9188	-6.22988	125	6.55	Piston core
Minch Ice Stream	JC123-039VC	59.09388	-7.14055	183	3.95	Vibro core
Minch Ice Stream	JC123-045VC	58.85708	-6.63305	142.5	4.94	Vibro core
Minch Ice Stream	JC123-049VC	58.78002	-4.80542	86.5	2.37	Vibro core
Deep ocean cores						
Goban Spur	MD04-2820CQ	49.0697	-13.4128	3633	10.04	Giant box core
Rockall Trough	MD04-2822	56.8423	-11.3827	2344	37.7	Giant piston core
Rosemary Bank	MD04-2829CQ	58.9488	-9.57167	1743	10.08	Giant box core

## **2.2 Fingerprinting ice-rafted detritus**

The BIIS was a highly dynamic ice sheet with a relatively large proportion of its margin terminating in the ocean. The marine terminating margins would have been major sources of IRD to the deep ocean reflecting the retreat/readvance phases of the ice sheet (Scourse *et al.* 2009). Fingerprinting the source of the IRD in the adjacent deep ocean cores to individual ice streams has the potential to establish any marine margin instabilities within the BIIS and determine the synchronicity between the various ice streams. The IRD characterising any individual ice stream will be sourced mainly from local glacial erosion of the continental shelf and landmass within the catchment of the ice stream (Farmer *et al.* 2006; White *et al.* 2016)



(except for Heinrich events), hence the geology of the continental shelf and adjacent landmass will determine the composition of the glacial sediments and the IRD calving from any particular ice stream. It can be assumed that the ambient IRD signal will be from the proximal ice stream; there will be far-field IRD but, excluding Heinrich events, the majority will be sourced from the BIIS. Fingerprinting IRD in the adjacent deep ocean requires a two-step approach: 1) to geochemically characterise the presumed source material; and 2) to geochemically characterise the IRD signature in the deep ocean. These two approaches will be explained further below and the results presented in Chapters 4, 5 and 6.

### **2.2.1 Geochemical signature of the shelf end members**

#### **Core locations**

Marine sediment cores were collected on RRS James Cook cruise JC106/JC123 in 2014/2015 (BRITICE-CHRONO cruise report 2014/2015) (Figure 2.1; Table 1). Core locations were chosen based on sub-bottom profiles to capture the transition from basal till to glacimarine sediments. These sediments were recovered using a vibrocorer and a piston corer. The cores were split and visually described aboard both research cruises.

#### **Core Selection**

For the purpose of this study, cores were selected based on location, glacial lithofacies and geochronology. Cores were selected along the central flow pathway of the ice streams with additional cores collected perpendicular to ice stream flow to characterise the local catchment geology and to determine the spatial variability in their geochemical signature. Core logs and radiocarbon dates were compiled for BRITICE-CHRONO by BRITICE-CHRONO team members (radiocarbon dates in Appendix 1). These data were used to select cores with appropriate glacial lithofacies. Glacimarine and waterlain diamict lithofacies were the focus of analysis as they represent the ice-rafted detritus calving from the margin (Farmer *et al.* 2003). These lithofacies represent the continental shelf glacial end members and the source of the offshore IRD flux.

#### **Radiocarbon dates**

Radiocarbon dates were obtained from samples of marine carbonate (single or broken valves) and benthic foraminifera by BRITICE-CHRONO. A total of 38 radiocarbon dates were obtained for the cores which are the focus of this study. Radiocarbon sampling targeted lithofacies boundaries or the base of a core when it bottomed out in deglacial sediment, to

provide a minimum age constraint for ice sheet retreat. The radiocarbon dates have been corrected for isotopic fractionation and calibrated using the Marine13 calibration curve which has a marine reservoir effect (MRE) correction of 400 years.  $\Delta R$  values are the regional deviations in the marine radiocarbon reservoir age from the modelled reservoir age produced by Marine13. All radiocarbon dates have been corrected using a  $\Delta R$  of 0 in this study, however  $\Delta R$  values of 300 and 700 are also reported (Appendix 1) to assess the potential variability of the MRE in the North Atlantic during the collapse of the BIIS (Wanamaker *et al.* 2012). In contrast to the deep ocean, the reservoir age of shelf seas are controlled by shelf hydrodynamics not deep ocean circulation. In well-ventilated shallow settings  $\Delta R$  can be close to 0 whereas stratified waters will have elevated reservoir ages; this is further complicated by meltwater from glacial margins. Glacial meltwater can elevate the reservoir age by forming a ‘meltwater lid’ which inhibits the exchange with the atmosphere (Voelker *et al.* 2000). During the last glacial substantial meltwater release disrupted deep water ventilation resulting in the breakdown of the AMOC thereby restricting the exchange with the atmosphere and elevating reservoir ages (Peck *et al.* 2006). Also, meltwater/icebergs may contain aged  $\text{CO}_2$  which can bias the  $\text{CO}_2$  concentrations of (sub)surface water (Voelker *et al.* 2000; Peck *et al.* 2006).

#### XRF geochemistry

XRF is the excitation of a sample by a primary X-ray source. This generates secondary (fluorescent) X-rays which are characteristic for the elements present within the sample. The XRF spectra produced indicate the elements present and their concentration (Boyle *et al.* 2000). The geochemical composition of the shelf cores was determined using two different  $\mu\text{XRF}$  instruments, one to determine the wet geochemistry of the sediment cores and the other to develop a training set for the calibration of the wet scan data. All of the wet sediment cores were analysed using a non-destructive Olympus DELTA handheld energy dispersive XRF (ED-XRF) gun mounted onto a GEOTEK core scanner (University of Liverpool). The split cores were analysed using a 4-watt rhodium X-ray tube and a thermoelectrically cooled large area Si drift detector. Cores were scanned at a 0.5 cm resolution in soil mode (15, 40, 40 (filtered) kV beam conditions) each beam for 20 seconds. Data output from the Olympus DELTA is in the form of elemental concentrations based on internal calibrations from raw X-ray spectra.

To calibrate these  $\mu\text{XRF}$  scan data to mass specific values a calibration training set is subsampled from a selection of cores. The subsamples (5 cm<sup>3</sup>) were weighed, freeze-dried and re-weighed to measure water content and were then homogenised using a pestle and mortar.

These loose powders are then transferred to powder cups prepared with 6  $\mu\text{m}$  polypropylene film. A SPECTRO XEPOS energy dispersive XRF spectrometer was used at the University of Liverpool to measure dry mass specific geochemistry. The Spectro XEPOS ED-XRF emits a combined binary Pd and Co excitation radiation and has a high resolution low spectral interference silicon drift detector. Each sample was measured for 600 s. The XRF analyser undergoes a daily standardisation procedure using certified reference materials (Boyle *et al.* 2015). Tests to correct for water content using the training set are outlined in Chapter 3.

### **2.2.2 Fingerprinting the ice-rafted detritus record in the deep ocean**

#### **Core locations**

The deep ocean cores analysed for this study are: MD04-2820CQ; MD04-2822 and MD04-2829CQ (Figure 2.1; Table 1). These cores were selected because they are adjacent to each of the major ice streams that are the focus of this study and will therefore be sentinels for IRD deposition from the respective ice streams.

#### **Age control**

To assess the timing of IRD flux to the deep ocean core sites it is necessary to establish age control. The age control for MD04-2822 and MD04-2829CQ have both been published (Abbott *et al.* 2013; Hall *et al.* 2011). The MD04-2822 age model is based on the tuning of % Nps to the NGRIP  $\delta 18\text{O}$  on the GICC05 age model, further details provided in Abbott *et al.* (2013). The MD04-2829CQ age model is based on 24 AMS  $^{14}\text{C}$  dates and the tuning of % Nps to GISP 2, further details provided in Hall *et al.* (2011). There is no published age model for MD04-2820CQ, age control was provided by determining the location of Heinrich events. The Heinrich events were identified by using the XRF scan data in addition to previous analysis of these horizons (Lopez 2004; Happoniemi 2006; Cooke 2008).

#### **$\mu\text{XRF}$ geochemistry**

To determine the geochemical fingerprint of the IRD in relation to the demise of the BIIS, this study will focus on the 38-14 kyr interval in the deep ocean cores. MD04-2829CQ was scanned at the University of Liverpool using the same method as detailed above (Olympus DELTA handheld gun mounted onto a GEOTEK core scanner) at a 0.5 cm resolution. MD04-2820CQ was scanned at Aberystwyth University using an ITRAX core scanner by Francis Cooke (Appendix data CD). Core sections were analysed at a 1 cm resolution, with a 20 second count time; excluding section 1.5-3 m which was scanned at 0.5 mm with an exposure time of 20 seconds. The ITRAX has a 3kW Mo X-ray tube which operates at 30kV. MD04-2822 was

scanned using ITRAX core scanner at BOSCORG, Southampton by Fiona Hibbert (Appendix data CD). The ITRAX has a 3kW Mo X-ray tube which operates at 30kV and 30 mA with a 40 s count time. The core was scanned at a 1 cm resolution. The ITRAX output is in a counts per second format, in contrast to the elemental concentrations derived from the other XRF methods used. These differences in output necessitate the need for calibration so direct comparison can be made between datasets. A training set was also developed for each deep ocean core using subsamples. These were analysed using the same method outlined previously using the SPECTRO XEPOS. Tests to correct for water content using the training set are outlined in Chapter 3.

### **2.2.3 Multivariate analysis**

The wet XRF scan data was corrected for water content and converted to dry mass concentration using the procedure that will be outlined in Chapter 3. The corrected XRF data from the continental shelf cores were then averaged every 2.5 cm to reduce the number of data points. These data were then analysed using the R software programme. Due to the large spread in data, all values were standardised before performing multivariate analysis. Standardising involves calculating the mean and standard deviation of the entire vector then scale each element by those values by subtracting the mean and dividing by the standard deviation. For large multivariate datasets reducing the data complexity is necessary to assess the patterns within the data (Syms, 2008). Principal Component Analysis (PCA) was used to explore the geochemical composition of the continental shelf cores and the deep ocean cores. The aim of these analyses was to assign a geochemical signature to the continental shelf end members and to identify the influence of these end members in the deep ocean cores thereby attributing IRD to specific ice stream sources.

### **2.2.4 Grain size**

Grain size classifications of the cores analysed were determined by using the core logs (which were produced by Callard, Ó Cofaigh, Saher and Schiele). As discussed in section 2.2.3, the corrected XRF data were averaged, consequently the grain size classifications were also averaged over 2.5 cm.



## **3 Methodological considerations**

The aim of this chapter is to address the methodological uncertainties associated with  $\mu$ XRF scanning. This chapter also outlines the calibration approach utilised to convert wet sediment concentrations to dry mass equivalent concentrations.

### **3.1 Quality control**

Consistency checks have been performed for the SPECTRO XEPOS using a set of 17 certified reference materials (CRMs) (Table 2). CRMs are a reliable way to calibrate instruments for sediment analysis. The elemental concentrations of these samples are known and therefore the data generated can be compared to the certified values.

		Average St Dev	N
K	mg/g	0.12	17
Ca	mg/g	0.30	17
Ti	µg/g	6.16	17
Mn	µg/g	6.47	17
Fe	mg/g	0.05	17
Cu	µg/g	0.45	17
Zn	µg/g	0.94	17
Rb	µg/g	0.30	17
Sr	µg/g	0.87	17
Y	µg/g	0.12	17
Zr	µg/g	1.43	17

Table 2. Summary table of the average standard deviation of repeat measurements on certified reference materials analysed by the SPECTRO XEPOS XRF. Number of certified reference materials used, *N*. Reference material used: Stream73373, LGC6139, GBW7604, Rock73302, Tibet70317, Stream73309, GBW7602, Tibet70314, SJQNI2709, GBW7605, NIST1632b, GBW7603, Carb70309, CRM7002, Rock73301, Carb70302, Tibet70319.

### **3.2 Artifacts in micro XRF scan data**

Care must be taken when interpreting micro XRF scan data due to the presence of artifacts. Artifacts in µXRF scan data may occur due to sediment surface heterogeneity, grain size and surface roughness (Hennekam and De Lange 2012; Rothwell and Croudace 2015). These problems do not occur when using conventional XRF. Deviations because of surface heterogeneities can be limited by analysing flattened surfaces and fine grain size particles (such as clays and silts). In contrast, coarser sediments will increase surface roughness and sample heterogeneity problems due to enhanced radiation scatter (Jansen *et al.* 1998; Richter *et al.* 2006). Particle size is an issue that needs to be addressed in this study. The particle size variation for the deep ocean cores is minimal so an effect on the X-ray signal is not expected. However, the glacial sediments across the continental shelf display large particle size variations. This study is mainly focusing on the glacial marine mud lithofacies and muddy diamicts, however some coarser grained lithofacies are incorporated into the analysis. Measurements on clasts were excluded from analysis by visual inspection of core images and XRF scan data. Many provenance studies have highlighted the impact of grain size in provenance determinations (Bloemsma *et al.* 2012; von Eynatten *et al.* 2012). Von Eynatten *et al.* (2012) advise caution when determining provenance without strict grain size control, because grain size can have a strong influence on sediment composition. Natural biases occur in provenance data because of the physical properties of the source lithology and how easily

their constituent minerals are weathered (Licht and Hemming, 2017). Licht and Hemming (2017) review provenance methods that have been applied to glacial sediments in Antarctica. Their analysis also highlights that in glacial settings it is important to understand glacial erosion, bed conditions (hard or deformable), bed topography and basal ice temperatures; because these parameters all have an impact on the provenance of glacial sediments.

### **3.3 Correlation matrices**

Provenance determination relies on the analysis of key lithogenic elements such as Al, Si, K, Ti, Fe, Rb and Zr. Ti, Rb and K are often associated with clay mineral assemblages whereas Zr and Si are usually linked to coarser silt and sand sized fractions (Kylander *et al.* 2011). Rothwell and Croudace (2015) discuss extensively the use of elemental proxies and their application and interpretation; for example, Zr/Rb can be used as a grain size proxy because Zr is enriched in coarse sediment (because zircon is a resistant mineral), whereas Rb is associated with clays. Ca is a proxy for carbonate content but can be either biogenic or detrital in origin. Biogenic Ca would co-vary with Sr and negatively correlate with Fe (a terrigenous indicator), whereas detrital Ca would co-vary with Fe.

Figure 3.1 displays the core log and raw XRF data for core JC106-068VC. The core has a diamict lithofacies at the base which sharply transitions into a fining upwards sandy mud. The next lithofacies is a laminated clay with two sand layers and a sand unit between 1.05-1.32 m. The uppermost lithofacies is a coarse gravel with shell fragments. These lithofacies are clearly visible in the raw XRF data. The Zr/Rb ratio distinguishes between the coarser lithofacies and finer lithofacies. The Ca/Fe profile reflects marine productivity and terrigenous input. The increase in Ca/Fe in the uppermost lithofacies indicates a transition to Holocene sediment (Kuijpers *et al.* 2003). The Ti profile does not co-vary with the Zr/Rb, Ca/Fe and Zr profiles and is a useful indicator of terrigenous sediment flux.



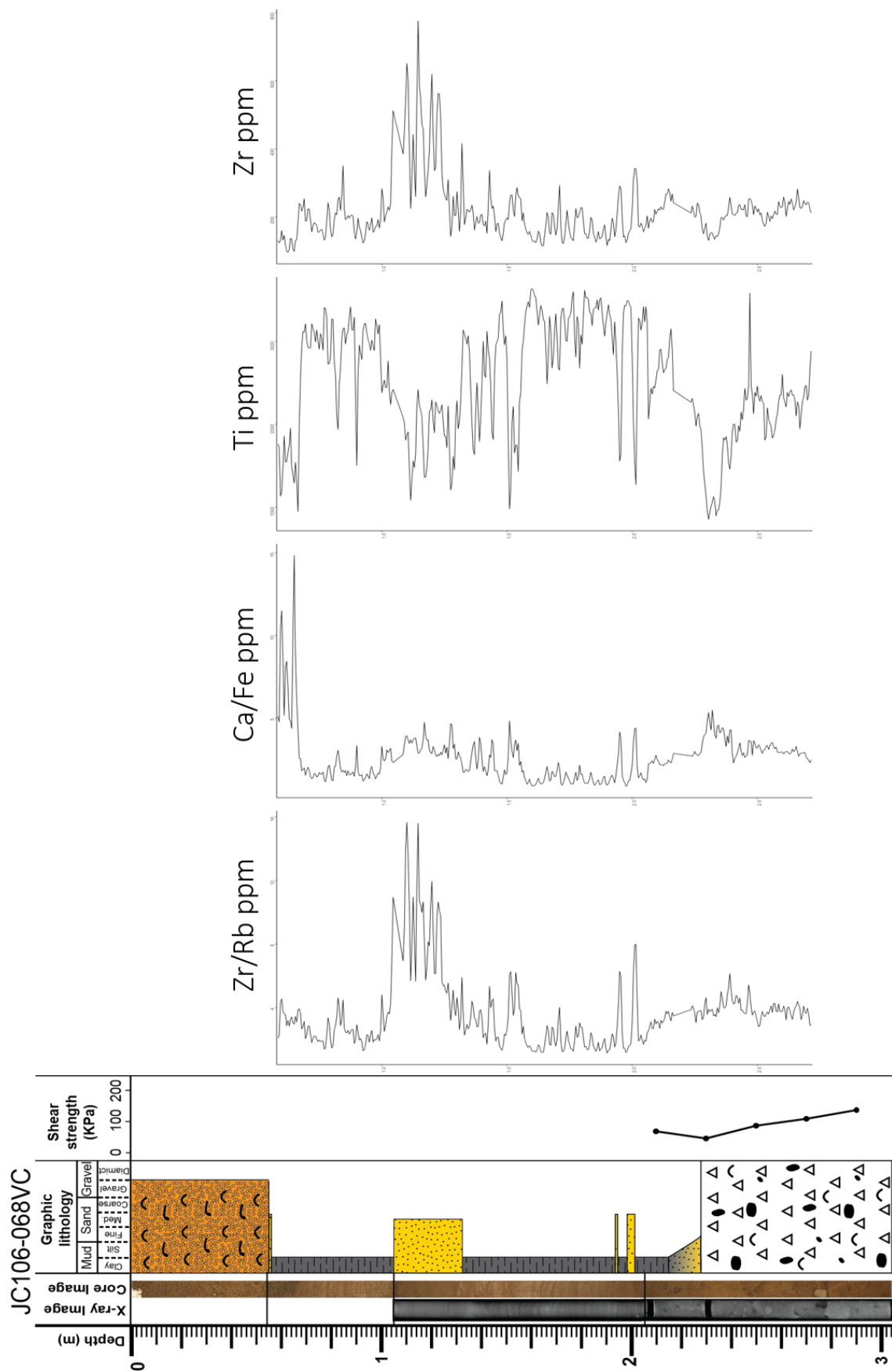


Figure 3.1. Ti, Zr peaks and Zr/Rb, Ca/Fe ratios vs lithostratigraphic core log JC106-068VC. Core log produced by Margot Saher.

Figure 3.2 displays the core log and raw XRF data for core JC106-084VC. The core has a diamict lithofacies at the base overlain by a fine sand and a coarsening upwards silty clay mud. From 1.90 m upwards there are silt laminae and coarse sand inclusions from 0.80 m. The top of the core is a coarse sand. The Ca and Zr/Rb profiles co-vary reflecting the different lithofacies and higher carbonate content in the coarser sediments. The Fe/Rb and Ti profiles also co-vary, highlighting variations in terrigenous input and clay content. Figure 3.3 displays the core log and raw XRF data for core JC106-063VC. The core mainly consists of laminated mud overlain by 0.68 m of coarse gravel. The Zr/Rb profile illustrates the XRF signature of the laminated mud.

### **3.4 Adjusting for water content**

Core scanners are quick and effective methods for generating high-resolution geochemical records, however due to the water content within the sediment cores the data remains semi-quantitative (Weltje and Tjallingii, 2008). Unlike conventional XRF which produces dry mass concentrations, the wet scan data is diluted by water and this influences the elemental concentration detected. Kido *et al.* (2006) highlighted the need to quantify and correct for the absorption effects of water on XRF intensities, especially for lighter elements. The precision of XRF intensities is lower for wet sediment than dry sediment because of interstitial water, water film development on the sediment surface and Mylar film (which is used to prevent the drying out of the sediment). Due to the issues raised above, it is necessary to correct for water content and to convert the wet scan data to equivalent dry mass concentrations. Kido *et al.* (2006) used X-ray intensity (TXI) to estimate water content, which they then used to calculate the absorption effects of water and convert the data to dry sample equivalent XRF intensities. Cl intensities can also be used as a proxy for water content when analysing marine sediments (Hennekam and De Lange 2012; Tjallingii *et al.* 2007). Elemental ratios have also been used to remove the uncertainties associated with water content, organic matter and sample heterogeneities (Croudace *et al.* 2006; Lowemark *et al.* 2011); however this approach, due to its asymmetry, can affect the geochemical interpretation of the data and it is recommended that log-ratios are used instead (Weltje and Tjallingii 2008).

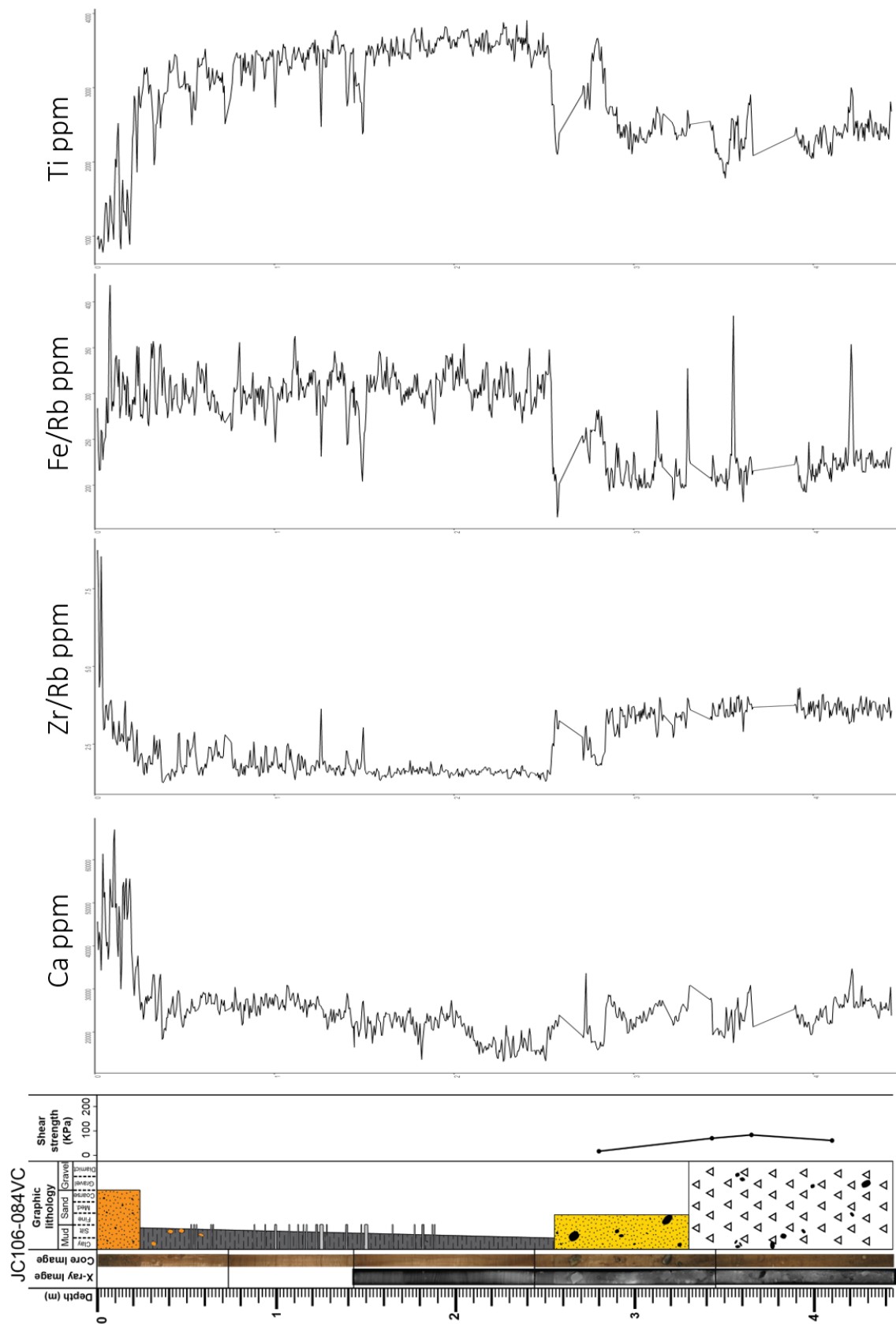


Figure 3.2. Ca, Ti peaks and Zr/Rb, Fe/Rb ratios vs lithostratigraphic core log JC106-084VC. Core log produced by Margot Saher.

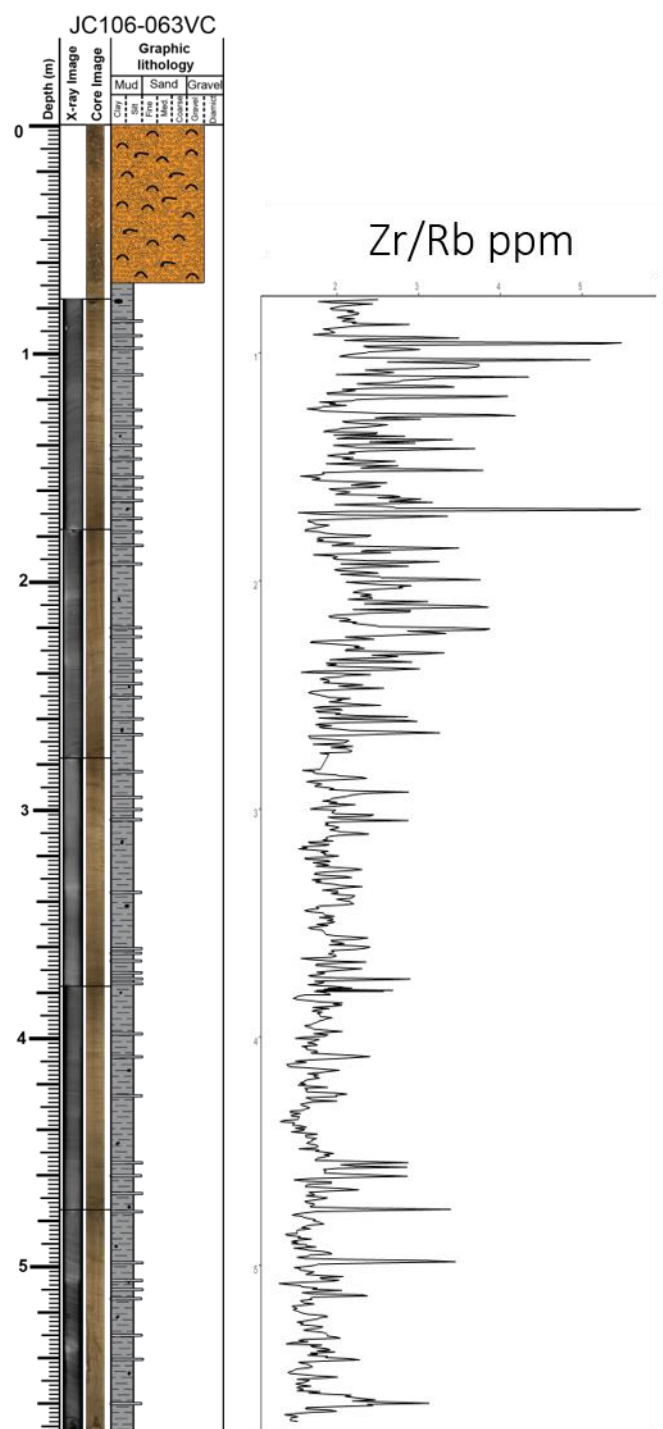


Figure 3.3. Zr/Rb ratio vs lithostratigraphic core log JC106-063VC. Core log produced by Margot Saher.

This study uses the method outlined by Boyle *et al.* (2015), whereby wet scan data is corrected using a simple regression developed through obtaining a training set of dry sediment elemental concentrations.

A series of steps were applied to the data:

- 1) Comparison between wet core scanned elemental concentrations (the Olympus DELTA and ITRAX) and dry mass concentrations of the training set (measured on the SPECTRO XEPOS).
- 2) The recalculation of wet scan data on a dry mass basis by using the coefficients determined by the regression analysis in step 1.

Figure 3.4 and 3.5 compare the measured concentration values obtained from the Olympus DELTA XRF (JC106 and JC123 cores and MD04-2829CQ) and the SPECTRO XEPOS. The SPECTRO XEPOS were measured on the training set of subsamples. The Olympus DELTA data used for comparison are the mean value for the depths that correspond to the subsample. For each element, there is a graph which displays the relationship between the wet scan data and the SPECTRO XEPOS dry subsample data. Outliers (Outliers are defined as points that exceed the boundary of  $(IQR*3) + Q3$  for each element) and zeros were removed from the x-y scatterplots to improve relationship between the scan data and dry subsamples; an example of this is shown in Figure 3.6 and further examples are included in Appendix 2.

The scatterplots (Figures 3.4 and 3.5) display variable relationships between the dry subsamples and the wet scan data. All elements excluding Pb have a positive linear relationship. Ti, Mn, Zn, Rb, Sr, K, Ca and Fe all show a statistically significant relationship. Cu, Zr and Si show a weaker but statistically significant relationship and Y, Pb and Al have weak and highly scattered relationship.

Figures 3.7-3.10 compare the measured concentration values obtained from the ITRAX XRF core scanner and the SPECTRO XEPOS. Outliers were removed from the x-y scatterplots to improve the relationship between the scan data and dry subsamples. The scatterplots for MD04-2820CQ (Figures 3.7 and 3.8) show a positive linear relationship for all elements excluding Al. Rb, Sr and Fe display statistically significant relationship but all the other elements are quite scattered. The scatterplots for MD04-2822 (Figures 3.9 and 3.10) all display a positive linear relationship. Mn, Sr and Zr show statistically significant relationship, however the other elements are quite scattered and show a weak relationship.

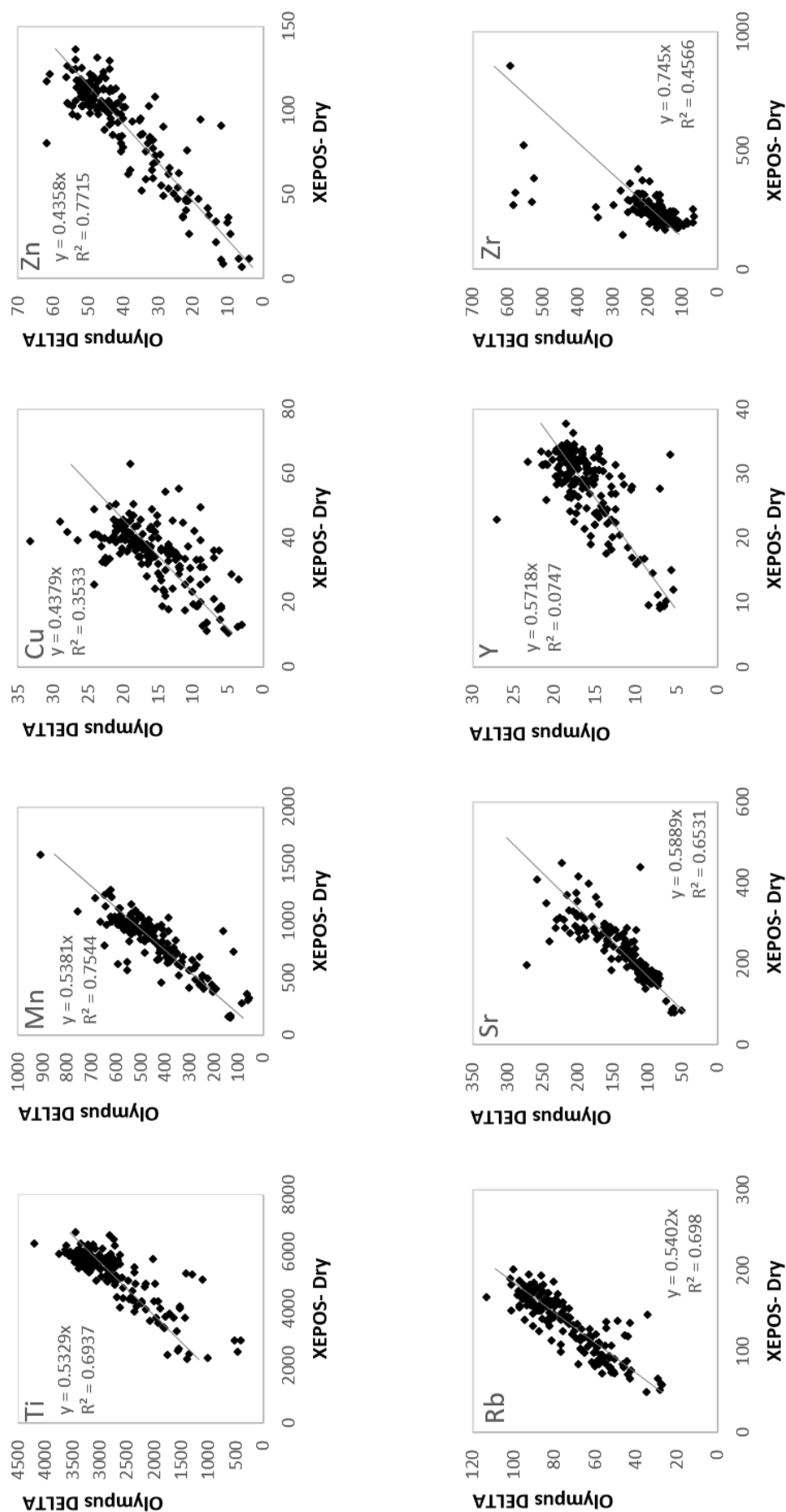


Figure 3.4 Correlations for the element concentrations of Ti, Mn, Cu, Zn, Rb, Sr, Y and Zr for the JC106, JC123 and MD04-2829CQ cores. Wet scan data measured by the Olympus DELTA (ppm) and dry subsamples measured by the SPECTRO XEPOS (ppm). The intercept has been set through zero.

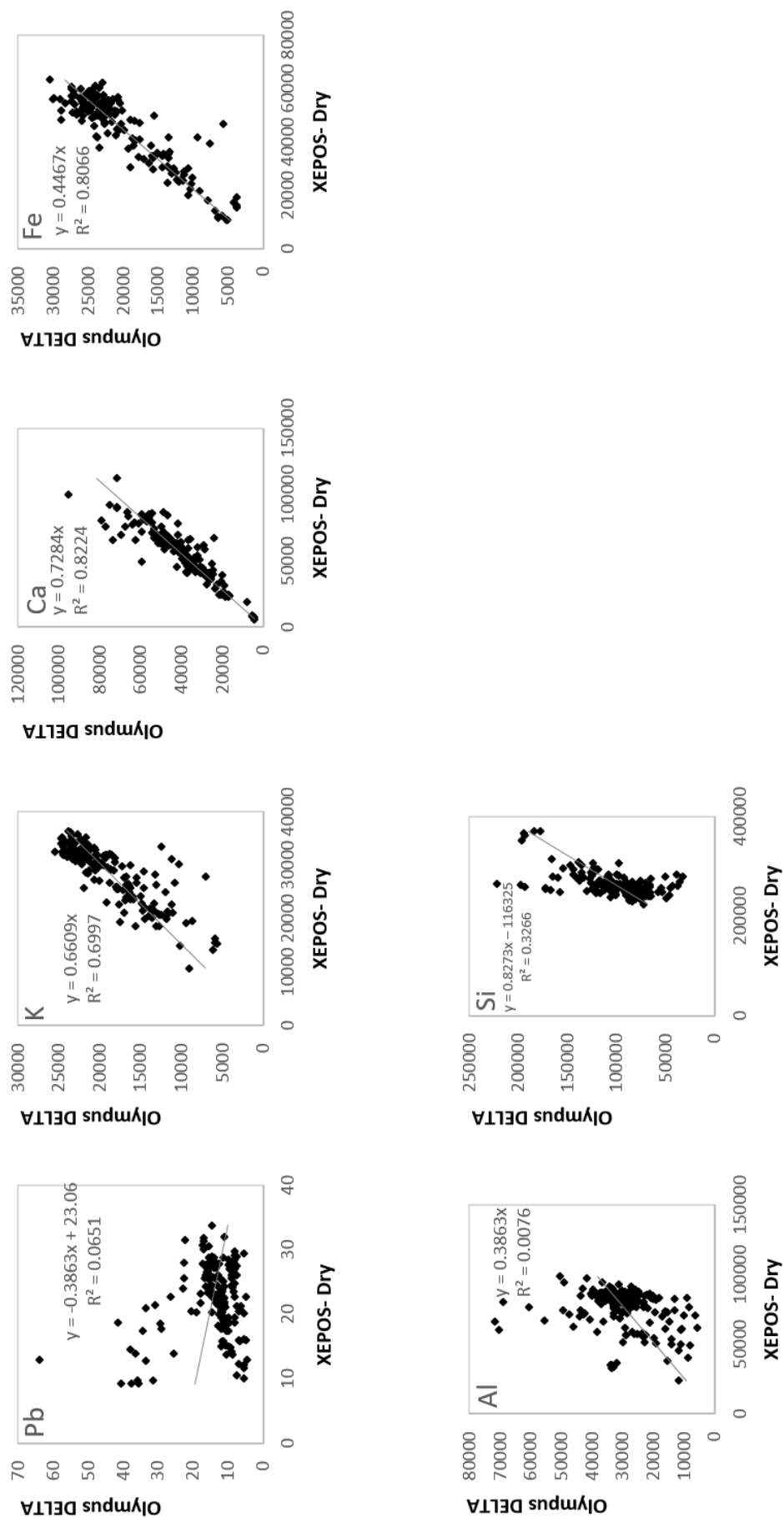


Figure 3.5 Correlations for the element concentrations of Pb, K, Ca, Fe, Al and Si for the JC106, JC123 and MD04-2829CQ cores. Wet scan data measured by the Olympus DELTA (ppm) and dry subsamples measured by the SPECTRO XEPOS (ppm). The intercept has been set through zero excluding Pb and Si.

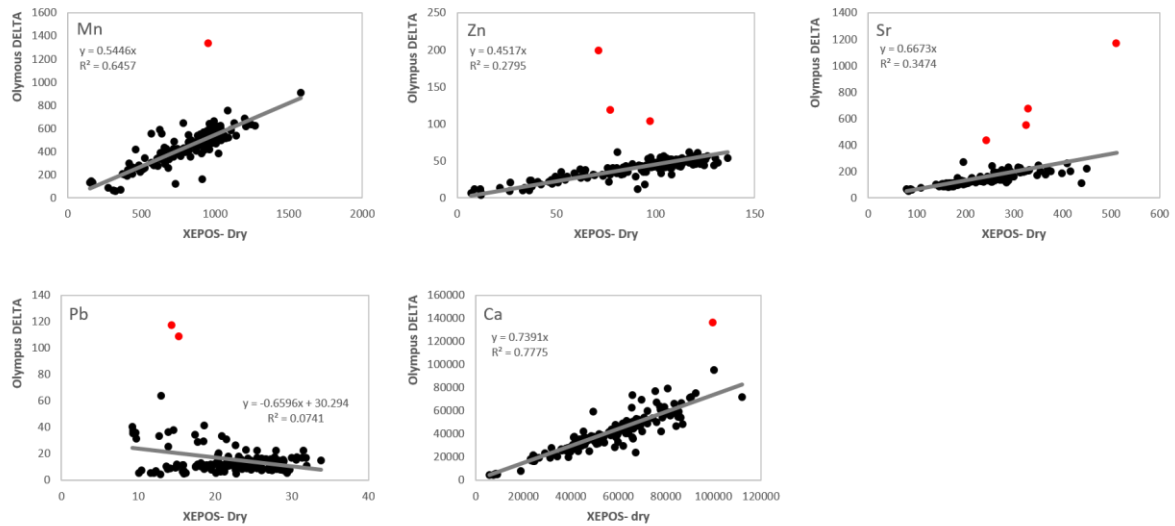


Figure 3.6 Correlations for the element concentrations of Mn, Zn, Sr, Pb and Ca for the JC106, JC123 and MD04-2829CQ cores. Wet scan data measured by the Olympus DELTA (ppm) and dry subsamples measured by the SPECTRO XEPOS (ppm). Red data points are the deleted outliers. These points have been classified as outliers because they exceed the boundary of  $(IQR \times 3) + Q3$  for each element. The intercept has been set through zero excluding Pb.

Further analysis will not include elements Pb, Al and Si because of their weak relationship, which will hinder the correction of these elements.

The simple regression correction has been applied to the wet scan data (both Olympus DELTA and ITRAX) using Equation 1 and the  $b_1$  coefficient shown on Figures 3.4, 3.5 and 3.7-3.10.

$$DryScan = \frac{WetScan}{b_1} \quad (\text{Equation 1})$$

It is necessary to correct for water effects before interpretation. After correction, the data correspond much better to the subsample dry SPECTRO XEPOS XRF data (Figures 3.11, 3.12 and 3.13).



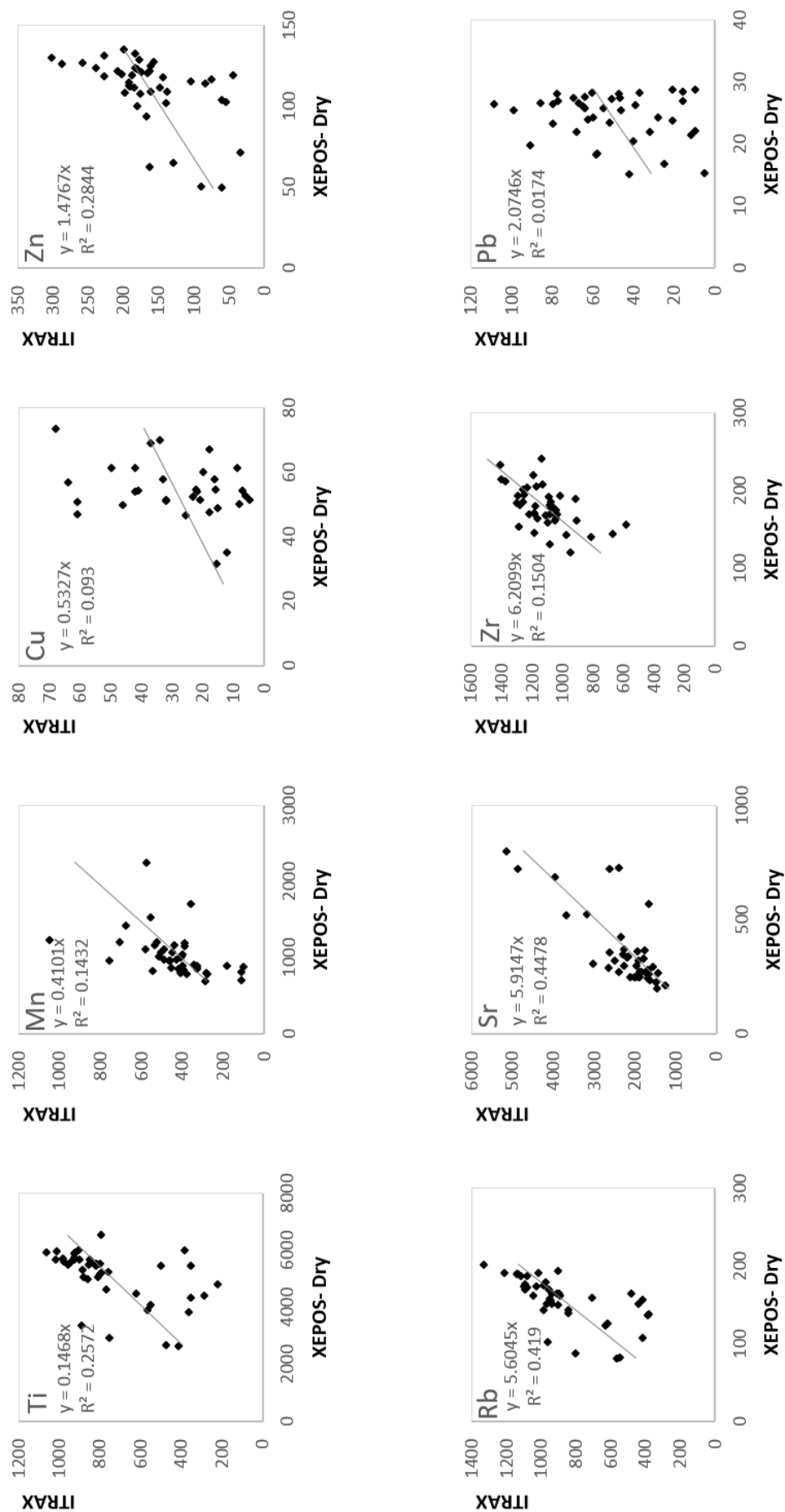


Figure 3.7 Correlations for the element concentrations of Ti, Mn, Cu, Zn, Rb, Sr, Zr and Pb for MD04-2820CQ core. Wet scan data measured by ITRAX (cps) and dry subsamples measured by the SPECTRO XEPOS (ppm). The intercept has been set through zero.

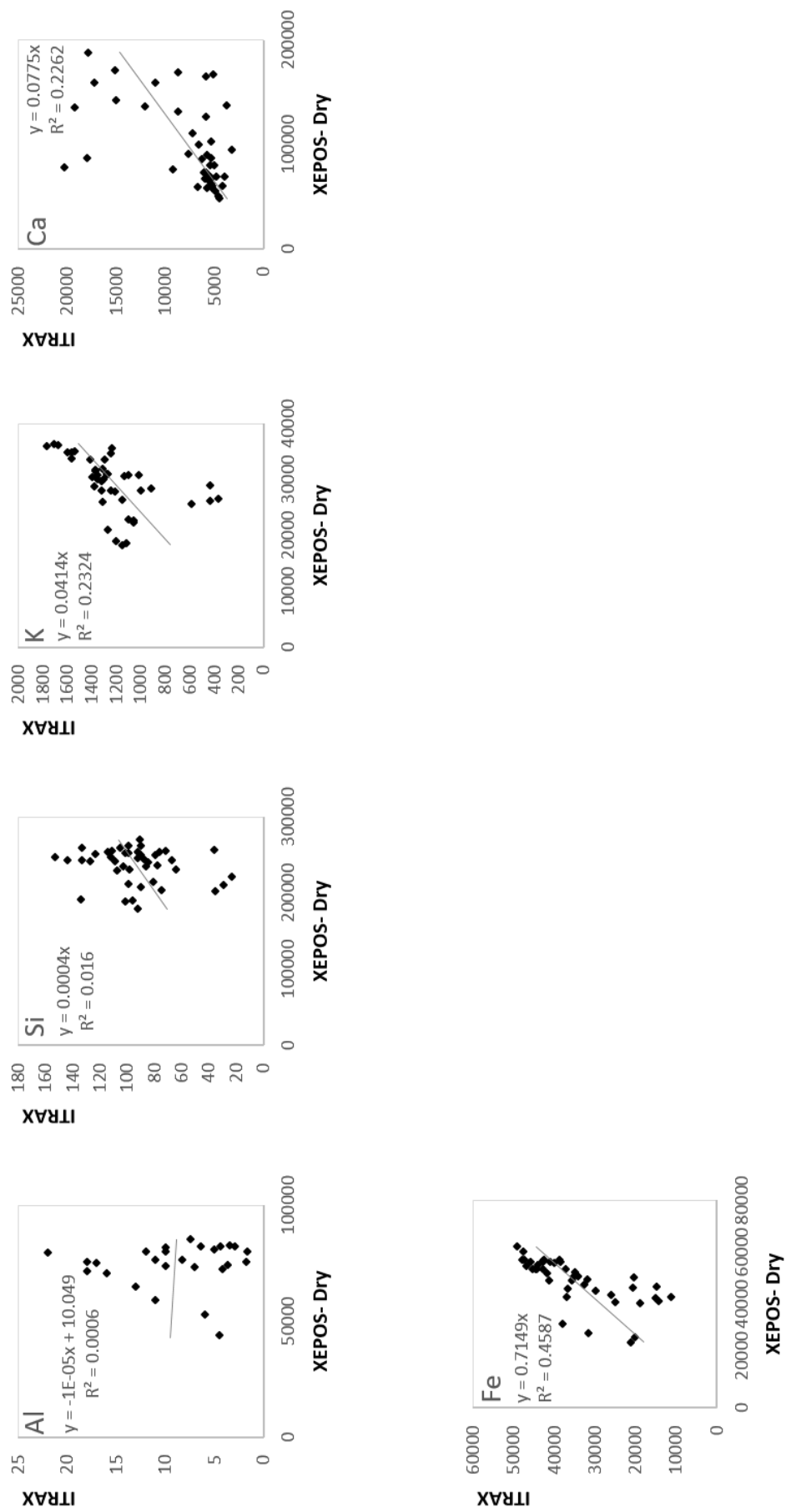


Figure 3.8 Correlations for the element concentrations of Al, Si, K, Ca and Fe for MD04-2820CQ core. Wet scan data measured by ITRAX (cps) and dry subsamples measured by the SPECTRO XEPOS (ppm). The intercept has been set through zero excluding Al.

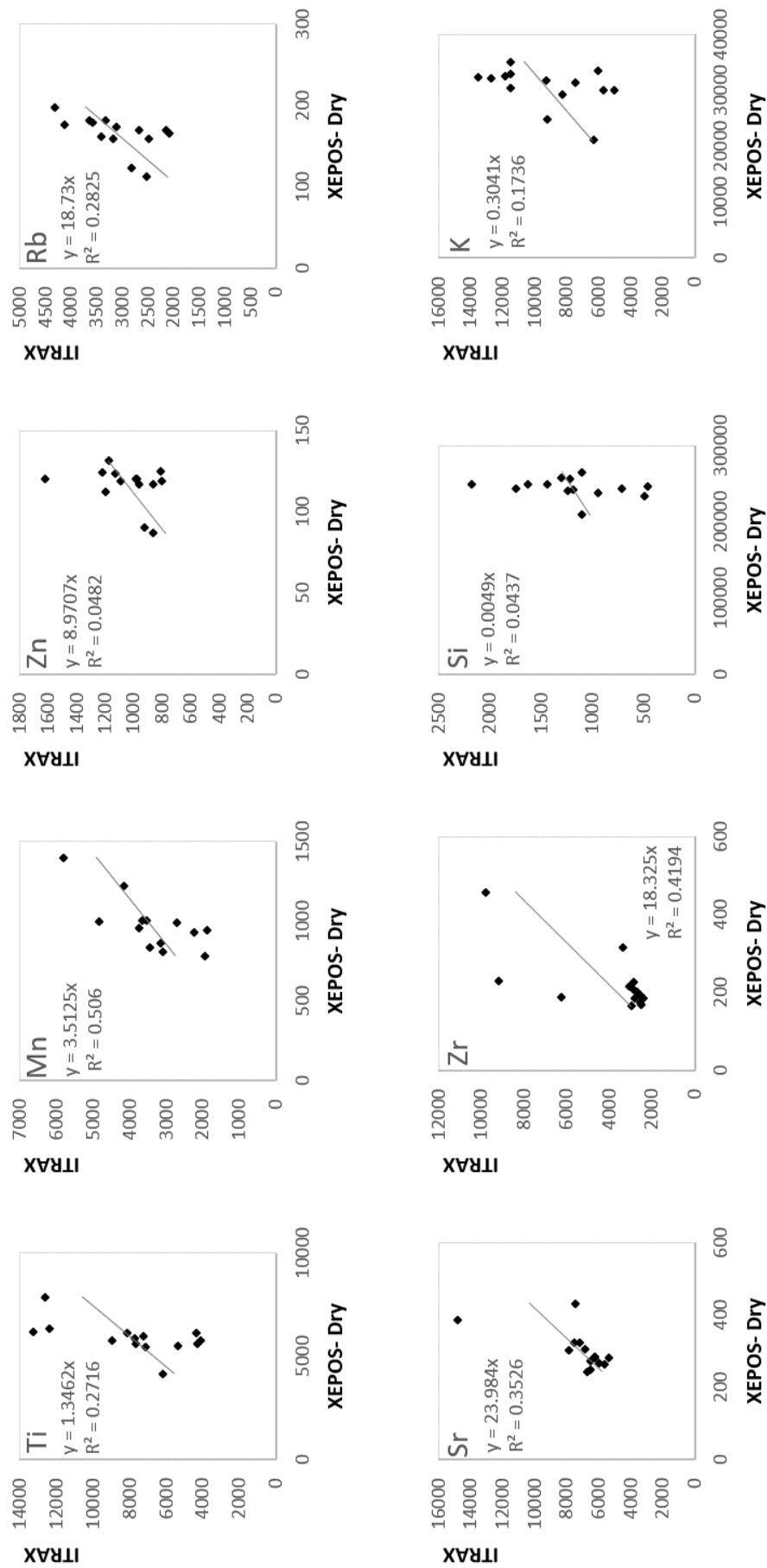


Figure 3.9 Correlations for the element concentrations of Ti, Mn, Zn, Rb, Sr, Zr, Si and K for MD04-2822 core. Wet scan data measured by ITRAX (cps) and dry subsamples measured by the SPECTRO XEPOS (ppm). The intercept has been set through zero.

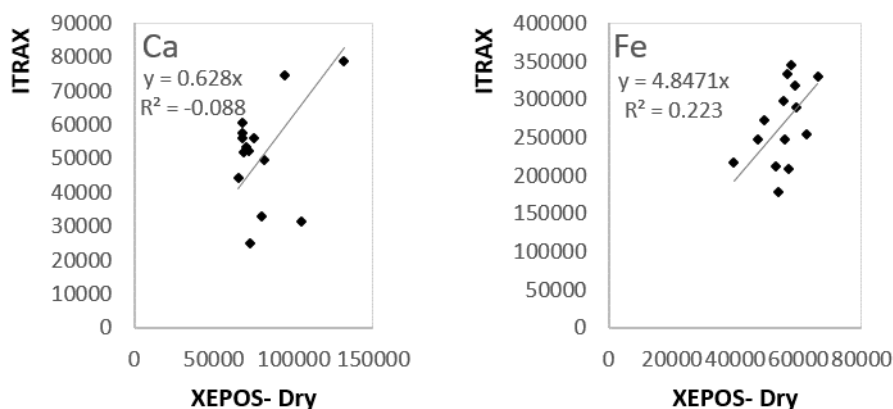


Figure 3.10 Correlations for the element concentrations of Ca and Fe for MD04-2822 core. Wet scan data measured by ITRAX (cps) and dry subsamples measured by the SPECTRO XEPOS (ppm). The intercept has been set through zero.

The corrected Olympus DELTA data correlate well to the XEPOS dry subsample measurements in comparison to the uncorrected scan data (Figure 3.11). The uncorrected scan data display lower values. Ti, Mn, Zn, Rb, Sr, Y, K, Ca and Fe show good correlation with the XEPOS dry subsamples with limited noise. Cu and Zr also show good general agreement with the subsample data however more noise than the other elements.

The corrected ITRAX data for MD04-2820CQ greatly improve the agreement between the scan data and the XEPOS dry subsample data (Figure 3.12). The corrected ITRAX data for MD04-2822 also has a good agreement with the subsample data (Figure 3.13). Ti, K and Ca display a weak relationship and are quite scattered in Figures 3.09 and 3.10 and consequently, their agreement is not as good as the other elements but nevertheless still bring the ITRAX data more in line with the XEPOS dry subsamples.

These corrections work because the water content of the sediments analysed are relatively constant (Boyle *et al.* 2015). Water content within sediment directly affects the scattering of X-rays (Boyle *et al.* 2015). The higher the water content the more scattering occurs (Figure 3.14). There are two types of scattering; Rayleigh (or coherent) scattering and Compton (or incoherent) scattering. The Rayleigh scattering exhibits unchanged photon energy, whereas Compton scattering represents the partial energy loss of photons. High water

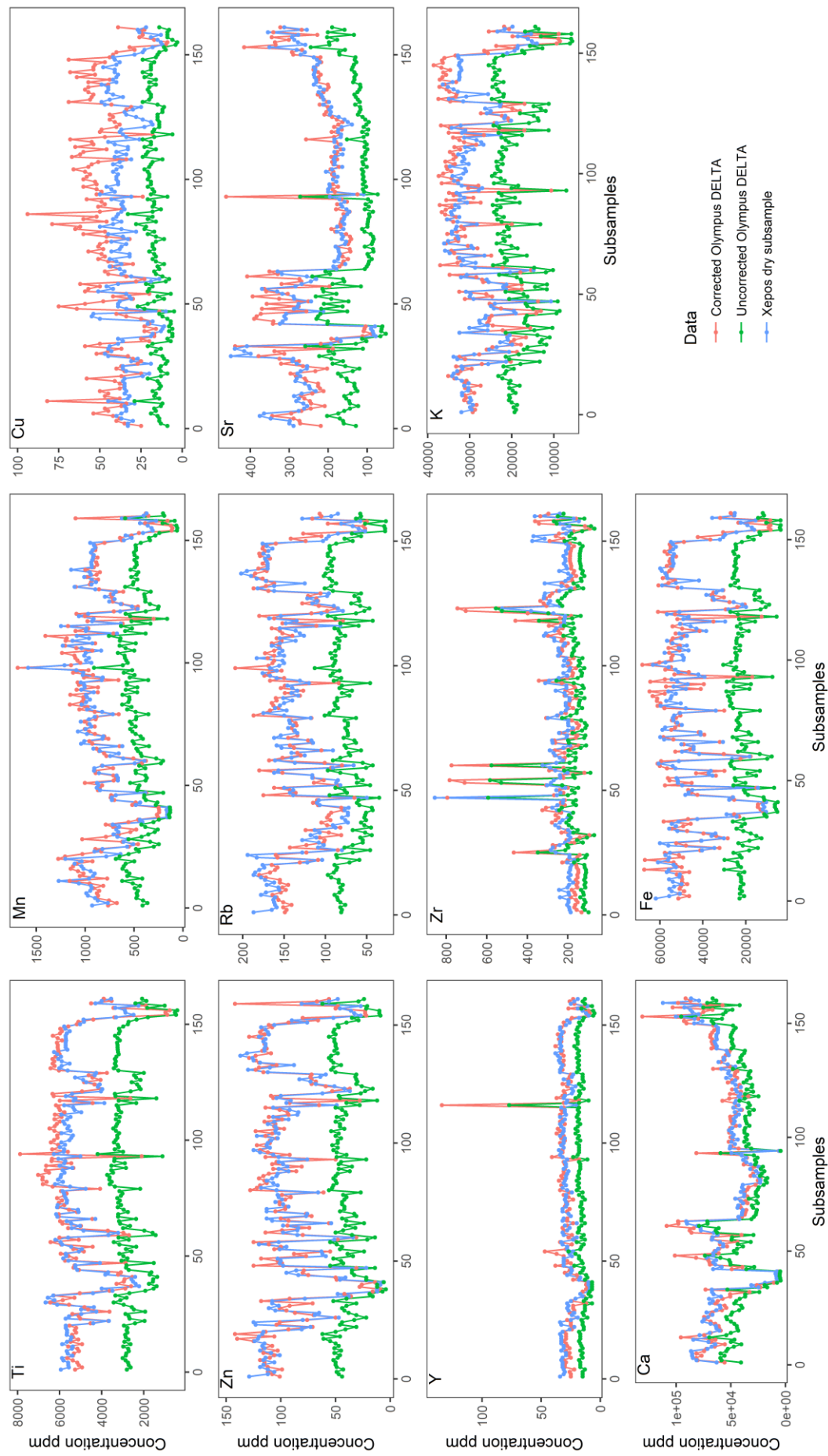


Figure 3.11 Element concentration data for JC106, JC123 and MD04-2829CQ cores. Green line represents Olympus DELTA uncorrected data. Blue line reflects the SPECTRO XEPoS subsample data. Red line represents the Olympus DELTA data corrected by regression on wet Olympus Delta data.

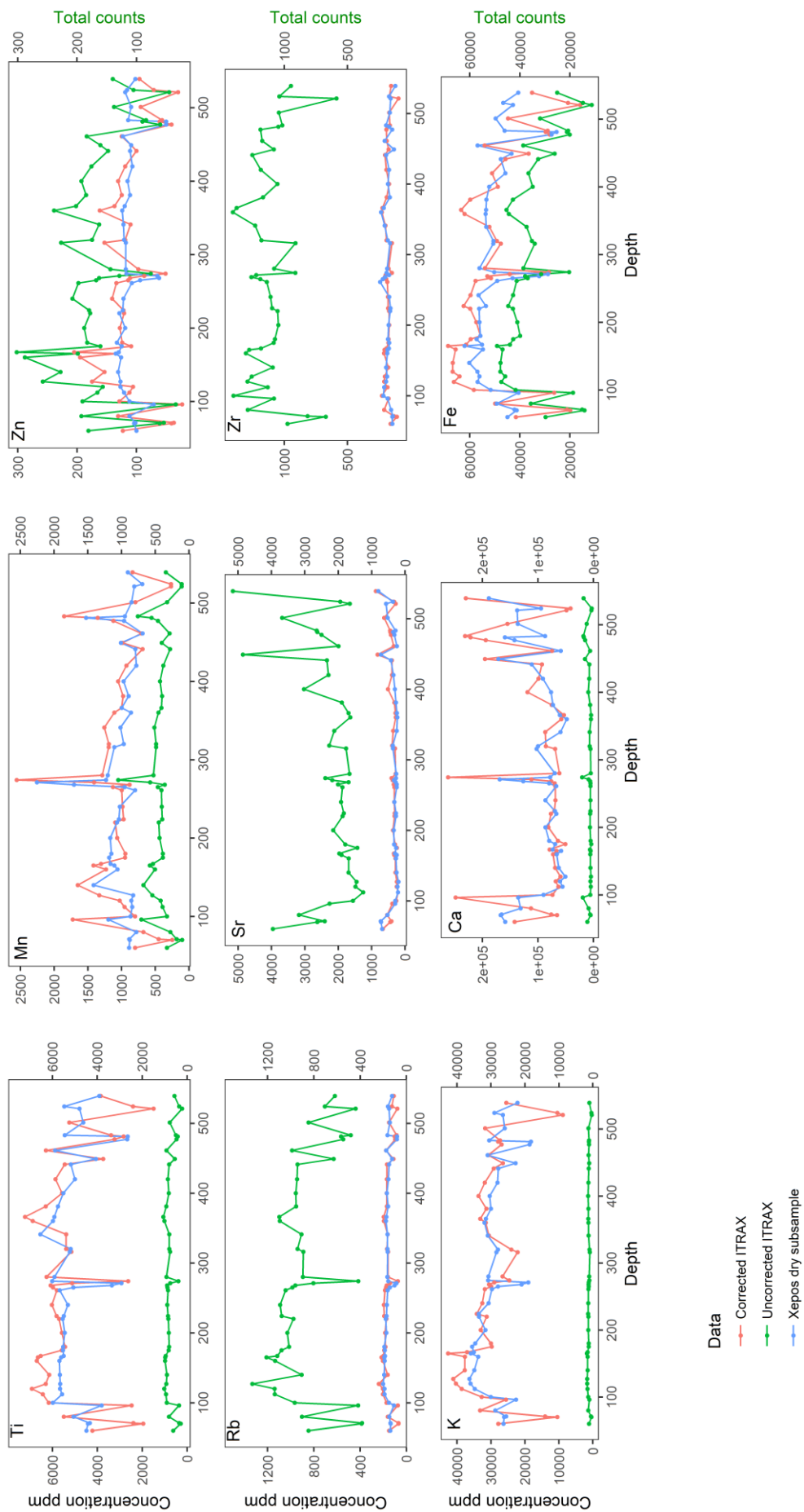


Figure 3.12 Element concentration data for MD04-2820CQ core. Green line represents ITRAX uncorrected data. Blue line reflects the SPECTRO XEPOS subsample data. Red line represents the ITRAX data corrected by regression on wet ITRAX data.

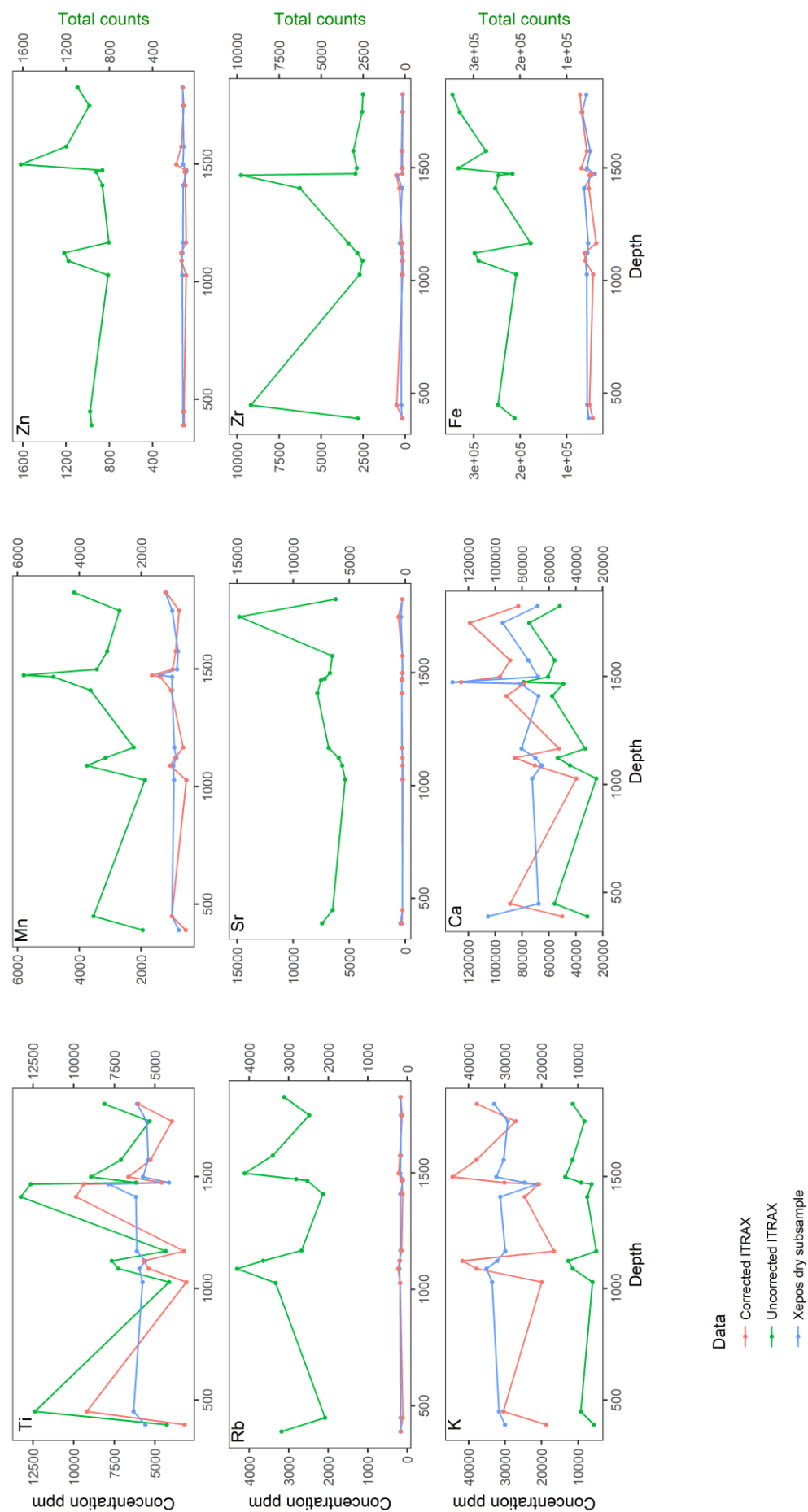


Figure 3.13 Element concentration data for MD04-2822 core. Green line represents ITRAX uncorrected data. Blue line reflects the SPECTRO XEPOS subsample data. Red line represents the ITRAX data corrected by regression on wet ITRAX data.

content favour Compton scattering as shown by Figure 3.14. The data in Figure 3.15 clearly demonstrate the positive relationship between the ratio of Rayleigh to Compton scattering and the sediment dry mass concentration. Figure 3.16 explores the weakly significant ( $R^2 = 0.3367$ ) relationship between measured dry mass concentration determined by subsample freeze-drying and the XRF inferred dry mass concentration. This x-y scatterplot shows that the Olympus DELTA core scanner can broadly determine the water content of the sediments analysed using the XRF spectra.

Henceforth only corrected XRF scan data will be presented and analysed. Using the appropriate training set and associated regression co-efficients (Figures 3.4, 3.5 and 3.7-3.10) all scan data will be corrected for water content.

XRF scan data (raw and calibrated) and SPECTRO XEPOS data are included in the Appendix on a CD.

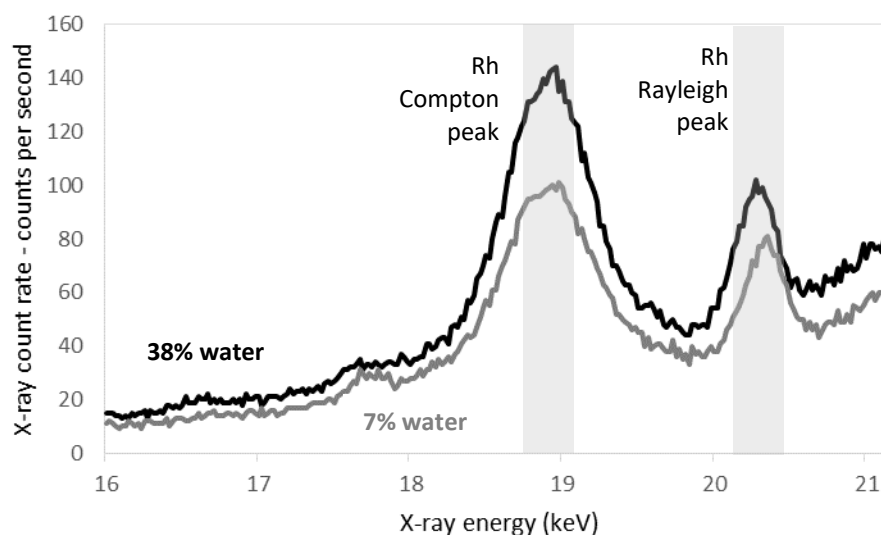


Figure 3.14 Scattering of primary rhodium X-rays as a function of sediment water content. The 38% water content sediment is from JC106-087VC (2.5 m depth) and the 7% water content sediment is from JC123-012VC (2.49 m depth). The wetter sample has a greater proportion of Compton scattering.



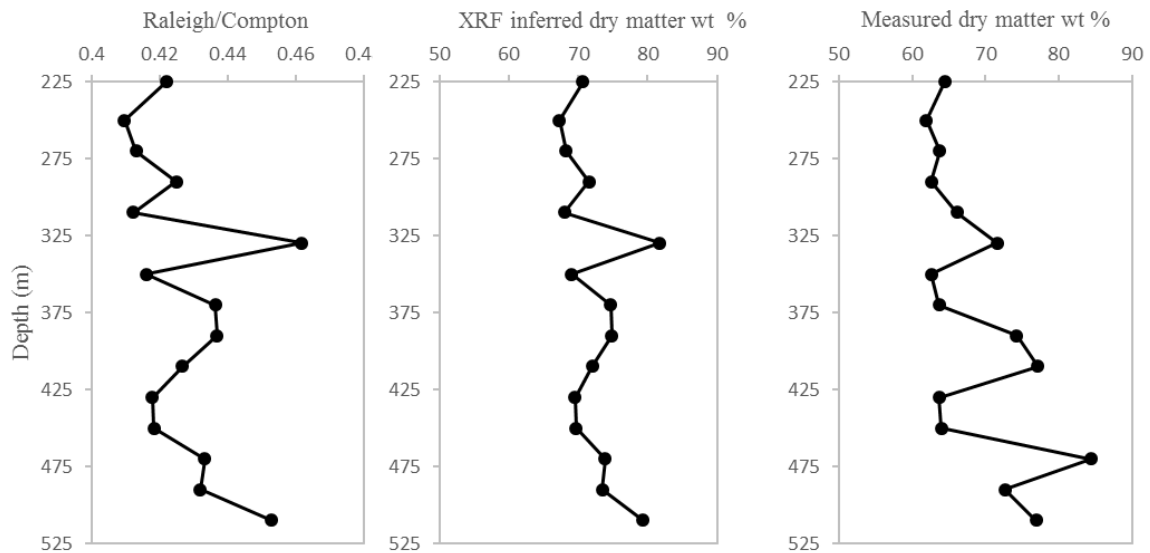


Figure 3.15 Rayleigh/Compton scattering ratio measured by the Olympus DELTA for the corresponding depths for the subsamples from JC106-087VC, the XRF inferred dry matter content for these subsamples and the measured subsample dry matter content.

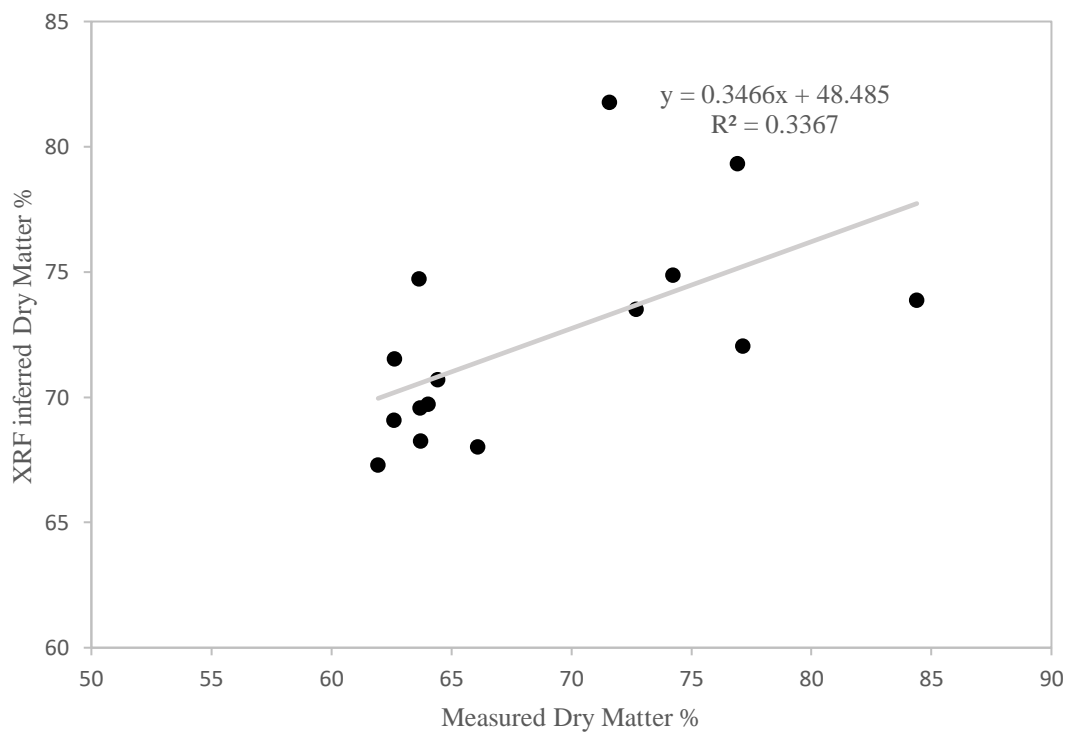


Figure 3.16 Relationship between measured subsample water content and the XRF inferred water content derived using the Rayleigh/Compton scattering ratio measured by the Olympus DELTA for the corresponding depths for the subsamples from JC106-087VC.

## 4 Irish Sea Ice Stream sector

The Irish Sea Ice Stream was the largest ice stream that drained the BIIS and was fed by ice from the Scottish Highlands, the Lake District and Ireland (Chiverrell *et al.* 2013). The ice flowed south through the Irish Sea Basin and into the Celtic Sea, its limit was the southernmost extension of the BIIS (Praeg *et al.* 2015). Eighteen continental shelf cores and one deep ocean core have been analysed (Figure 4.1) with the aim to:

1. Use  $\mu$ XRF to determine the geochemical signature of the glacial sediments along the continental shelf flowpath of the Irish Sea Ice Stream;
2. Demonstrate the geochemical variations in the glacial end members across the study area;
3. Use  $\mu$ XRF to determine the geochemical variability within an adjacent deep ocean core (MD04-2820CQ)
4. Determine whether the offshore IRD record from the Goban Spur (MD04-2820CQ) can be linked to these shelf glacial end members

This chapter presents the lithostratigraphy and radiocarbon dates of the 18 cores analysed for the Irish Sea Ice Stream, the calibrated  $\mu$ XRF scan data and the statistical analysis performed.

This chapter also presents the lithostratigraphy for MD04-2820CQ, the calibrated  $\mu$ XRF scan data and the statistical analysis performed.

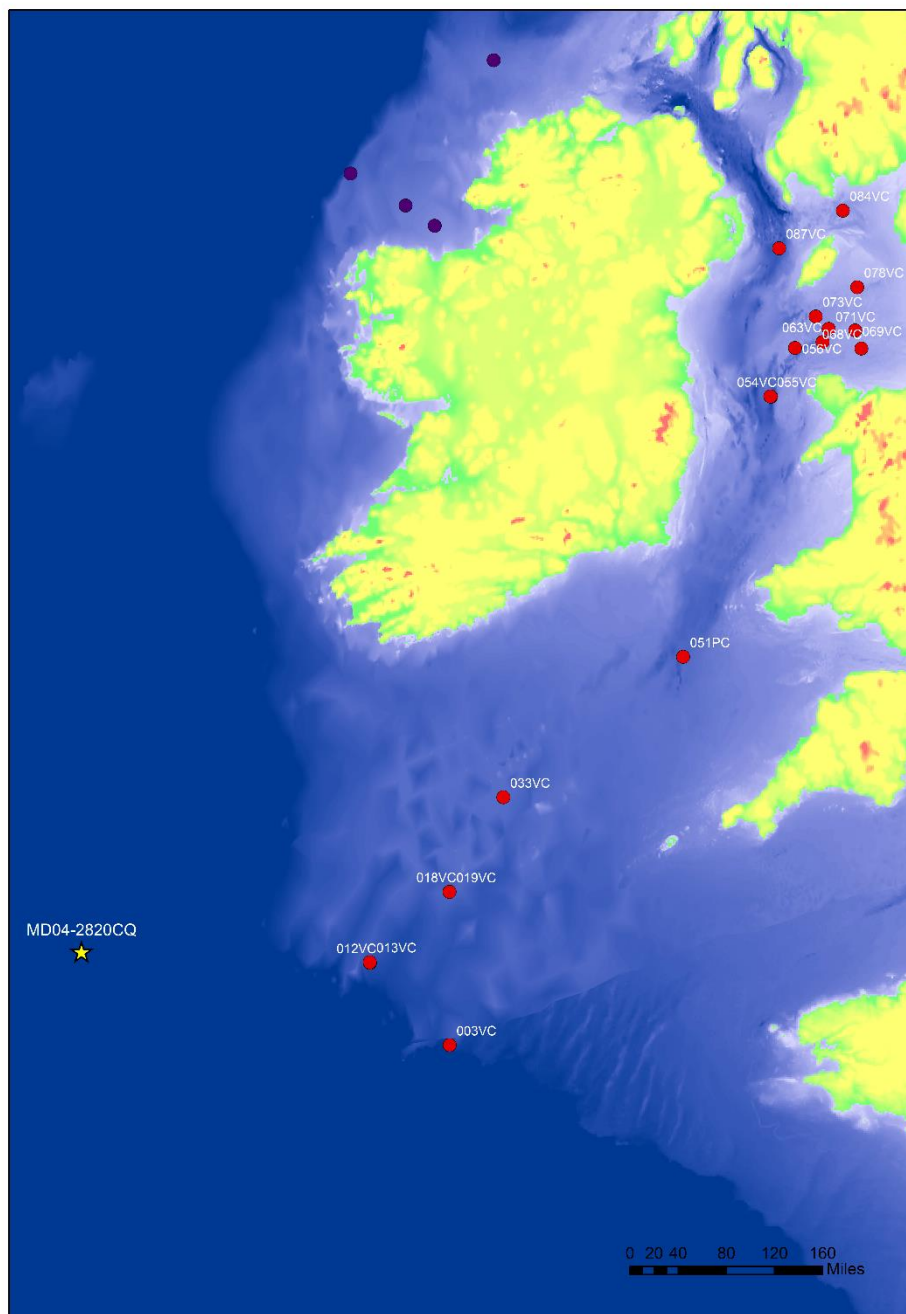


Figure 4.1 Location map of the 18 JC106 cores analysed for the former Irish Sea Ice Stream and adjacent deep ocean core MD04-2820CQ.

## **4.1 Irish Sea Ice Stream continental shelf cores**

### **4.1.1 Lithostratigraphy**

The lithostratigraphy of all 18 cores (Figure 4.2-4.4) can be summarised generally into three lithofacies associations; 1) subglacial 2) glacimarine and 3) postglacial.

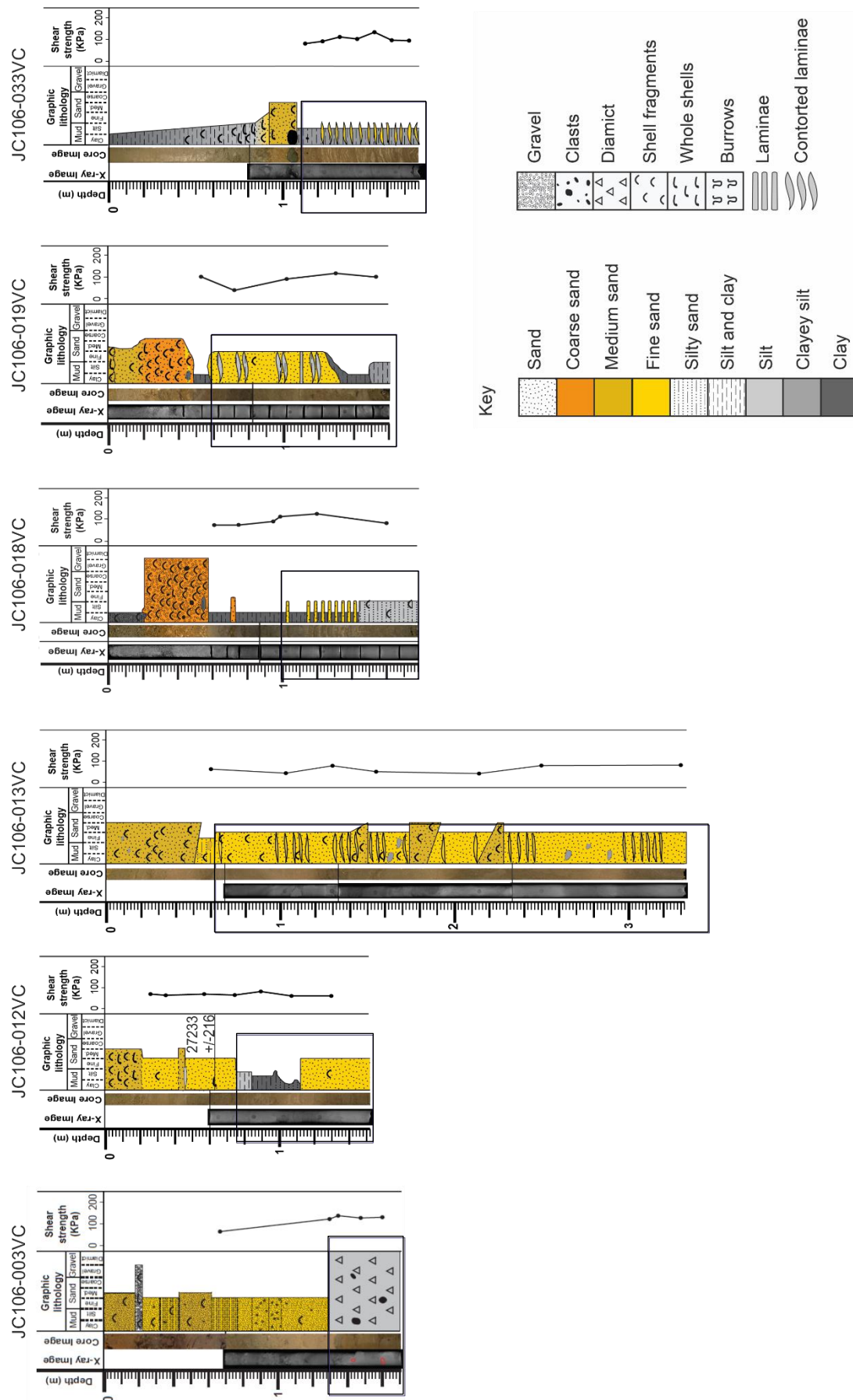


Figure 4.2 Lithostratigraphy for six cores from the Celtic Sea region of the former Irish Sea Ice Stream. Core logs, x-ray imagery, core image, shear strength, radiocarbon dates ( $\Delta R=0$ ) and lithostratigraphy key. Black outline boxes highlight the sediment analysed for this study. Core logs were produced by Margot Saher.

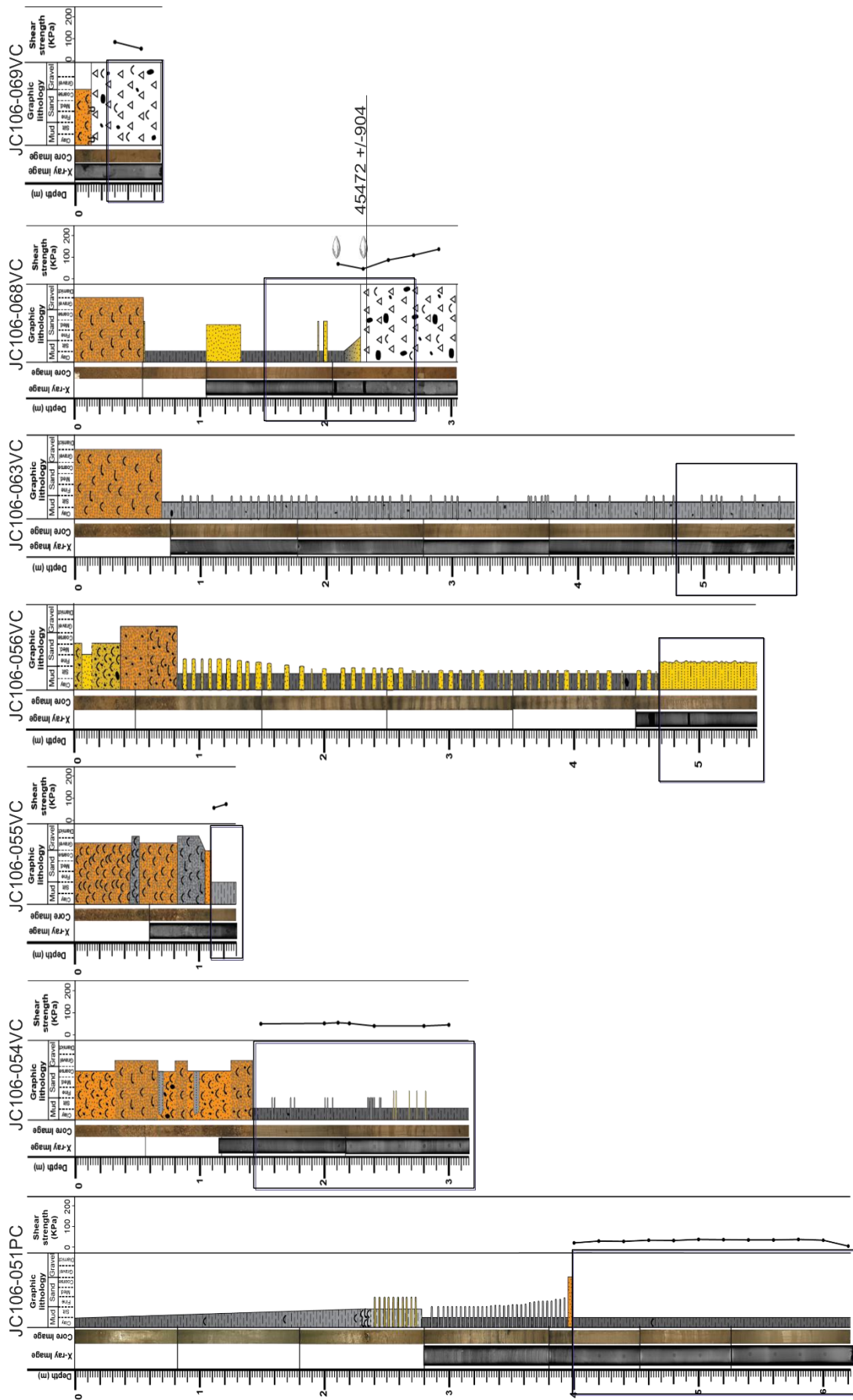


Figure 4.3 Lithostratigraphy for seven cores from the Irish Sea region of the former Irish Sea Ice Stream. Core log, x-ray imagery, core image, shear strength and radiocarbon dates ( $\Delta R=0$ ). Black outline boxes highlight the sediment analysed for this study. Core logs were produced by Margot Saher.

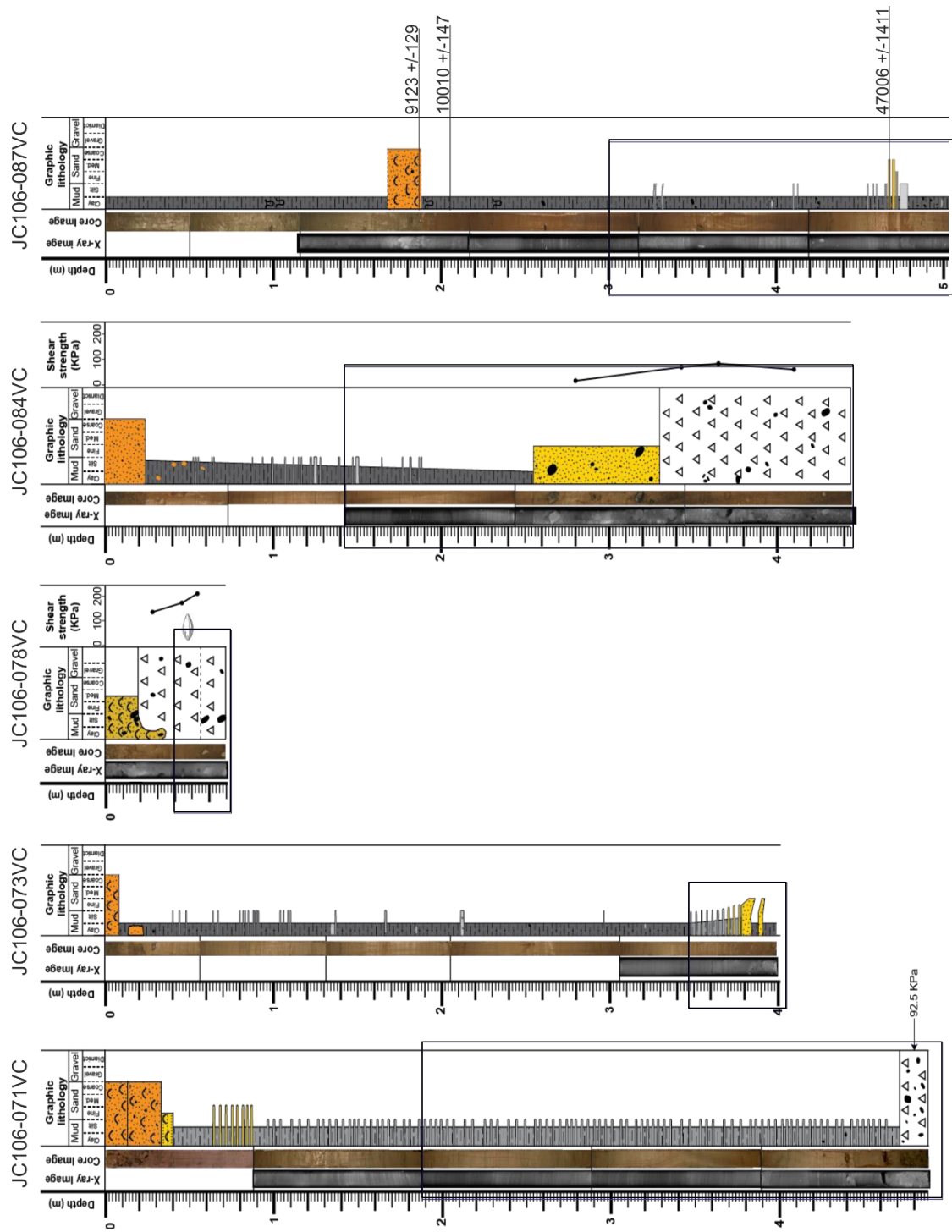


Figure 4.4 Lithostratigraphy for six cores from the Irish Sea region of the former Irish Sea Ice Stream. Core log, x-ray imagery, core image, shear strength and radiocarbon dates ( $\Delta R=0$ ). Black outline boxes highlight the sediment analysed for this study. Core logs were produced by Margot Saher.

## **Celtic Sea**

The Celtic Sea is defined here as comprising two regions, the ‘outer’ and ‘central’ Celtic Sea. The outer Celtic Sea cores (JC106-003VC, JC106-012VC and JC106-013VC; Figure 4.2) are comprised of silty diamict, fine laminated sands, and silty clays. These lithofacies also display quite high shear strengths. The central Celtic Sea cores (JC106-018VC, JC106-019VC and JC106-033VC; Figure 4.2) are comprised of sandy silt, laminated clay and laminated sand lithofacies.

## **Irish Sea**

The Irish Sea is defined here as comprising four regions, southern Irish Sea, central Irish Sea, Liverpool Bay and Irish Sea (West of Isle of Man). The southern Irish Sea cores (Figure 4.3) contain massive and laminated silty clay. The Liverpool Bay cores (Figure 4.3) consist of massive fine silty sand, laminate clayey silt and diamict overlain by a sandy clay, with the occasional sandy laminae. Cores from the central Irish Sea region (Figure 4.3 and 4.4) are comprised of diamict (which display very high shear strengths), laminated clayey silt and massive sand. Core JC106-087VC from the Irish Sea (West of the Isle of Man) (Figure 4.4) region consists of massive clay, with some sandy and silty laminae.

Henceforth this study will be focussing on the subglacial and glacial marine lithofacies.

## **4.2 XRF geochemistry of the continental shelf cores**

### **Irish Sea Ice Stream end members**

Figure 4.5 is a biplot displaying the PCA results of the 18 sediment cores. All PCA plots from henceforth will be described using the points of a compass. The PCA demonstrates a high explanatory power for the first two axes; principal component 1 (PC-axis 1) explains 72% of the total dataset variance whereas principal component 2 (PC-axis 2) accounts for 13%. Samples/cores that plot closer together will have similar PC scores and therefore similar elemental assemblages. On the other hand, samples of cores that plot further apart will have dissimilar PC scores and therefore dissimilar elemental assemblages. The parameter scores (indicated by the vectors on Figure 4.5) indicate that the North West (NW) samples are enriched in Ca and Sr, whereas the South East (SE) samples are depleted in Ca and Sr. Positive PC 1 scores correspond to samples rich in Fe, Ti, K, Rb, Cu and Zn. Grouping the cores into regions shows clear separation in the elemental assemblages between the Celtic Sea cores and the Irish Sea cores with only minor overlap (Figure 4.6). Celtic Sea cores are characterised by high Ca and Sr and to a lesser extent Zr, whereas the Irish Sea cores are enriched in the terrigenous elements (K, Ti, Fe and Rb). Fe is the largest contributor to PC 1, and consequently accounts



for much of the variability across PC 1 (Figure 4.5 and 4.6). To illustrate the range in the elemental concentration of Fe across the shelf end members, Fe values are presented for each core analysed (Figure 4.7). The results indicate that Fe concentration is variable across the

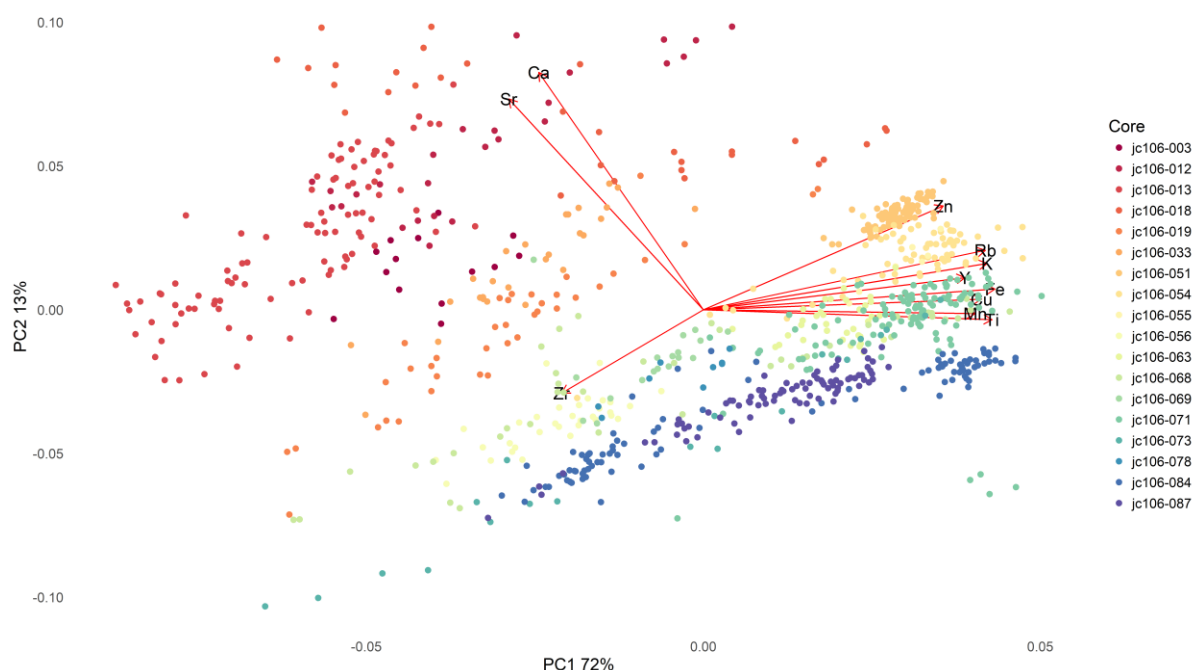


Figure 4.5 PCA biplot for the Irish Sea Ice Stream sediment cores. PC 1 summarises 72% of the total variance in the dataset and PC 2 13%. Each core has been colour coded.

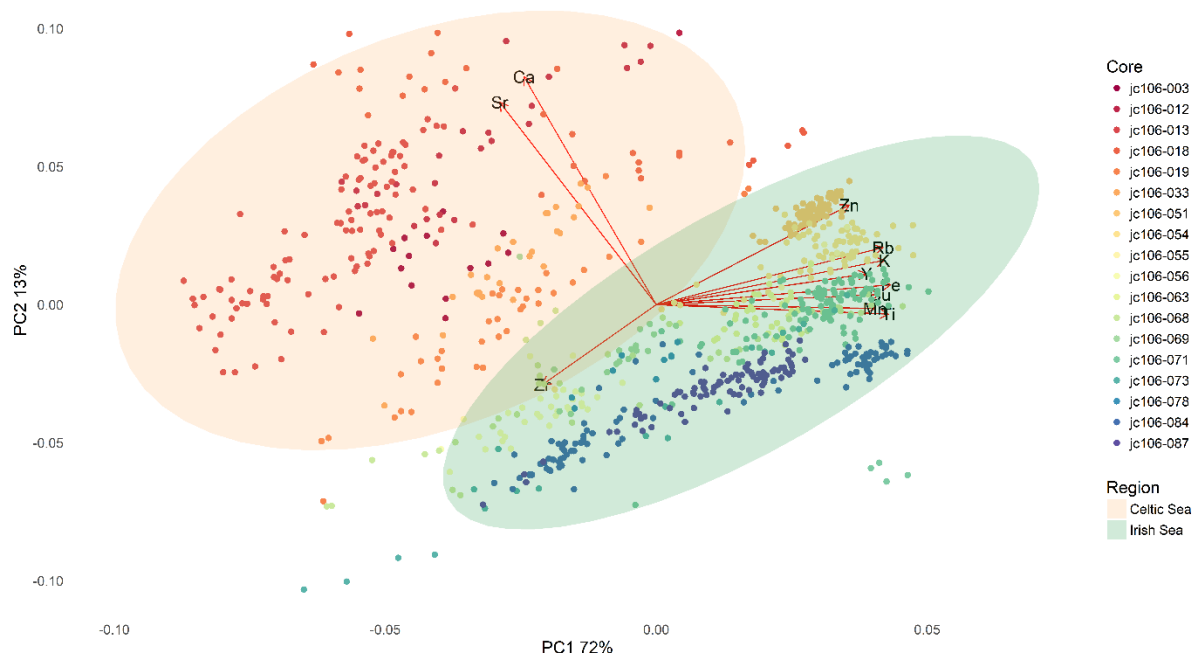


Figure 4.6 PCA biplot for the Irish Sea Ice Stream sediment cores divided into regions. PC 1 summarises 72% of the total variance in the dataset and PC 2 13%. Each core and region has been colour coded. Ellipses represent 0.95 confidence level. Henceforth all figures which include ellipses will be at 0.95 confidence level.



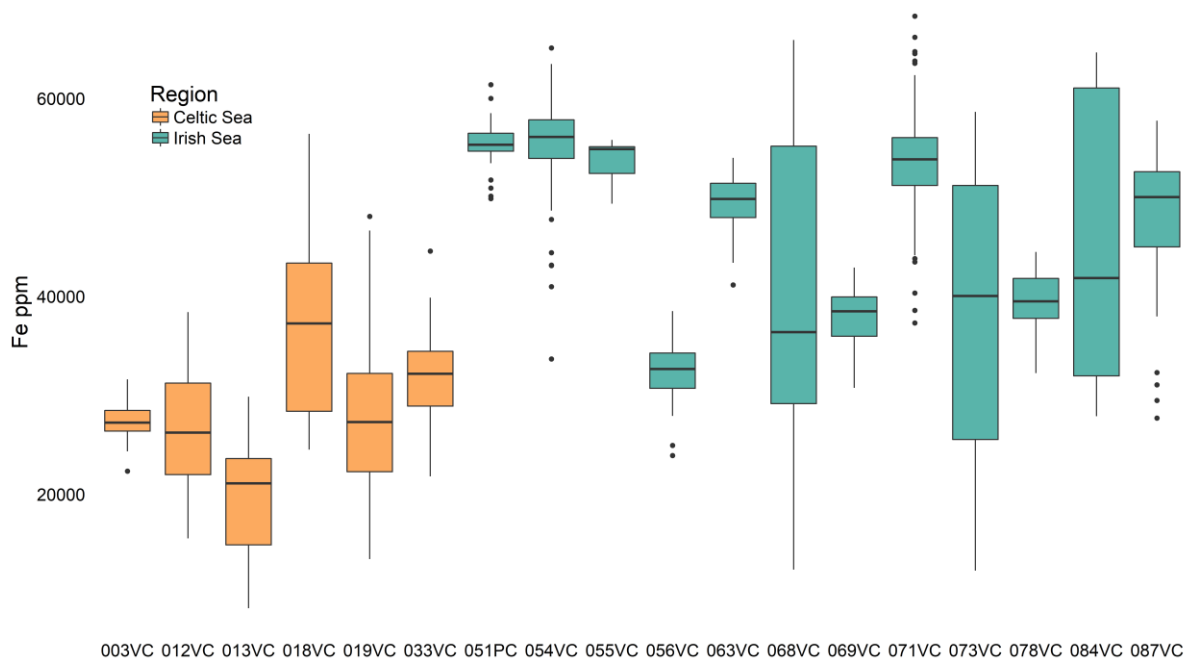


Figure 4.7 Boxplot displaying Fe concentrations of the 18 sediment cores from the former Irish Sea Ice Stream. The cores have been colour coded by region. The lower and upper hinges correspond to the 25<sup>th</sup> and 75<sup>th</sup> percentiles. The upper whisker extends from the hinge to the largest value no further than 1.5\* inter quartile range ( $IQR(IQR=UQ-LQ)$ ) from the hinge. The lower whisker extends from the hinge to the smallest value at most 1.5\* IQR of the hinge. Data beyond the whiskers are plotted individually and called 'outliers'. The black lines in the middle of the boxes are median values.

cores. Furthermore, the Irish Sea cores contain, on average, higher concentrations of Fe than the Celtic Sea cores. Figure 4.8 A and B are plots of the same PCA data but also display the grain size of each of the samples. No distinct clusters are visible, however the negative PC 1 scores are associated with sand and silt lithofacies, whereas positive PC 1 scores correspond to clay and clayey silt lithofacies.

To assess whether there is a stratigraphic gradient within the individual cores, the original PCA has been transformed (Figures 4.9- 4.12). Figure 4.9 and 4.10 shows the internal elemental assemblages and grain size variability for three Celtic Sea cores (JC106-012VC, JC106-018VC and JC106-033VC) as a function of stratigraphy. Blue data points are more proximal sediments transitioning to more distal sediments (red data points). JC106-012VC (Figure 4.9A) proximal sediments are sand and plot negatively along PC 1, whereas the more distal sediments have comparatively higher PC 1 scores and are clay and silt grain sizes. In JC106-018VC (Figure 4.9B) the proximal sediments are silt and are enriched in Ca and Sr, whereas the more distal sediments have higher PC 1 scores and are clay. JC106-033VC (Figure 4.10) does not display as clear a stratigraphic gradient as the other two Celtic Sea cores, and much of the core has a clayey silt grain size, however there is still spread across both PC axes.

Figure 4.11 and 4.12 show the internal elemental assemblages and grain size variability for three Irish Sea cores (JC106-063VC, JC106-069VC, JC106-073VC) as a function of stratigraphy. JC106-063VC (Figure 4.11) is dominated by clayey silt and the data points are clustered quite tightly. There is a subtle stratigraphic gradient with proximal sediment plotting to the West and more distal sediment to the East. JC106-069VC (Figure 4.12A) is dominated by diamict and there is a stratigraphic gradient along the PC 1 axis. JC106-073VC (Figure 4.12B) displays a large spread along the PC 1 axis, and there is a clear stratigraphic gradient.

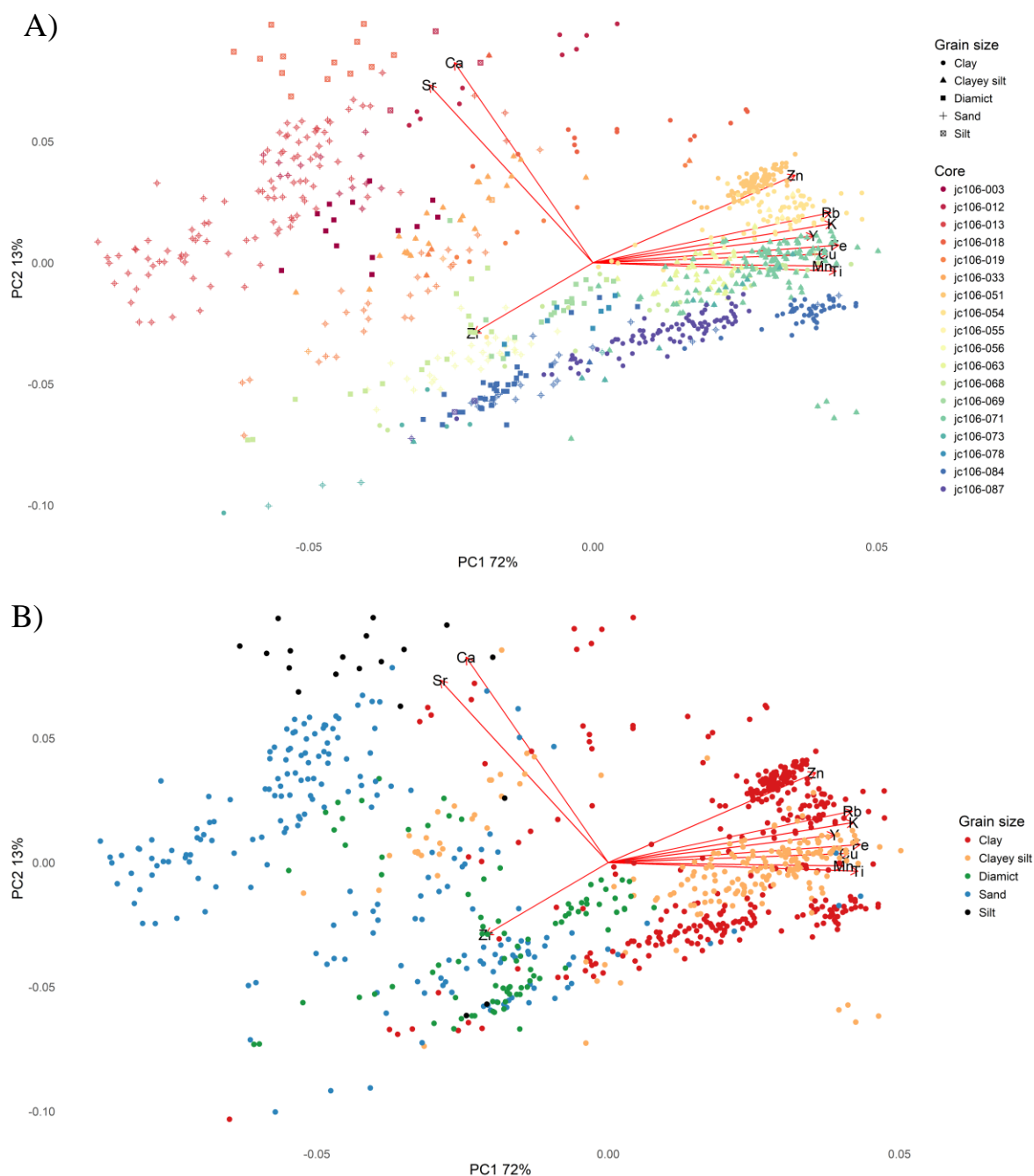


Figure 4.8 PCA biplot for the Irish Sea Ice Stream sediment cores focusing on grain size A) Each core has been colour coded and symbols display the grain size of each data point. B) Every data point has been colour coded by grain size.

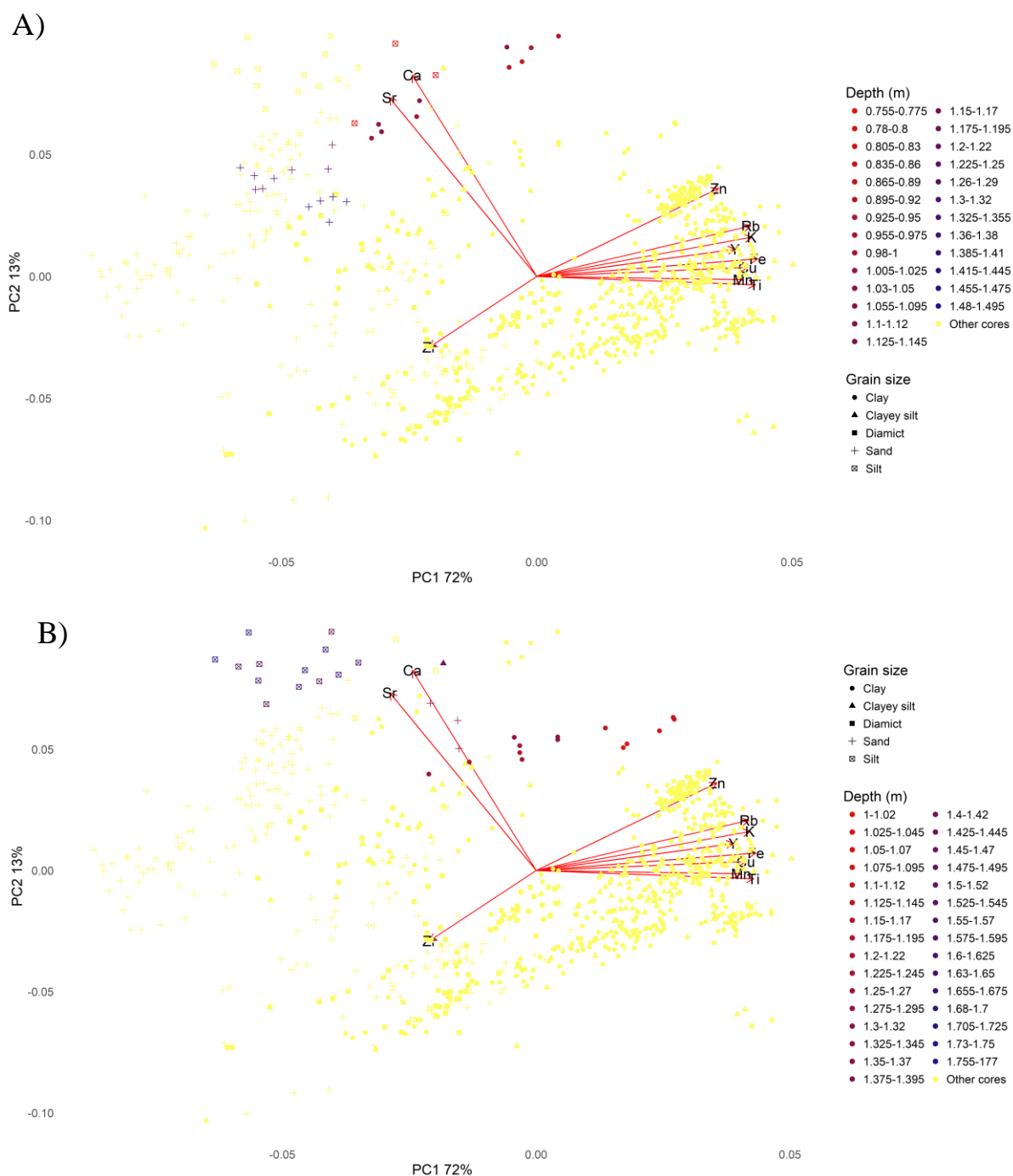


Figure 4.9 PCA biplot displaying internal elemental concentration and grain size variability for two Celtic Sea cores as a function of stratigraphy. A) JC106-012VC B) JC106-018VC. Blue data points are proximal sediments transitioning to distal sediments (red data points). The remaining Irish Sea Ice Stream cores are shown by the yellow data points.

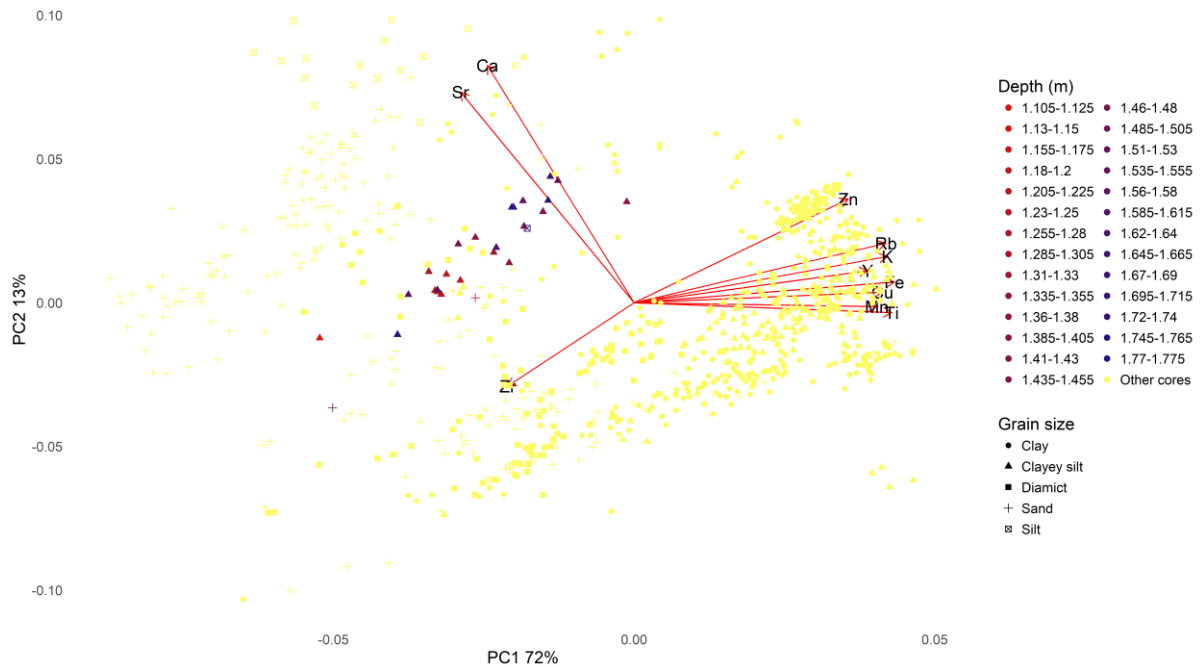


Figure 4.10 PCA biplot displaying internal elemental concentration and grain size variability for one Celtic Sea core as a function of stratigraphy JC106-033VC. Blue data points are proximal sediments transitioning to distal sediments (red data points). The remaining Irish Sea Ice Stream cores are shown by the yellow data points.

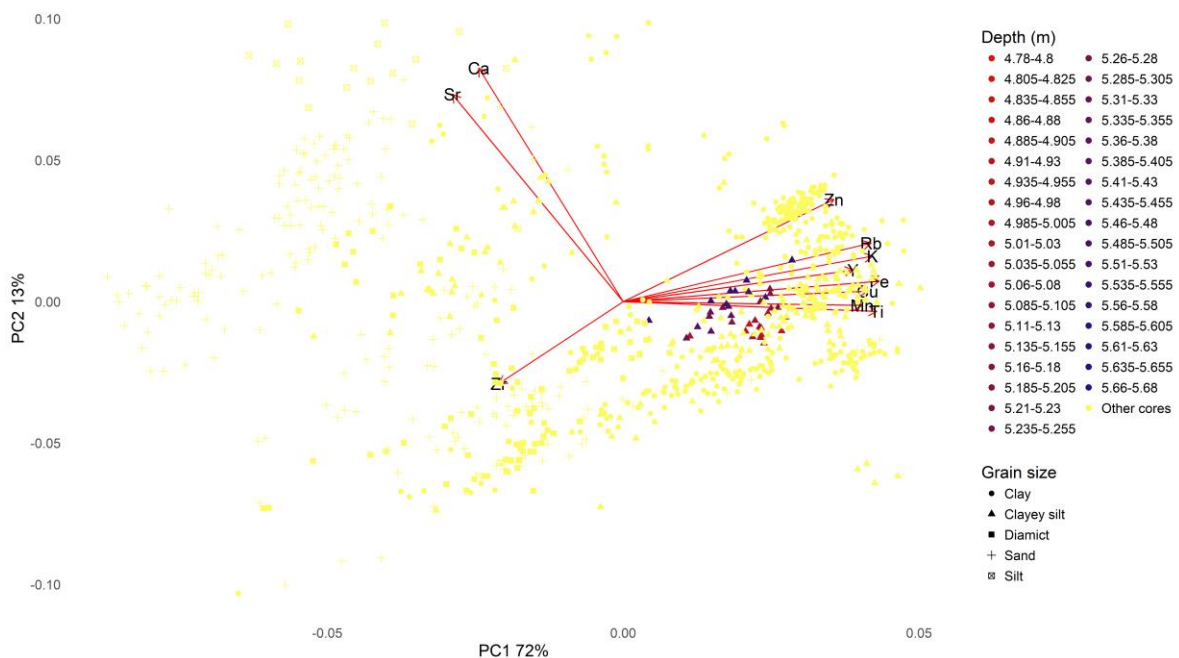


Figure 4.11 PCA biplot displaying internal elemental concentration and grain size variability for one Irish Sea core as a function of stratigraphy JC106-063VC. Blue data points are proximal sediments transitioning to distal sediments (red data points).

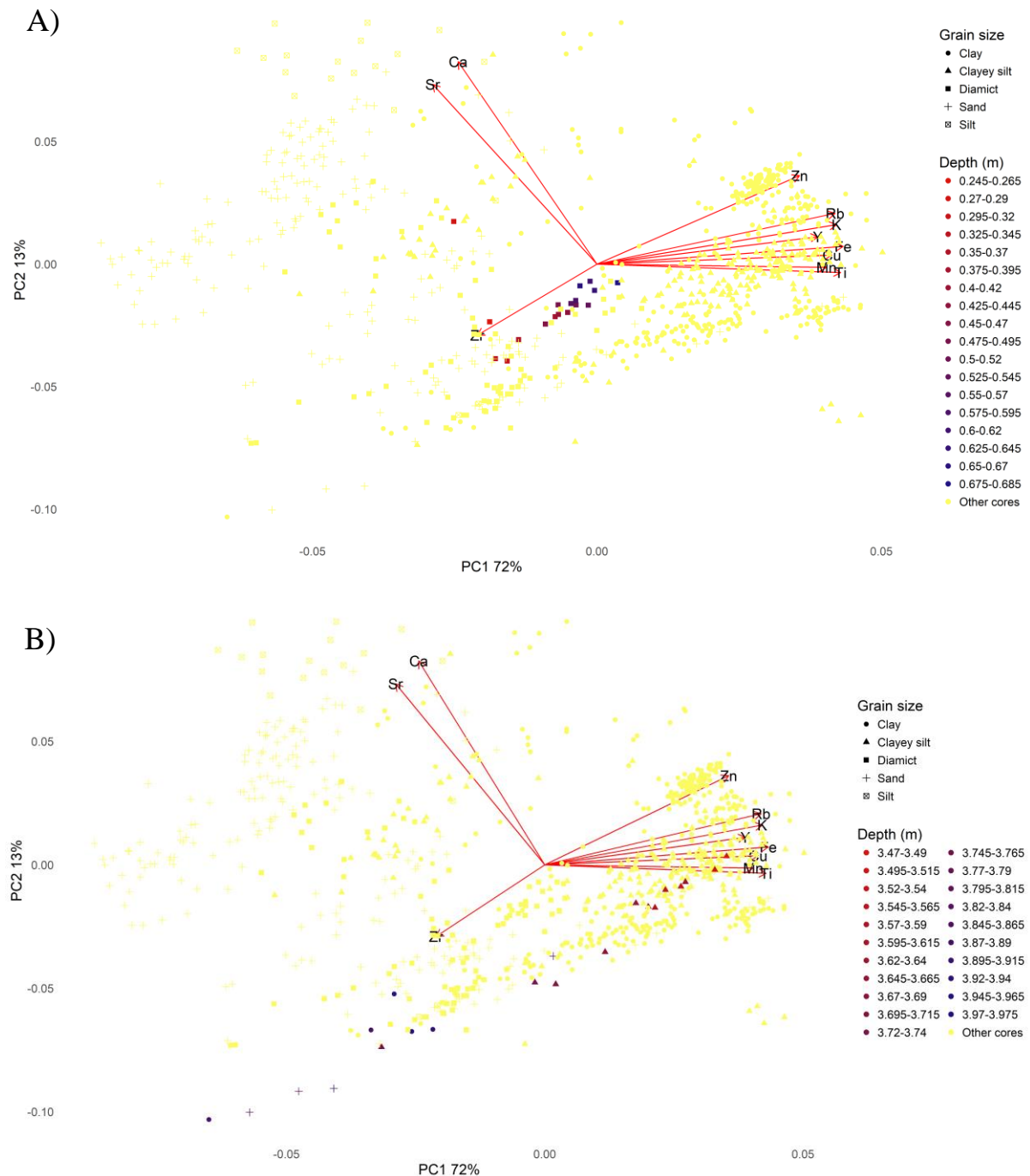


Figure 4.12 PCA biplot displaying internal elemental concentration and grain size variability for two Irish Sea cores as a function of stratigraphy. A) JC106-069VC B) JC106-073VC. Blue data points are proximal sediments transitioning to distal sediments (red data points).

The proximal sediment has negative values along both PC axes, whereas the more distal sediment is associated with positive PC 1 scores and therefore higher values for the terrigenous elements.

### **4.3 MD04-2820CQ**

#### **4.3.1 Lithostratigraphy**

Core MD04-2820CQ primarily consists of silty clay and calcareous oozes (core log produced by Francis Cooke Figure 4.13). There are a few dropstones present and some sandier horizons. The section of interest for this study is 0.6-5.4 m, which encompasses Heinrich events 1, 2, 3 and 4 (H1, H2, H3 and H4; Figure 4.13 and 4.14). A question mark is displayed next to H3 because it is not as clearly defined in MD04-2820CQ as the other Heinrich events. The core can be subdivided into two lithofacies; Heinrich layers and ambient clay-silt. There is no age control for this core because no age model has been developed. The base of this core is ~120-130 kyr BP and for the purpose of this study the Heinrich events will be used to provide chronostratigraphic markers.

#### **4.4 XRF geochemistry of MD04-2820CQ**

Figure 4.15A presents the PCA results of MD04-2820CQ. PC 1 explain 45% of the variance and PC 2 16%. Positive PC 1 scores correspond to high values in Fe, Rb, Ti, K, Zn and Zr whereas negative PC 1 scores are associated with high values of Ca, Sr and Mn. Most sample depths cluster in the 0 % region on both PC axes. H2 samples display negative PC 1 and PC 2 scores and are associated with high Ca and Sr values and to a lesser extent Mn. H1 and H4 also plot along the Ca, Sr and Mn vector, whereas H3 plots within the central main cluster.

Figure 4.15B is a biplot displaying the MD04-2820CQ PCA results excluding Heinrich events, purely focusing on the ambient clay-silt lithofacies. The NW arm represents the samples with a similar elemental signature to the Heinrich lithofacies; these samples plot alongside the H1, H2 and H4 events in Figure 4.15A. Figure 4.16 shows that that these samples occur in the post-H1, post-H4 and pre-H4 sectors of the deep ocean core. The NW grouping in Figure 4.15A corresponds to the SW grouping in Figure 4.15B. This cluster plots negatively along PC 1 and therefore has high values of Ca and Sr, however these data points are distinctly separated along the PC 2 axis from the Heinrich lithofacies. Figure 4.17 displays where these samples plot in relation to core stratigraphy. Stratigraphically they occur at depths throughout the core.

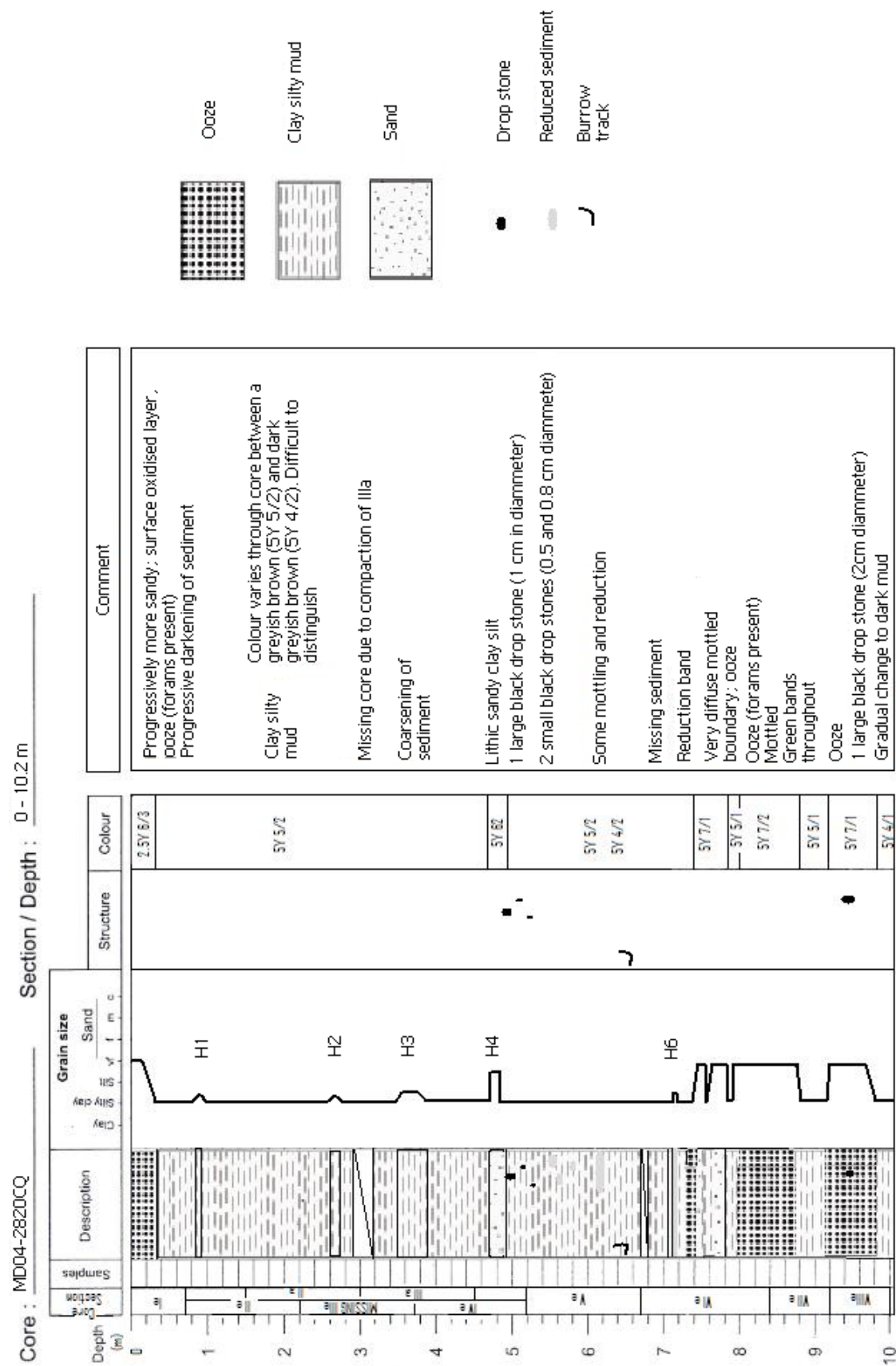


Figure 4.13. Lithological log for MD04-2820CQ produced by Cooke, 2008.

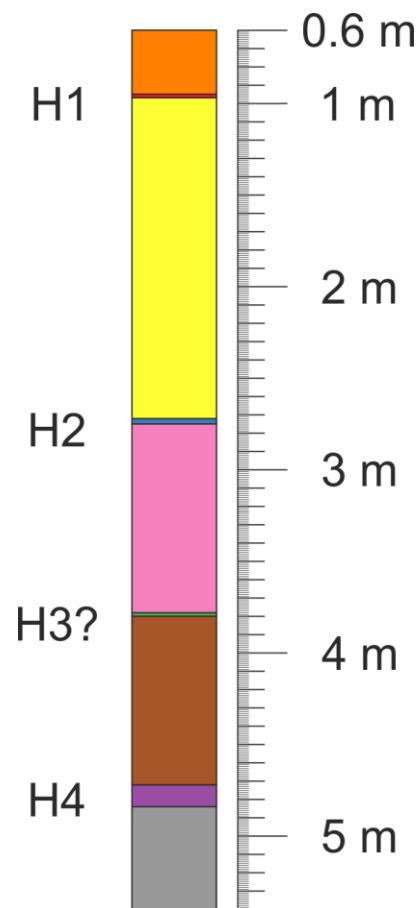


Figure 4.14 Lithostratigraphic core log for MD04-2820CQ. Heinrich events and the ambient clay silt lithofacies have been colour coded. H1-Red, H2- Blue, H3- Green and H4 Purple. Post H1-Orange, Post H2-Yellow, Pre-H2- Pink, Post H4-Brown and Pre-H4 Grey. These same colours will be used in subsequent analysis.



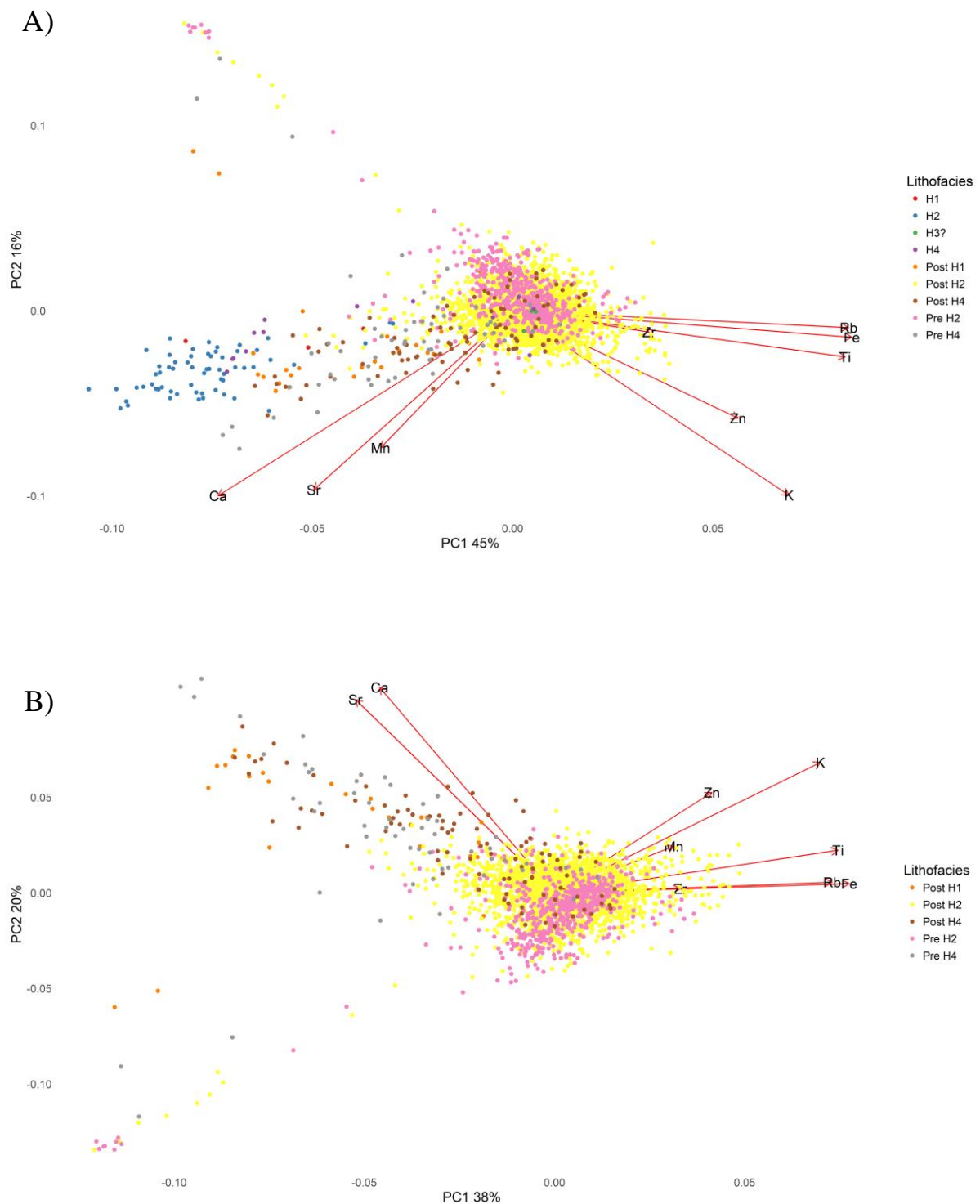


Figure 4.15 PCA biplot for MD04-2820CQ. A) PC 1 summarises 45% of the total variance in the dataset and PC 2 16%. Heinrich events and the ambient clay silt lithofacies have been colour coded. H1-Red, H2- Blue, H3-Green and H4-Purple. Post H1-Orange, Post H2-Yellow, Pre-H2-Pink, Post H4-Brown and Pre-H4 Grey. B) PCA biplot for MD04-2820CQ excluding Heinrich events, the ambient lithofacies have been colour coded. PC 1 accounts for 38% of the variance and PC 2 20%. The PC 2 scores have flipped from Figure 4.15A, so what was negative is now positive and vice versa.

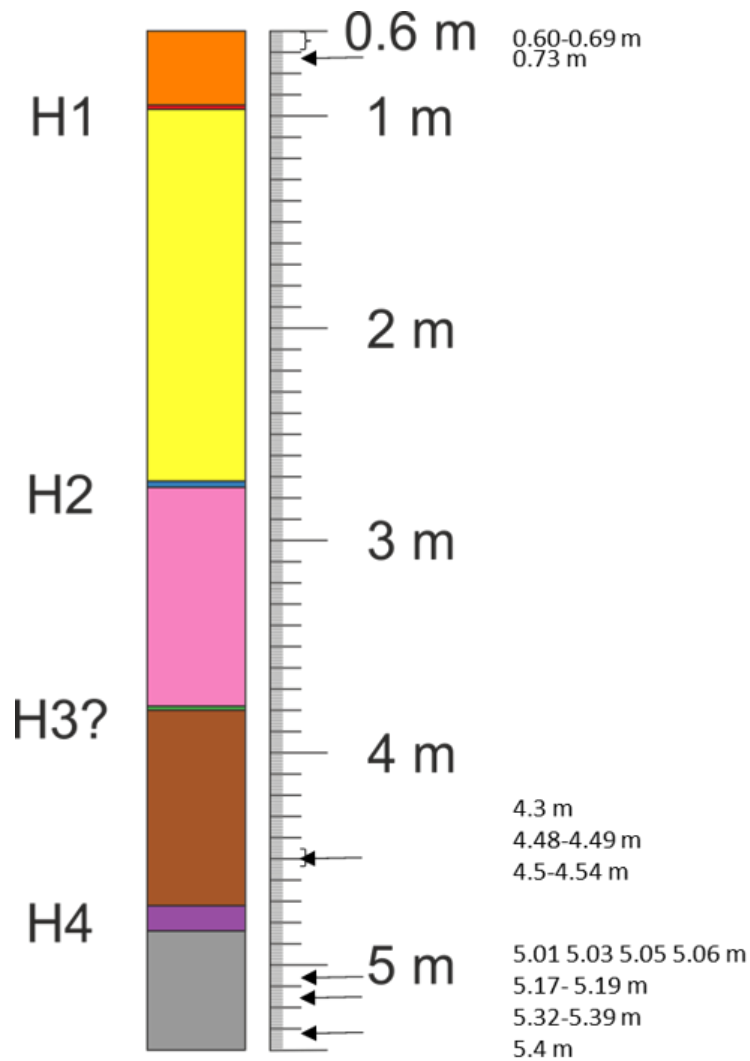


Figure 4.16 Lithostratigraphic core log for MD04-2820CQ. H1-Red, H2-Blue, H3-Green and H4-Purple. Post H1-Orange, Post H2-Yellow, Pre-H2-Pink, Post H4-Brown and Pre-H4 Grey. Arrows correspond to the stratigraphic position of the ambient samples that occur along the main SW Heinrich vector of the PCA in Figure 4.15A, and NW vector of Figure 4.15B.

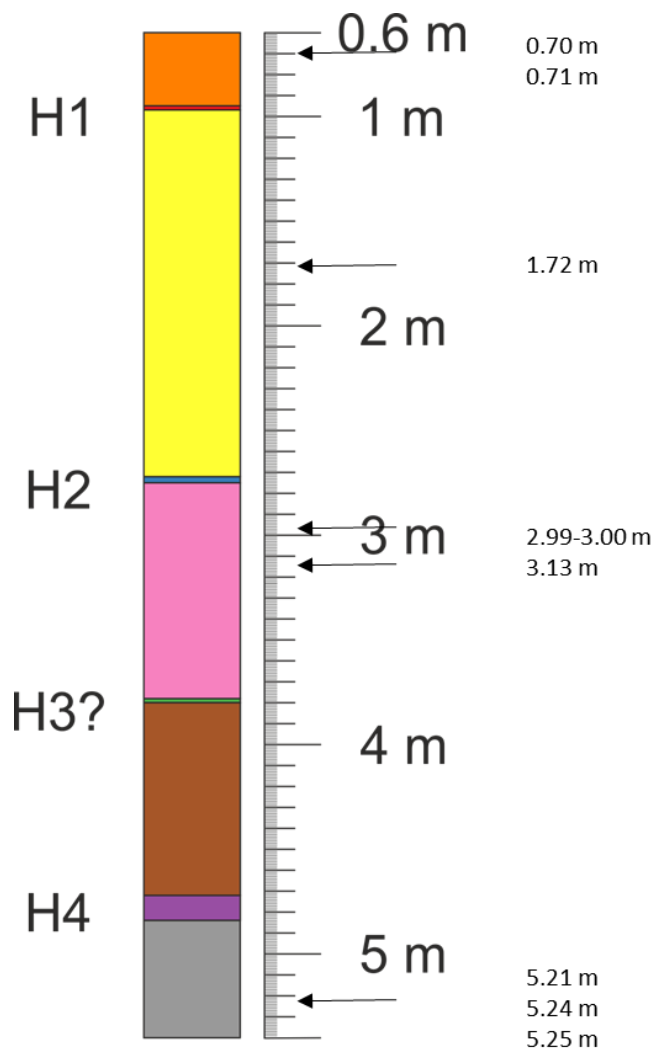


Figure 4.17. Lithostratigraphic core log for MD04-2820CQ. H1-Red, H2- Blue, H3- Green and H4 Purple. Post H1-Orange, Post H2- Yellow, Pre-H2- Pink, Post H4-Brown and Pre-H4 Grey. Arrows correspond to the stratigraphic position of the ambient samples that occur along the NW arm of the PCA in Figure 4.15A and SW arm of the PCA in Figure 4.15B.

#### **4.5 Integration of the shelf end members and MD04-2820CQ XRF data**

Figure 4.18 A and B are biplots illustrating the PCA results obtained by integrating the shelf end members and MD04-2820CQ XRF data. PC 1 accounts for 47 % and PC 2 accounts for 24 % of the variance. Samples with high PC 1 scores have high Fe, Rb, K, Ti and Zn values. Negative PC 1 scores indicate samples with high Zr and Ca values. PC 2 axis corresponds to Ca and Sr concentrations, positive PC 2 scores indicate high values of Ca, Sr and Mn. The ISIS cores plot mostly within the negative sectors on both PC axes, and retain their within-ice stream elemental variability. MD04-2820CQ clusters around the 0 % region of both PC axes,

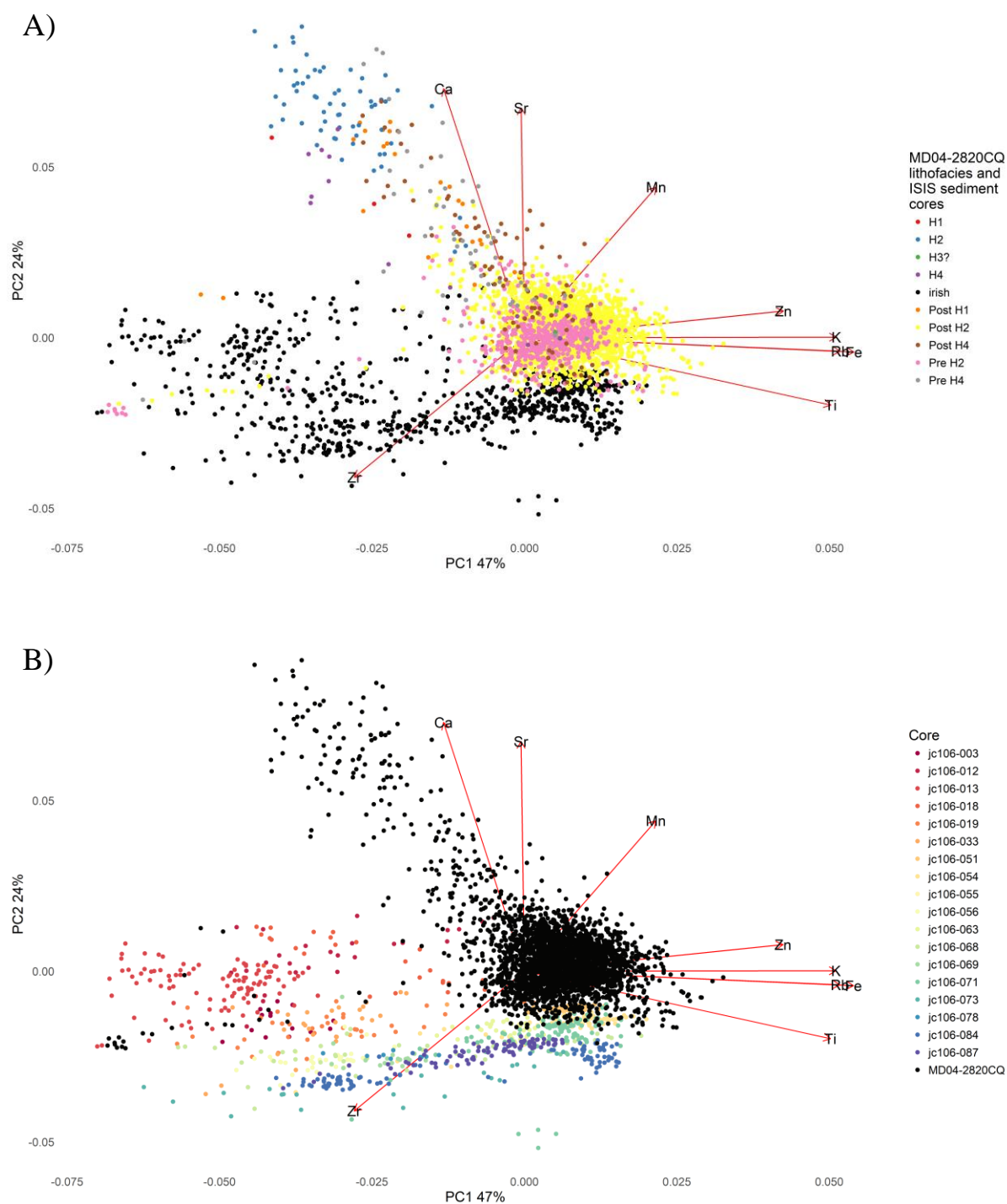


Figure 4.18 Biplots illustrating the PCA results obtained by integrating the shelf end members and MD04-2820CQ XRF data. PC 1 explains 47% of the variance and PC 2 24%. A) MD04-2820CQ has been colour coded by its lithofacies and the Irish end members are black. B) MD04-2820CQ is black and the Irish end members are colour coded by core.

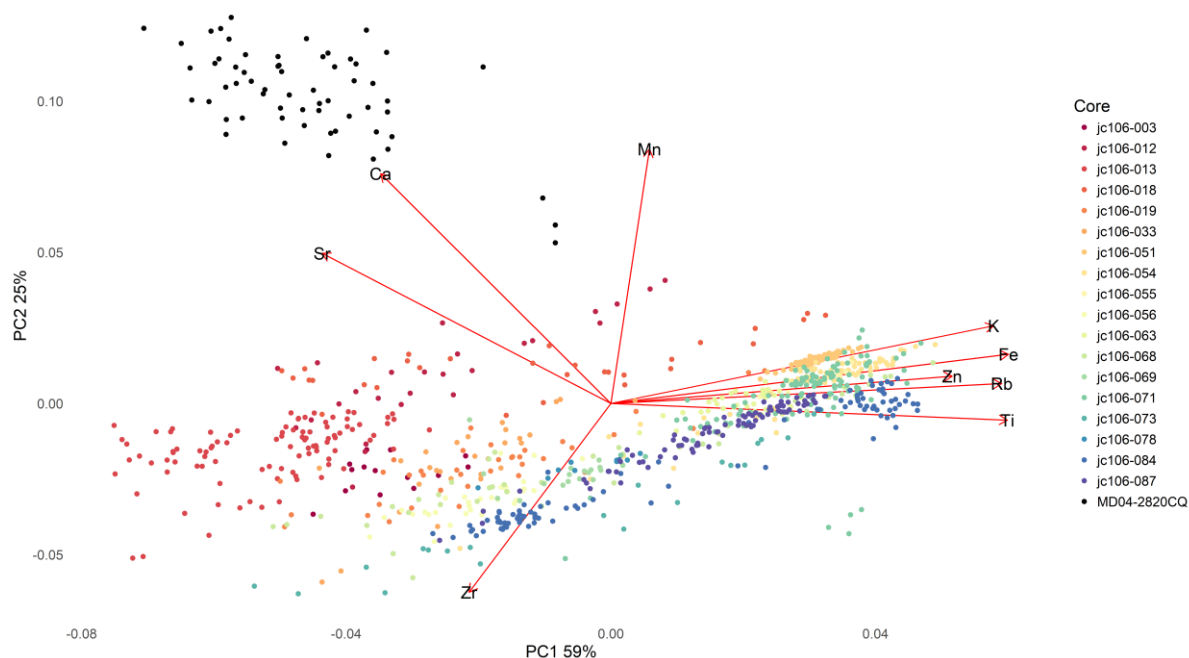


Figure 4.19 Biplot displaying the results of a PCA analysing both the shelf end members and H2 samples from MD04-2820CQ. H2 sediments are black and the Irish Sea end members are colour coded by core. PC 1 explains 59% of the total variance, PC 2 25%.

except for the two arms which will be referred to as the ‘Heinrich affinity’ and the ‘non-Heinrich affinity’. The Heinrich affinity plots NW on this PCA, whereas the non-Heinrich affinity plots to the SW. There is a degree of overlap between the two datasets, especially with the non-Heinrich arm and the central ambient cluster. The Heinrich affinity arm does not correspond elementally to the Irish continental shelf end members. This is evident in Figure 4.19, which is a biplot displaying the results of a PCA analysing both the shelf end members and H2 samples from MD04-2820CQ. There is a clear separation between the two datasets, however there are three points that do plot close to the ISIS end members (these are from depths 2.75-2.76 m). Henceforth the ISIS end members will be analysed with just the ambient MD04-2820CQ sediment (excluding the depths associated with Heinrich events).

Figures 4.20A & B are biplots of the PCA results of the ambient MD04-2820CQ lithofacies and the ISIS end members. The exclusion of the Heinrich events does not have a significant impact on the clustering of the datasets. However, Ca and Sr now correspond with positive PC 1 scores rather than negative.

The Celtic Sea end member overlaps with the non-Heinrich arm of the PCA (Figures 4.21A and B), whereas the Irish Sea end members display similarities to the central cluster of the ambient MD04-2820CQ depths. Subsequent exploration of the integrated datasets

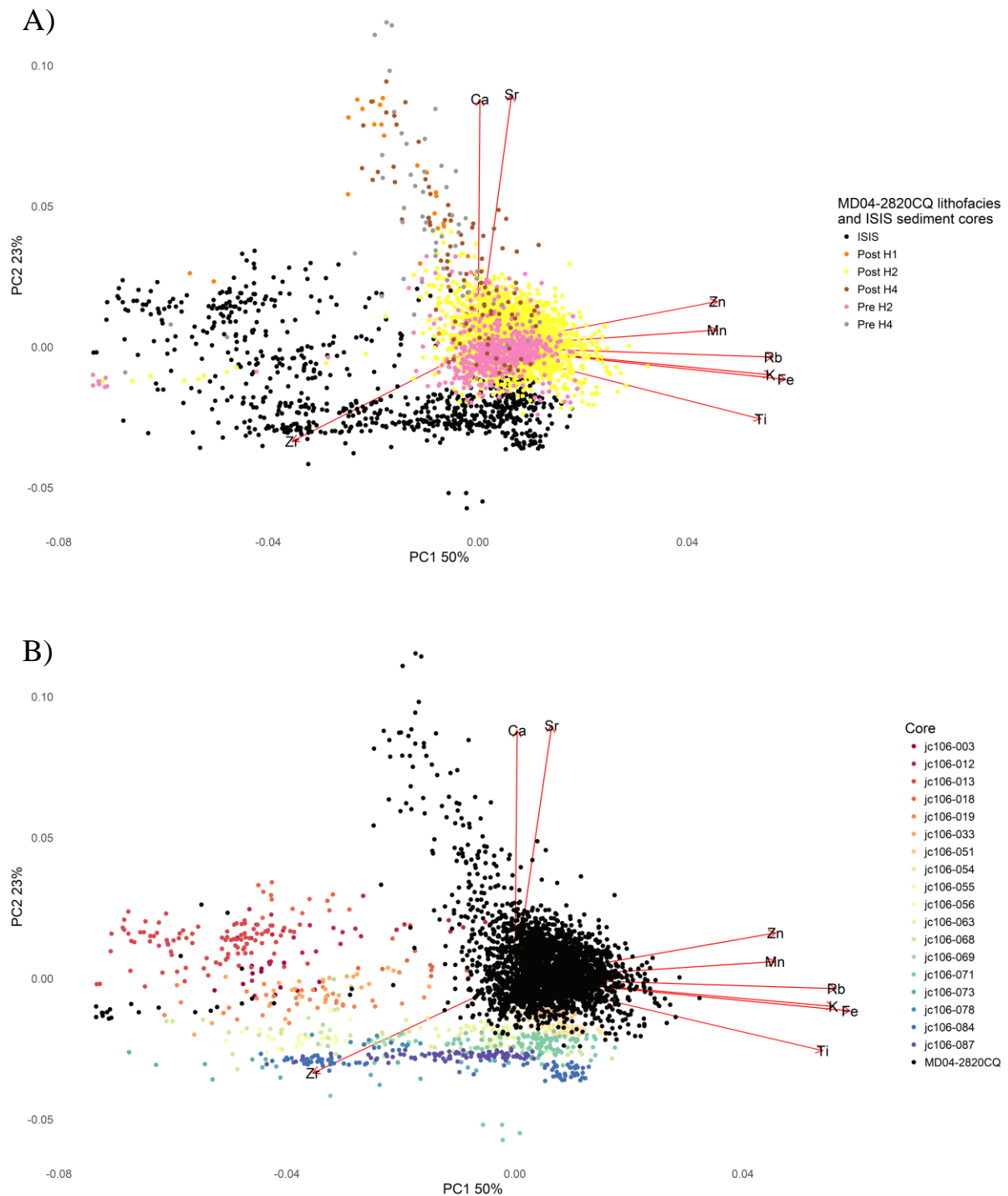


Figure 4.20 Biplots of the PCA results of the ambient MD04-2820CQ lithofacies and the ISIS end members. PC summarises 50% of the total variance and PC 2 23%. A) MD04-2820CQ ambient lithofacies have been colour coded and the Irish end members are black. B) MD04-2820CQ ambient lithofacies are black and the ISIS end members have been colour coded by core.

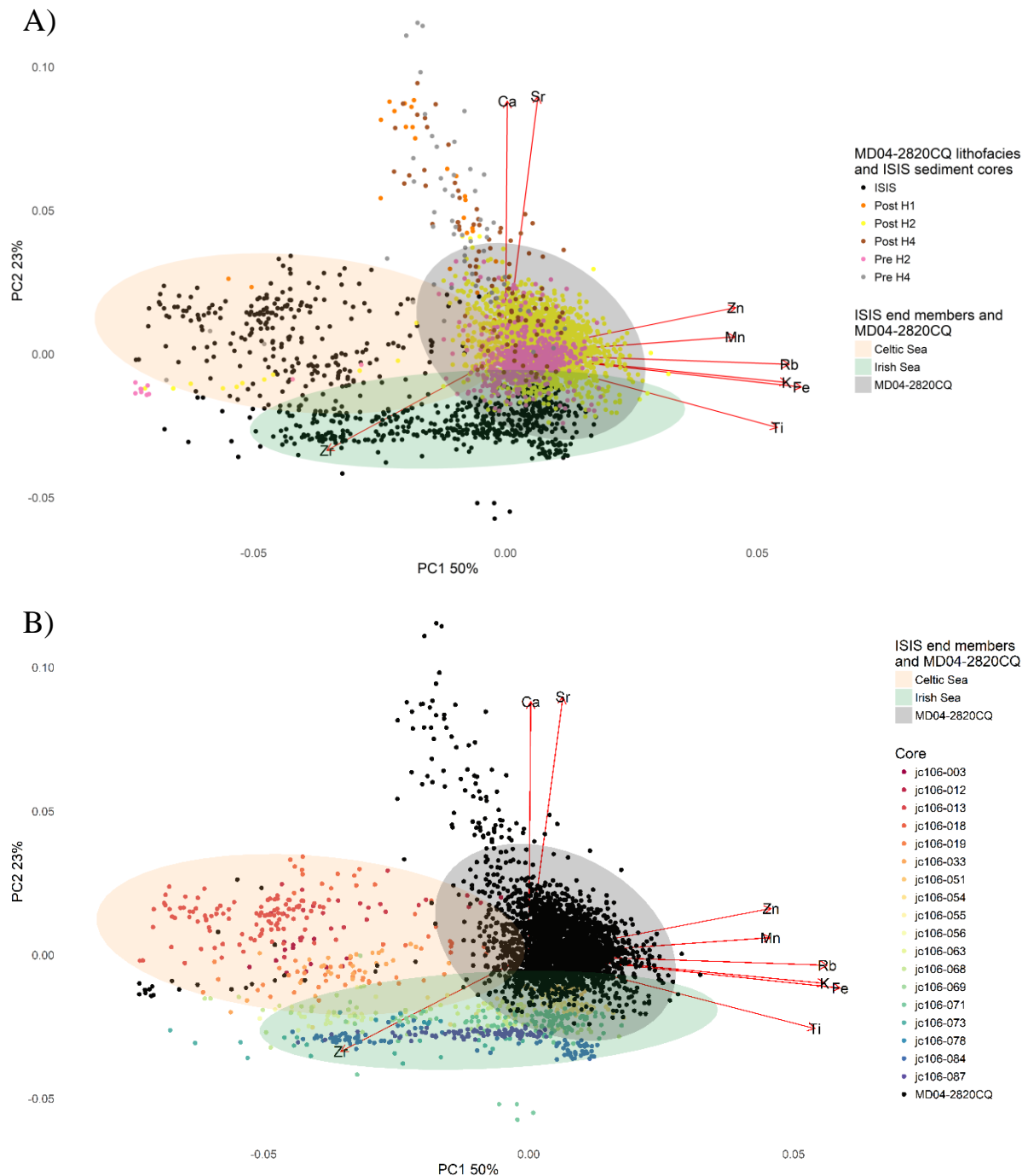


Figure 4.21. Biplots of the PCA results of the ambient MD04-2820CQ lithofacies and the ISIS end members. PC1 summarises 50% of the total variance and PC2 23%. A) MD04-2820CQ ambient lithofacies have been colour coded, the ISIS end members are black and have been categorised by region. B) MD04-2820CQ ambient lithofacies are black and the ISIS end members have been colour coded by core and categorised by region.

focuses on determining which end members corresponded to certain intervals in MD04-2820CQ, thereby fingerprinting depths within the deep ocean core to the shelf end members. Figure 4.22 and 4.23 show the elemental similarities and dissimilarities between the shelf cores and MD04-2820CQ. Figure 4.22 A displays the biplot of the results from the PCA analysing

the similarities between JC106-019VC and MD04-2820CQ. The biplot demonstrates there are similarities between the elemental signature of JC106-019VC and the ‘non-Heinrich’ arm of the PCA. Both have high values for Ca and Sr but are depleted in the terrigenous

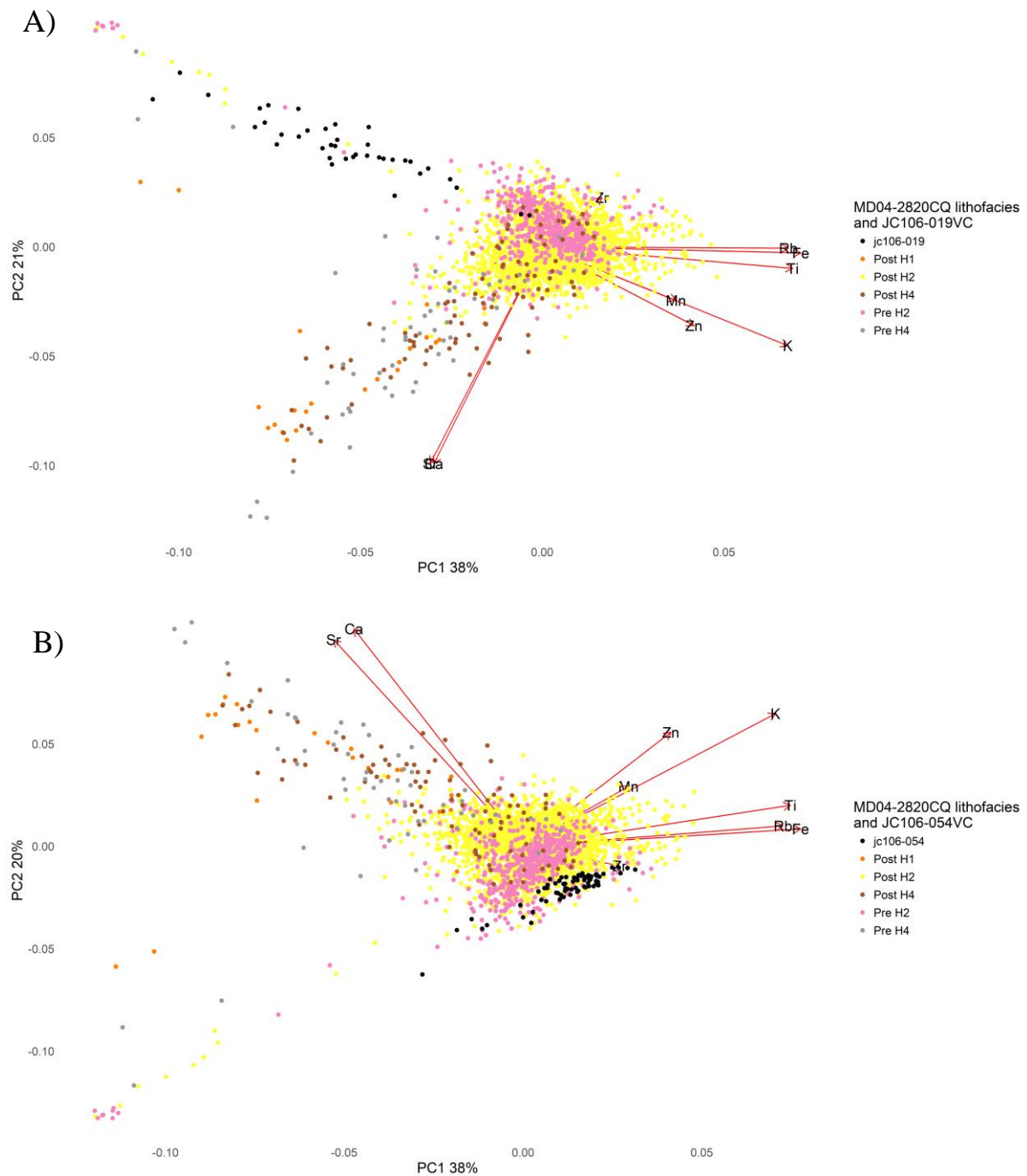


Figure 4.22 Biplots of the PCA results of the ambient MD04-2820CQ lithofacies and two sediment cores from the former ISIS. A) JC106-019VC and MD04-2820CQ ambient lithofacies. PC 1 summarises 38% of the variance, PC 2 21%. B) JC106-054VC and MD04-2820CQ ambient lithofacies. PC 1 accounts for 38% of the variance and PC 2 20%.



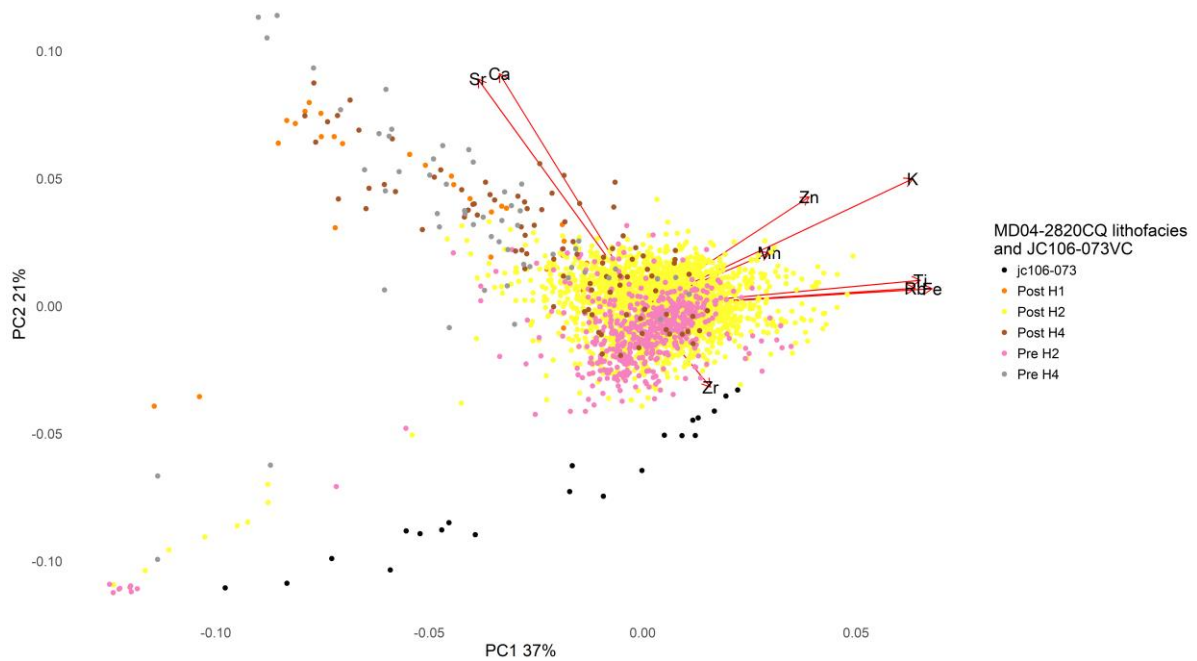


Figure 4.23 Biplot of the PCA results of the ambient MD04-2820CQ lithofacies and one sediment cores from the former ISIS. JC105-073 and MD04-2820CQ ambient lithofacies. PC 1 summarises 37% of the total variance and PC 2 21%.

elements. The biplot for JC106-054VC and MD04-2820CQ (Figure 4.22B) shows that JC106-054VC clusters very closely to the central ambient cluster of MD04-2820CQ, and the samples are associated with high PC 1 scores. Figure 4.23 is the biplot for JC106-073VC and MD04-2820CQ. The biplot shows that JC106-073VC has a SW orientation, which resembles the ‘non-Heinrich’ SW arm, however there is no significant overlap between the two datasets. The interpretation of these analyses will be discussed in Chapter 7.

# 5 Hebrides Ice Stream and Donegal Bay sector

The Hebrides Ice Stream drained western Scotland, the North Channel and Northern Ireland; and the Donegal Bay ice lobe drained northwest Ireland. Both ice margins supplied sediment to the Barra-Donegal Fan system (Wilson and Austin, 2002). Nine continental shelf cores and one deep ocean core have been analysed with the aim to:

1. Use  $\mu$ XRF to determine the geochemical signature of the glacial sediments across the continental shelf which formerly drained the Hebrides Ice Stream and Donegal Bay ice lobe;
2. Demonstrate the geochemical variations in the glacial end members across the study area;
3. Use  $\mu$ XRF to determine the geochemical variability of an adjacent deep ocean core (MD04-2822)
4. Determine whether the offshore IRD record from the Rockall Trough (MD04-2822) can be linked to the shelf glacial end members

This chapter presents the lithostratigraphy and radiocarbon dates of the nine cores analysed for the Hebrides Ice Stream and Donegal Bay sector, the calibrated  $\mu$ XRF scan data and the statistical analysis performed.

This chapter also presents the lithostratigraphy for MD04-2822, the calibrated  $\mu$ XRF scan data and the statistical analysis performed.

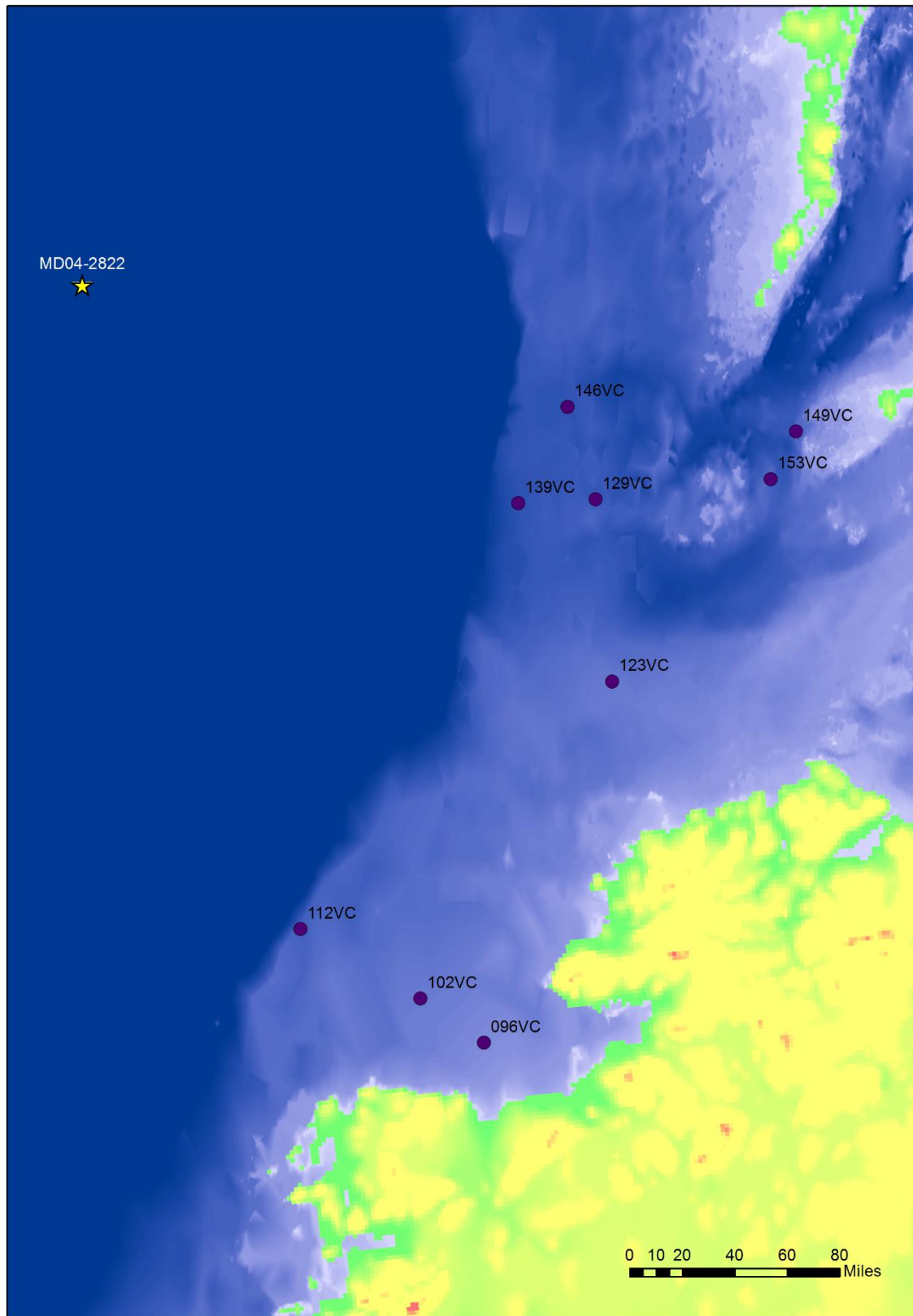


Figure 5.1. Location map of the nine JC106 cores analysed for the Hebrides Ice Stream, Donegal Bay ice lobe and adjacent deep ocean core MD04-2822.

## **5.1 Hebrides Ice Stream and Donegal Bay continental shelf cores**

### **5.1.1 Lithostratigraphy**

The lithostratigraphy of all nine cores (Figure 5.2-5.3) can be summarised generally into three lithofacies associations 1) subglacial 2) glacimarine and 3) postglacial.

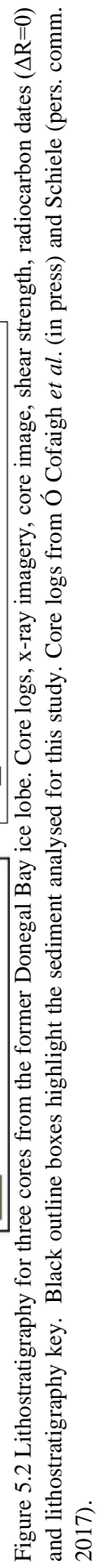
#### **Donegal Bay**

This study analyses three cores from the Donegal Bay transect (JC106-096VC, JC106-102VC and JC106-112VC; Figure 5.2). JC106-096VC and JC106-112VC have diamict at the base of the core which is overlain by a sandy diamict for the former and a matrix-supported gravel lithofacies for the latter. JC106-102VC on the other hand is characterised by laminated clay which is interspersed with massive silt and massive sand lithofacies.

#### **Malin Sea**

JC106-123VC (Figure 5.3) is from the central Malin Sea region, it consists of very high shear strength diamict, overlain by gravel and coarse sand lithofacies. The northern Malin Sea region encompasses a transect of five sediment cores from the shelf break to west of Tiree. JC106-129VC and JC106-139VC (Figure 5.3) are characterised by diamict bases with high shear strengths overlain by coarse sand and shelly gravel lithofacies. The other three cores (JC106-146VC, JC106-149VC and JC106-153VC; Figure 5.3) are dominated by clay, clayey silt and silt lithofacies. All three cores have a diamict unit at the base with variable shear strengths. JC106-146VC has three diamict units which are separated by silt and clay units. The top of the three cores comprise a mixture of medium/coarse sand and gravel lithofacies.

Analysis will focus on the subglacial and glacimarine lithofacies.



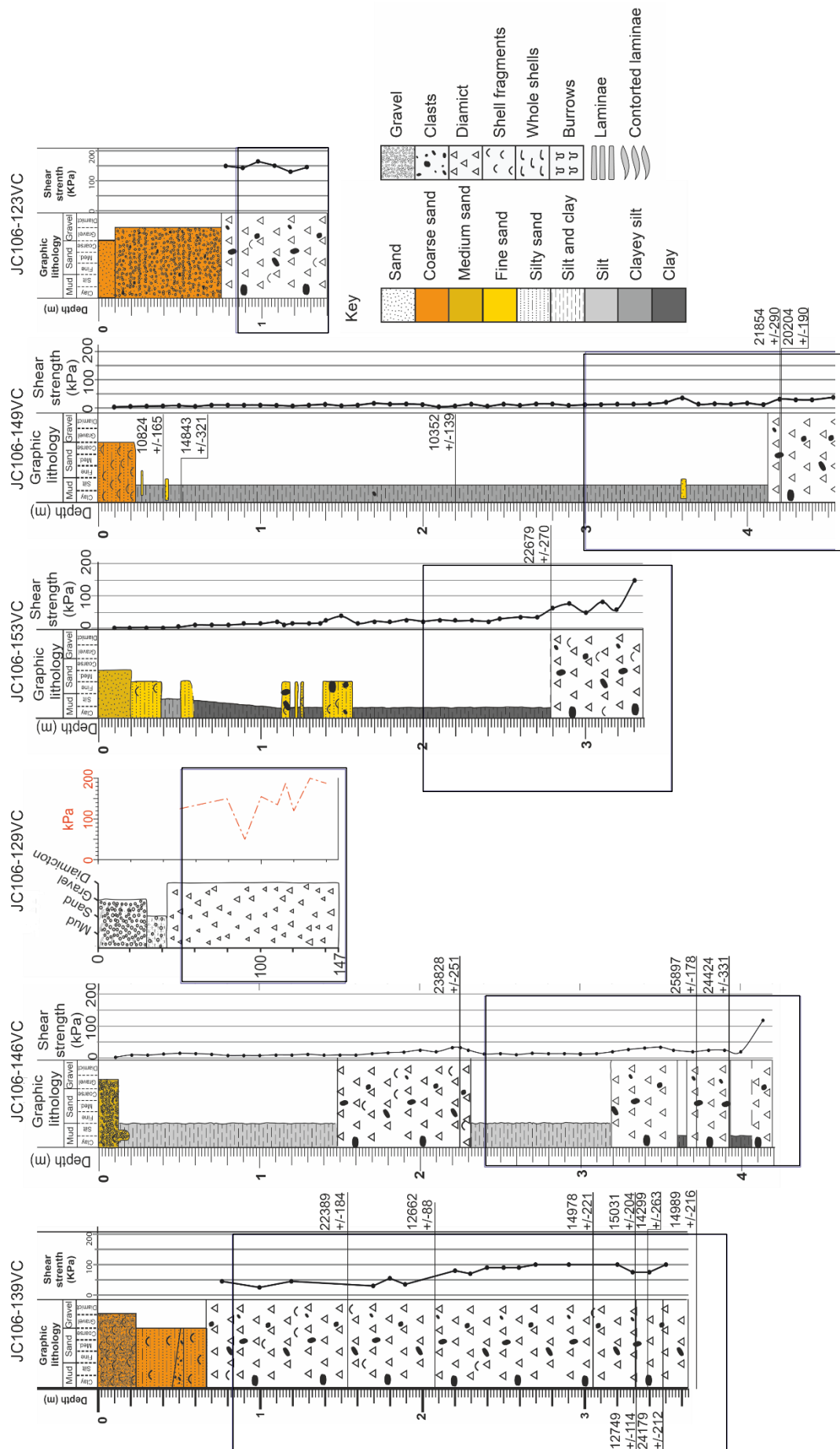


Figure 5.3 Lithostratigraphy for six cores from the former Hebrides Ice Stream. Core logs, x-ray imagery, core image, shear strength, radiocarbon dates ( $\Delta R=0$ ) and lithostratigraphy key. Black outline boxes highlight the sediment analysed for this study. Core logs produced by Louise Callard.

## **5.2 XRF geochemistry of the continental shelf cores**

### **Hebrides Ice Stream and Donegal Bay end members**

The geochemical signature of the nine continental shelf cores have been determined using PCA (Figure 5.4). The geochemical variations are summarised by the first two PC axes, PC 1 52% and PC 2 17%. Positive PC 1 scores are associated with Fe, Zn, Ti, Cu, Mn, Rb, K and Y, whereas negative PC 1 scores are linked to high Ca, Sr and Zr values. There is large overlap between the geochemical signature of the Donegal cores and the central Malin Sea core (Figure 5.5). The Northern Malin Sea cores cluster together but there are still geochemical similarities between the three regions. The Donegal cores are richer in Ca, Sr and Zr, in contrast to the Northern Malin Sea cores which mostly plot negatively along the PC 2 axis (Low Ca values). Fe has the highest loading for PC 1, which means it is an important contributor to the variance across the PC 1 axis (Figure 5.6). Northern Malin Sea cores have a higher concentration of Fe than the Donegal cores. The cores mainly consist of diamict, clay and clayey silt, positive PC 1 scores and negative PC 2 scores correspond to silt and clayey silt lithofacies (Figure 5.7 and 5.8).

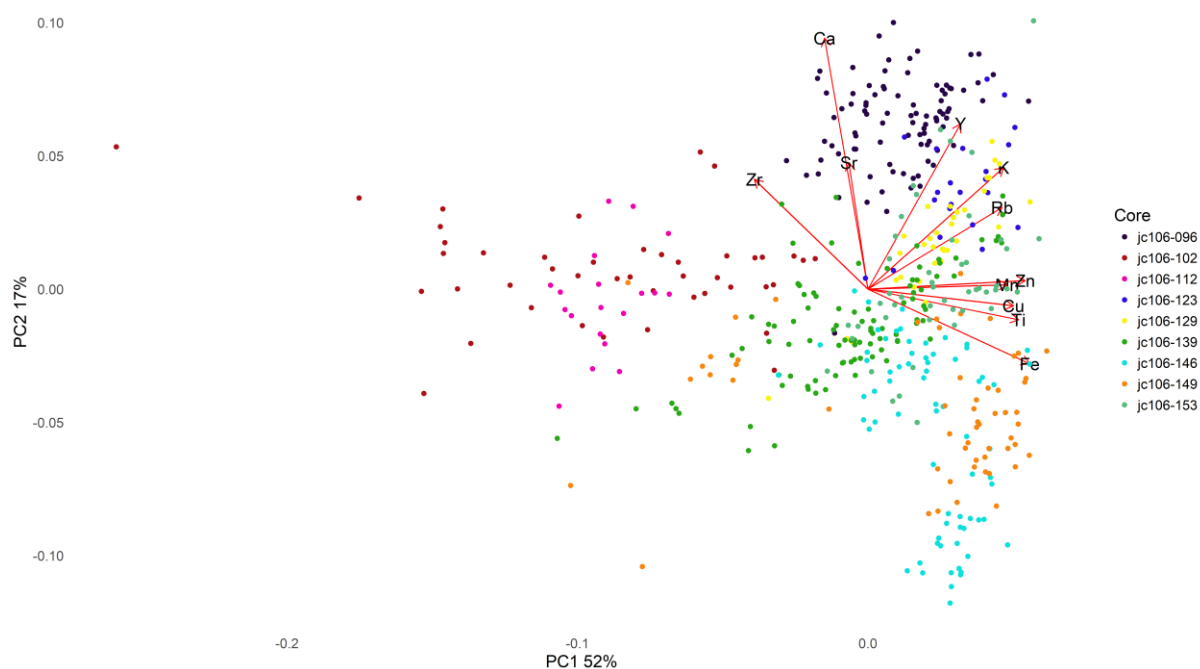


Figure 5.4 PCA biplot for the Hebrides Ice Stream and Donegal Bay sediment cores. PC 1 summarises 52% of the total variance in the dataset and PC 2 17%. Each core has been colour coded.

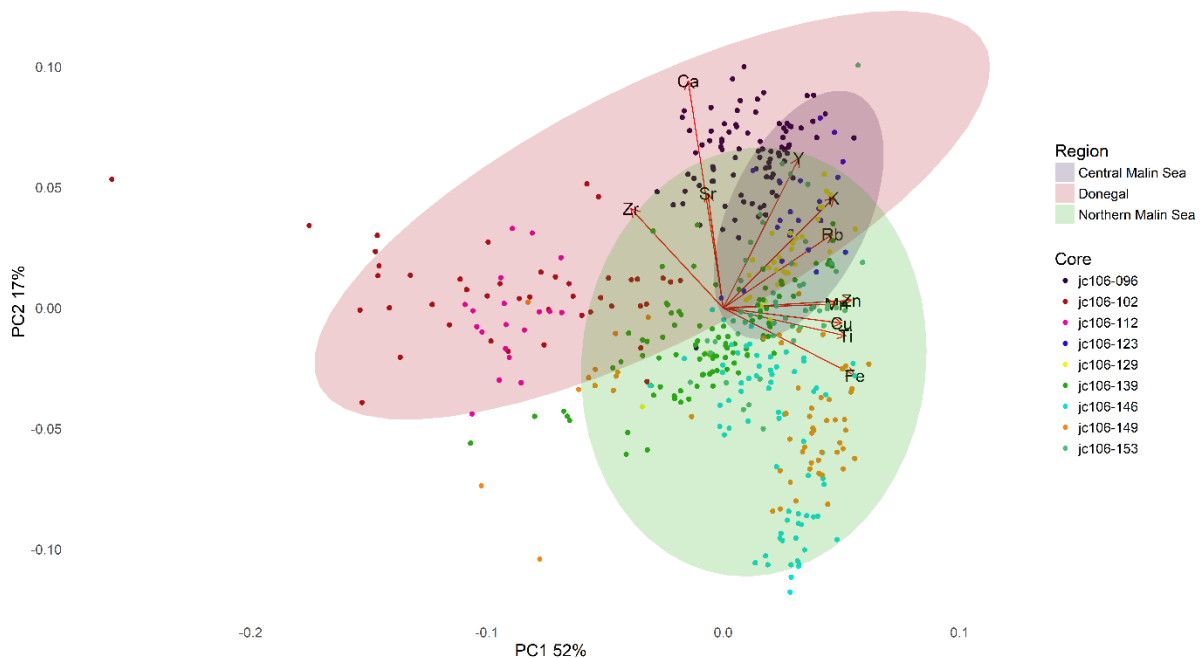


Figure 5.5 PCA biplot for the Hebrides Ice Stream and Donegal Bay sediment cores divided into regions. PC 1 summarises 52% of the total variance in the dataset and PC 2 17%. Each core and region has been colour coded.

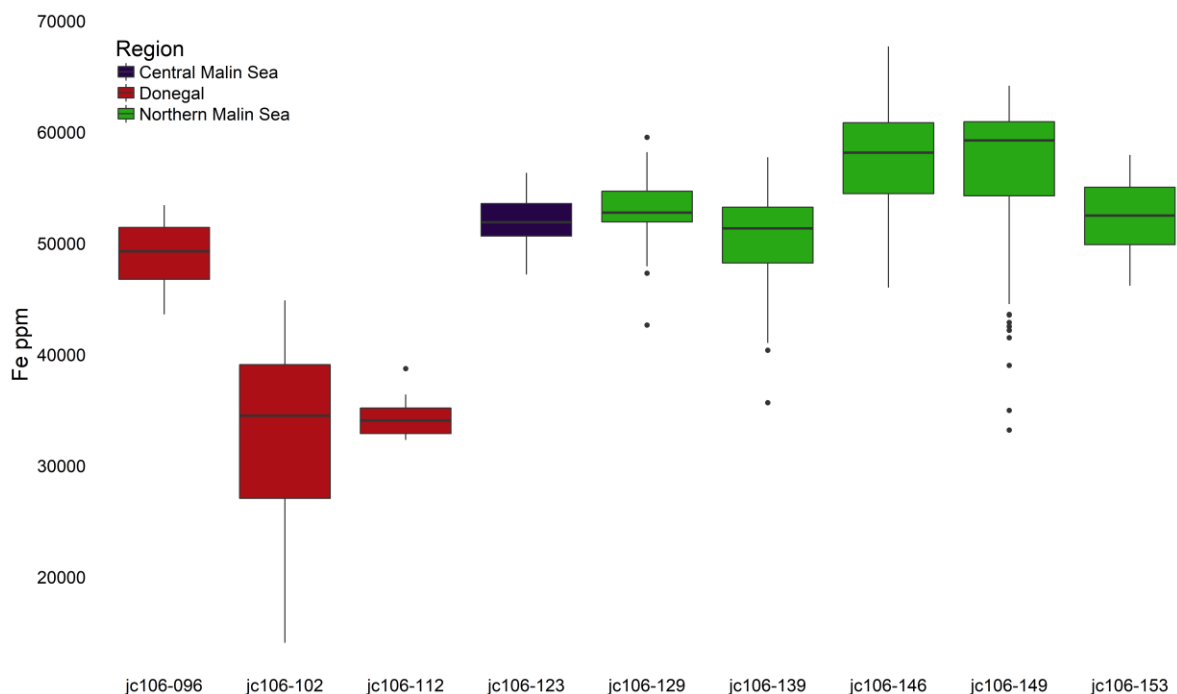


Figure 5.6 Boxplot displaying Fe concentrations of the nine sediment cores from the former Hebrides Ice Stream and Donegal Bay ice lobe. The cores have been colour coded by region. The lower and upper hinges correspond to the 25<sup>th</sup> and 75<sup>th</sup> percentiles. The upper whisker extends from the hinge to the largest value no further than 1.5\* inter quartile range ( $IQR(IQR=UQ-LQ)$ ) from the hinge. The lower whisker extends from the hinge to the smallest value at most 1.5\* IQR of the hinge. Data beyond the whiskers are plotted individually and called ‘outliers’. The black lines in the middle of the boxes are median values.



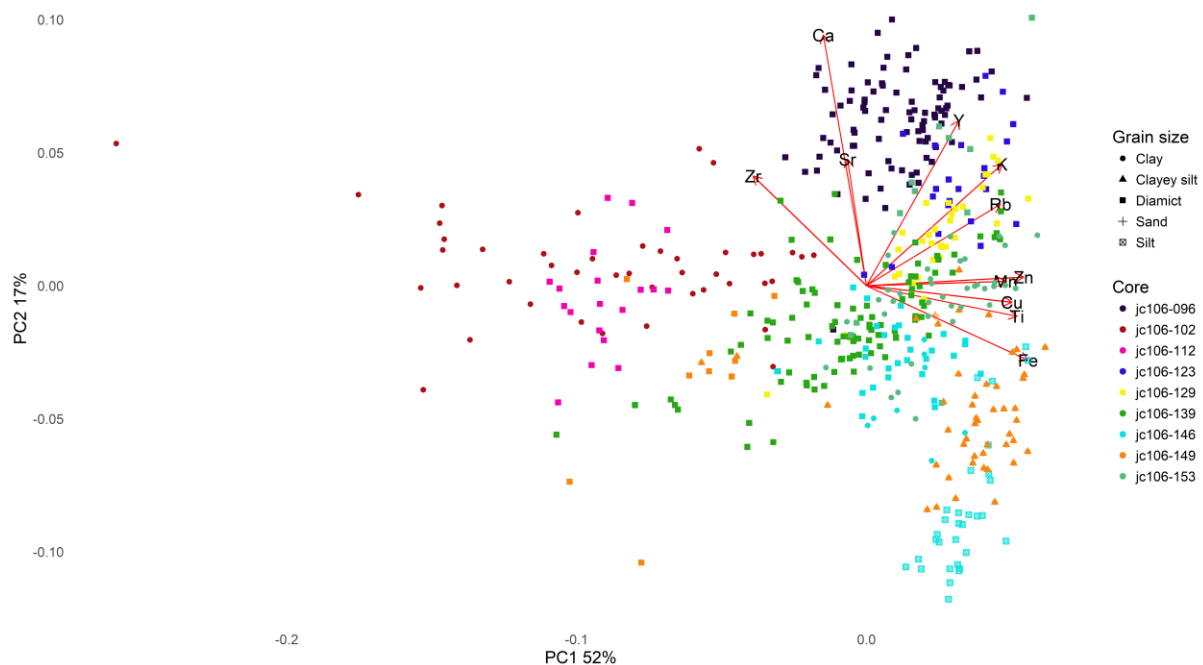


Figure 5.7 PCA biplot for the Hebrides Ice Stream and Donegal Bay sediment cores focusing on grain size. Each core has been colour coded and symbols display the grain size of each data point.



Figure 5.8 PCA biplot for the Hebrides Ice Stream and Donegal Bay sediment cores focusing on grain size. Every data point has been colour coded by grain size.

Some of the cores display quite a large spread in the data, which could relate to core stratigraphy or grain size variation; this is explored in Figures 5.9 and 5.10. JC106-102VC has negative PC 1 scores which indicate it has high values for Zr, Ca and Sr. The core has been colour coded based on depth (Blue data points represent proximal sediments, red indicates more distal sediments) and symbols indicate grain size. There is no clear stratigraphic gradient visible within the core, however the section analysed is dominated by clay. JC106-146VC has mostly positive PC 1 scores and negative PC 2 scores. There is a distinct stratigraphic gradient; the more distal sediments have lower Ca and Sr concentrations than the proximal sediments. The proximal sediments are mainly diamict and clay lithofacies, whereas the distal sediments are silt.

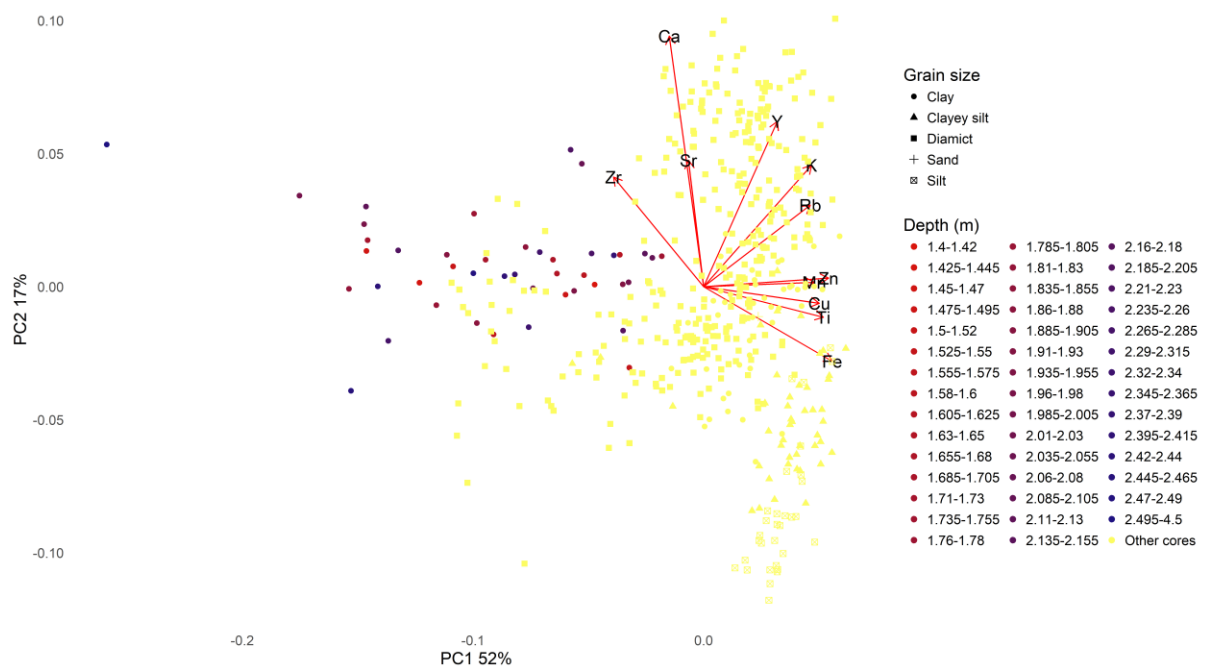


Figure 5.9 PCA biplot displaying internal elemental concentration and grain size variability for JC106-102VC as function of stratigraphy. Blue data points are proximal sediments transitioning to distal sediments (red data points).

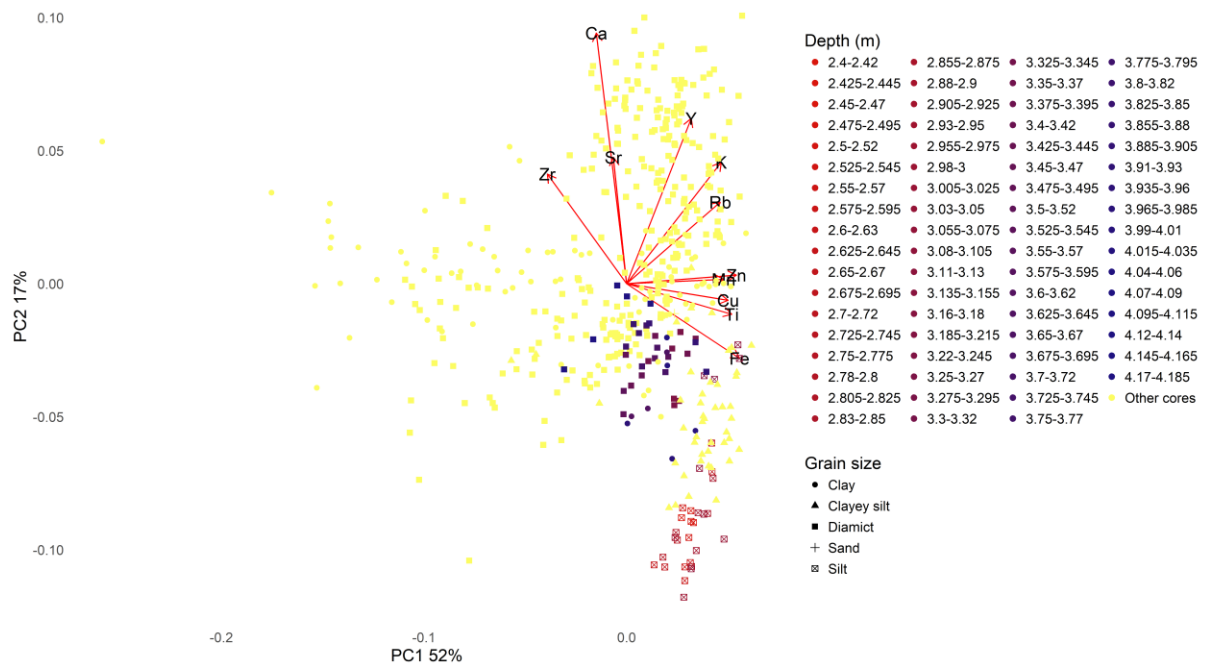


Figure 5.10. PCA biplot displaying internal elemental concentration and grain size variability for JC106-146VC as function of stratigraphy. Blue data points are proximal sediments grading to distal sediments (red data points).

## 5.3 MD04-2822

### 5.3.1 Lithostratigraphy

MD04-2822 primarily consists of clayey silt lithofacies with varying Ca content and magnetic susceptibility (core log located in Appendix 3, produced by Fiona Hibbert); there are also some silty to fine sand and silty-mud lithofacies. There are occasional dropstones and evidence of bioturbation. The section of interest for this study is 3.83-18.55 m (~14-31 kyr BP), which Hibbert (pers. comm. 2016) has interpreted as a clayey silt glaciomarine mud with low Ca content (Figure 5.11).

### 5.4 XRF geochemistry of MD04-2822

The PCA for MD04-2822 has been coloured coded based on age/depth of the sediment (Figure 5.12). PC 1 accounts for 33% of the total variance whereas PC 2 accounts for 30%. High PC 1 scores corresponds to high values of K, Fe, Zn, Ti, Rb and Mn, whereas negative PC 1 scores indicate high values of Zr, Sr and Ca. Ca and Sr are the main contributors to the variance along the PC 2 gradient; negative values indicate high Ca content, whereas positive PC 2 scores are affiliated with high Rb and to a lesser extent Fe. The geochemical data for MD04-2822CQ seems to show an age/depth related gradient along the PC 2 axis (Figure 5.13). The 24-31 kyr

BP sediments contain higher values of Ca and Sr than the 12-24 kyr BP sediments, which is also noted on the Hibbert core log (Figure 5.11). There is overlap between the two ellipses but still a notable pattern present.

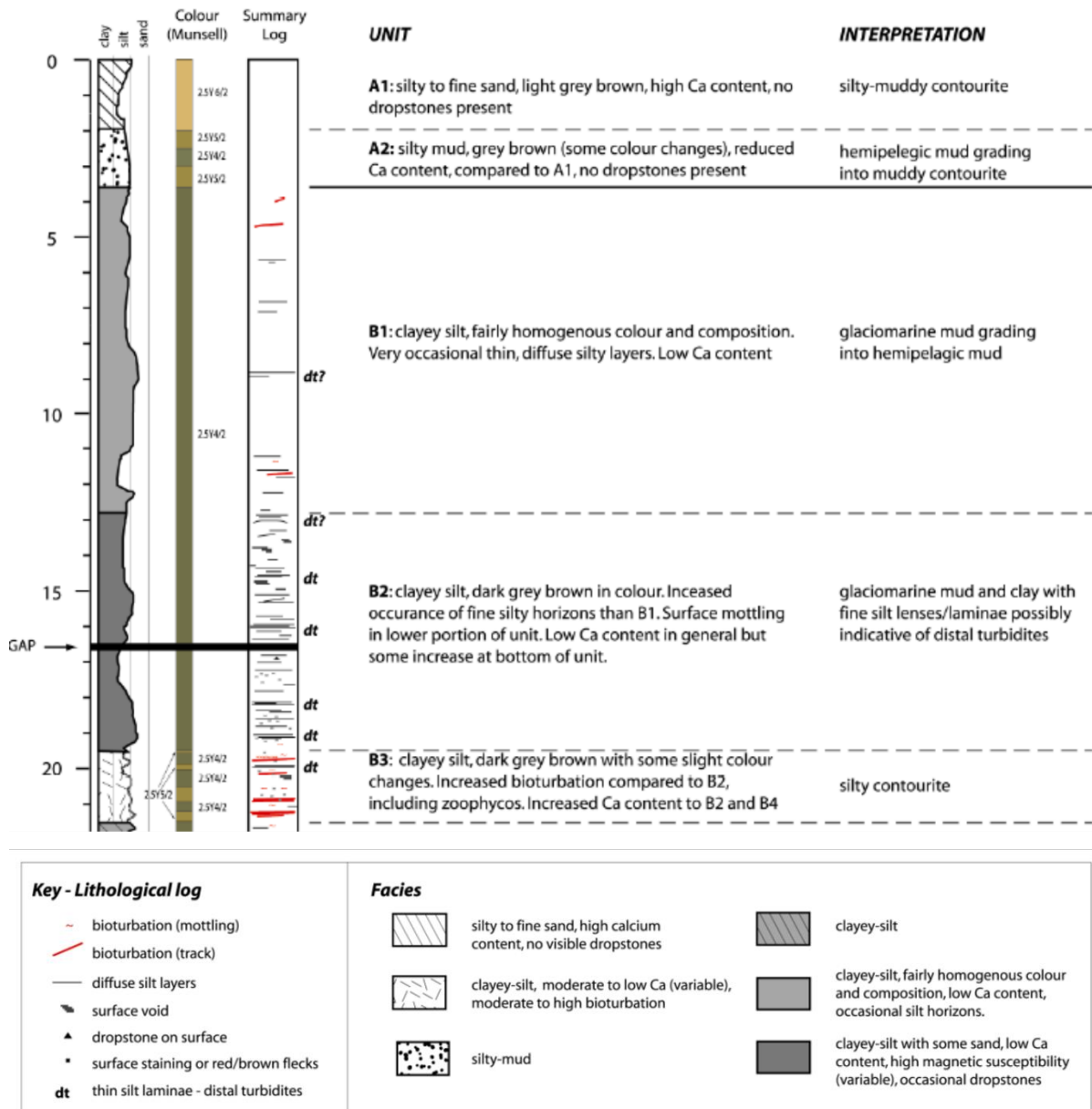


Figure 5.11 Lithostratigraphic core log and key for MD04-2822. The section of interest for this study is 3.83-18.55 m (~14-31 kyr BP). Edited from Hibbert (pers. comm. 2016).



Figure 5.12 PCA biplot for MD04-2822. PC 1 summarises 33% of the total variance in the dataset and PC 2 30%. The core has been subdivided into age intervals which are colour coded.

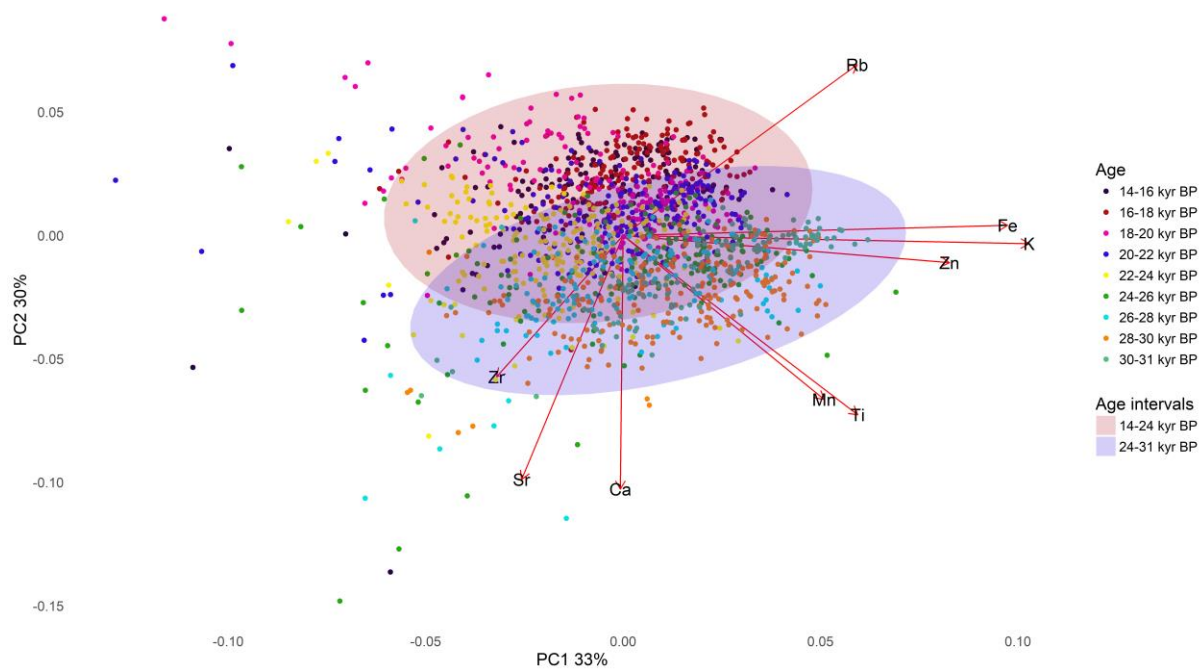


Figure 5.13 PCA biplot for MD04-2822. PC 1 summarises 33% of the total variance in the dataset and PC 2 30%. The core has been colour coded by age intervals and further grouped into broader age intervals (14-24 kyr BP and 24-31 kyr BP).

## 5.5 Integration of the shelf end members and MD04-2822 XRF data

The PCA of the two datasets displays a gradient along the PC 1 axis. PC 1 accounts for 49% of the total variance, PC 2 22% (Figure 5.14). The Hebrides Ice Stream and Donegal Bay end members have negative PC 1 scores and are therefore richer in Zr and Sr, and depleted in Fe, K, Zn and Rb (as well as the other elements to a lesser extent). All cores excluding JC106-102VC and JC106-112VC, show a degree of integration with the geochemical composition of MD04-2822, illustrating geochemical similarity (Figure 5.15 and 5.16). The shelf end members have a more similar geochemical affinity to the 14-24 kyr BP sediments than the 24-31 kyr BP sediments (Figure 5.16 and 5.17). JC106-146VC and JC106-149VC plot mostly within the 14-24 kyr BP ellipse, whereas some of the JC106-123VC, JC106-129VC and JC106-139VC data points plot within the 24-31 kyr BP ellipse (Figure 5.17). On the other hand, some of the data points for JC106-153VC plot within the intersection of the two MD04-2822 age ellipses. All three regions in the Hebrides Ice Stream and Donegal Bay sector overlap with MD04-2822 (Figure 5.18), however the central and northern Malin Sea cores show a more similar relationship to MD04-2822 than the Donegal region. Further analysis focused on exploring the relationship between the individual end members and age/depth intervals of MD04-2822 with the aim of fingerprinting intervals to specific shelf end members. JC106-096VC plot quite

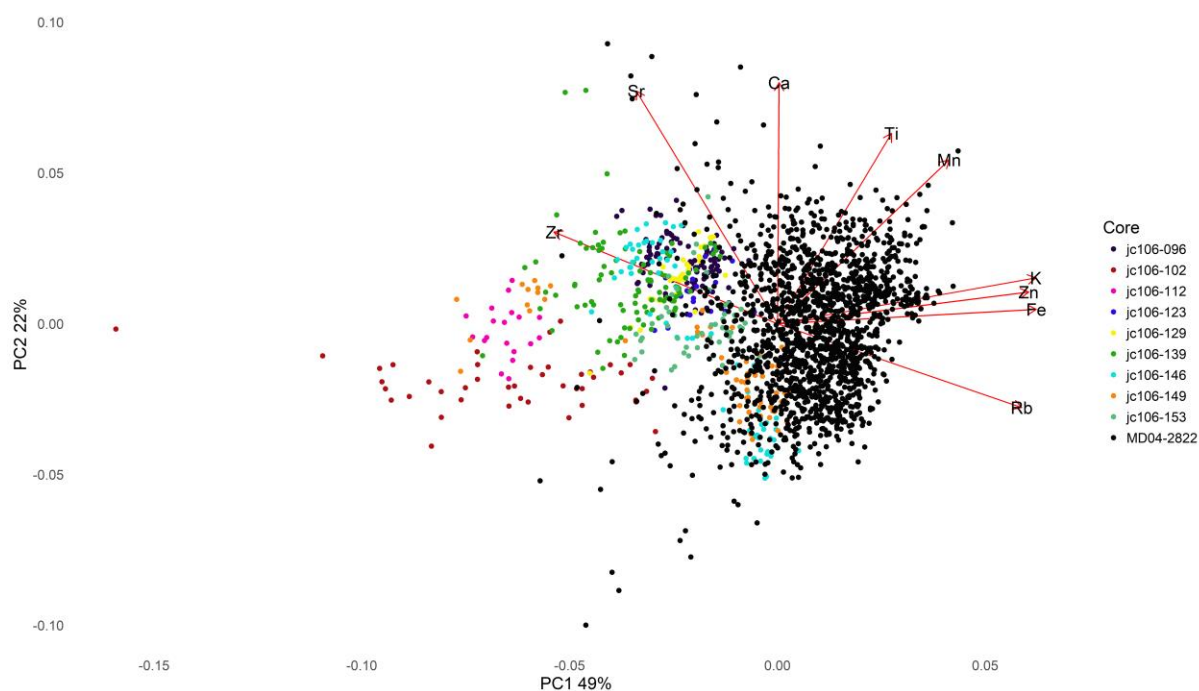


Figure 5.14. Biplot illustrating the PCA results obtained by integrating the shelf end members and MD04-2822 XRF data. PC 1 explains 49% of the variance and PC 2 22%. MD04-2822 has been colour coded by its age intervals and the Hebrides Ice Stream and Donegal Bay end members are black.

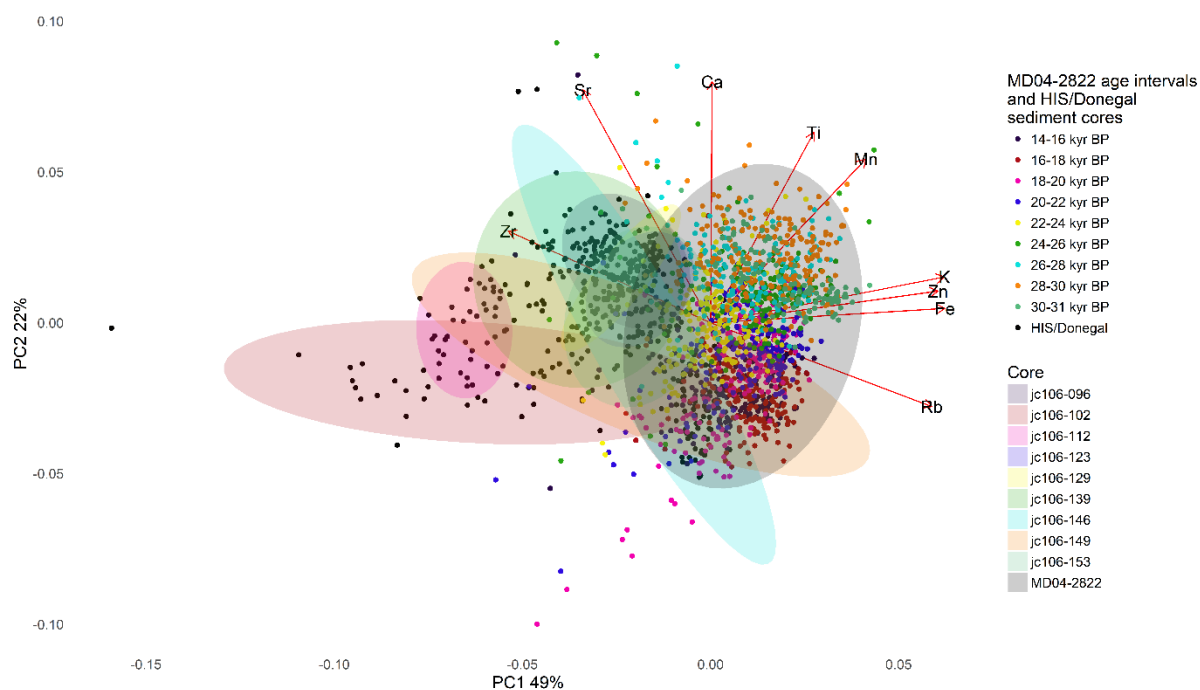


Figure 5.15 Biplot of the PCA results of MD04-2822 and Hebrides Ice Stream (HIS) and Donegal Bay end members. PC 1 summarises 49% and PC 2 22%. The age intervals of MD04-2822 have been colour coded, the Hebrides Ice Stream and Donegal Bay end members are black and each core is shown by an ellipse.

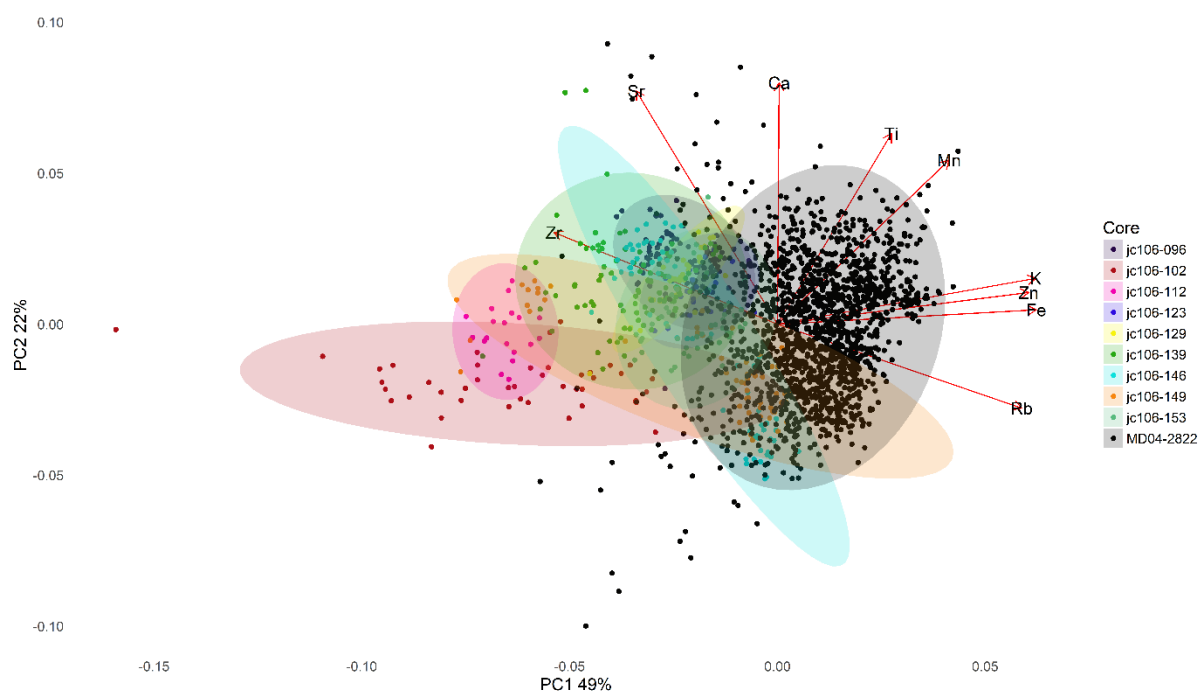


Figure 5.16. Biplot of the PCA results of MD04-2822 and Hebrides Ice Stream and Donegal Bay end members. PC 1 summarises 49% and PC 2 22%. Each core is shown by an ellipse and has been colour coded.



closely to the central MD04-2822 cluster (Figure 5.19). JC106-096VC has negative PC scores for both axes, and clusters mostly with the 22-30 kyr BP sediments, whereas JC106-112VC does not plot closely to MD04-2822 (Figure 5.20) and consequently is dissimilar geochemically. JC106-112VC has very negative PC 1 scores which indicates high values in Zr, Sr and Ca, and low values for the remaining elements. JC106-149VC shows both a great deal of geochemical similarity and dissimilarity to MD04-2822 (Figure 5.21). The geochemically similar cluster of JC106-149VC has negative PC 2 scores and is therefore high in Rb and depleted in Ca and Sr. This cluster plots mostly with the 14-24 kyr BP sediments, whereas the dissimilar cluster has positive scores on both axes which indicates it has high values for Ca and Sr and is depleted in the terrigenous elements. This analysis will be further explored and discussed in Chapter 7.

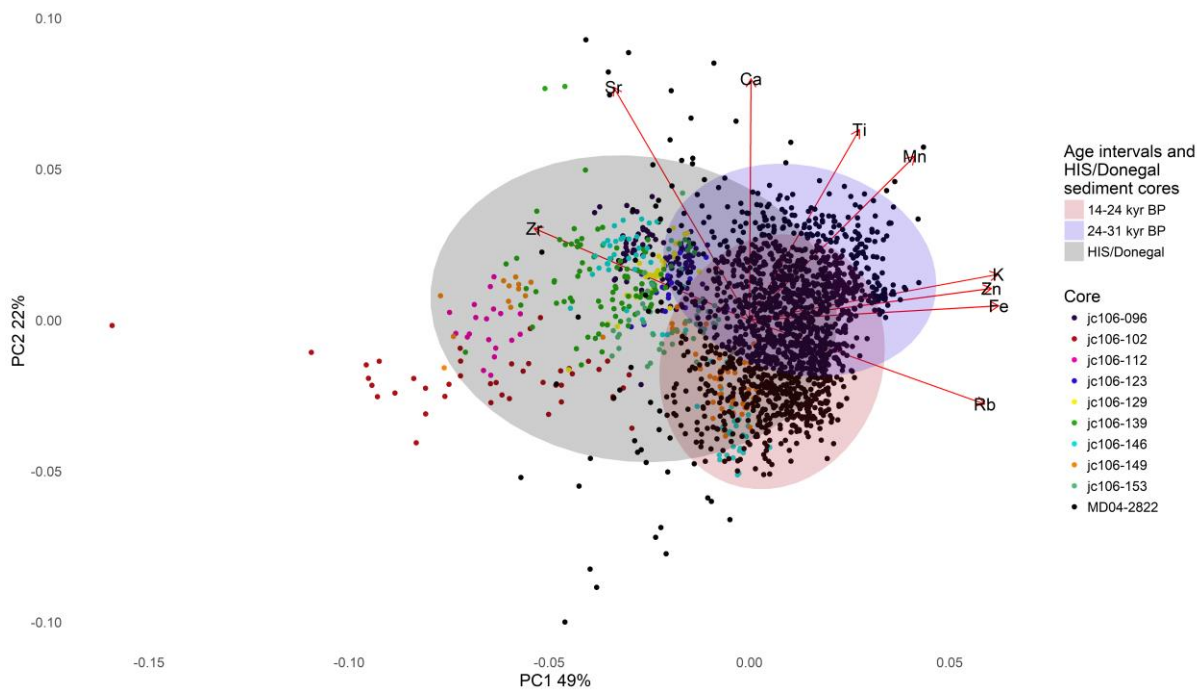


Figure 5.17 Biplot of the PCA results of MD04-2822 and Hebrides Ice Stream (HIS) and Donegal Bay end members. PC 1 summarises 49% and PC 2 22%. The cores have been colour coded and further grouped by ellipses into broader age intervals and Hebrides Ice Stream and Donegal Bay sediments.



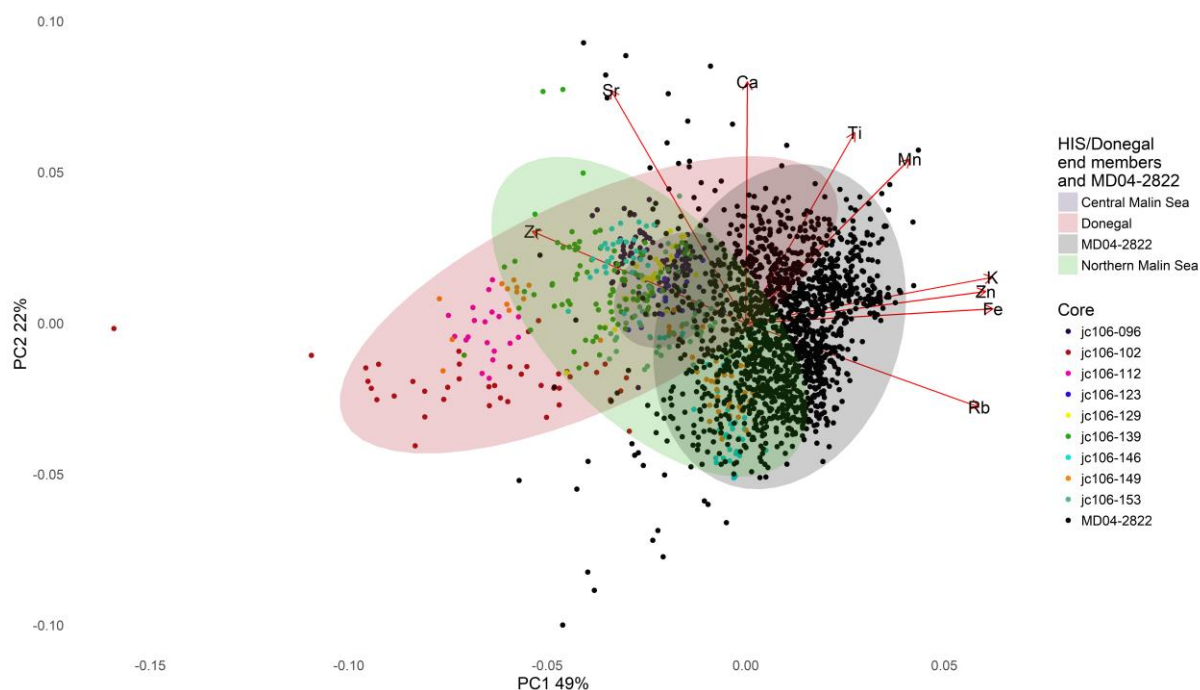


Figure 5.18 Biplot of the PCA results of MD04-2822 and Hebrides Ice Stream (HIS) and Donegal Bay end members. PC 1 summarises 49% and PC 2 22%. The cores have been colour coded and further grouped by ellipses into regional areas and MD04-2822.

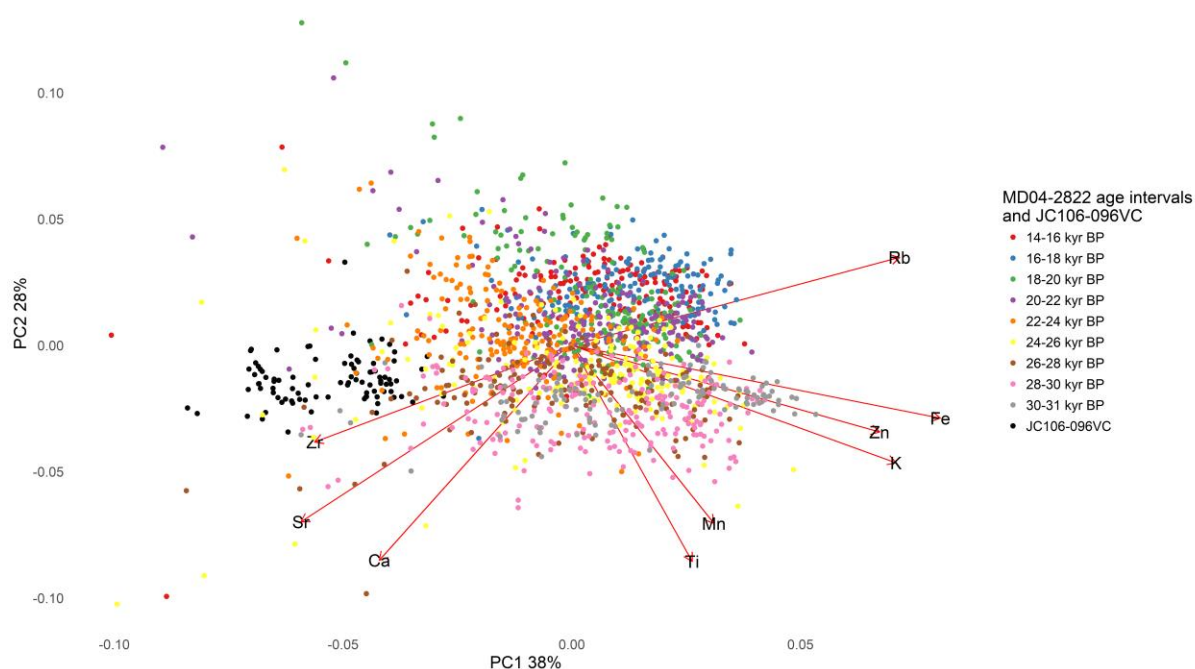


Figure 5.19 Biplot of the PCA results of MD04-2822 and JC106-096VC. PC 1 summarises 38% and PC 2 28%. The age intervals of the MD04-2822 have been colour coded and JC106-096VC is black.

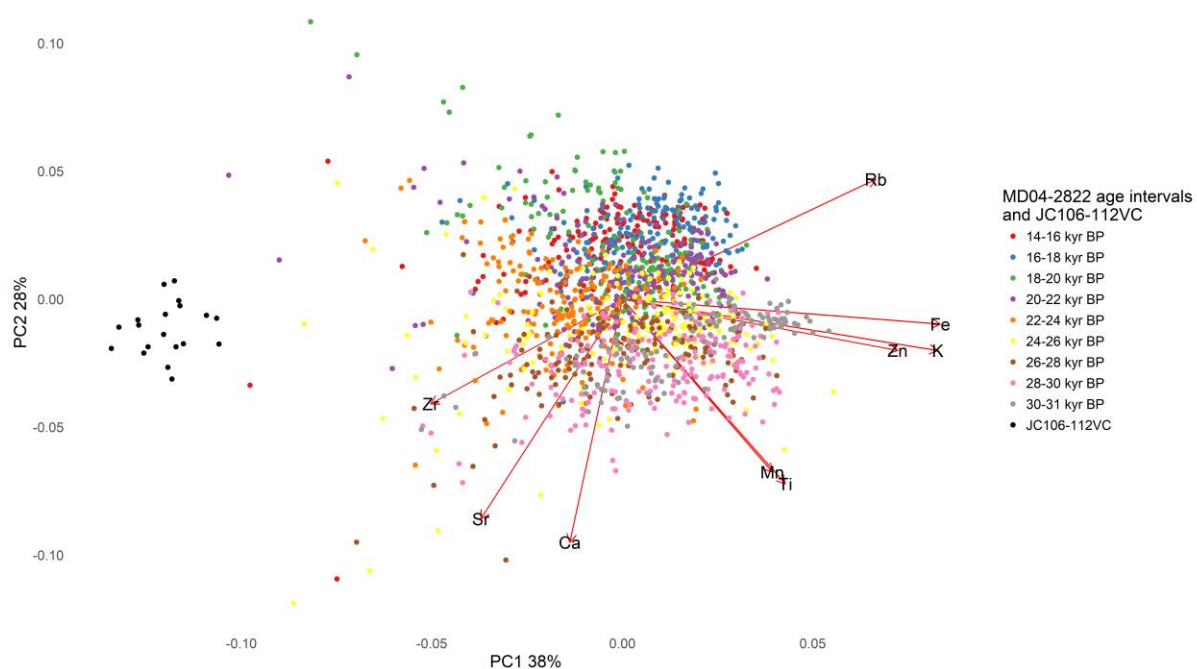


Figure 5.20 Biplot of the PCA results of MD04-2822 and JC106-112VC. PC 1 summarises 38% and PC 2 28%. The age intervals of the MD04-2822 have been colour coded and JC106-112VC is black.

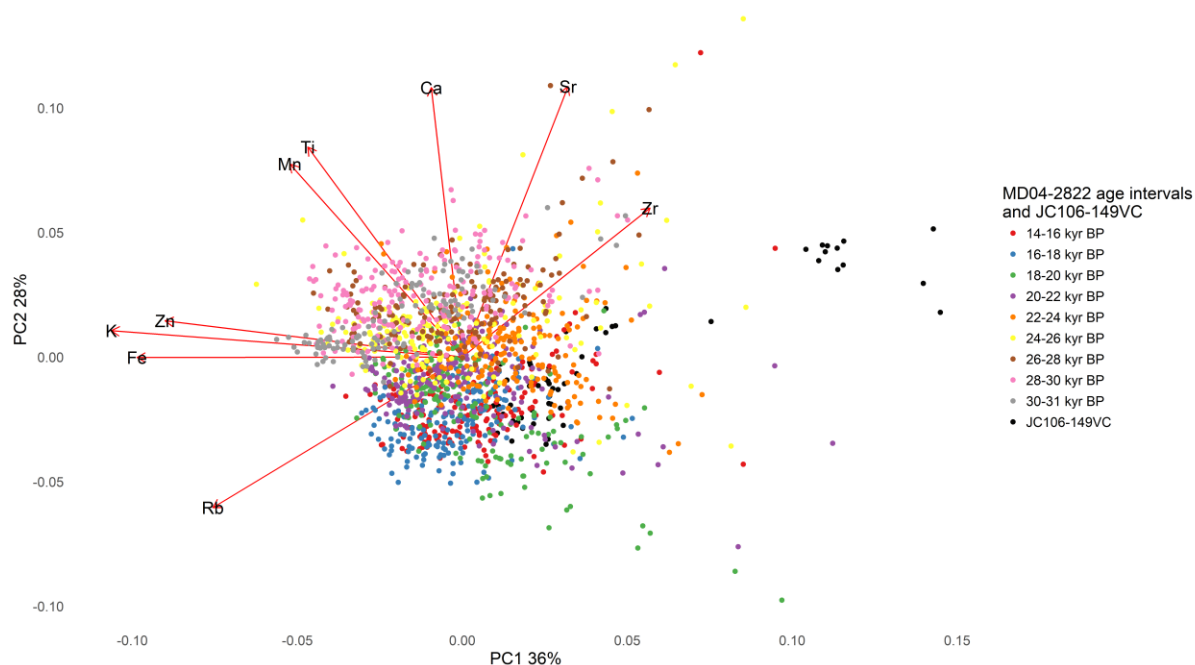


Figure 5.21 Biplot of the PCA results of MD04-2822 and JC106-149VC. PC 1 summarises 36% and PC 2 28%. The age intervals of the MD04-2822 have been colour coded and JC106-149VC is black.



## 6 Minch Ice Stream sector

The Minch Ice Stream drained north western Scotland, supplying sediment to the Sula Sgeir Fan (Bradwell and Stoker, 2015). Eight continental shelf cores and one deep ocean core have been analysed (Figure 6.1) with the aim to:

1. Use  $\mu$ XRF to determine the geochemical character of the glacial sediments across the continental shelf which formerly drained the Minch Ice Stream;
2. Demonstrate the geochemical variations in the glacial end members across the study area;
3. Use  $\mu$ XRF to determine the geochemical variability of the deep ocean core (MD04-2829CQ)
4. Determine whether the offshore IRD record from the Rosemary Bank (MD04-2829CQ) can be linked to these shelf glacial end members

This chapter will present the lithostratigraphy and radiocarbon dates of the eight cores analysed for the Minch Ice Stream, the calibrated  $\mu$ XRF scan data and the statistical analysis performed.

This chapter will also present the lithostratigraphy for MD04-2829CQ, the calibrated  $\mu$ XRF scan data and the statistical analysis performed.

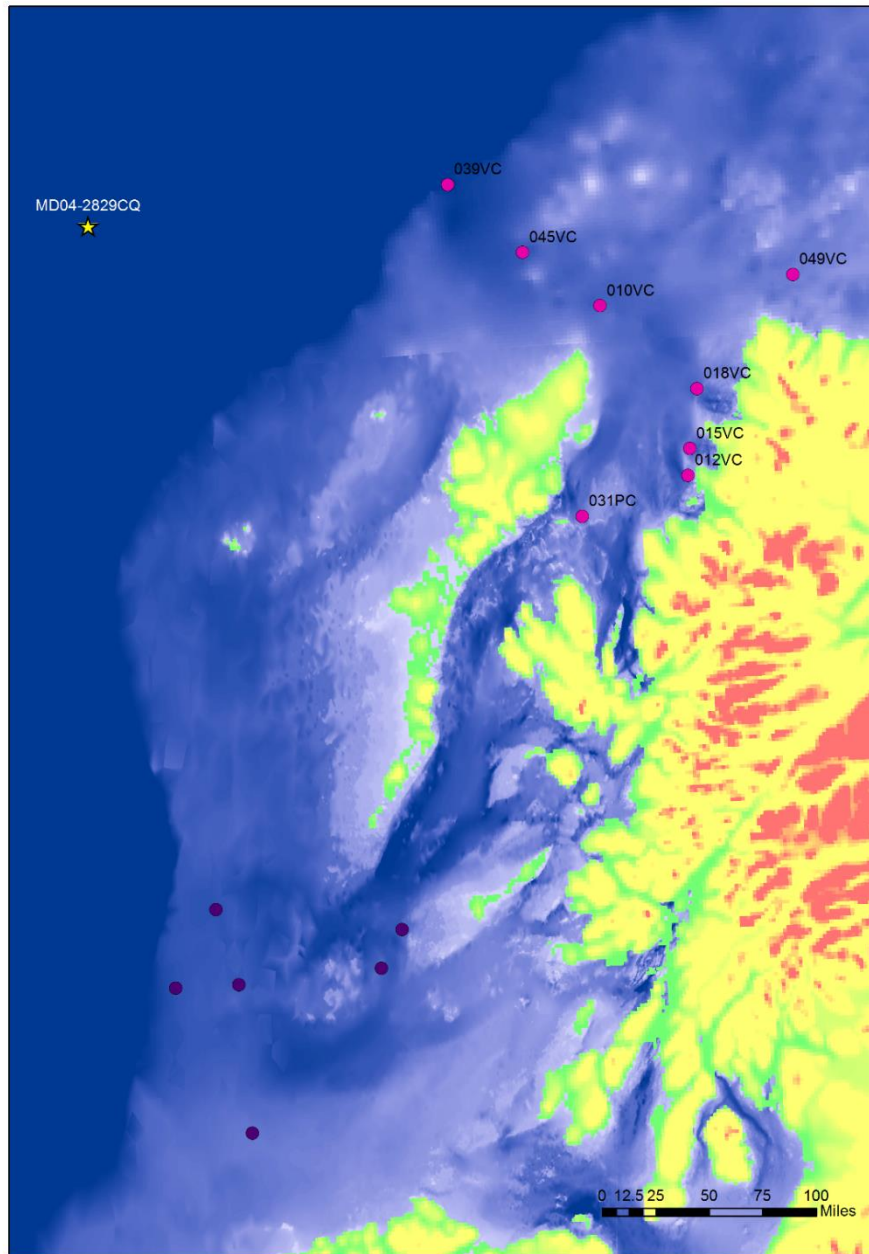


Figure 6.1 Location map of the eight JC123 cores analysed for the former Minch Ice Stream and adjacent deep ocean core MD04-2829CQ.

## **6.1 Minch Ice Stream continental shelf cores**

### **6.1.1 Lithostratigraphy**

The lithostratigraphy of all eight cores (Figure 6.2) can be summarised generally into three lithofacies associations 1) subglacial 2) glacimarine and 3) postglacial.

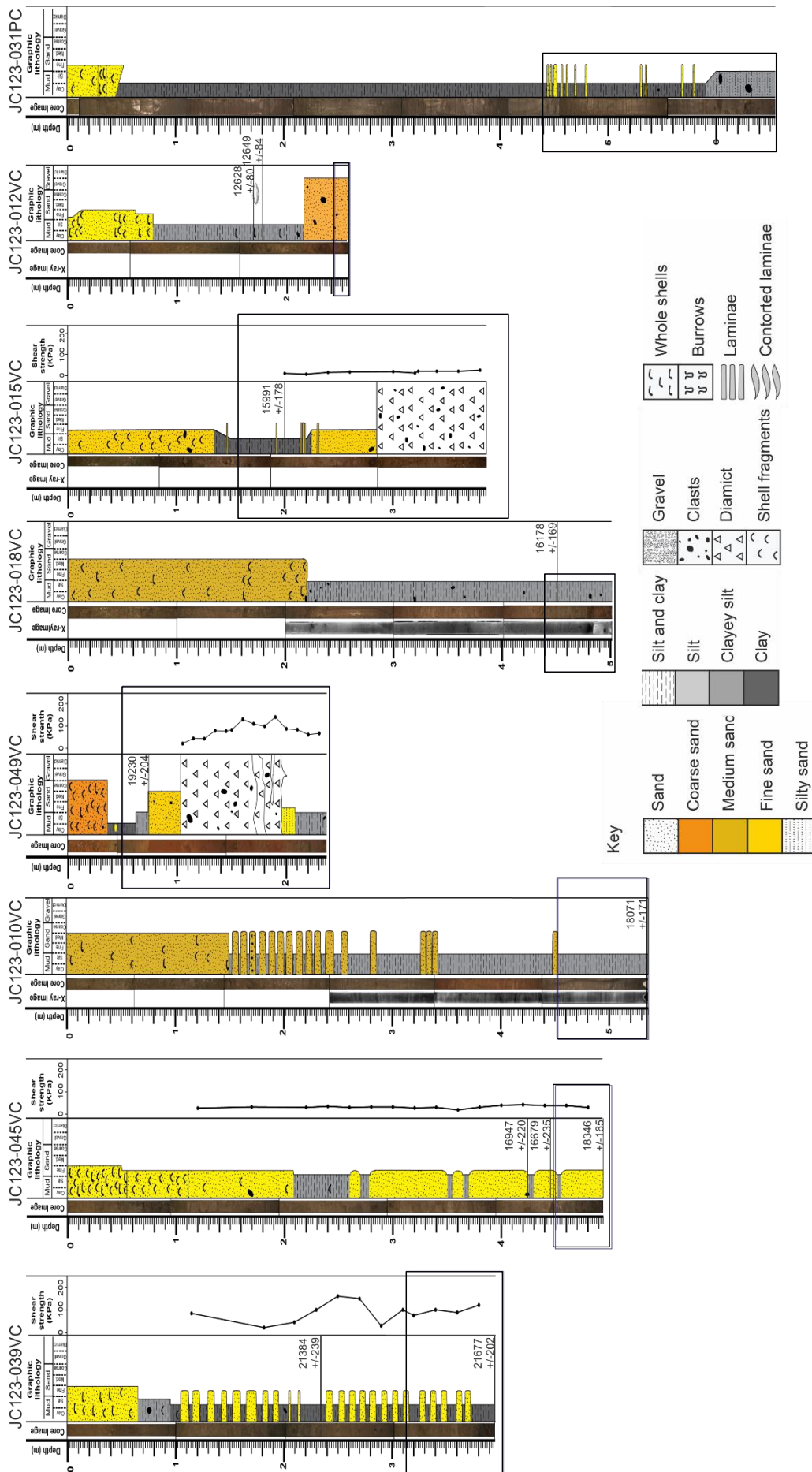


Figure 6.2 Lithostratigraphy for eight cores from the former Minch Ice Stream. Core logs, x-ray imagery, core image, shear strength, radiocarbon dates ( $\Delta R=0$ ) and lithostratigraphy key. Black outline boxes highlight the sediment analysed for this study. Core logs were produced by Margot Saher.

The cores have been grouped into four regions: 1) Outer shelf, 2) Cape Wrath, 3) Inner Minch and 4) Inner Minch Piston Core. The 'outer shelf' region is comprised of three cores JC123-010VC, JC123-039VC and JC123-045VC (Figure 6.2). JC123-039VC consists of mainly clay lithofacies with fine sand laminae. The top meter of the core consists of a silty clay and a shelly fine sand. JC123-045VC comprises fine sand lithofacies interspersed by clayey silt units. The top meter of the core is also a fine shelly sand. From the base to 1.48m, JC123-010VC has clayey silt lithofacies with medium sand laminae; the uppermost lithofacies is a medium sand with shell fragments. JC123-049VC (Figure 6.2) is from the Cape Wrath region, has clayey silt and fine sand lithofacies at the base of the core, which are overlain by diamict (high shear strength), fine sand and clayey silt. The top ~0.6 m of the core consists of clay and shelly coarse sand. The inner Minch consists of three cores JC123-018VC, JC123-015VC and JC123-012VC (Figure 6.2). JC123-018VC comprises clayey silt and medium sand lithofacies. JC123-015VC has a diamict base, then two fine sand lithofacies which are separated by a clay unit with sand laminae. JC123-012VC has a coarse sand base which transitions to a clayey silt. The top lithofacies is a shelly fine sand. JC123-031PC (Figure 6.2) has been categorised as the inner Minch piston core, and primarily consists of a clay lithofacies with some fine sand laminae. The piston core has a clayey silt base and a fine sand unit from ~0.5-0 m.

This study focusses on the subglacial and glacial marine lithofacies.

## **6.2 XRF geochemistry of the continental shelf cores**

### **Minch Ice Stream end members**

The geochemical signature of the eight sediment cores from the Minch sector of the BIIS has been determined by PCA (Figure 6.3). The first two PC axes explain 79% of the total variance of the dataset. PC 1 explains 58% of the variance, whereas PC 2 explains 21%. Positive PC 1 scores correspond to high values of Fe, Zn, Ti, Y, Cu, Ca, Mn, Sr, Rb and K, whereas negative PC 1 scores indicate high Zr values. Figure 6.4 presents the cores grouped into the four geographic regions. The inner Minch piston core has high values of Ca, Sr and Cu and is clearly separated from the other regions. There is significant overlap among the other regions, but more so between the Inner Minch and the Cape Wrath regions.

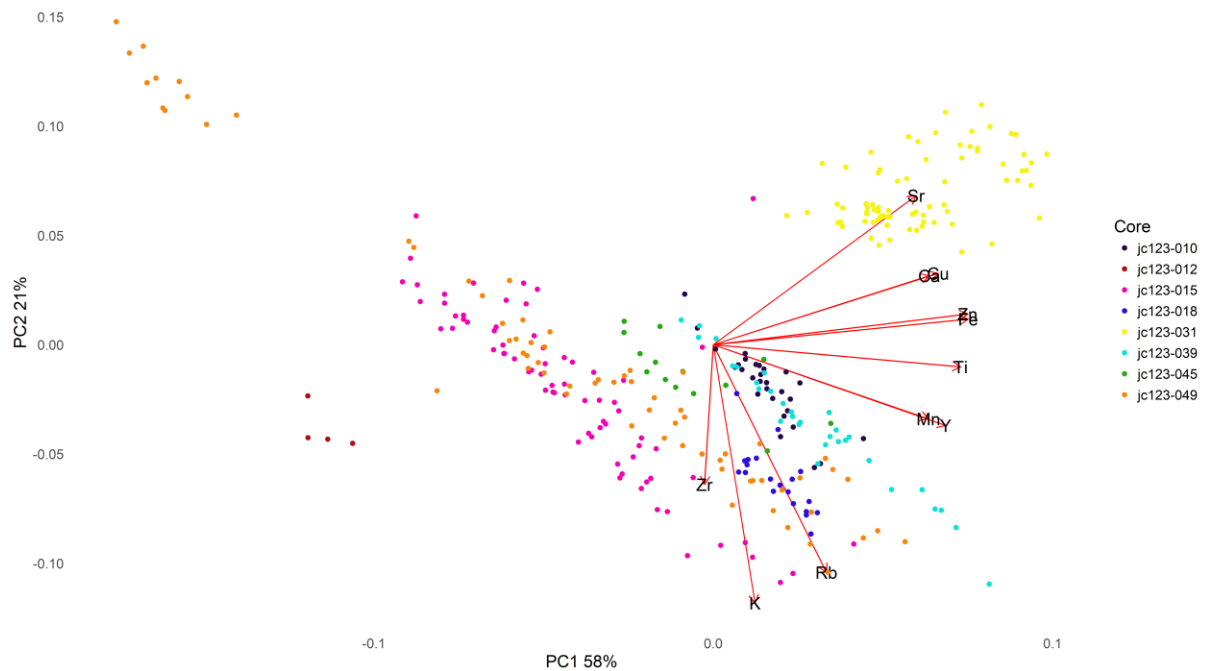


Figure 6.3 PCA biplot for the Minch Ice Stream sediment cores. PC 1 summarises 58% of the total variance of the dataset and PC 2 21%. Each core has been colour coded.

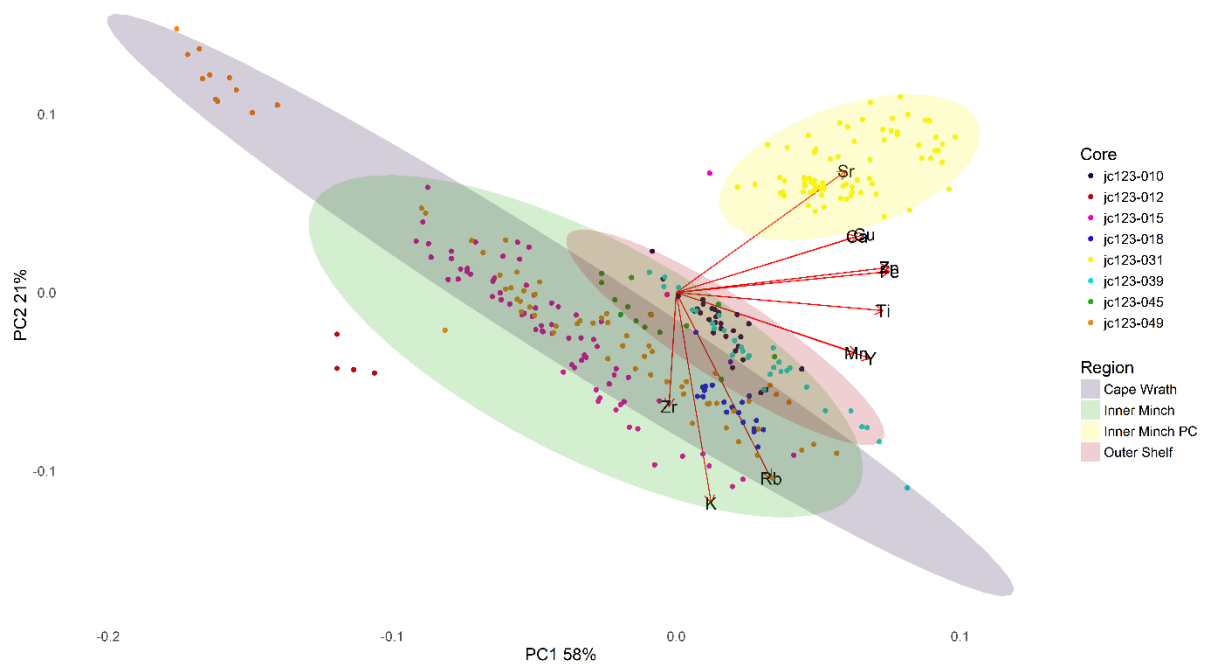


Figure 6.4 PCA biplot for the Minch Ice Stream sediment cores divided into regions. PC 1 summarises 58% of the total variance in the dataset and PC 2 21%. Each core and region has been colour coded.



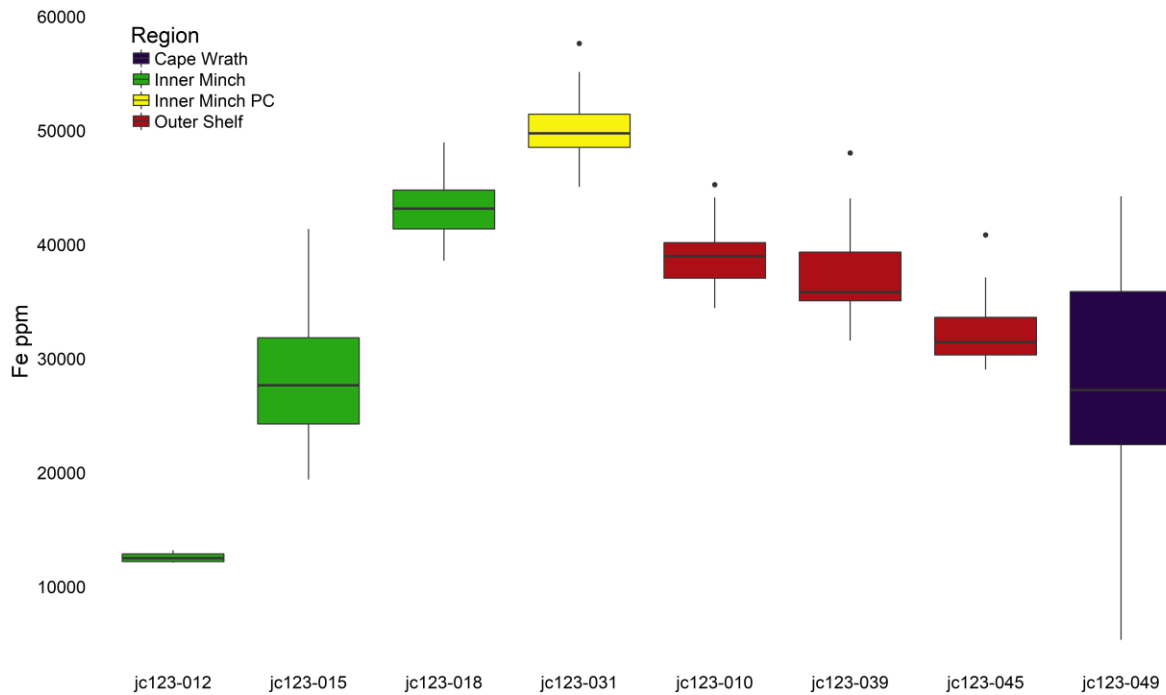


Figure 6.5 Boxplot displaying Fe concentrations of the eight sediment cores from the former Minch Ice Stream. The cores have been colour coded by region. The lower and upper hinges correspond to the 25<sup>th</sup> and 75<sup>th</sup> percentiles. The upper whisker extends from the hinge to the largest value no further than 1.5\* inter quartile range ( $IQR(IQR=UQ-LQ)$ ) from the hinge. The lower whisker extends from the hinge to the smallest value at most 1.5\* IQR of the hinge. Data beyond the whiskers are plotted individually and defined as 'outliers'. The black lines in the middle of the boxes are median values.

Fe is the biggest contributor to PC 1, and therefore is one of the key elements driving variance across the PC 1 axis. Figure 6.5 displays this variation, showing a clear separation between the inner Minch piston core and the other cores. It also accounts for the considerable overlap amongst the other regions, since there is considerable overlap in Fe concentrations. Negative PC 1 scores correspond to mostly diamict and sand lithofacies, whereas positive PC 1 scores relate to clay and clayey silt lithofacies (Figures 6.6A and 6.6B). Some of the cores display quite a large spread in the data, which could relate to core stratigraphy or grain size variation; this is further explored in Figures 6.7, 6.8 and 6.9. JC123-015VC displays large spread across both PC axes along a NW-SE direction (Figure 6.7). The more distal data points (red colour) are clay and are enriched in K, Rb and Zr, whereas the proximal sediments plot within the positive region of both PC axes. In contrast, the purple data points (sediments that show the transition from proximal to distal) have positive PC 1 scores and negative PC 2 scores and are dominated by sand and diamict lithofacies. JC123-039VC plots in a NW-SE direction and has positive PC 2 scores and negative PC 1 scores (Figure 6.8). The core mainly consists of clayey silt and sand lithofacies with no clear stratigraphic gradient. JC123-049VC is from the Cape Wrath region and shows a large spread across both PC axes in a NW-SE direction (Figure 6.9).

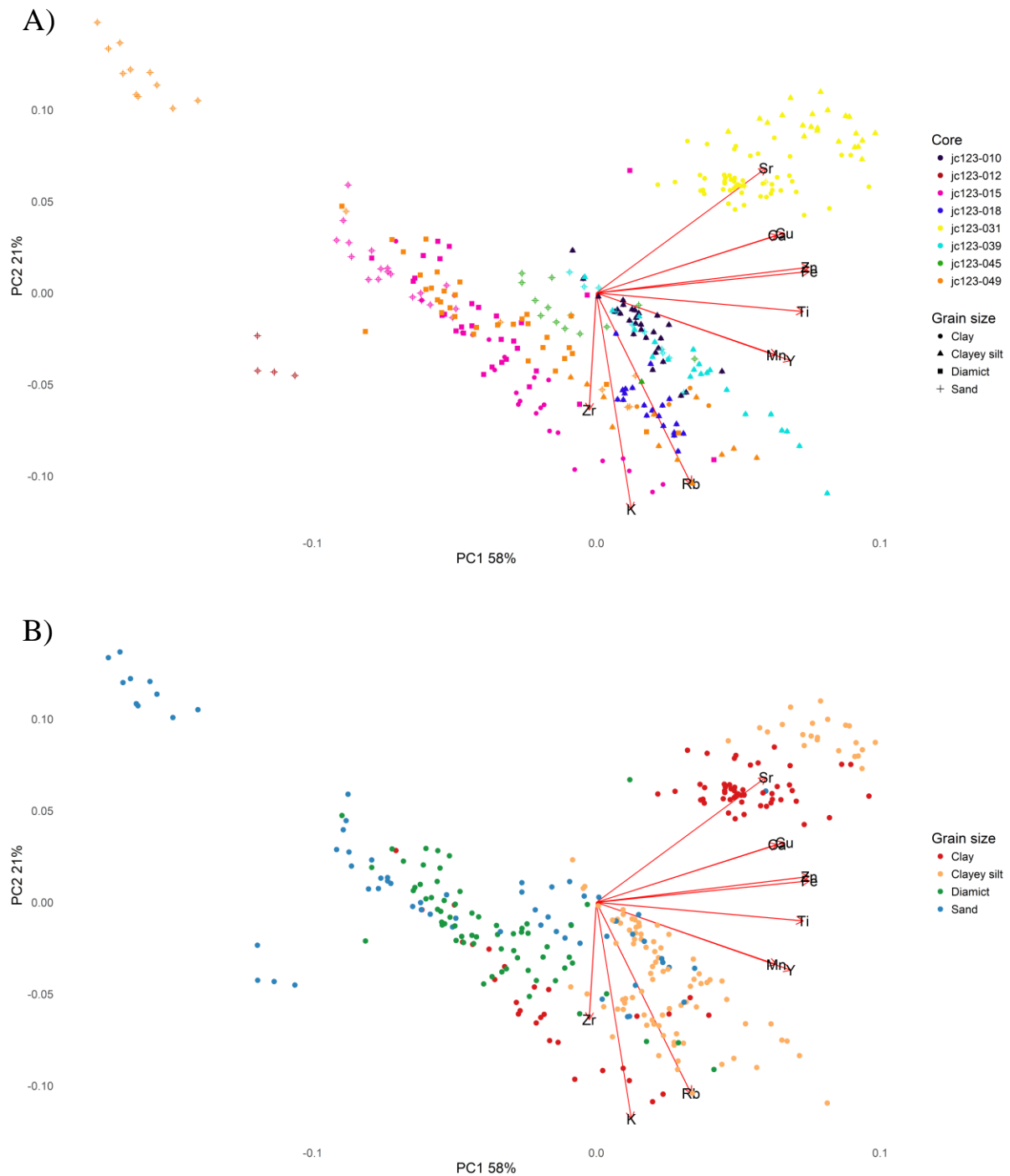


Figure 6.6. PCA biplots for the Minch Ice Stream sediment cores focusing on grain size. A) Each core has been colour coded and symbols display the grain size of each data point; B) Every data point has been colour coded by grain size.

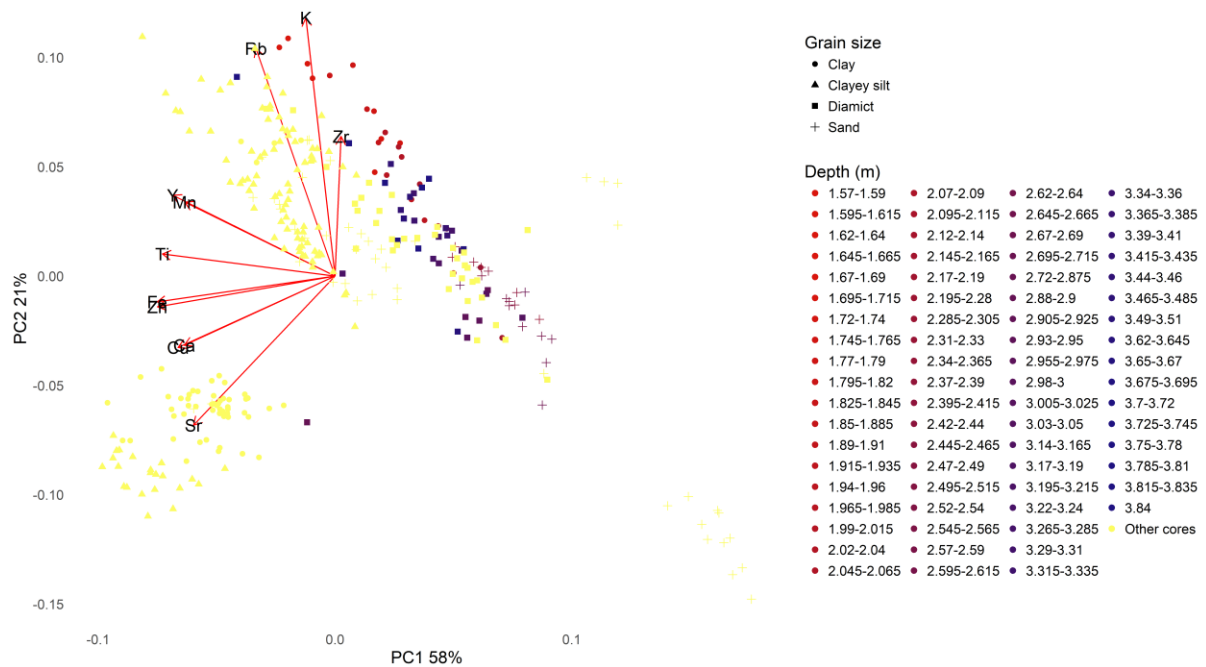


Figure 6.7 PCA biplot displaying internal elemental concentration and grain size variability for JC123-015VC as a function of stratigraphy. Blue data points are proximal sediments transitioning to distal sediments (red data points).

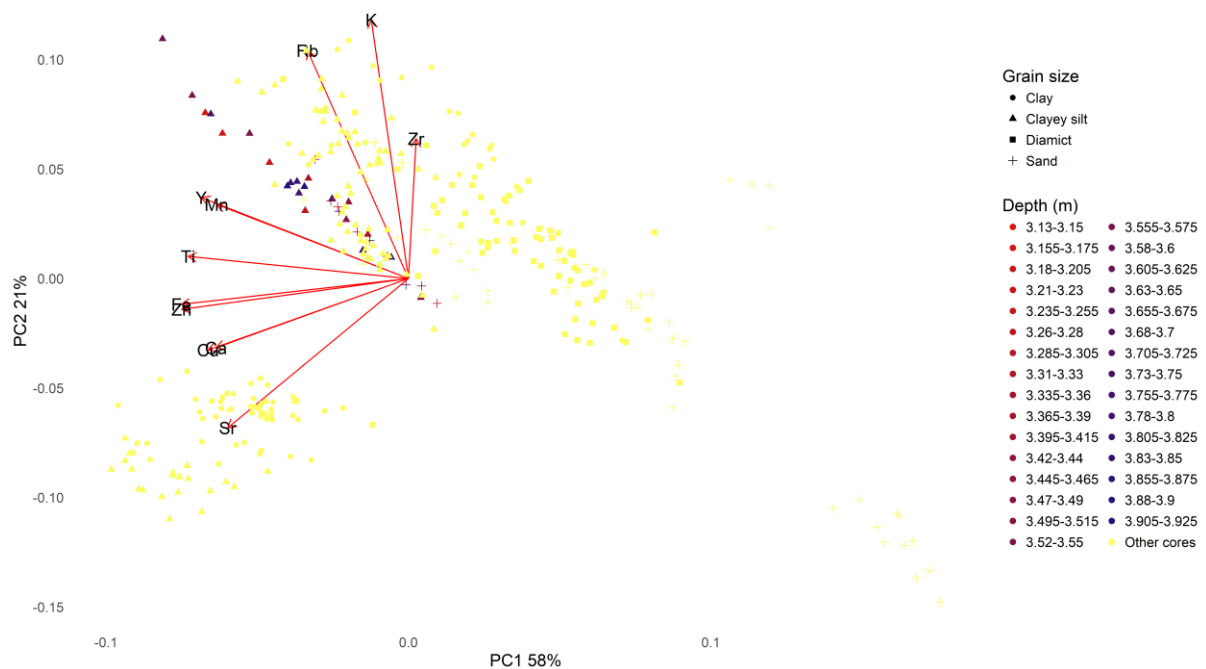


Figure 6.8 PCA biplot displaying internal elemental concentration and grain size variability for JC123-039VC as a function of stratigraphy. Blue data points are proximal sediments grading to distal sediments (red data points).

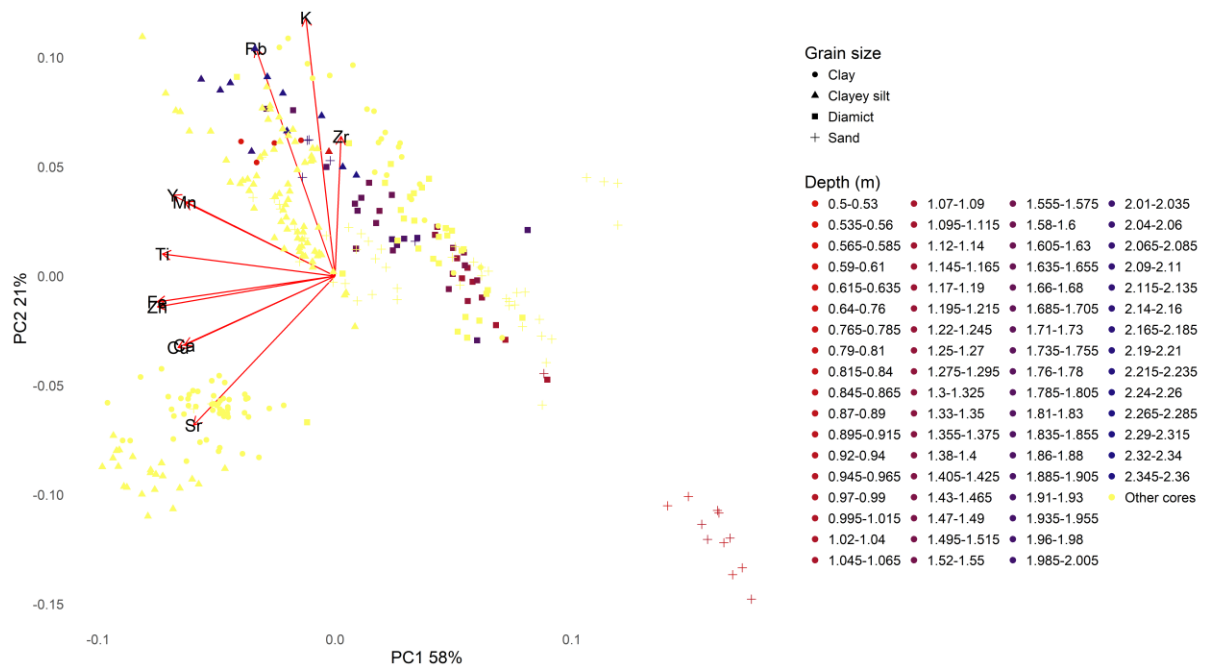


Figure 6.9 PCA biplot displaying internal elemental concentration and grain size variability for JC123-049VC as a function of stratigraphy. Blue data points are proximal sediments grading to distal sediments (red data points).

The PCA shows two main clusters; one cluster comprises a mixture of grain size and depths (from proximal to distal) and the second cluster which has high PC 1 scores, low PC 2 scores and primarily consists of sand. Although the first cluster is stratigraphically unconstrained, in general the proximal sediments are mostly clayey silt and plots further NW than the other samples, and the transitional sediments are mostly diamict and plot within the 0-0.05% region on both PC axes.

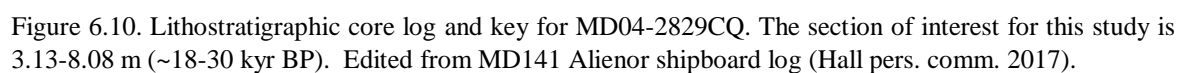
## **6.3 MD04-2829CQ**

### **6.3.1 Lithostratigraphy**

MD04-2829CQ primarily consists of silt with occasional dropstones and laminated sand and clay lithofacies (Figure 6.10). There is evidence of bioturbation near the base of the core, and iron sulphides speck throughout the core. The section of interest is 3.13-8.08 m (~18-30 kyr BP).

### **6.4 XRF geochemistry of MD04-2829CQ**

The PCA for MD04-2829CQ has been colour coded based on age/depth of the sediment (Figure 6.11). The PC 1 accounts for 33% of the total variance and PC 2 accounts for 20%. Negative PC 1 and 2 scores correspond to high Sr, Ca and Zr values, whereas positive PC 1 and negative PC 2 scores indicate high Rb, K, Ti, Zn, Y, Cu, Fe and Mn values. The core can be divided

**Core MD04-2829CQ**

into three age/depth groups (18-22 kyr BP, 22-26 kyr BP and 26-30 kyr BP) as displayed in Figure 6.12. The age groups do overlap but there is a general SW to NE trend. The 26-30 kyr BP group is enriched in Sr, Ca and Zr, whereas the 18-22 kyr BP group is depleted in Sr, Ca and Zr, and enriched in Rb, K, Fe and Mn.

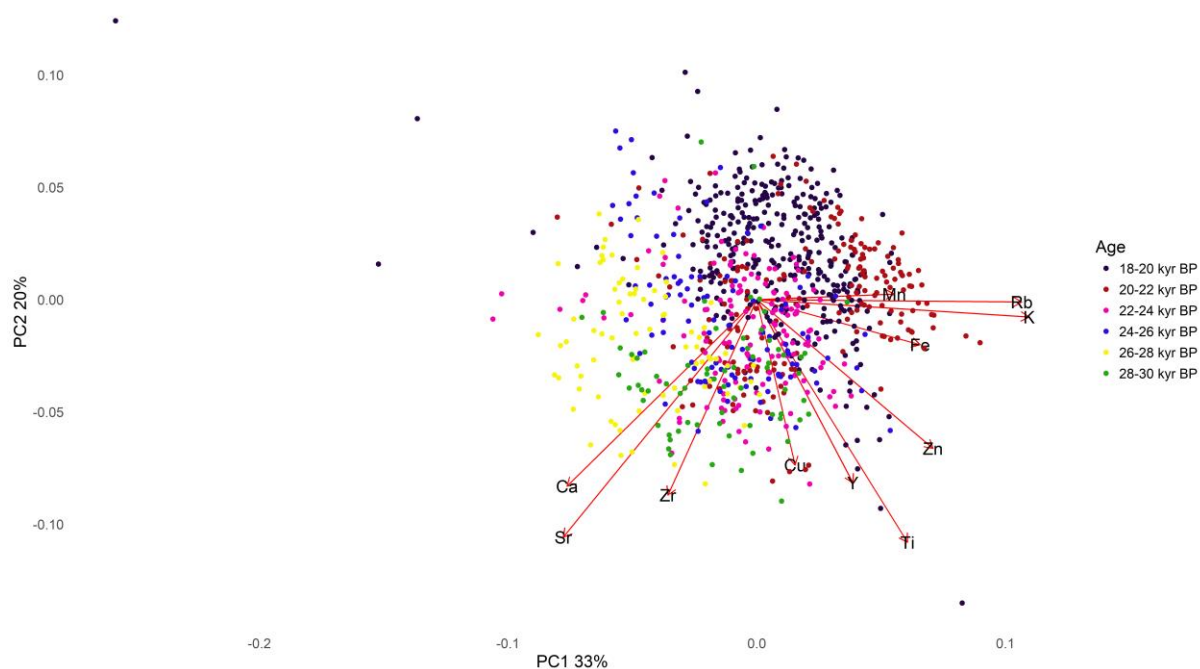


Figure 6.11 PCA biplot for MD04-2829CQ. PC 1 summarises 33% of the total variance in the dataset and PC 2 20%. The core has been subdivided into age intervals which are colour coded.

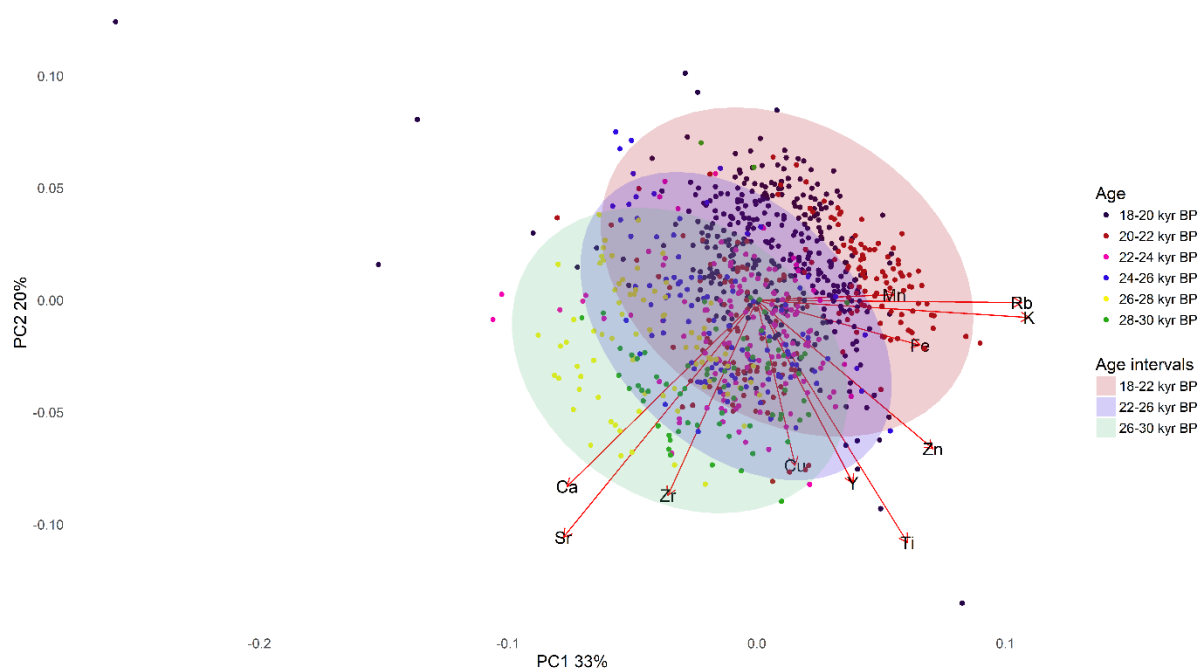


Figure 6.12 PCA biplot for MD04-2829CQ. PC 1 summarises 33% of the total variance in the dataset and PC 2 20%. The core has been colour coded by age intervals and further grouped into broader age intervals (18-22 kyr BP, 22-26 kyr BP and 26-30 kyr BP).

## 6.5 Integration of the shelf end members and MD04-2829CQ XRF data

The PCA of the two datasets shows a gradient along the PC 1 axis (Figure 6.13 and 6.14). PC 1 accounts for 60% of the total variance, PC 2 accounts for 18%. The PCA shows a clear separation between the shelf end members and the deep ocean core. The shelf end members have high values of Zr in contrast to MD04-2829CQ, which has comparatively higher values

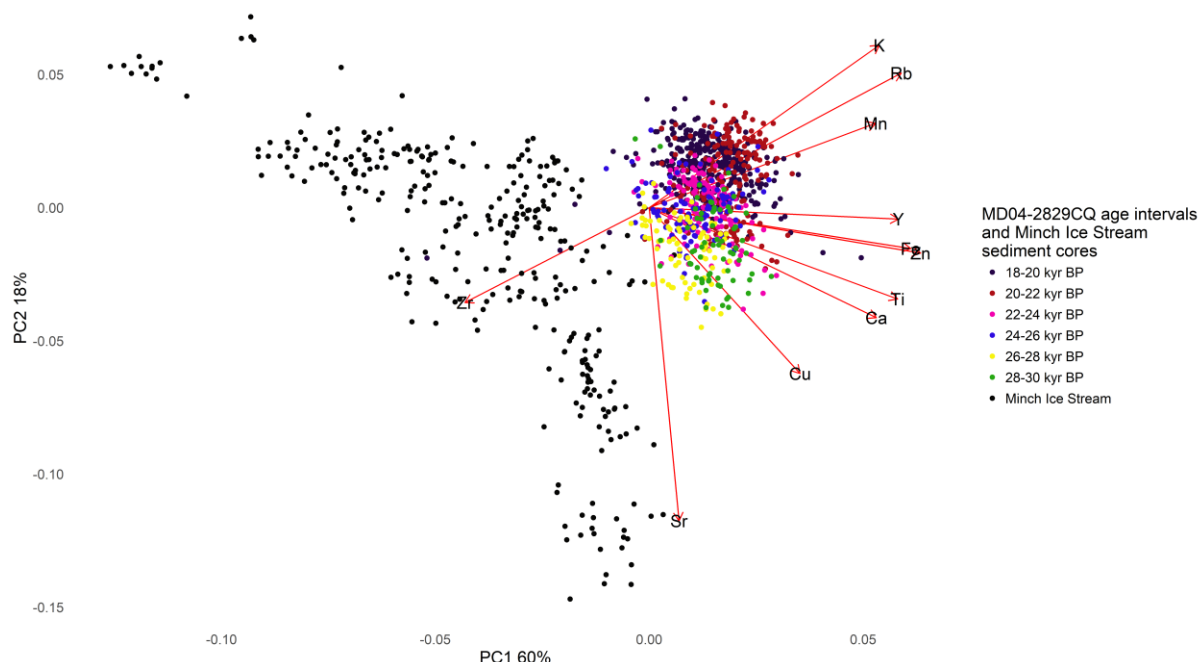


Figure 6.13 Biplot illustrating the PCA results obtained by integrating the shelf end members and MD04-2829CQ XRF data. PC 1 explains 60% of the variance and PC 2 18%. MD04-2829CQ has been colour coded by its age intervals and the Minch Ice Stream end members are shown in black.

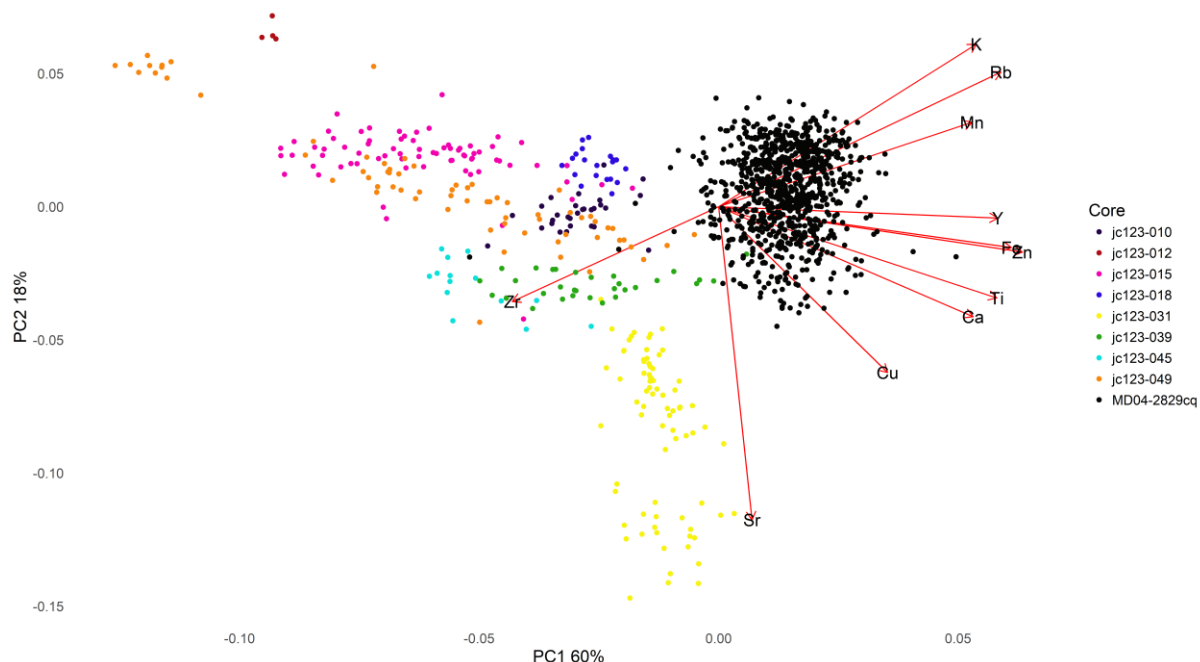


Figure 6.14 Biplot of the PCA results of MD04-2829CQ and Minch end members. PC 1 explains 60% of the variance and PC 2 18%. Each core has been colour coded.

in most of the other elements (Zn, Fe, Ti, Rb, Y, Ca, Mn, K, Cu and Sr to a lesser extent). There is some overlap between MD04-2829CQ and cores JC123-010VC, JC123-039VC, JC123-045VC and JC123-049VC (Figures 6.15 and 6.16). The 26-30 kyr BP sediments plot closer to the shelf end members than the other age/depth sediment groups (Figure 6.17), but there is no

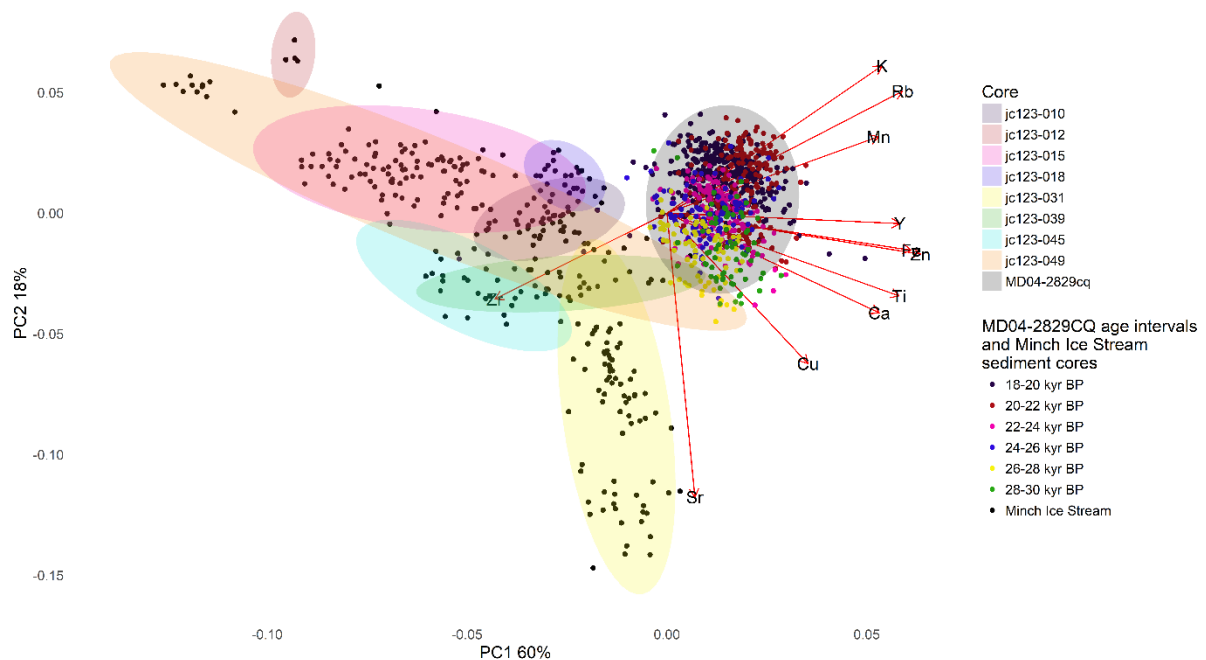


Figure 6.15. Biplot of the PCA results of MD04-2829CQ and Minch end members. PC 1 explains 60% and PC 2 18% of the variance. The age intervals of MD04-2829CQ have been colour coded; the Hebrides Ice Stream and Donegal Bay end members are shown in black and each core is shown by an ellipse.

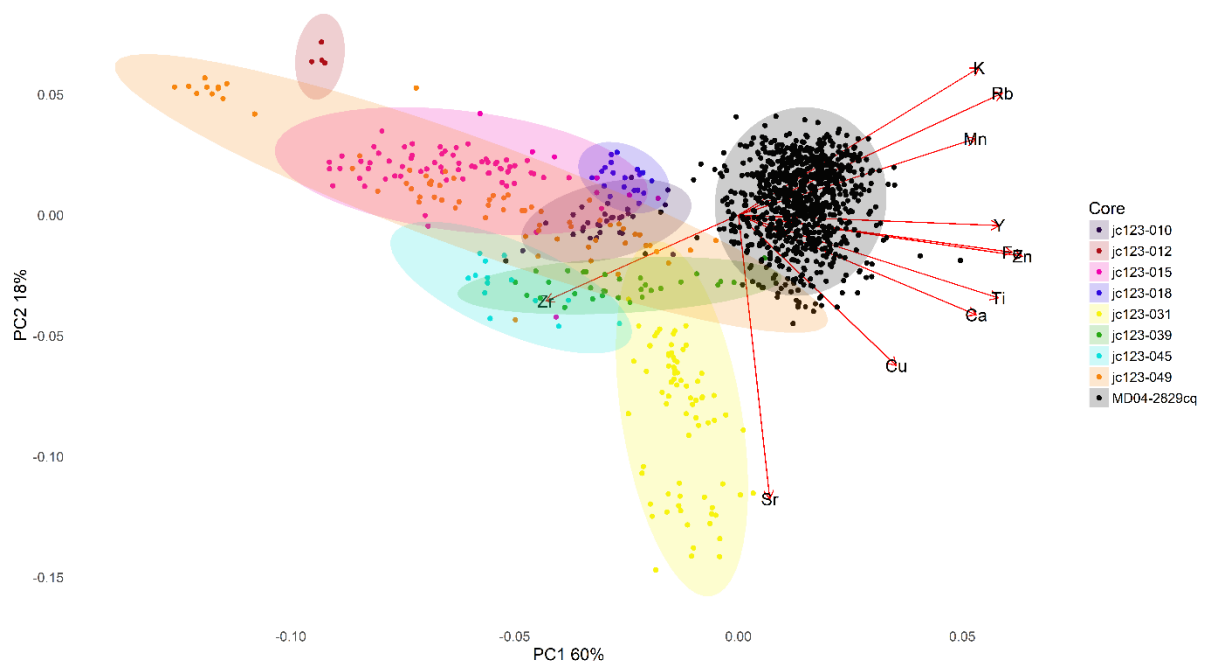


Figure 6.16 Biplot of the PCA results of MD04-2829CQ and Minch end members. PC 1 explains 60% and PC 2 18% of the variance. Each core is shown by an ellipse and has been colour coded.



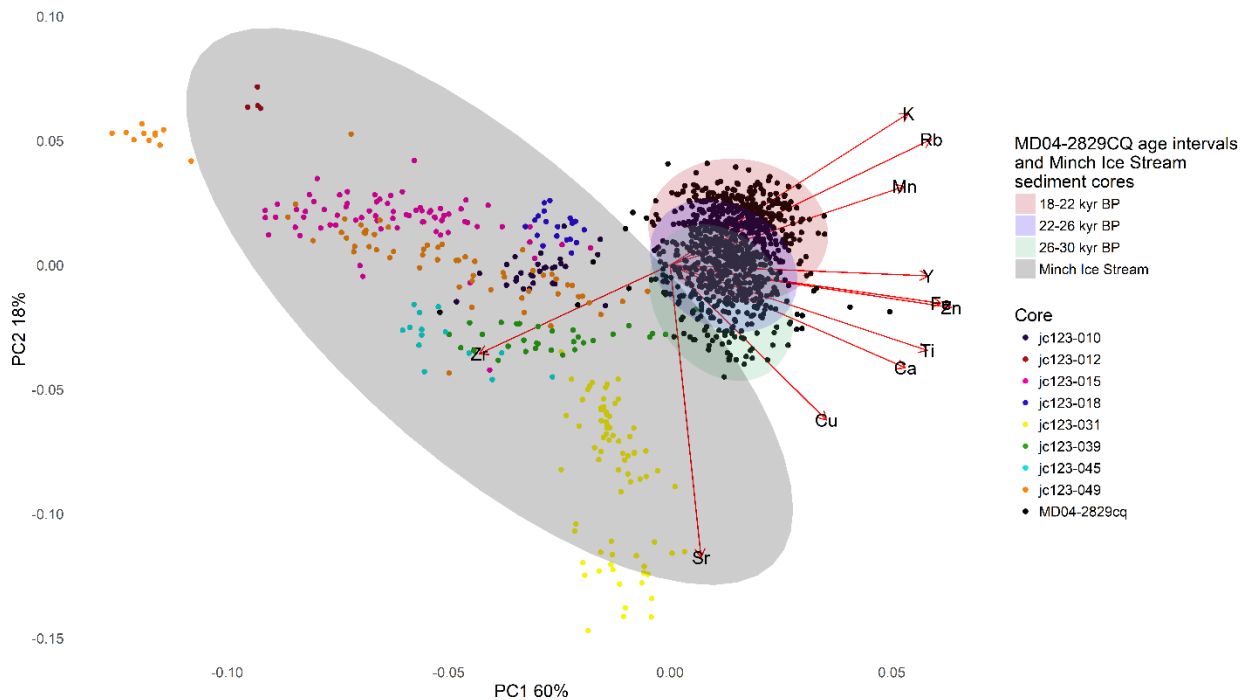


Figure 6.17 Biplot of the PCA results of MD04-2829CQ and Minch end members. PC 1 explains 60% and PC 2 18% of the variance. The cores have been colour coded and further grouped by ellipses into broader age intervals (MD04-2829CQ) and Minch Ice Stream sediments.

significant overlap. The Cape Wrath, Inner Minch and outer shelf regions do show some overlap with MD04-2829CQ (Figure 6.18), but overall MD04-2829CQ is geochemically dissimilar to the shelf end members. Further analysis focused on exploring the relationship between the individual Minch end members and age/depth intervals of MD04-2829CQ with the aim of fingerprinting intervals to specific shelf end members. JC123-018VC has negative PC 1 scores and positive PC 2 scores and is geochemically dissimilar to MD04-2829CQ (Figure 6.19). JC123-039VC shows a SW to NE trend and has mostly negative PC scores along both axes (Figure 6.20). Some of the JC123-039VC data points plot closely to the 26-28 kyr BP sediments. JC123-049VC from the Cape Wrath (Figure 6.21) comprises negative PC 1 scores and mostly positive PC 2 scores. The core has a NW to SE orientation, and some of the data points plot closely to the 20-22 kyr BP, 24-26 kyr BP and 26-28 kyr BP sediments. This analysis will be further explored and discussed in Chapter 7.

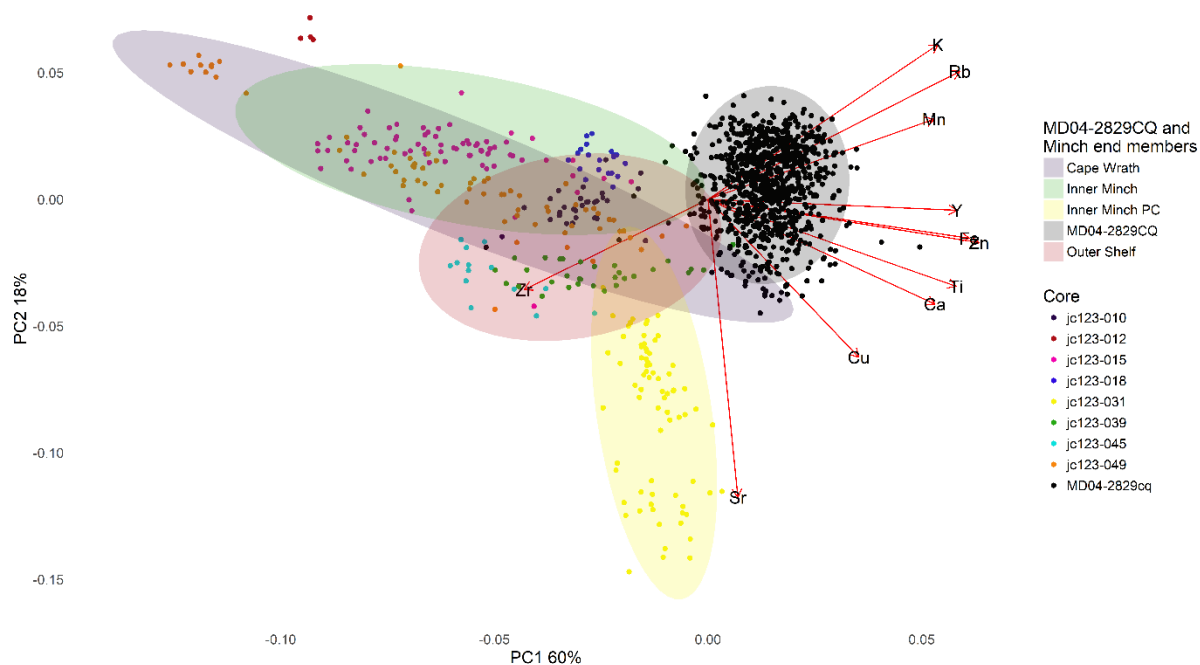


Figure 6.18 Biplot of the PCA results of MD04-2829CQ and Minch end members. PC 1 explains 60% and PC 2 18% of the variance. The cores have been colour coded and further grouped by ellipses into regional areas and MD04-2829CQ.

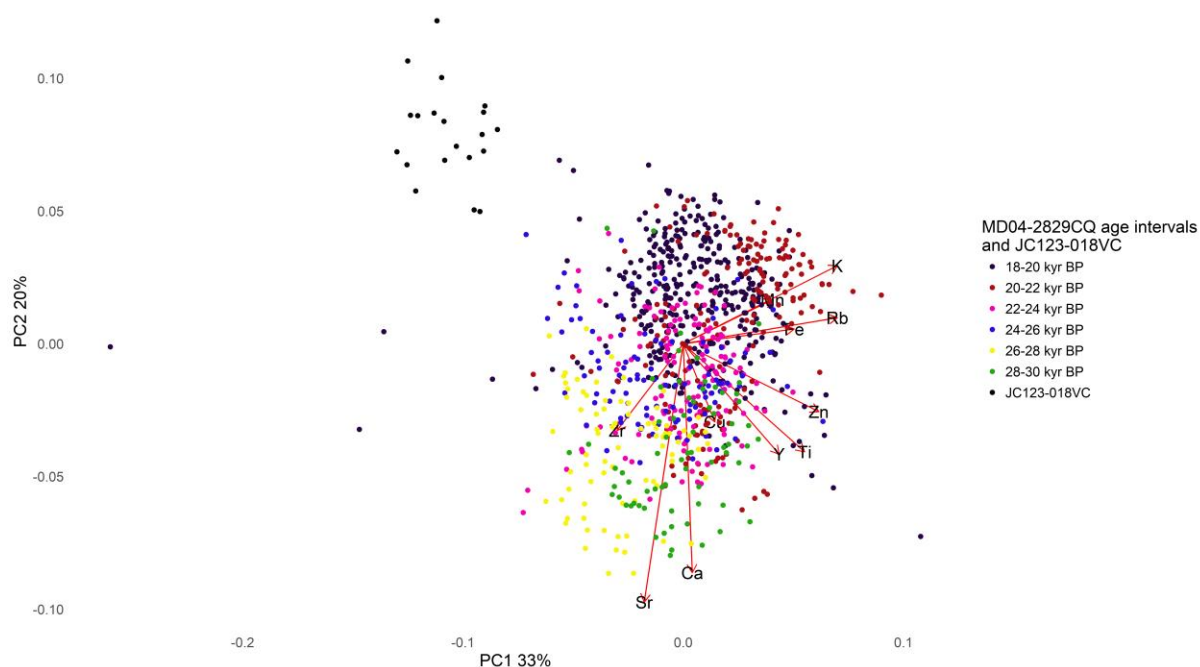


Figure 6.19 Biplot of the PCA results of MD04-2829CQ and JC123-018VC. PC 1 explains 33% and PC 2 20% of the variance. The age intervals of the MD04-2829CQ have been colour coded and JC123-018VC is shown in black.

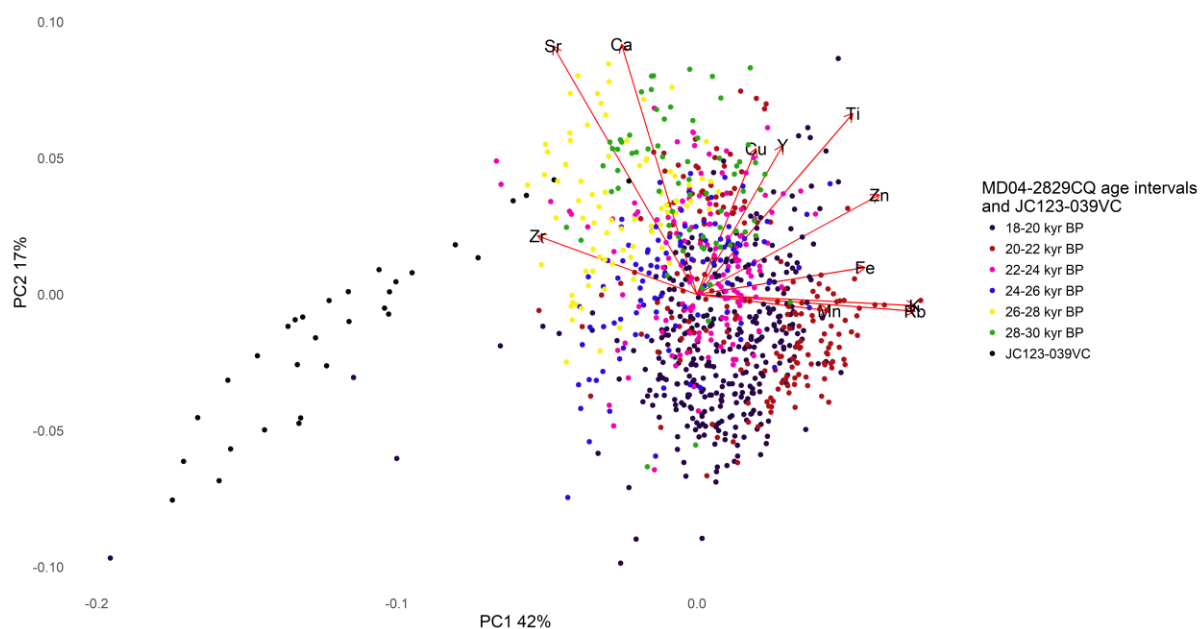


Figure 6.20 Biplot of the PCA results of MD04-2829CQ and JC123-039VC. PC 1 explains 42% and PC 2 17% of the variance. The age intervals of the MD04-2829CQ have been colour coded and JC123-039VC is shown in black.

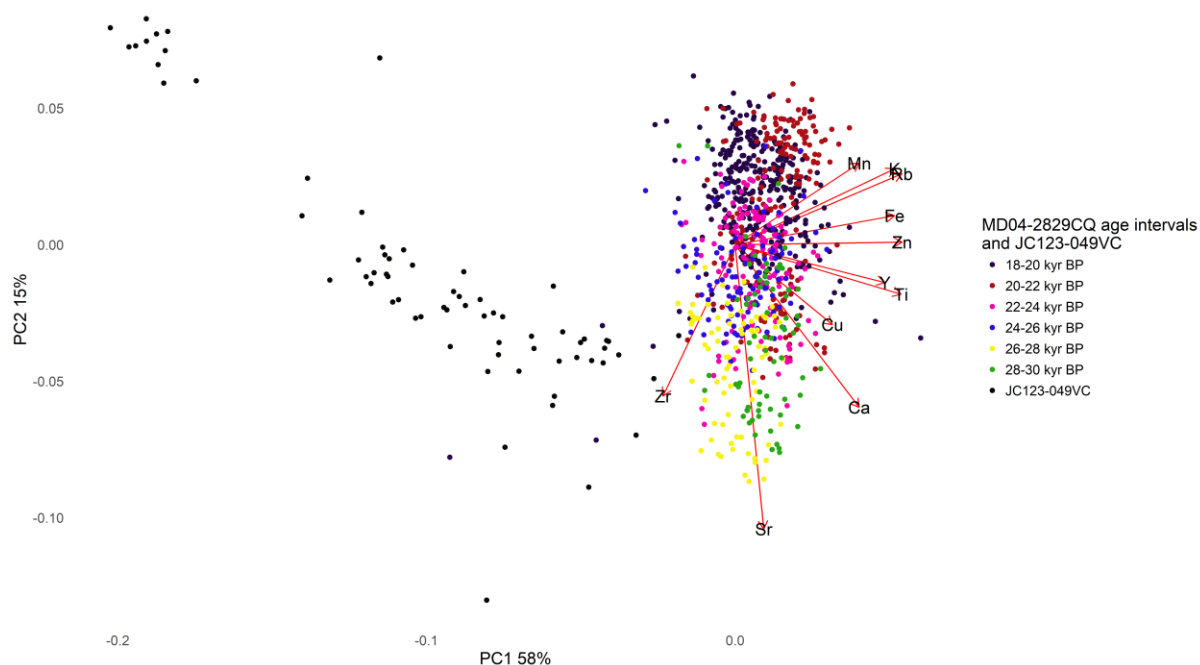


Figure 6.21 Biplot of the PCA results of MD04-2829CQ and JC123-049VC. PC 1 explains 58% and PC 2 15% of the variance. The age intervals of the MD04-2829CQ have been colour coded and JC123-049VC is shown in black.

## 7 Discussion

This chapter discusses the findings presented in the previous three results chapters. The results will be discussed by sector followed by an integration of all ice stream data, deep sea data and a synthesis section.

### Establishing end member proximity

Critical for understanding IRD flux to the deep ocean is determining the source of the IRD (Scourse *et al.* 2009). It has been established that glacimarine and diamict lithofacies are ideal end members for determining the source of IRD (Farmer *et al.* 2003; White *et al.* 2016); however, glacigenic sediments can be deposited in an ice distal environment. All glacimarine sediments are comprised of two elements: lithic material and biogenic. The lithic material reflects the local catchment geology and is supplied glacigenically, and the biogenic input is from the water column. In proximal tidewater margins, biogenic carbonate content is not high because of high rates of meltwater and sediment flux close to the grounding line (Killfeather *et al.* 2011). Consequently, the ratio of these two inputs will reflect ice margin position (distal sediments will have higher biogenic carbonate content). For this study, lithostratigraphy and radiocarbon dates have been used to identify the most appropriate proximal lithofacies. Ideally finer grained lithofacies and muddy diamicts are better for XRF, however, proximal sediments are usually coarser and finer sediments are usually more distal (Powell, 1981, Syvitski, 1991). Two piston cores were included in this study, one from the ISIS (JC106-051PC) and the other from the Minch Ice Stream (JC123-031PC). Piston cores are inherently associated with softer

fine grain sediments, so it is important to address their proximity to the ice margin and therefore suitability for this study. Previous analysis showed that JC106-051PC had a similar geochemistry to the other Irish Sea cores (Figure 4.6), therefore these sediments are glaciogenic and were deposited by the retreating ISIS. The core also contains high values of biogenic carbonate indicated by the co-varying of Ca and Sr, and the anti-correlation with Fe (Figure 7.1). High values of biogenic carbonate indicate the distal nature of these sediments and therefore they will not be included in further analysis or discussion. Previous analysis of the Minch cores showed that JC123-031PC was geochemically dissimilar to the other shelf cores. It has been suggested that during deglaciation the Minch Ice Stream could have transitioned into an ice shelf. The difference in geochemical signature of the piston core could reflect deposition within an ice shelf environment; however, the fine nature of the facies and the absence of muddy gravel (Killfeather *et al.* 2012), indicate the setting is distal and therefore still not suitable for analysis. A different source region is the most likely reason for the distinctive geochemical signature of the inner Minch piston core. Hypothesised flow lines for the Minch Ice Stream (Bradwell *et al.* 2008), suggest the source material for 031PC would most likely be derived from the Isle of Skye. The core is rich in Fe, as shown by the boxplot in Figure 6.5 and this likely derives from the Tertiary basalts of Skye. JC123-031PC however like JC106-051PC also has high biogenic carbonate content (Figure 7.1), which confirms the distal nature of this core and consequently will not be included in any further analysis or discussion.

## **7.1 Geochemical signature of the Irish Sea Ice Stream sector**

### **7.1.1 Establishing Irish Sea Ice Stream end members**

Eighteen cores were analysed from the continental shelf region of the former ISIS (only 17 will be discussed due to the exclusion of JC106-051PC). The geochemical analysis of individual cores provided context for the overall geochemical pattern seen across the shelf of the former ISIS. Grain size data from six of the 17 cores are presented in Figures 7.2-7.4; three from the Celtic Sea region and three from the Irish Sea region. Four of the six cores analysed displayed a clear stratigraphic gradient (JC106-012VC, JC106-018VC, JC106-069VC and JC106-073VC). The distal sediments for these cores are mostly clay or clayey silt (excluding JC106-69VC which will be discussed separately) and are affiliated with higher PC 1 scores (terrigenous elements; Rb is associated with clay content). The grain size of the proximal

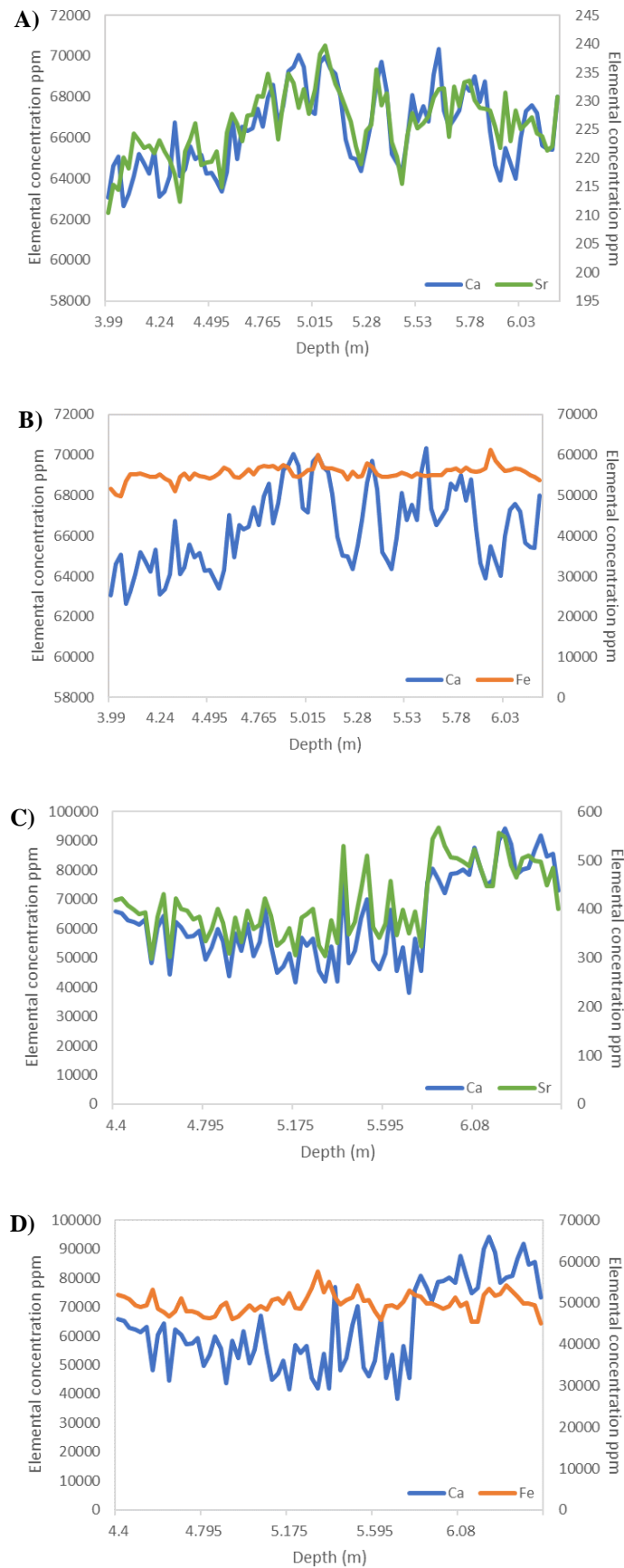


Figure 7.1 Element concentration profiles A) JC106-051PC, Ca and Sr B) JC106-051PC, Ca and Fe C) JC123-031PC, Ca and Sr D) JC123-031PC, Ca and Fe.

sediments for these same cores (JC106-012VC, JC106-018VC and JC106-073VC) varies (sand, silt and clay), but all of these plot more negatively on the PC 1 axis in comparison to the distal sediments (affiliated with higher Ca, Sr and Zr values). In contrast, JC106-069VC consists solely of diamict. The base of the diamict is enriched in the terrigenous elements and the top of the diamict is richer in Zr, Ca and Sr. The most likely reason for this is that the upper part of the diamict has been influenced by bioturbation and therefore an increasing amount of sand; or it could reflect an increase in shells present in comparison to the base of the unit. Cores JC106-033VC and JC106-63VC display a subtler stratigraphic gradient. These cores are laminated, and the predominant grain size is clayey silt but, the coarser laminae will have a different geochemical affinity to the finer clayey silt. The grain size data presented in Figures 7.2-7.4 demonstrates that there is a relationship between geochemical signature of the sediments and the grain size/stratigraphy of some of the cores. The strength of this relationship varies however, some of the cores do show that proximal sediments are in general coarser and higher in Zr, Ca and Sr; whereas distal sediments are usually finer and richer in elements such as Rb and K.

When all 17 cores are analysed together they display a clear gradient that reflects core location. This is clearly shown by grouping the cores into regions (Figure 7.5). The Celtic Sea cores are characterised by high values of Ca, Sr and to a lesser extent Zr. High values of Ca and Sr are an indicator of carbonate, either biogenic or detrital (Rothwell and Croudace 2015). As discussed previously, co-variation of Ca and Sr would indicate a biogenic origin, however co-variation of Ca and Fe would indicate a detrital origin. Figure 7.6 and 7.7 show that for all the Celtic Sea sediments the value for Ca and Sr show a similar relationship, however it also displays that Fe also co-varies for the most part with Ca. For this reason, it is interpreted that the Celtic Sea cores plot NW on the PCA plot because they are influenced by a detrital carbonate source. The source of this carbonate could be the outcrop of Upper Cretaceous Chalk in the Celtic Sea as shown in Figure 7.8. This supports the observations of Farmer *et al.* (2003) whereby glacialmarine sediments are a function of the local catchment geology. Fe is the largest contributor to PC 1 and consequently accounts for much of the variability across PC 1. The Irish Sea cores contain on average higher concentrations of Fe than the Celtic Sea cores (Figure 7.9). The local catchment geology of the Irish Sea is dominated by Permian-Triassic

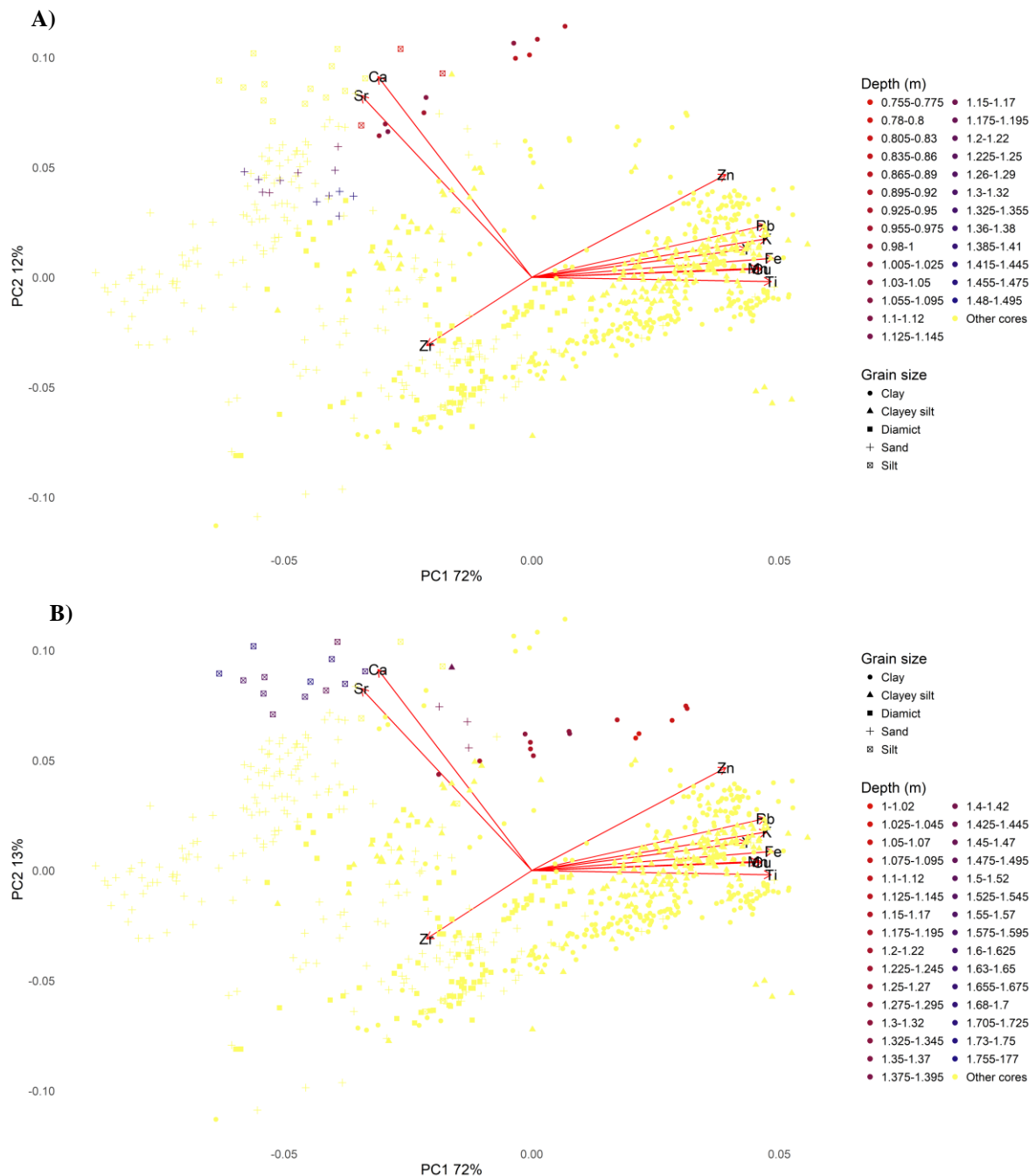


Figure 7.2 PCA biplots displaying internal elemental concentration and grain size variability for two Irish Sea Ice Stream cores as a function of stratigraphy. A) JC106-012VC B) JC106-018VC. Blue data points are proximal sediments transitioning to distal sediments (red data points). The remaining Irish Sea Ice Stream cores are shown by the yellow data points.



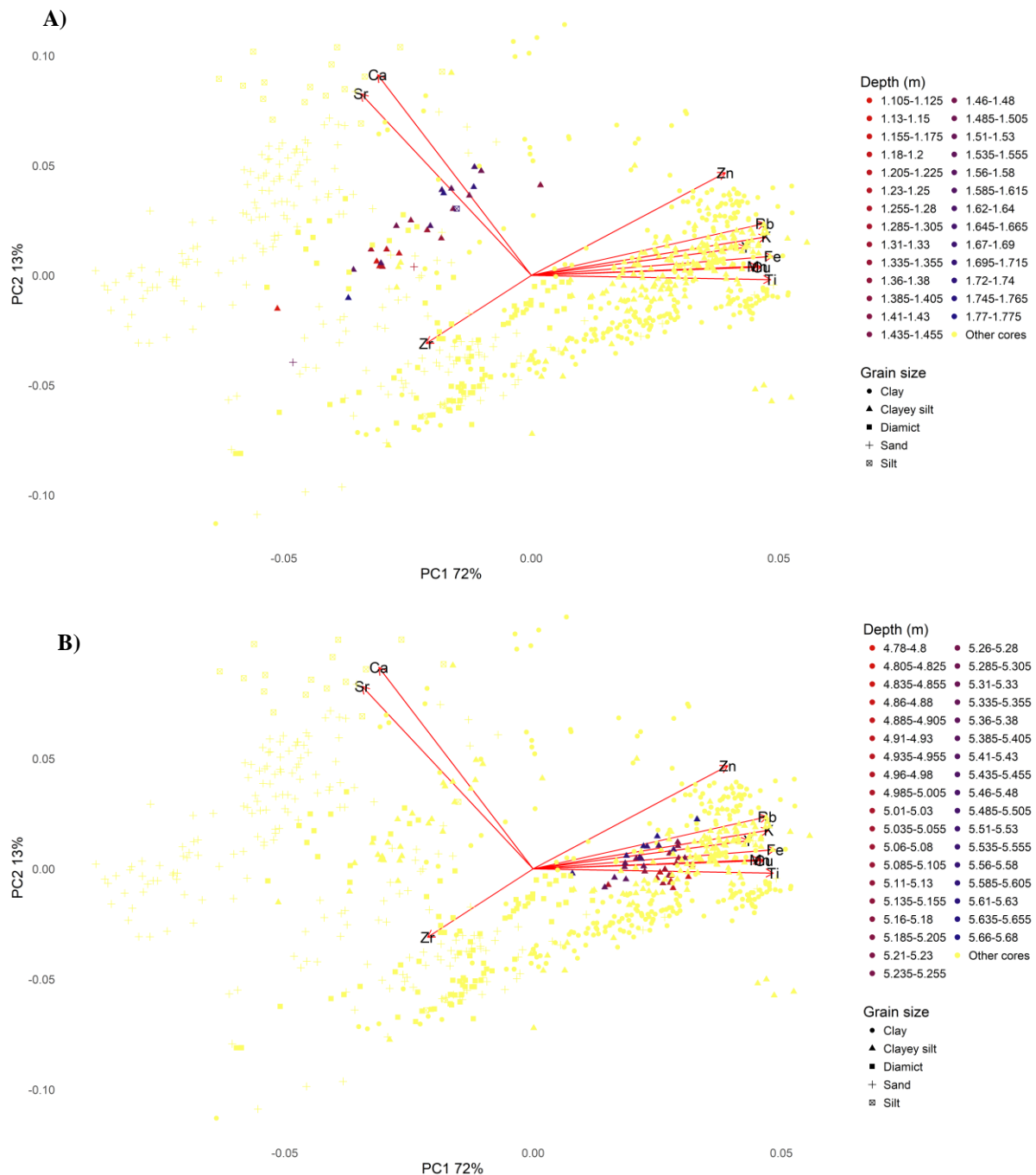


Figure 7.3 PCA biplots displaying internal elemental concentration and grain size variability for two Irish Sea Ice Stream cores as a function of stratigraphy. A) JC106-033VC B) JC106-063VC. Blue data points are proximal sediments transitioning to distal sediments (red data points). The remaining Irish Sea Ice Stream cores are shown by the yellow data points.

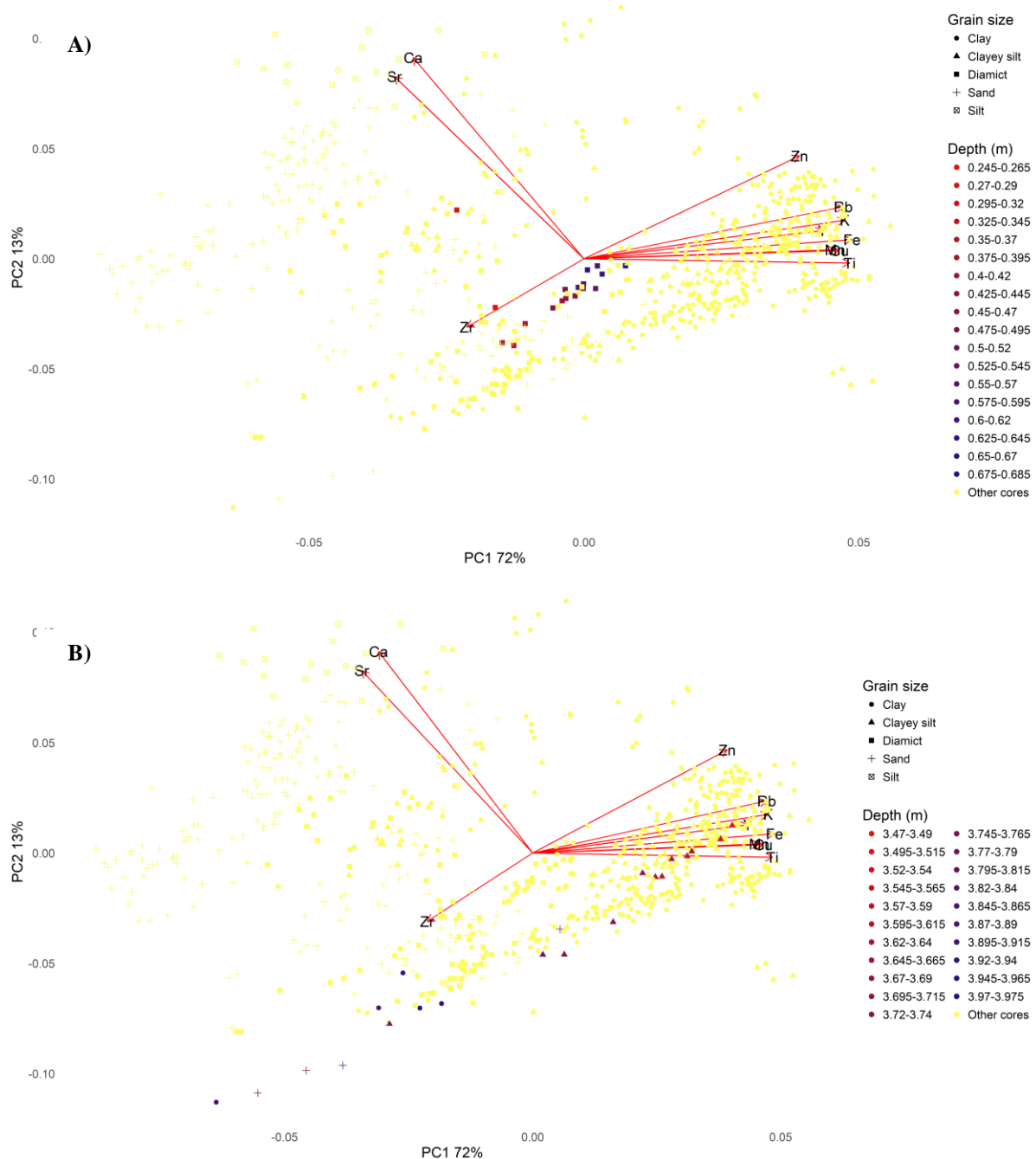


Figure 7.4 PCA biplots displaying internal elemental concentration and grain size variability for two Irish Sea Ice Stream cores as a function of stratigraphy. A) JC106-069VC B) JC106-073VC. Blue data points are proximal sediments transitioning to distal sediments (red data points). The remaining Irish Sea Ice Stream cores are shown by the yellow data points.

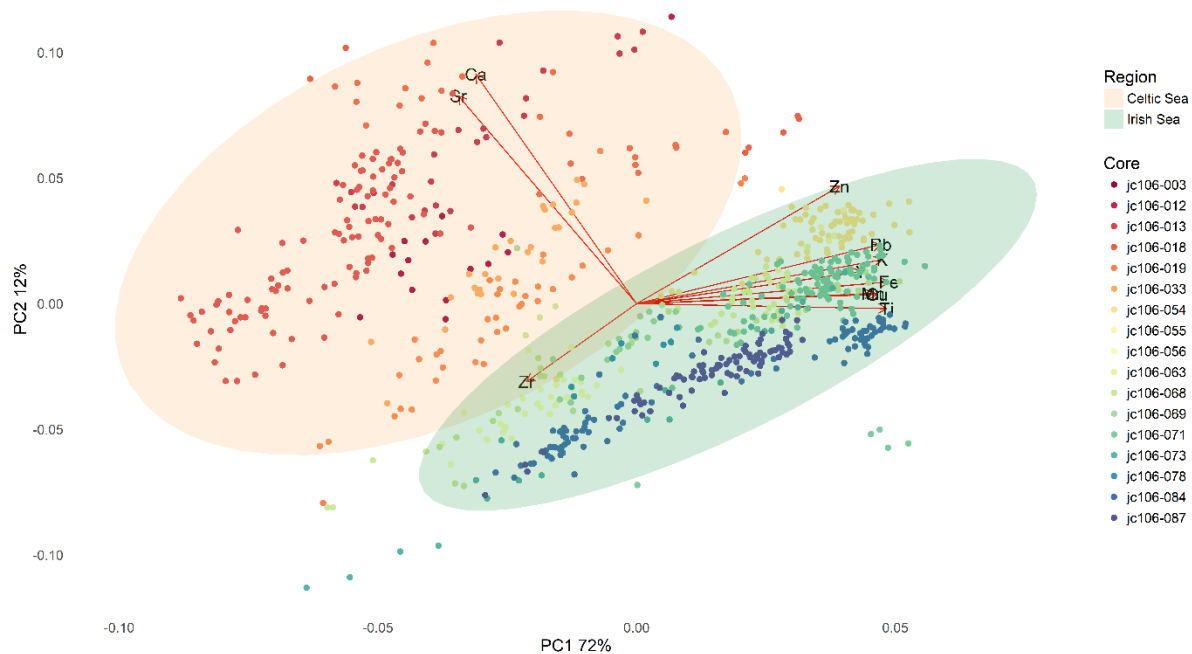


Figure 7.5 PCA biplot for the Irish Sea Ice Stream sediment cores divided into regions. PC 1 explains 72% of the total variance in the dataset and PC 2 13%. Each core and region has been colour coded.

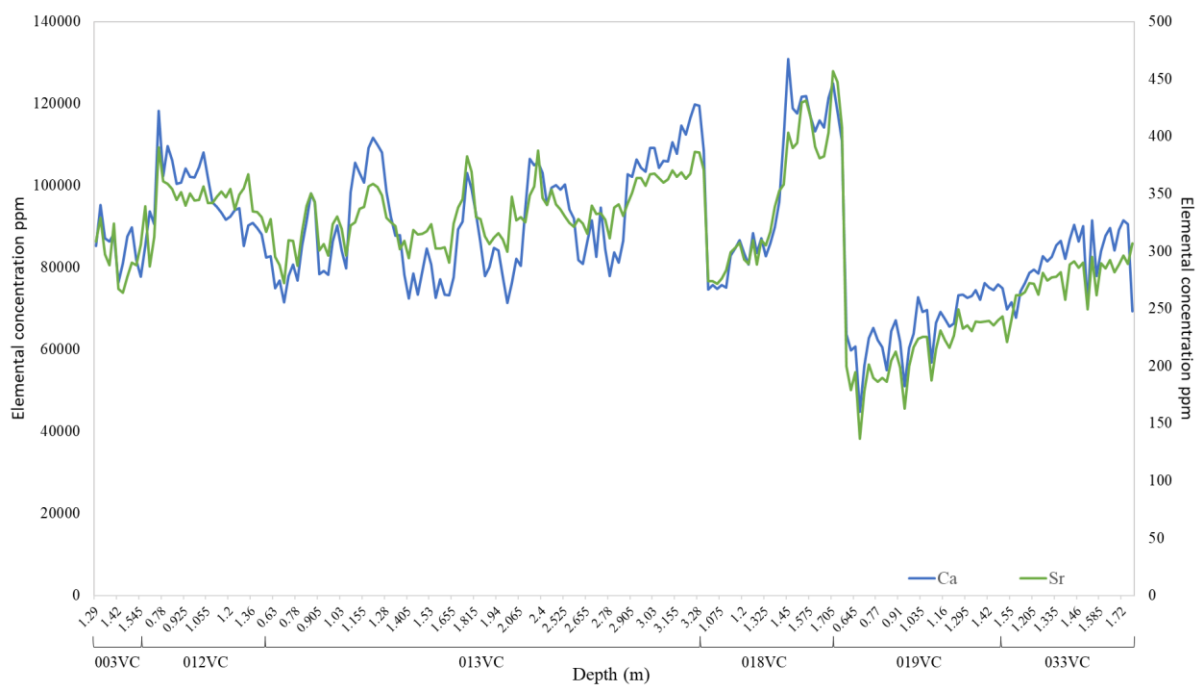


Figure 7.6 Elemental concentrations for the Celtic Sea sediment cores have been integrated. The plots show the downcore variation of Ca and Sr for the six sediment cores.

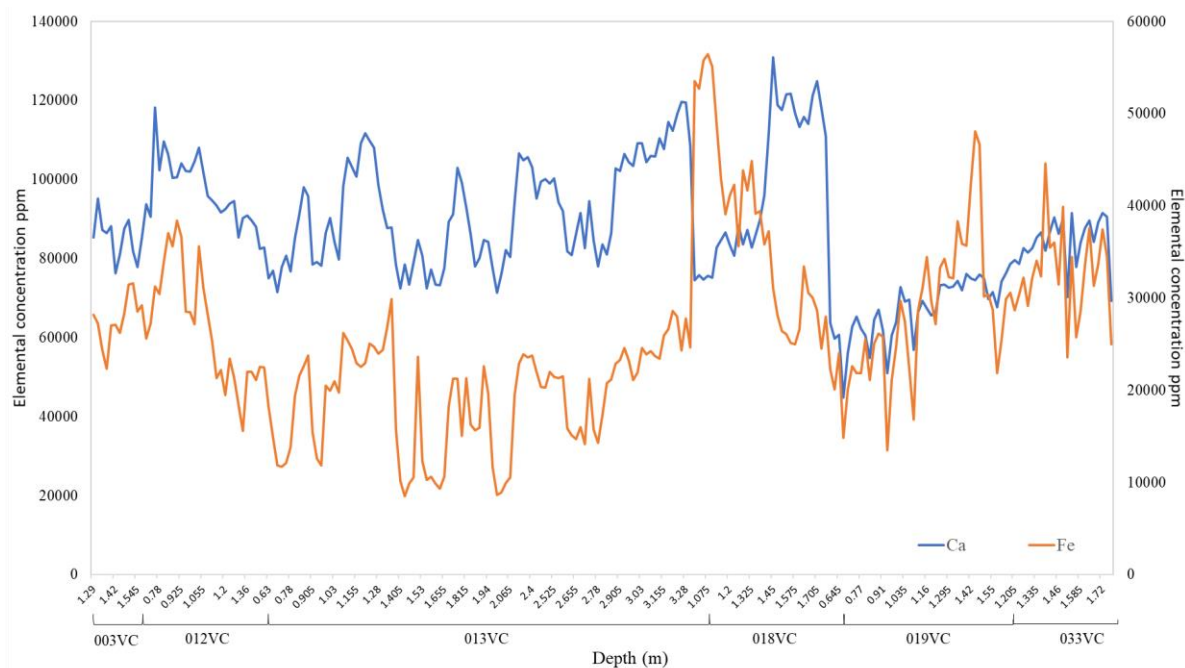


Figure 7.7 Elemental concentrations for the Celtic Sea sediment cores have been integrated. The plots show the downcore variation of Ca and Fe for the six sediment cores.

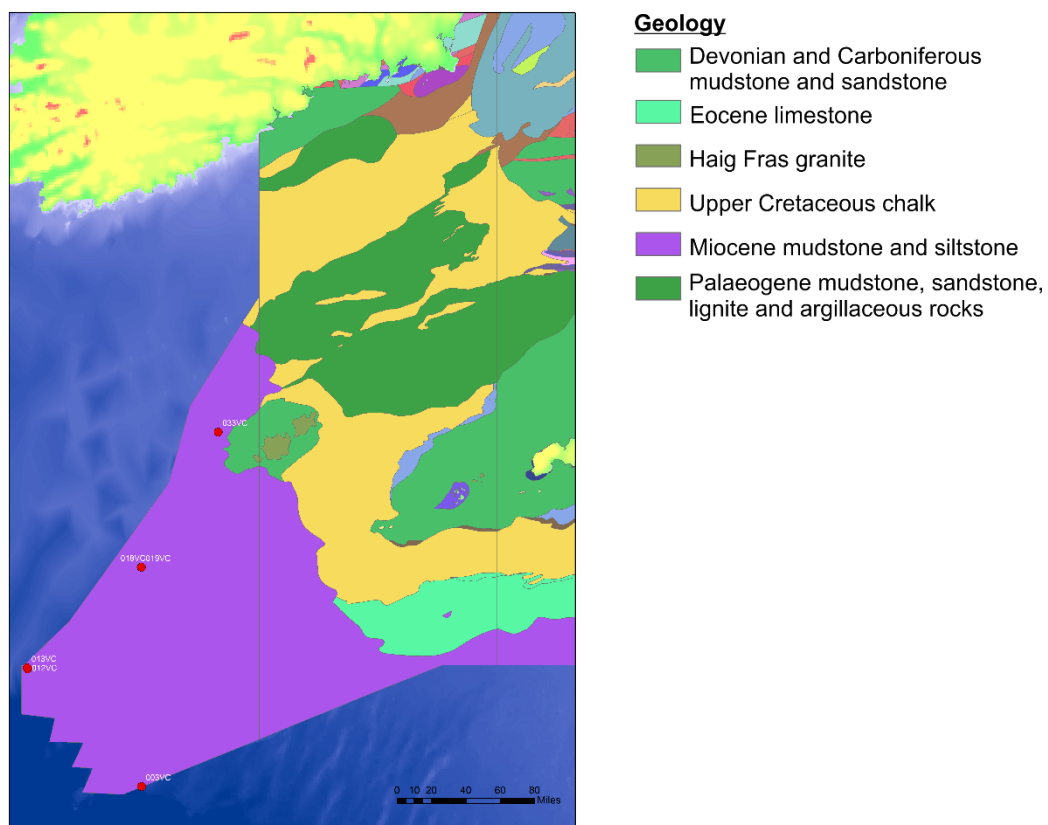


Figure 7.8 Geological map of the Celtic Sea region. The key illustrates the main formations present (British Geological Survey, 2008).

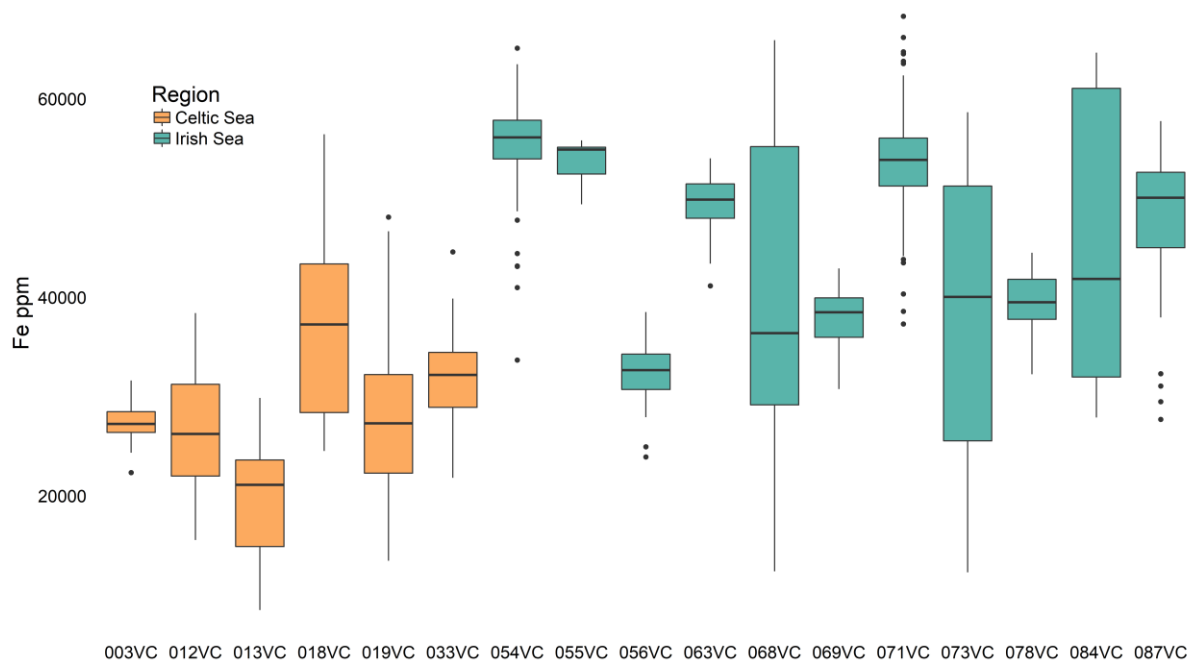


Figure 7.9 Boxplot displaying Fe concentrations of the 17 sediment cores from the former Irish Sea Ice Stream. The cores have been colour coded by region.

red beds which are associated with high Fe concentrations which could account for the higher concentrations of Fe (Figure 7.10).

Figure 7.11 demonstrates that there is also a grain size effect across the entire ISIS. The Irish Sea end members are in general characterised by clay and clayey silt lithofacies, whereas the Celtic Sea cores are in general associated with sand and silt lithofacies. Distinct grain size clusters are not apparent in the analysis, and therefore these analyses identify grain size as a second order driver of the geochemical signature of the end members behind the location/local catchment geology. It is possible to conclude from these data that:

- There is a clear gradient across the continental shelf along the flowpath of the former ISIS that is driven by the local catchment geology
- The Celtic Sea and Irish Sea end members have distinct geochemical signatures
- The Celtic Sea is characterised by high concentrations of Ca and Sr which have a detrital origin relating to the outcropping Upper Cretaceous Chalk
- Irish Sea end members are influenced by the Permian-Triassic red beds which account for the high Fe values
- There is a grain size effect both along the whole ice stream flowpath and within some of the individual cores

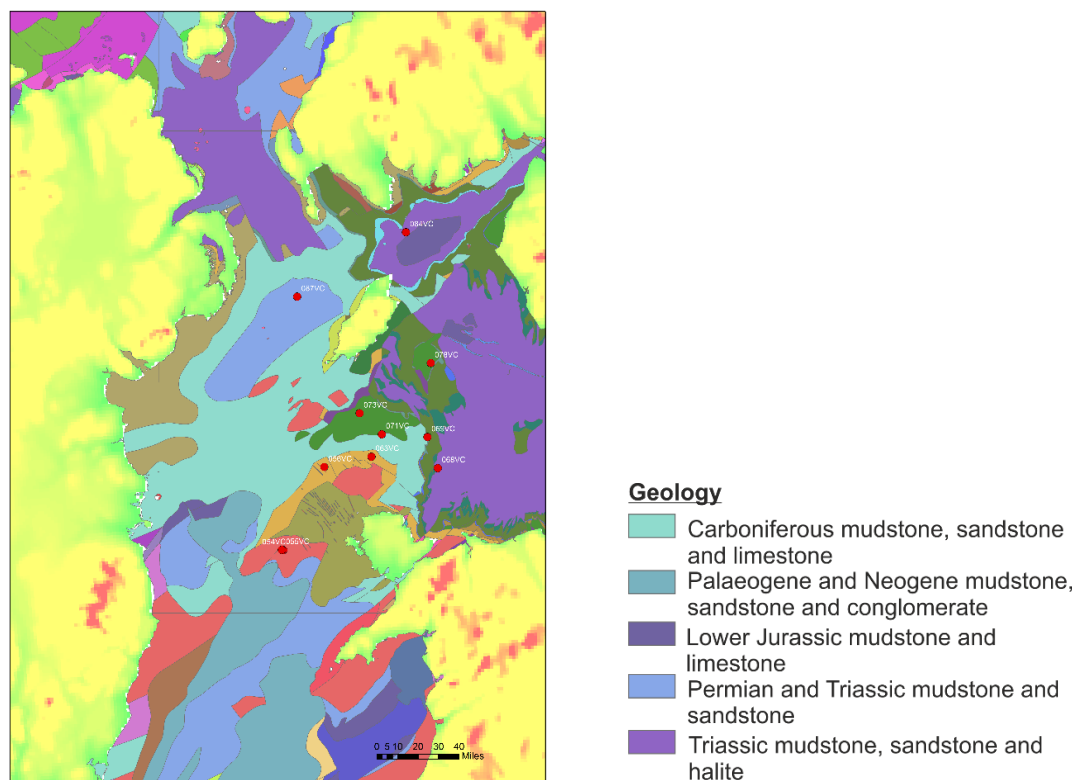


Figure 7.10 Geological map of the Irish Sea region. The key illustrates the main formations present (British Geological Survey, 2008).

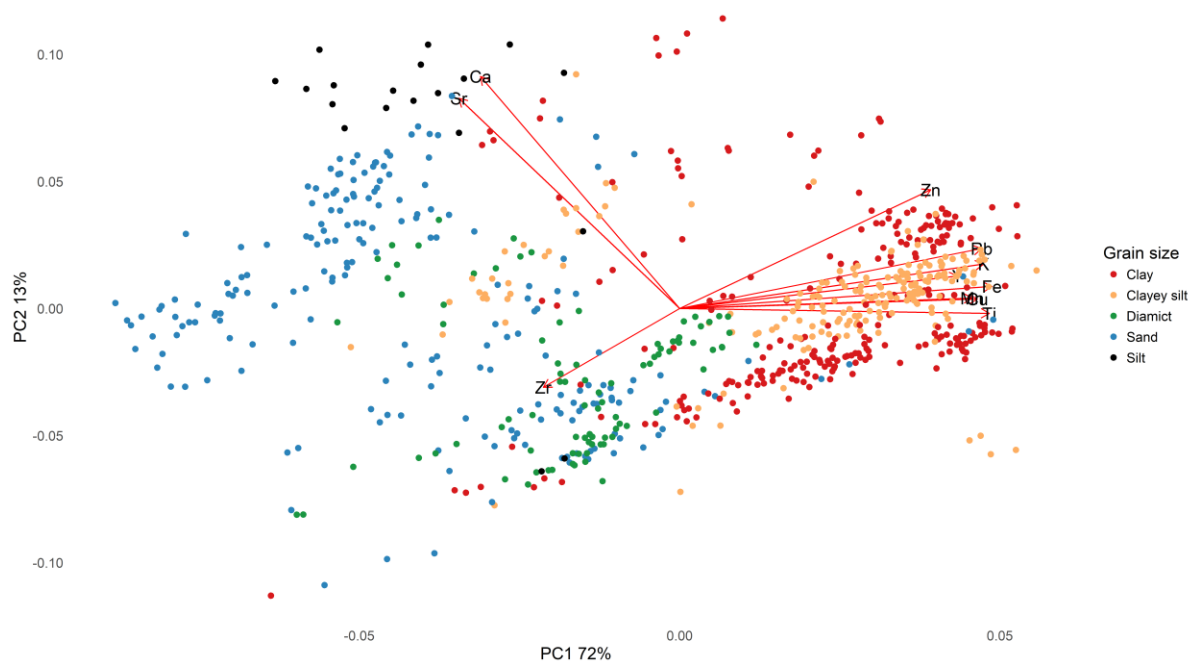


Figure 7.11 PCA biplot for the Irish Sea Ice Stream sediment cores colour coded by grain size.

### **7.1.2 Geochemical signature of MD04-2820CQ**

The PCA of MD04-2820CQ (Figure 7.12) shows a central cluster with two ‘arms’, one arm associated with the Heinrich events (H1, H2, H4, ‘Heinrich affinity’) and another arm which

has high Ca and Sr but which is geochemically dissimilar from the Heinrich events and associated sediments ('non-Heinrich affinity'). The Heinrich events (H1, H2 and H4) mostly plot at the furthest end of the Ca and Sr vector, which is expected due to their dolomitic carbonate content from the Churchill Province within the Laurentide Ice Sheet catchment (Hemming, 2004). This lithological characteristic has become a distinct signature for identifying Heinrich events in North Atlantic marine sediments. On the other hand, H3 plots within the central cluster of the ambient MD04-2820CQ sediment. This supports previous interpretation of H3 as a predominantly non-Laurentide source, because of the absence of the characteristic dolomitic carbonate signature (e.g., Grousset *et al.* 1993; Bond and Lotti, 1995; Gwiazda *et al.* 1996; Snoeckx *et al.* 1999, Peck *et al.* 2007). The sediments that plot along the Heinrich event vector ('Heinrich affinity') occur post-H1, post-H4 and pre-H4 (Figure 7.13A). These sediments likely represent IRD from another North Atlantic terminating margin. These sediments do not display as high Ca and Sr values as the Heinrich events but could still be from a Laurentide source diluted by other terrigenous sources. The depths that constitute the 'non-Heinrich affinity' arm occur stratigraphically throughout the core (Figure 7.13B). These sediments could reflect increased biogenic signature, but it is necessary to compare how these sediments correspond to the ISIS end members.

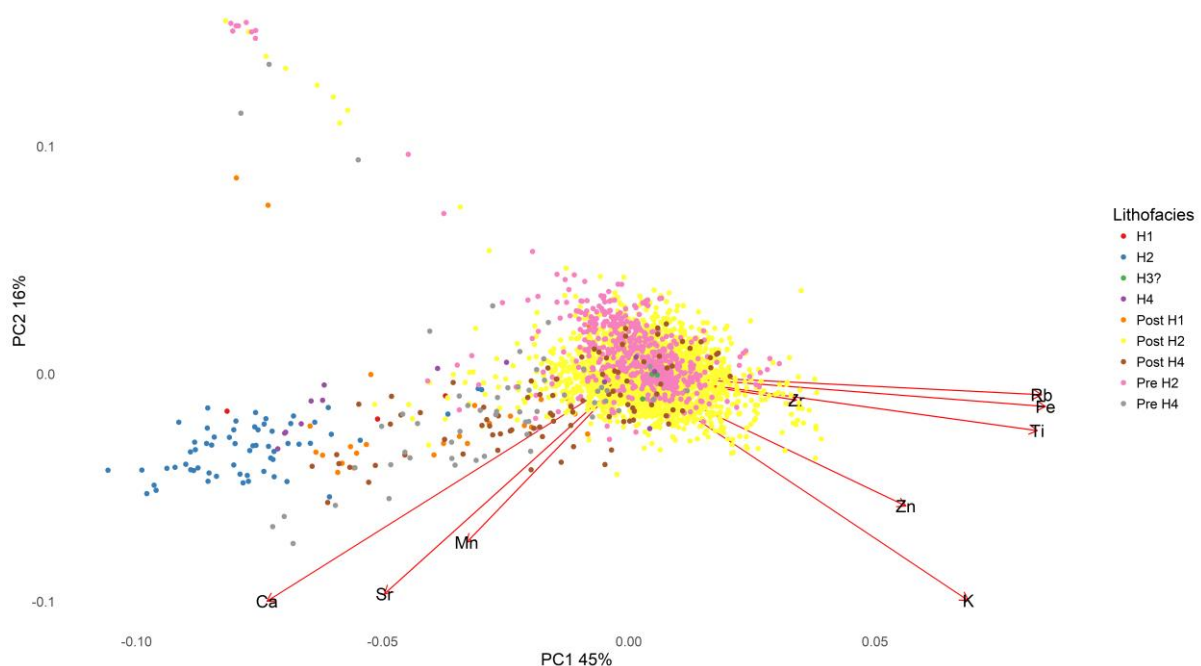


Figure 7.12 PCA biplot for MD04-2820CQ. PC 1 summarises 45% of the total variance in the dataset and PC 2 16%. Heinrich events and the ambient clay-silt lithofacies have been colour coded. H1-Red, H2- Blue, H3- Green and H4 Purple. Post H1-Orange, Post H2- Yellow, Pre-H2- Pink, Post H4-Brown and Pre-H4 Grey.

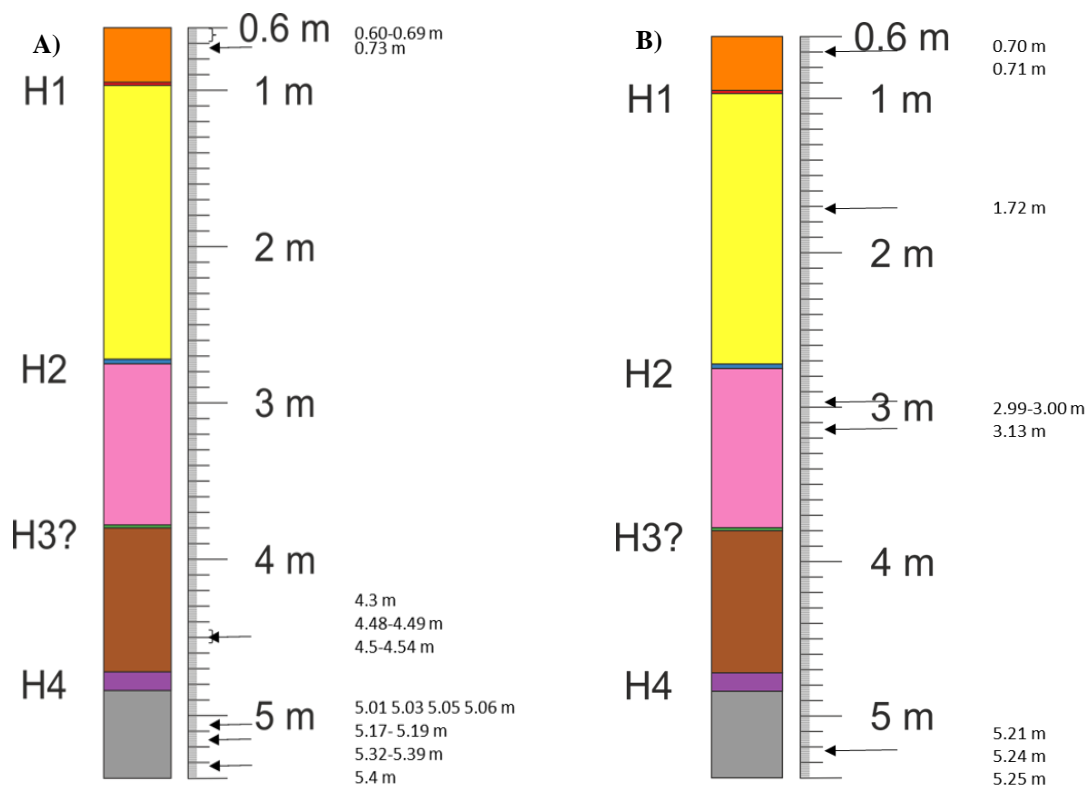


Figure 7.13 Lithostratigraphic core log for MD04-2820CQ. H1-Red, H2- Blue, H3- Green and H4 Purple. Post H1-Orange, Post H2- Yellow, Pre-H2- Pink, Post H4-Brown and Pre-H4 Grey. A) Arrows correspond to the stratigraphic position of the ambient samples that occur along the main SW Heinrich vector of the PCA in Figure 7.12. B) Arrows correspond to the stratigraphic position of the ambient samples that occur along the NW arm of the PCA in Figure 7.12.

### **7.1.3 Exploring the geochemical relationship between MD04-2820CQ and the Irish Sea Ice Stream end members**

The Heinrich layers are clearly separated from the ISIS end members (Figure 7.14); however, when analysing H2 with the ISIS end members (Figure 7.15), three data points do plot closer to the Celtic Sea end members. These H2 depths could be influenced by Celtic Sea sediment; Haapaniemi *et al.* (2010) document the presence of chalk (ISIS proxy) during the main H2 dolomitic carbonate peak. The ‘Heinrich affinity’ arm does not display any geochemical similarities with the ISIS end members (Figure 7.14), and therefore this supports another North Atlantic source for these sediments. On the other hand, the ‘non-Heinrich affinity arm’ overlaps with the Celtic Sea end members (Figure 7.14). The Irish Sea end members display similarities to the central cluster of the ambient MD04-2820CQ depths (Figure 7.14).

Analysis also explored fingerprinting depths within the deep ocean core to link to specific shelf end members. Data points for MD04-2820CQ were labelled by depth and using the nearest neighbour approach, whichever depth plotted close to a shelf data point were thereby fingerprinted to specific end members as explained by Figure 7.16. Figure 7.17 displays the



results from this analysis. Pre-H4 MD04-2820CQ has a clear Celtic Sea affinity, but from this point to H3 no similarities can be drawn between the deep ocean core and the ISIS end members. Following H3 however, there is correlation to the Irish Sea end members which continues until 3.13 m where similarities to JC106-033VC and JC106-019VC occur. But, for the most part, pre-H2 MD04-2820CQ corresponds more to the Irish Sea end members. Post-H2, Celtic Sea contributions are more common, particularly from shelf edge cores such as JC106-012VC, but more so JC106-018VC, JC106-019VC and JC106-033VC. Irish Sea end members still dominate the similarities. After 1.7 m there is no resemblance between the two datasets, but just before and after H1 there are similarities to JC106-068VC and two cores from the Celtic Sea (JC106-013VC, JC106-018VC). This analysis indicates that flux to MD04-2820CQ is dominated by the Irish Sea end members, but that post-H2 Celtic Sea end members are more common with some Celtic Sea affinity also occurring pre-H2. From this we can deduce that from post-H3 to pre-H2, the ISIS had an ice marginal position within the Irish Sea sector and not in the Celtic Sea sector, a conclusion supported by Scourse *et al.* (1990) and Ó Cofaigh and Evans (2007). The input of Celtic Sea sediments circa H2 supports previous interpretations of a short-lived advance to the Celtic Sea and retreat during H2 (Ó Cofaigh and Evans, 2007; Scourse *et al.* 2009; Chiverell *et al.* 2013; Praeg *et al.* 2015). Pre-H4 there is a Celtic Sea signature. This is difficult to explain but Peck *et al.* (2007) discuss the establishment of a less extensive BIIS with a marine margin as early as 46 kyr BP. This is supported by terrestrial evidence of ice sheet build up during MIS 4-3 (Ó Cofaigh *et al.* 2012). OSL dates on the Courtmacsherry Raised Beach (County Cork, Southern Ireland) and overlying shallow marine sands, indicate high relative sea level and submergence related to glacioisostatic depression during ice sheet build up. A less extensive BIIS does not therefore support a Celtic Sea ice margin position, however the Celtic Sea end members are characterised by detrital carbonate. This detrital carbonate signature during times of restricted ice sheet extent could represent a different source, such as the Carboniferous limestones of Ireland (Knutz *et al.* 2001). This could explain the early/late onset of detrital carbonate pre-H4 and post-H1, however if there was an emergent landbridge this would impede the transport of IRD to the deep ocean core site (Scourse *et al.* 2000; Haapaniemi *et al.* 2010). An alternative mechanism for the Celtic Sea signature could be from formerly landfast and anchor sea ice, as discussed by Haapaniemi *et al.* (2010). This mechanism would deposit Celtic Sea affinity sediments at the deep ocean core site without the need of an ice margin, however this cannot be substantiated by the evidence presented in this study. The analysis supports the following conclusions:

- Geochemical analysis established three distinct clusters within MD04-2820CQ: an ambient central cluster; Heinrich affinity cluster and a non-Heinrich affinity cluster
- H3 plots with the ambient central cluster which supports a predominantly non-Laurentide source
- The Heinrich events (H1, H2 and H4) show significant separation from the ISIS end members
- The Heinrich affinity cluster does not show any geochemical similarities to the ISIS end members, therefore it likely represents a different North Atlantic source
- The Irish Sea and Celtic Sea end members still display distinct geochemical signatures even when analysed with MD04-2820CQ
- The non-Heinrich cluster has a Celtic Sea origin
- The Irish Sea end members plot close to the central ambient cluster of MD04-2820CQ
- Nearest neighbour analysis reveals that:
  - Irish sea end members are the main contribution to MD04-2820CQ, which likely reflects a quasi-stable ice marginal position within the Irish Sea sector
  - Celtic Sea IRD flux occurs circa H2 which coincides with ice sheet advance into the Celtic Sea and subsequent collapse immediately following H2
  - Pre-H4 there is a Celtic Sea signature which could reflect a less extensive BIIS
  - It is possible to fingerprint the IRD flux in MD04-2820CQ to shelf end members

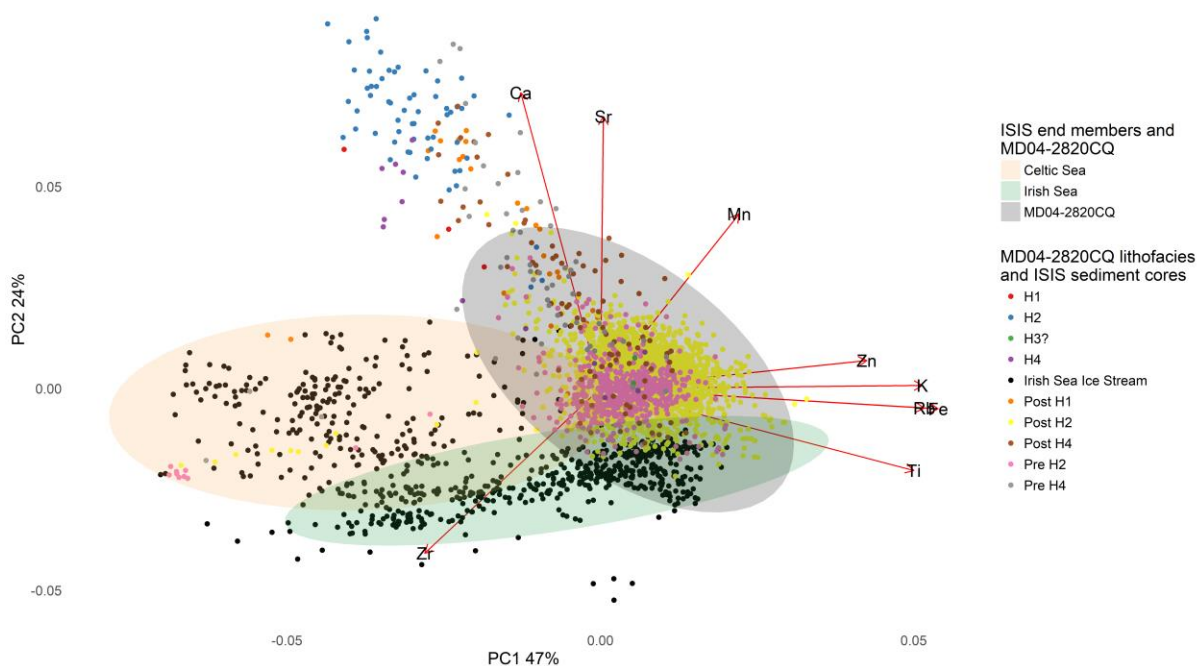


Figure 7.14 Biplots illustrating the PCA results obtained by integrating the shelf end members and MD04-2820CQ XRF data. MD04-2820CQ has been colour coded by its lithofacies and the Irish Sea Ice Stream end members are black and have been grouped into regions.

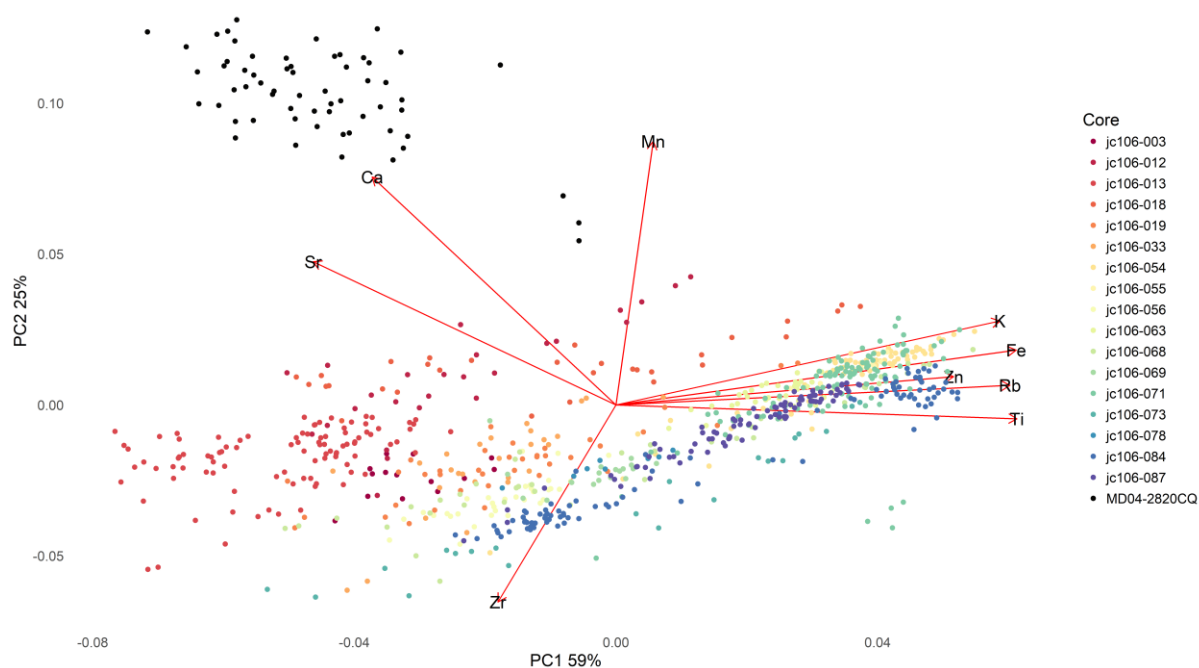


Figure 7.15 Biplot displaying the results of a PCA analysing both the shelf end members and H2 samples from MD04-2820CQ. H2 sediments are black and the Irish Sea Ice Stream end members are colour coded by core. PC 1 explains 59% of the total variance, PC 2 25%.

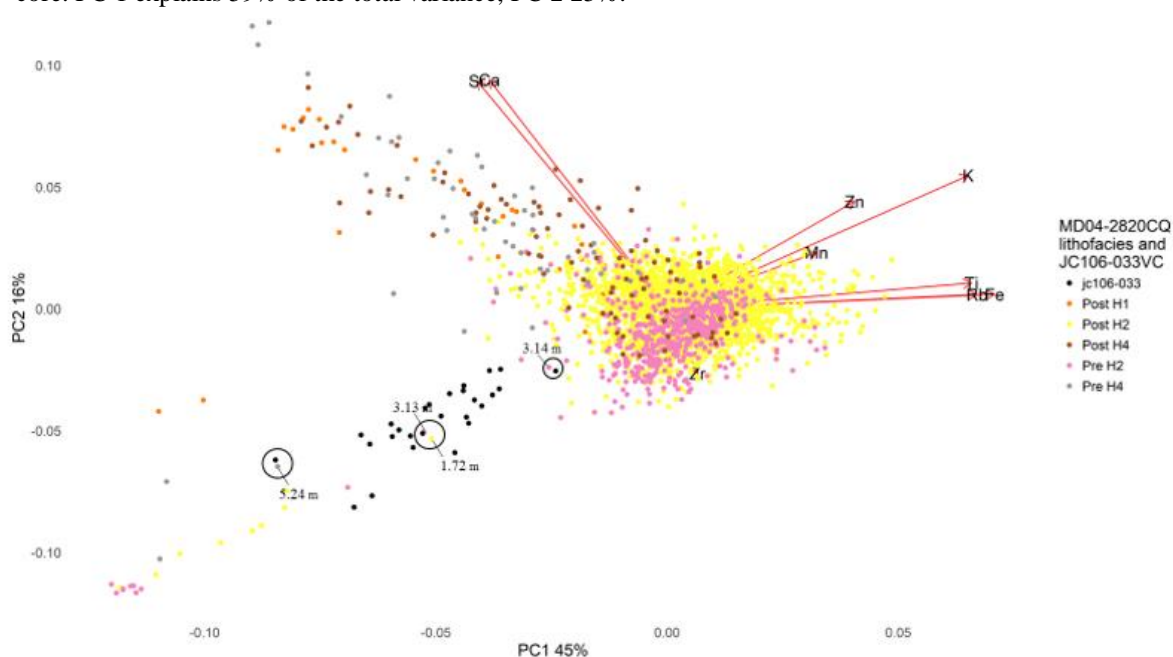


Figure 7.16 PCA for MD04-2820CQ and JC106-033VC, showing the nearest neighbour approach. Whichever depths within MD04-2820CQ plot most closely to JC106-033VC data points are assigned a JC106-033VC affinity. These are then plotted stratigraphically in Figure 7.17.

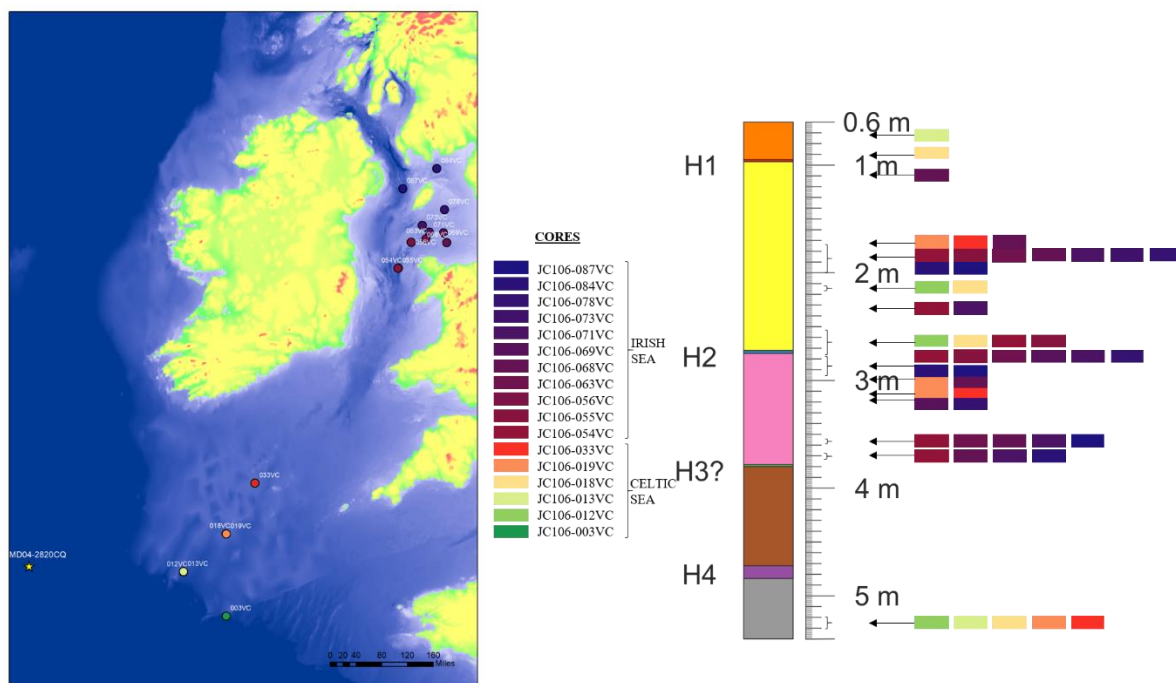


Figure 7.17 Schematic diagram displaying the location of the cores analysed and the colour that has been assigned to individual cores. Using the nearest neighbour approach, it has been possible to fingerprint depths within MD04-2820CQ to geochemically similar shelf end members.

## **7.2 Geochemical signature of the Hebrides Ice Stream and Donegal Bay sector**

### **7.2.1 Establishing Hebrides Ice Stream and Donegal Bay end members**

Nine cores were analysed from the continental shelf region of the former Hebrides Ice Stream and Donegal Bay ice lobe. The geochemical analysis of individual cores provided context for the overall geochemical pattern seen across the shelf of the former Hebrides Ice Stream and adjacent Donegal Bay ice lobe. Data from two cores were presented in Chapter 5 to show grain size variability in relation to stratigraphy. One of the cores is from the Donegal region and the other one is from the northern Malin Sea region of the Hebrides Ice Stream (Figure 7.18 and 7.19). JC106-102VC displays no clear stratigraphic gradient (Figure 7.18). Like JC106-033VC and JC106-063VC, as discussed in Section 7.1.1, this core is laminated and therefore includes some coarser grained laminae dispersed throughout the predominantly clay lithofacies, which would affect the geochemical signature of the core. JC106-146VC on the other hand, displays a clear stratigraphic gradient (Figure 7.19). The more distal sediments have lower Ca and Sr concentrations than the proximal sediments. The proximal sediments are mainly diamict and clay lithofacies, whereas the distal sediments are silt. The high values of Ca and Sr in the

diamict most likely indicate the overriding and reworking of pre-existing marine sediments (Ó Cofaigh *et al.* 2013).

When all nine cores are analysed together a gradient that reflects core location is revealed. This is clearly shown by grouping the cores into regions, however there is also overlap between the regions (Figure 7.20). The Donegal cores are characterised by high values of Ca, Sr and Zr, which is interpreted as a reflection of the Carboniferous Limestone catchment (Figure 7.21). The northern Malin Sea cores are depleted in Ca, Sr and Zr in comparison to the Donegal cores. The northern Malin Sea cores have higher concentration of Fe than the Donegal cores (Figure 7.22), which is most likely a reflection of the local catchment geology. The flow of ice into the northern Malin Sea would have been sourced from the Hebrides (Small *et al.* 2017). The geology of this region is comprised of Lewisian gneiss, Permian to Jurassic mudstone, sandstone and limestone, Torridon sandstone, siltstone and mudstone (British Geological Survey, 2008) and Tertiary basalts from mainland Scotland (Knutz *et al.* 2001) (Figure 7.21 and 7.23). However, it has been documented that thick pre-Devensian deposits occur in the Malin Sea region (Fyfe *et al.* 1993) and consequently the geochemical signature of the shelf sediments likely reflects the mainland geology of Scotland (Tertiary basalts) (Knutz *et al.* 2001) or resistant bedrock highs of Pre-Cambrian and Tertiary rocks (Howe *et al.* 2012). The central Malin Sea core (JC106-123VC; Figure 7.20) has positive PC scores on both axes

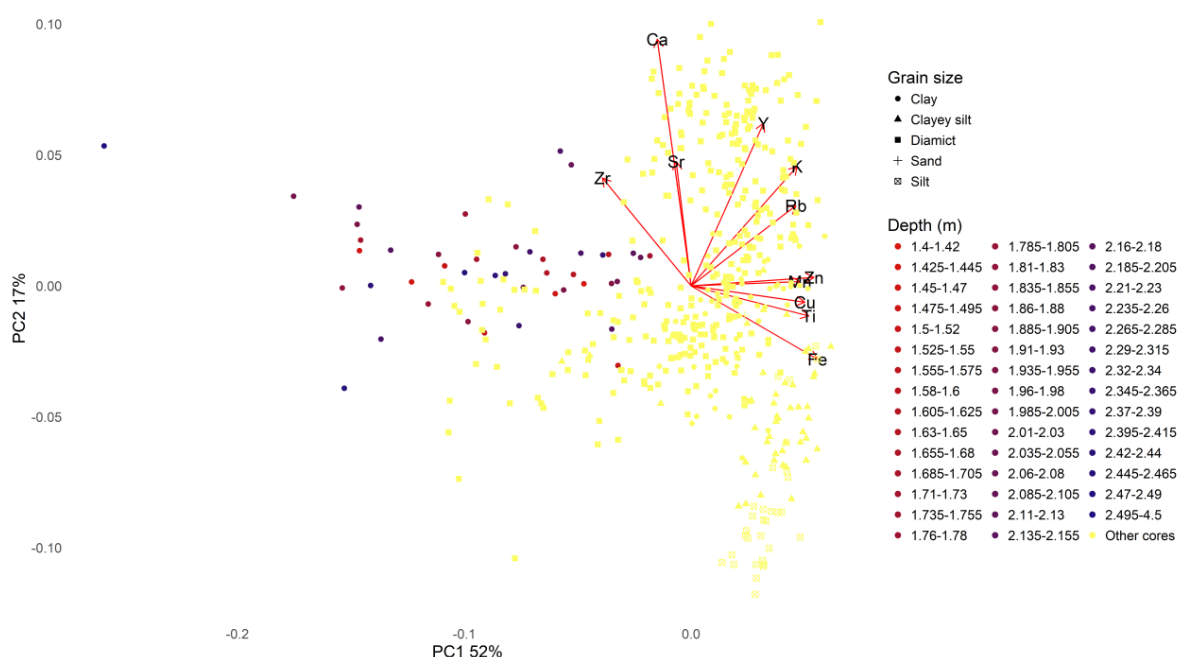


Figure 7.18 PCA biplot displaying internal elemental concentration and grain size variability for one Donegal Bay ice lobe core as a function of stratigraphy JC106-102VC.

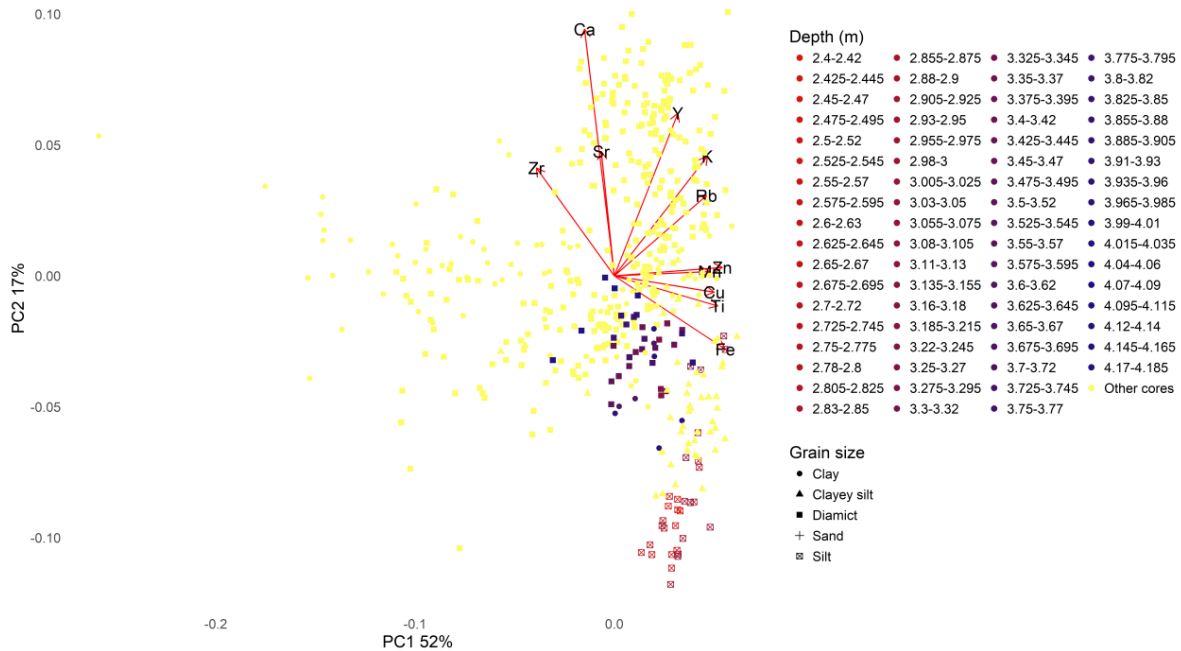


Figure 7.19 PCA biplot displaying internal elemental concentration and grain size variability for one Hebrides Ice Stream core as a function of stratigraphy JC106-146VC.

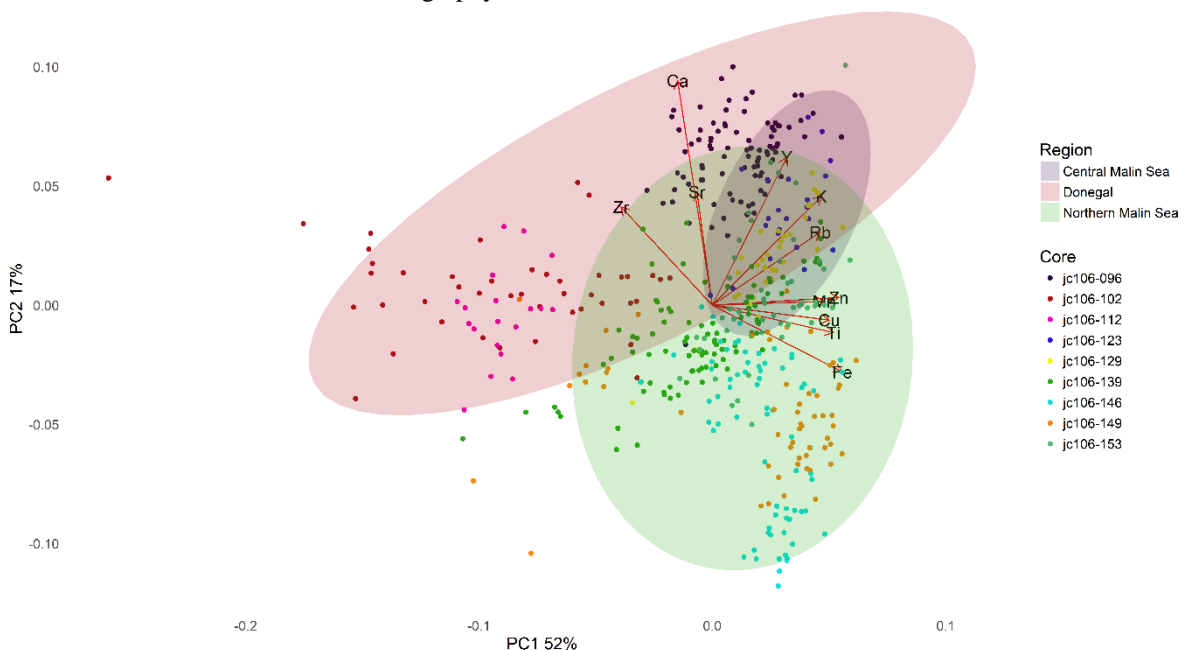


Figure 7.20 PCA biplot for the Hebrides Ice Stream and Donegal Bay sediment cores divided into regions. Each core and region has been colour coded.

and consequently, is enriched in Y, K and Rb. The central Malin Sea core has similar geochemistry to JC106-096VC (Donegal core), JC106-129VC and JC106-153VC (both northern Malin Sea cores). The similarities between JC106-096VC and JC106-123VC are to be expected because they both contain glacial sediments deposited by ice sourced from Ireland (Greenwood and Clark 2009; Dunlop *et al.* 2010). The sediments in JC106-129VC and JC106-153VC on the other hand would have been sourced from ice flowing from western

Scotland. The overlap of regions displayed in the PCA (Figure 7.20) most likely reflects similarities in the geochemistry of the catchment geology. Unlike the ISIS which had very different catchment geologies for the Celtic Sea and Irish Sea end members, the highlands of NE Ireland and the Hebrides are dominated by Tertiary basalts, thus similar geochemical signatures.

The difference between the Donegal cores is notable; JC106-102VC and JC106-112VC plot differently to JC106-096VC (Figure 7.20). This could be because the sediments were deposited during different stages of ice advance and retreat. The sediments in JC106-102VC

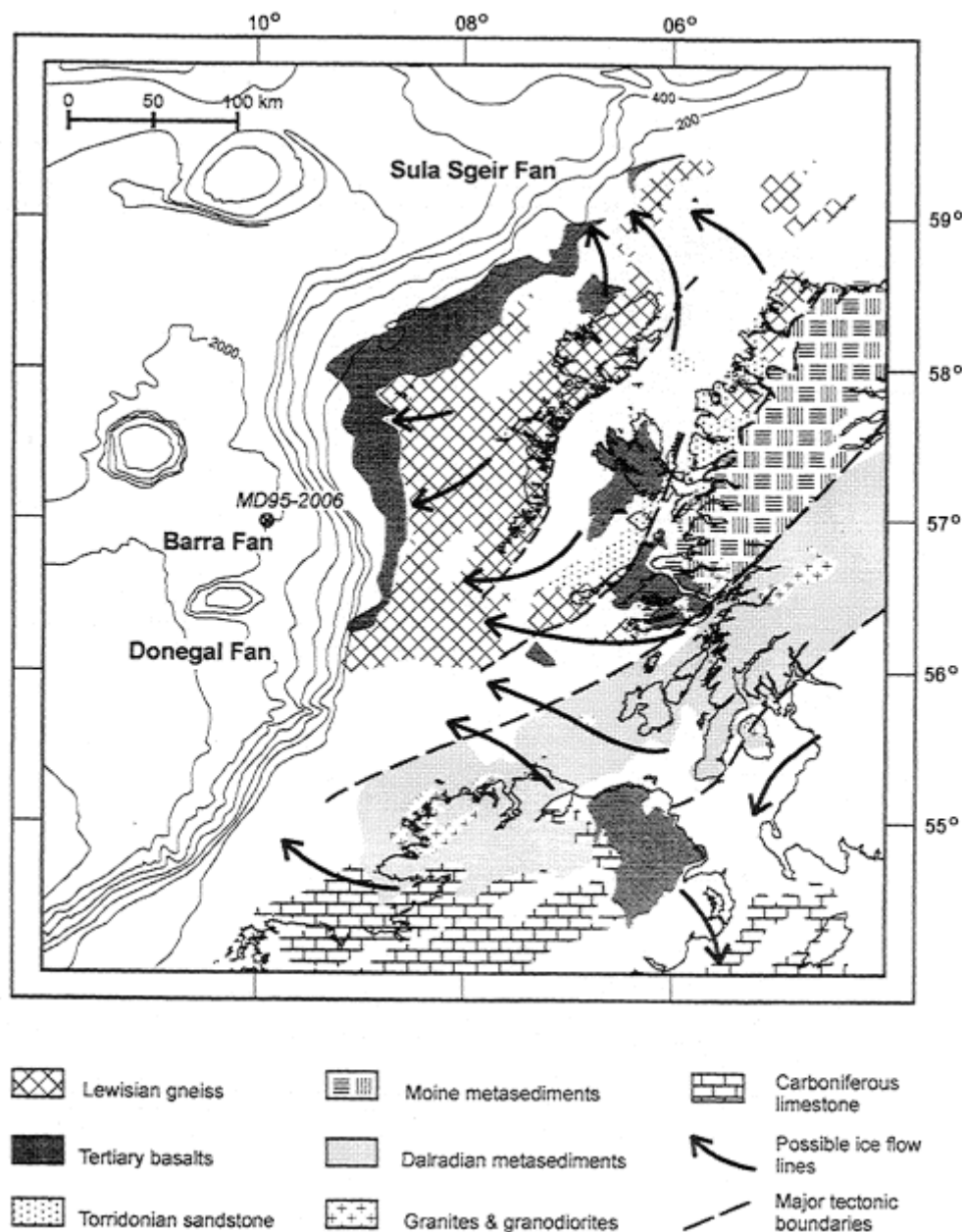


Figure 7.21 Geology of the northwestern margin of the BIIS. The key illustrates the main formations present. From Knutz *et al.* (2001).



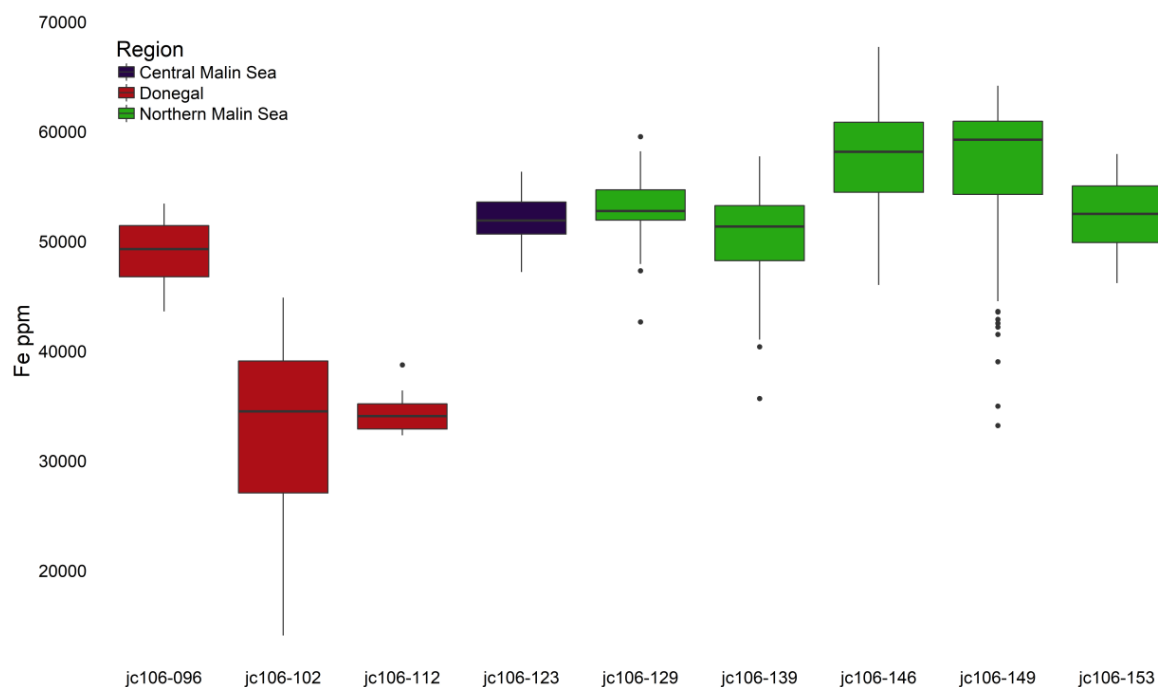


Figure 7.22 Boxplot displaying Fe concentrations of the nine sediment cores from the former Hebrides Ice Stream and Donegal Bay ice lobe. The cores have been colour coded by region.

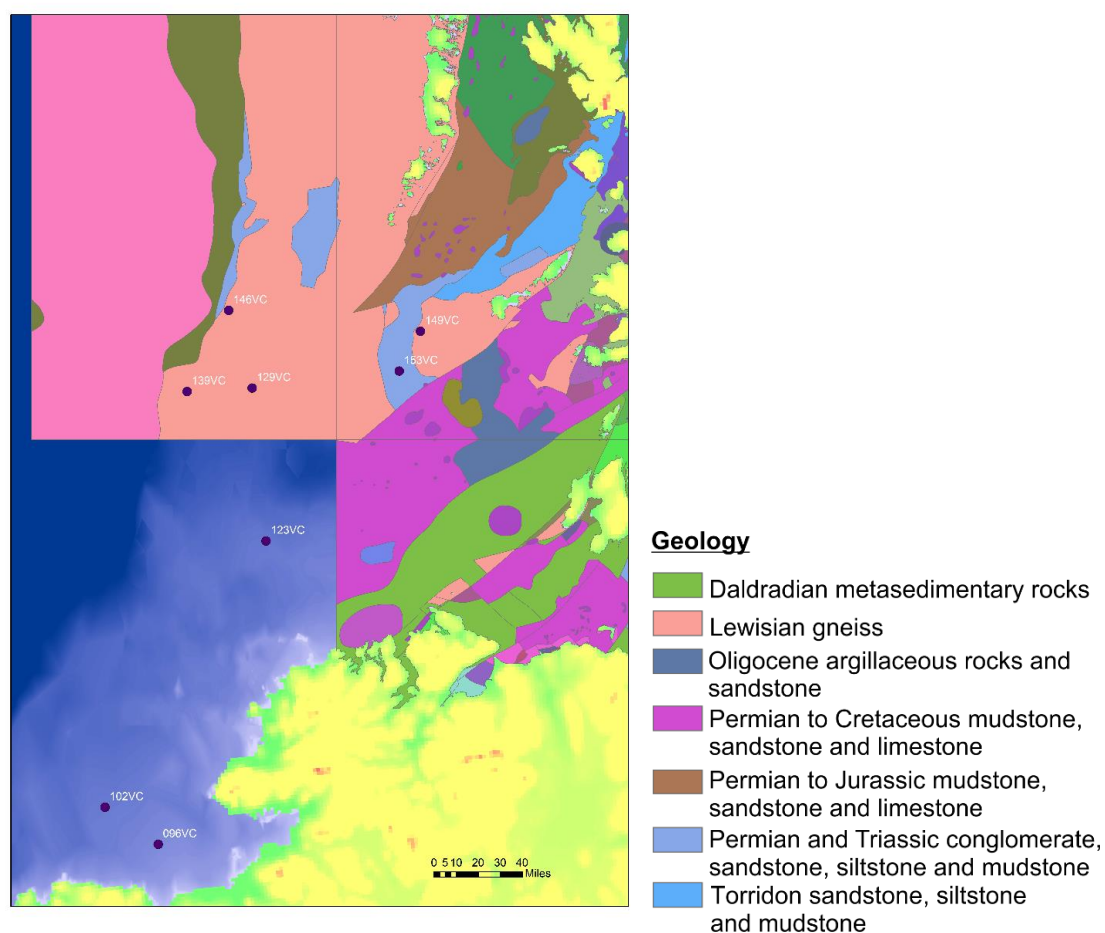


Figure 7.23 Geological map of the Malin Sea region. The key illustrates the main formations present (British Geological Survey, 2008).



and JC106-112VC were both deposited during the advance of the BIIS to the shelf edge during the LGM; this ice would have been sourced from an ice centre in the Donegal highlands (Ó Cofaigh *et al.* in press). The sediments that comprise JC106-096VC correspond to a later re-advance by an ice lobe advancing from Killala Bay; this ice would probably have been sourced from County Mayo (Ó Cofaigh *et al.* 2012). Most of mainland Ireland is comprised of Carboniferous Limestone; the geochemical analysis reveals that JC106-102VC and JC106-112VC are both enriched in Ca and Sr which has been interpreted to indicate a Carboniferous Limestone source. The highlands of Donegal and western parts of County Mayo have Caledonian granite outcrops and Dalradian quartzite; JC106-096VC could be more influenced by these source rocks. There is no clear grain size effect across the Hebrides Ice Stream and Donegal Bay sector (Figure 7.24); this is most likely because diamict and clay lithofacies dominate the cores analysed. The dominant modal grain size of these lithofacies is clay and therefore will have high values for the same clay associated elements (e.g. K and Rb).



Figure 7.24 PCA biplot for the Hebrides Ice Stream and Donegal Bay sediment cores colour coded by grain size.

On the outer shelf of the Malin Sea there is evidence of iceberg turbation (Dunlop *et al.* 2010). The diamict in JC106-139VC has been interpreted as an iceberg turbate, because of its physical characteristics, young radiocarbon ages and high shear strength values (Callard 2017, pers. comm. 2017, see Chapter 5, Figure 5.3). The implications of this for this study must be considered. Some of the outer shelf cores may have experienced reworking by the ploughing

of grounded icebergs (Dowdeswell *et al.* 2016), consequently the geochemical signature of these end members could be mixed. It has already been demonstrated that the geochemical signatures of the Hebrides Ice Stream and Donegal Bay end members are quite similar; this could be from the reworking of the glacimarine sediments by icebergs, but also similarities in the catchment geology. The iceberg turbate in JC106-139VC clusters with the Hebrides Ice Stream end members (Figure 7.20) and does not display any indicators of distal IRD source, thereby the turbate is attributed to the Hebrides Ice Stream. The radiocarbon dates within the JC106-139VC diamict range from dates of 12.6-24.1 kyr BP. Consequently, this evidence suggests that there were icebergs calving from a marine ice margin in Western Scotland during the Younger Dryas Stadial (12.9-11.7 kyr BP, Alley, 2000) which through iceberg turbation incorporated younger shells into the diamict. It is possible to conclude from these data that:

- There is a gradient across the continental shelf along the flowpath of the former Hebrides Ice stream and the Donegal Bay ice lobe that is driven by local catchment geology, but there is also overlap between the ice-flow regions most likely driven by geological similarities in the highland ice centres (Donegal, N. Ireland and the Hebrides region)
- The Donegal Bay region is characterised by high concentrations of Ca and Sr which have been attributed to outcrops of Carboniferous Limestone
- The northern Malin Sea cores have higher values of Fe sourced from the catchment geology, likely derived from the basaltic lavas within the region.
- The geochemical differences between JC106-096VC and the other two Donegal cores most likely reflect the geochemical signature of the catchment of a smaller ice lobe advancing north from Killala Bay
- The ice stream is dominated by diamict and clay and consequently there is no grain size effect across the ice stream flowpath
- The iceberg turbate in JC106-139VC has a Hebrides Ice Stream geochemical signature, and suggests there was a marine ice margin in Western Scotland during the Younger Dryas Stadial.

### **7.2.2 Geochemical signature of MD04-2822**

The PCA of MD04-2822 (Figure 7.25) shows an age/depth related gradient along the PC 2 axis. The 24-31 kyr BP sediments contain higher values of Ca and Sr than the 12-24 kyr BP sediments. Hibbert *et al.* (2010) interpret the higher values of Ca as an indication of an increase in calcium carbonate and the 24-31 kyr BP time span does incorporate the advance of the BIIS

(detrital carbonate has been used previously as an identifier of IRD flux from the BIIS (Knutz *et al.* 2001; Peck *et al.* 2007)).

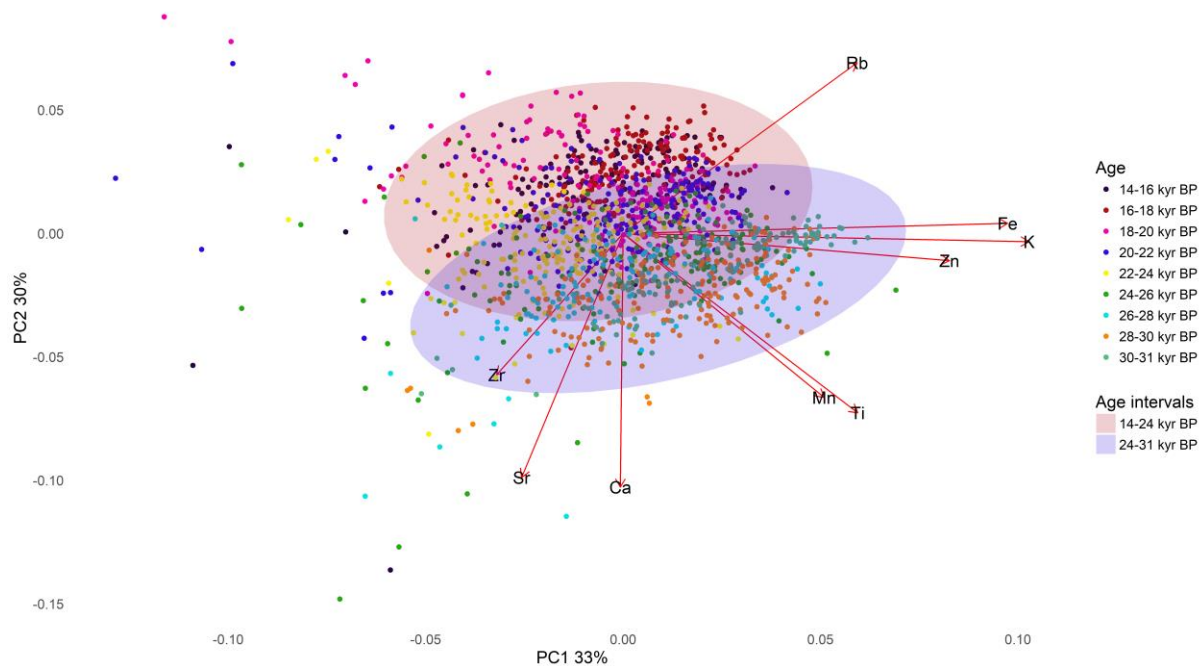


Figure 7.25 PCA biplot for MD04-2822. The core has been colour coded by age intervals and further grouped into broader age intervals (14-24 kyr BP and 24-31 kyr BP).

### **7.2.3 Exploring the geochemical relationship between MD04-2822 and the Hebrides Ice Stream and Donegal Bay end members**

The integration of the shelf end members with MD04-2822 shows geochemical similarities between the datasets (Figure 7.26), except for two Donegal cores (JC106-102VC and JC106-112VC). There is more geochemical overlap between MD04-2822 and the central and northern Malin Sea cores (Hebrides Ice Stream cores). JC106-123VC, JC106-129VC and JC139VC plot generally within the 24-31 kyr BP ellipse, whereas JC106-146VC and JC106-149VC plot mostly within the 12-24 kyr BP ellipse.

The data were subject to an analysis designed to explore fingerprinting depths within the deep ocean core to specific shelf end members. All nine cores were individually analysed by PCA with MD04-2822. Data points for MD04-2822 were labelled by depth and, using the nearest neighbour approach, whichever depth plotted close to a shelf data point were thereby fingerprinted to specific end members as explained in Section 7.1.2. Figure 7.27 displays the

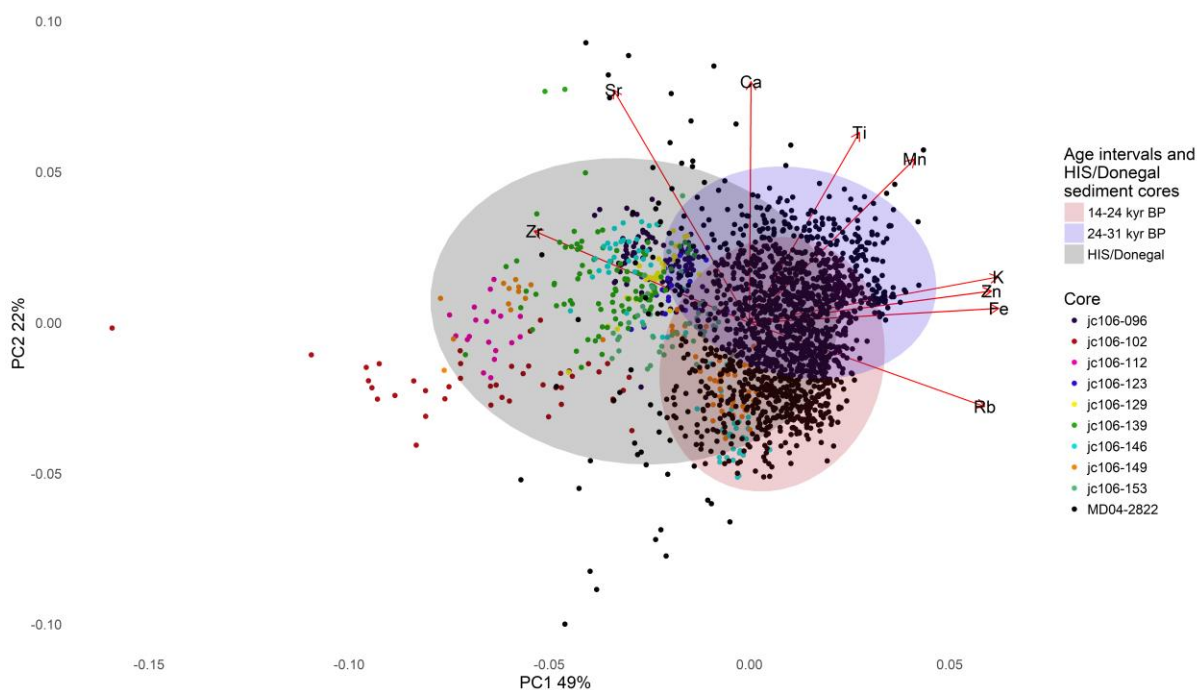


Figure 7.26 Biplot of the PCA results of MD04-2822 and Hebrides Ice Stream and Donegal Bay end members. Each core is shown by an ellipse and has been colour coded.

results from this analysis. MD04-2822 has been fingerprinted to every end member except JC106-112VC. No geochemical similarities could be drawn between MD04-2822 and the Donegal core JC106-112VC. A northern Malin Sea signature can be identified throughout the section studied of MD04-2822 (14-31 kyr BP). The Donegal signature is mainly occurring in the 22-31 kyr BP interval. JC106-096VC affinity has a particularly high occurrence in the deep ocean core during this interval. A similar pattern occurs for the geochemical signature of JC106-153VC, which also has a high occurrence between 22-31 kyr BP. From 14-22 kyr BP the geochemical signature of these two cores is less significant, although a strong northern Malin Sea signal is still present. These results indicate that there are four distinct clusters within the 22-31 kyr BP part of the dataset: 1) 17.12-17.66 m (~27-28 kyr BP); 2) 14.26-15.83 m (~24-26 kyr BP); 3) 12.95-13.97 m (23-24 kyr BP); 4) 11.56-12.40 m (21-22 kyr BP). Flux to MD04-2822 is dominated by Northern Malin Sea sediments throughout the studied section, particularly from JC106-146VC and JC106-149VC. These data indicate that the Hebrides Ice Stream and Donegal Bay ice lobe were active from 31 kyr BP. After 22 kyr BP the Donegal affinity appears to make only minor contributions to MD04-2822. On the basis of the fingerprinting analysis, there are four main influxes of shelf sediments to the deep sea core site that occur between 21-28 kyr BP. Such a pattern is consistent with the concept of BIIS expansion after 29 kyr BP and the arrival of the ice sheet margin at the shelf edge at 27 kyr BP

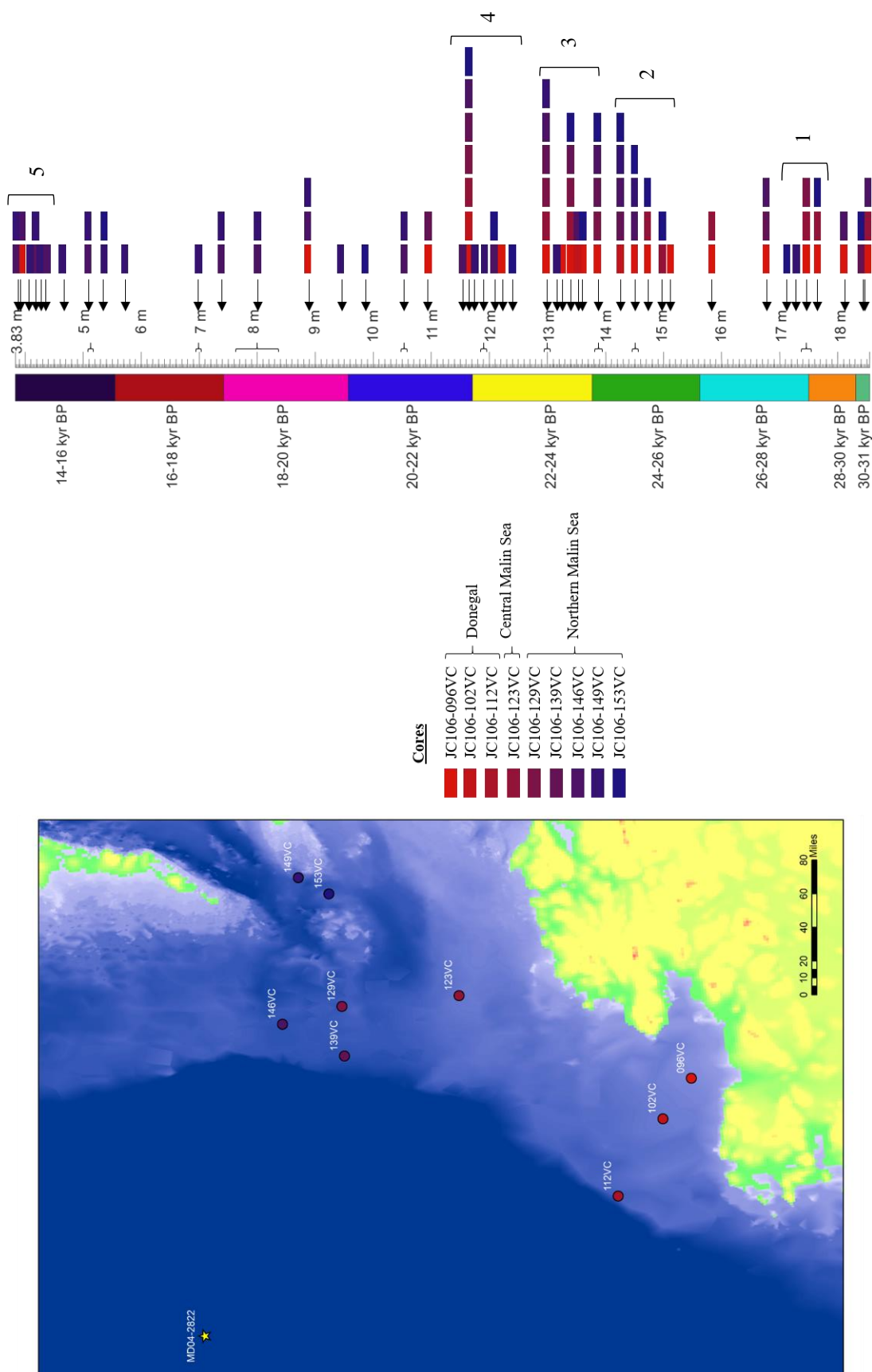


Figure 7.27 Schematic diagram displaying the location of the cores analysed and the colour that has been assigned to individual cores. Using the nearest neighbour approach, it has been possible to fingerprint depths within MD04-2822 to geochemically similar shelf end members.

(Cluster 1) (Wilson and Austin 2002; Scourse *et al.* 2009) and deglaciation from the shelf edge at ~25 kyr BP (Cluster 2) (Hughes *et al.* 2016). Subsequent clusters are interpreted to reflect the ongoing retreat of the ice sheet with possible minor re-advances. According to exposure ages from Tiree, ice stream cessation in the Northern Malin Sea occurred ~20 kyr BP with deglaciation of the marine sector by 17-16 kyr BP (Small *et al.* 2017). This could explain the fewer clusters after 22 kyr BP. Minor contributions from Donegal after 22 kyr BP could be explained by retreat of the ice sheet margin to a less extensive position in inner Donegal Bay. This interpretation is supported by the radiocarbon dates obtained by Ó Cofaigh *et al.* (In press), which show that the Donegal Bay moraine was formed ~20-19 kyr BP. As stated by Scourse *et al.* (2009), for BIIS IRD to be registered in the deep ocean cores the BIIS must have had a marine terminating margin. Figure 7.27 illustrates a cluster (Cluster 5) from 3.89-4.35 m (14.09-14.62 kyr BP). Ballantyne and Stone (2012) infer that there was rapid warming after ~14.7 kyr BP which resulted in the retreat from the submarine moraines identified by Bradwell *et al.* (2008) and Stoker *et al.* (2009). These moraines indicate the retreat of grounded ice from a fjord setting. Stoker *et al.* (2009) infer that retreat was most likely from internal instability triggered by a large calving event. Small *et al.* (2013b) identified a peak in IRD in Greenland Interstadial-1d (Lowe *et al.* 2008) from a core on the Hebridean shelf (MD95-2007). They did not dismiss the BIIS as a possible contributor and stated that because the grains were coarse it indicated a more local source (Andrews, 2000), however those authors prefer a distal origin for the IRD (Small *et al.* 2013a). This study interprets the uppermost cluster within MD04-2822 as indicating the flux of IRD from a smaller regionalised marine terminating margin possibly confined to the coastal fjords of the Inner Hebrides. The timing of the IRD flux coincides with the rapid warming after ~14.7 kyr BP (Ballantyne and Stone, 2012). Moraines have been identified both offshore and onshore along the west coast of Scotland that have been interpreted as readvance features after the deglaciation of the Minch Ice Stream and the Hebrides Ice Stream (Bradwell *et al.* 2008; Stoker *et al.* 2009; Ballantyne and Stone, 2012; Small *et al.* 2016). Small *et al.* (2016) dated the Scavaig moraine (Southern Skye, Figure 7.28) and determined that it was likely deposited during the Wester Ross Readvance; this evidence suggests that the Wester Ross Readvance event was more extensive than previously thought. Ballantyne and Stone (2012) suggest that this event occurred ~14.7 kyr BP. Consequently, this study interprets the IRD flux between 14.09-14.62 kyr BP as indicating ice margin retreat from the Wester Ross Readvance limits. This interpretation supports the presence of extensive ice masses possibly in the fjords of the Inner Hebrides during the lateglacial (GI-1e), however because the record does not extend beyond 14 kyr BP, this study cannot substantiate claims



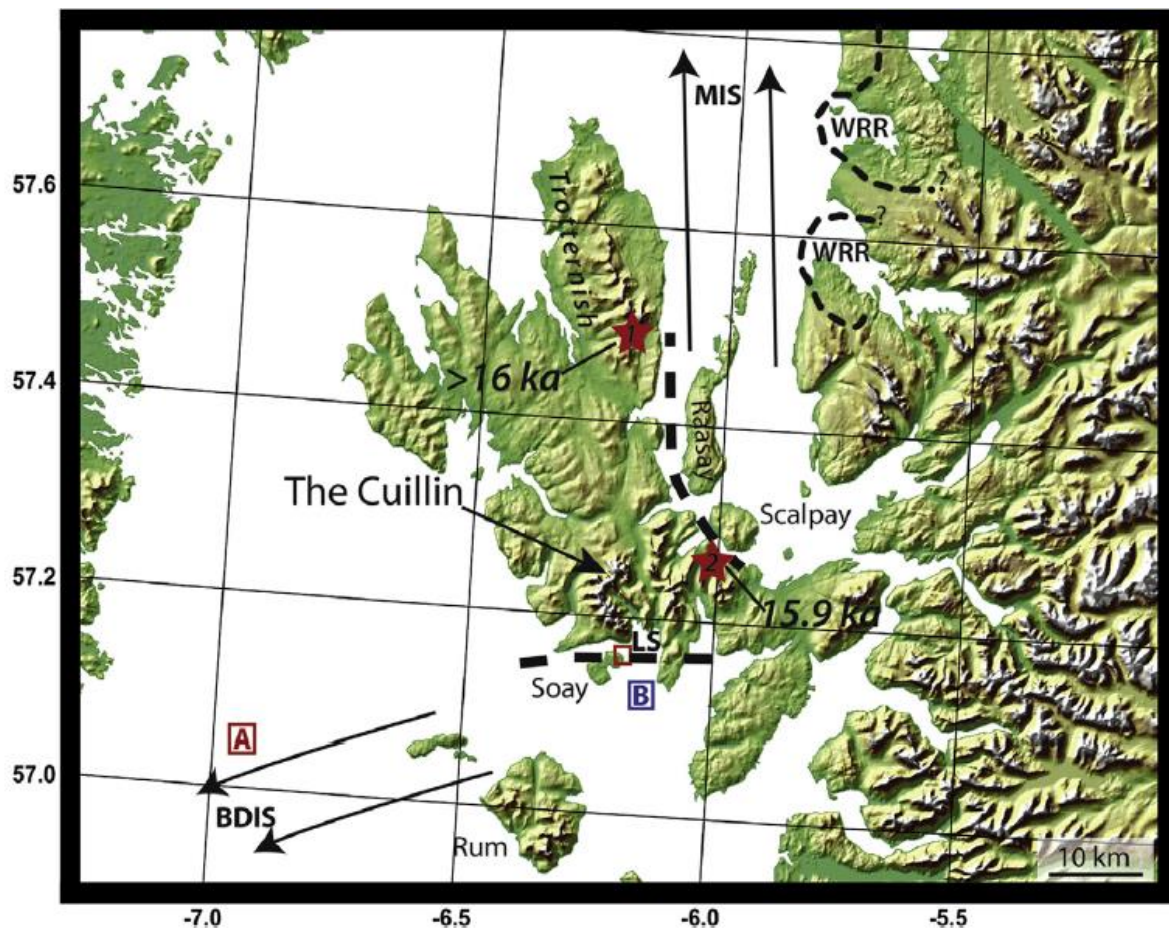


Figure 7.28. Location map of Skye and northwest Scotland showing locations mentioned in text. LS- Loch Scavaig, WRR- Wester Ross Readvance limits. Arrows show generalized ice flow directions of the Minch Ice Stream, (MIS) and the Hebrides Ice Stream (BDIS) From Small *et al.* (2016).

that large glaciers survived the Lateglacial Interstadial as proposed by Bradwell *et al.* (2008) and refuted by Ballantyne and Stone (2012).

Evidence of high relative sea-levels in Scotland between 15-16 kyr BP suggests the deglaciation of the BIIS and significant local isostasy in Western Scotland (Shennan *et al.* 2006). Northwest Scotland provides the longest record of relative sea-level change, with Arisaig (Figure 7.29) being the most complete record (Shennan *et al.* 2006). The marine limit identified at Arisaig ~16 kyr BP indicates a relative sea-level change of 34-36 m above present. When relative sea-level data from Arisaig and Kentra (Figure 7.29) are compared to the Earth model with a 71-km lithosphere used by Shennan *et al.* (2006), the observations are above the predictions. According to Shennan *et al.* (2006) a revised ice model with either more ice locally or later ice melt locally would capture these observations. Most other locations in northern Scotland show good agreement with the 71-km model used. The current ice models (Shennan

*et al.* 2006; Bradley *et al.* 2011; Brooks *et al.* 2008) used to represent the BIIS however do not factor in the current understanding of its retreat and its thickness. These models rely on the earlier interpretation of paleo-trimline data as maximum surface elevation of the BIIS rather than minimum (Fabel *et al.* 2012) and do not include the recalibrated exposure age data which uses locally derived  $^{10}\text{Be}$  production rates (Ballantyne and Stone, 2012). The recalibration increases the mean age of previously analysed geomorphological features by 6.5-12% (Ballantyne and Stone, 2012). Incorporating these new data into the ice models would alter the thickness and the deglacial chronology of the ice sheet, especially thicker ice which would result in greater rebound following the LGM. Therefore, current models are underestimating RSL post-LGM. My interpretation is that the high relative sea levels relate to the continued retreat of the BIIS from 16 kyr BP however with more extensive and thicker ice locally than indicated in the current models (Shennan *et al.* 2006; Bradley *et al.* 2011; Brooks *et al.* 2008). There was a subsequent readvance of the ice sheet to the Wester Ross Readvance limits which was then followed by retreat of the ice margin to the coastal fjords of the Inner Hebrides.

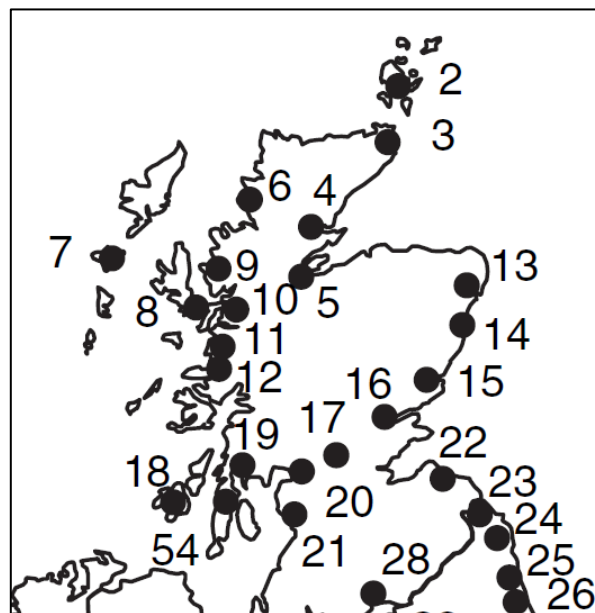


Figure 7.29 Location of sites with observations of relative sea-level change in Scotland from Shennan *et al.* (2006). Sites 11 (Arisaig) and 12 (Kentra) are referred to in text.



The conclusions and interpretations drawn for the fingerprinting analysis compare favourably to the other marine sediment cores in the near vicinity (Knutz *et al.* 2001; Wilson and Austin, 2002; Scourse *et al.* 2009; Hibbert *et al.* 2010). The analysis supports the following conclusions:

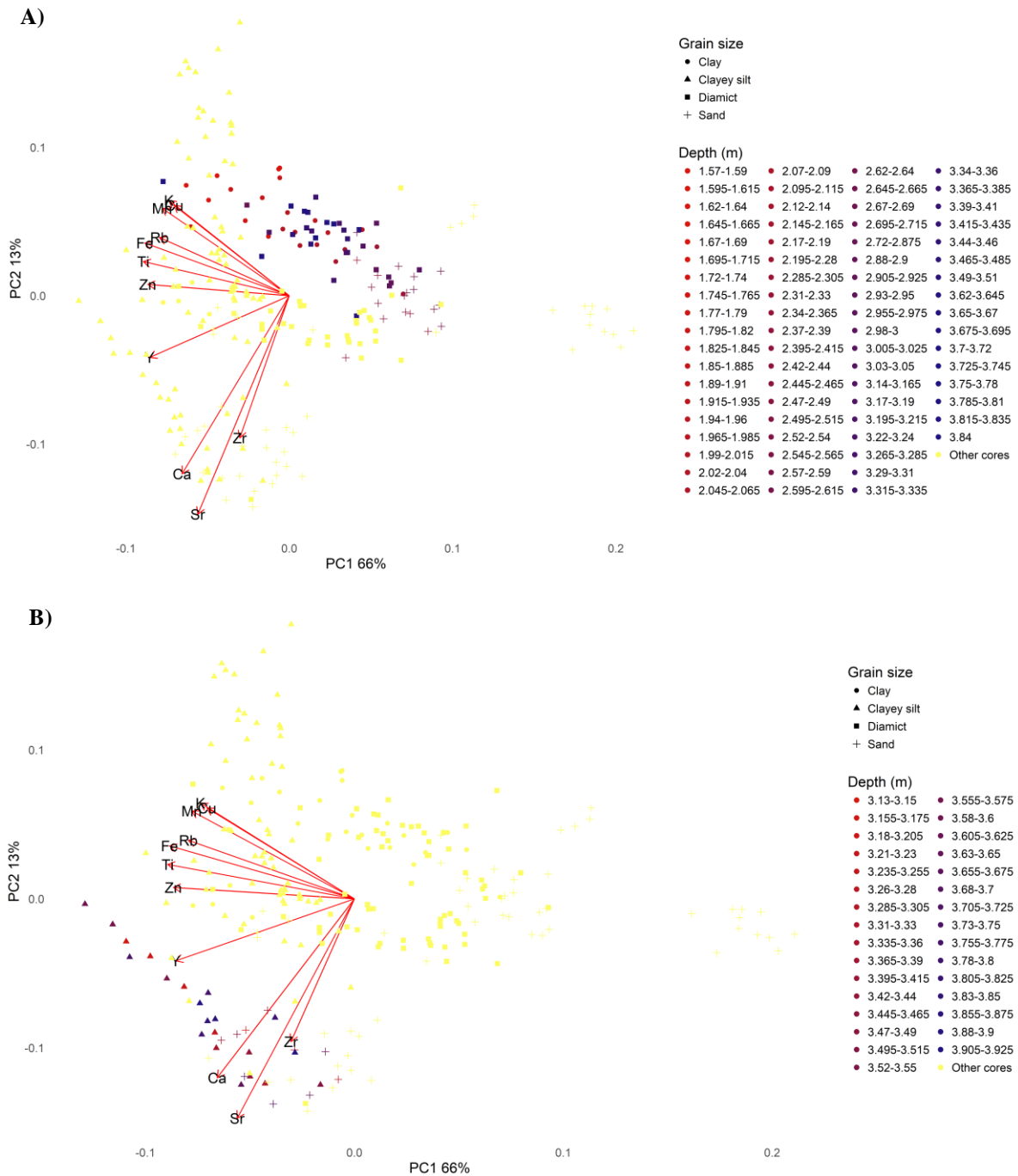
- Geochemical analysis established an age/depth gradient in MD04-2822; the 24-31 kyr BP interval has higher Ca values which likely represents the advance of the BIIS
- The Malin Sea end members plot closer to MD04-2822 than the Donegal end members
- Nearest neighbour analysis reveals that:
  - Northern Malin Sea end members are the main contributor to MD04-2822
  - The Hebrides Ice Stream and Donegal Bay Ice lobe were active from 31 kyr BP
  - After 22 kyr BP the Donegal affinity appears to only make minor contributions to MD04-2822
  - Four main influxes to MD04-2822 occur between 21-28 kyr BP; these coincide with a shelf edge position of the ice margin, deglaciation and the cessation of the Hebrides ice stream
  - A cluster identified ~14 kyr BP has been interpreted as IRD flux from a smaller regionalised marine terminating margin confined to the coastal fjords of the Inner Hebrides
  - It is possible to fingerprint IRD flux in MD04-2822 to shelf end members

### **7.3 Geochemical signature of the Minch Ice Stream sector**

#### **7.3.1 Establishing Minch Ice Stream end members**

Eight cores were analysed from the continental shelf region of the former Minch Ice Stream (only seven will be discussed due to the exclusion of JC123-031PC). The geochemical analysis of individual cores provided context for the overall geochemical pattern seen across the shelf of the former Minch Ice Stream. Grain size data from three of the seven cores are presented (Figure 7.30 and 7.31); each core is from a different region (Inner Minch, outer shelf and Cape Wrath). The analysis of JC123-015VC shows that the most proximal and most distal sediments plot together; these are diamict and clay lithofacies. On the other hand, the sand has more positive PC 1 scores. As discussed in the previous section 7.2.1 clay and diamict lithofacies will often have a similar geochemical signature because clay is the modal grain size. JC123-039VC also displays no stratigraphic gradient, however it does display a geochemical gradient between the clayey silt and sand lithofacies. In contrast, JC123-049VC displays a mix of grain size and proximal/distal sediments within the main cluster, however there is a clear geochemical separation between the main cluster and the sand unit which has high PC 1 scores. These data show that grain size can influence the geochemical signature but that this relationship varies between each individual sediment core.

When all seven cores are analysed together they show considerable overlap between the regions (Figure 7.32). The outer shelf cores are enriched in Ca, Sr and Zr in comparison to the inner Minch cores but the Cape Wrath core displays a large spread across the PC 1 axis which, from Figure 7.31, we know is from the geochemical separation of the sand unit. Fe accounts for most the variance seen across the shelf (Figure 7.33), but it does not differentiate between the regions. Geochemical similarities reflect similar catchment geology. The Scottish mainland geology is mainly Lewisian Gneiss, Torridon sandstone and the Moine supergroup (as discussed in section 7.2.1). The continental shelf on the other hand is comprised of Jurassic argillaceous rocks, Permian and Triassic conglomerate, sandstone, siltstone and mudstone and the Torridon group (Figure 7.34). The ice dispersal centre for the Minch Ice Stream would have been the Scottish Highlands (Bradwell *et al.* 2008), therefore the geochemical signature of the shelf sediments will reflect this catchment geology as well the continental shelf geology. On the shelf, there are locally thicker Plio-Pleistocene glacial sediments (more than 100 m thick) in the over-deepened basins (Bradwell and Stoker 2015) which would provide localised protection of the bedrock geology from erosion (Figure 7.35). These Plio-Pleistocene sediments were also derived from the adjacent bedrock





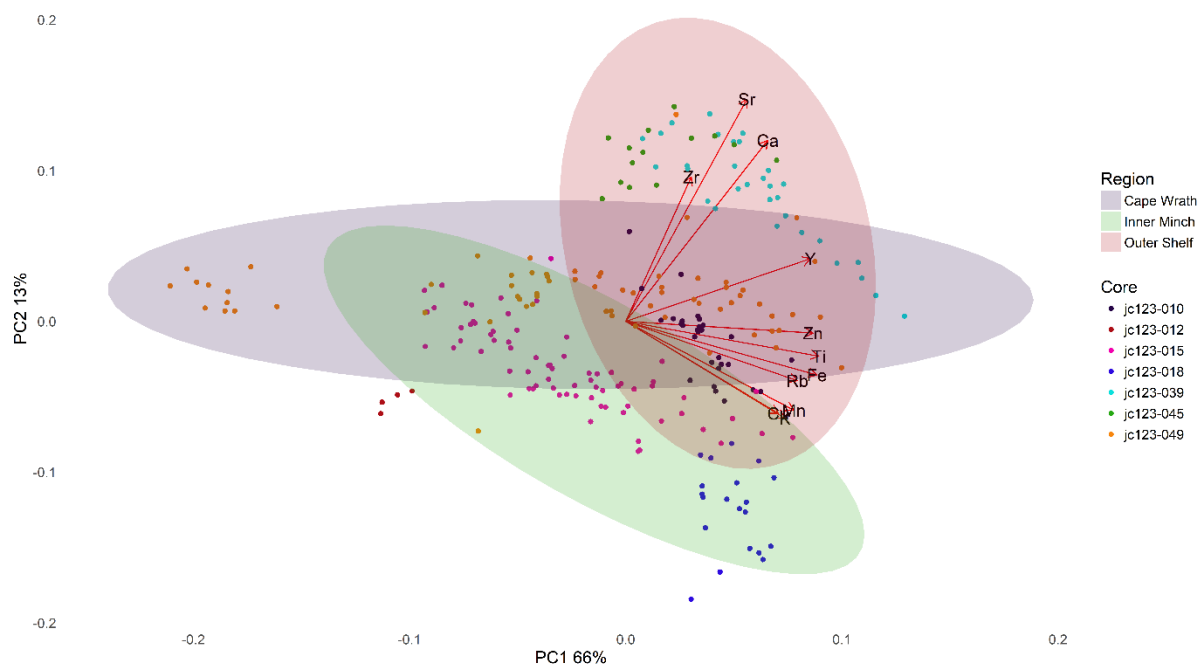


Figure 7.32 PCA biplot for the Minch Ice Stream sediment cores divided into regions. Each core and region has been colour coded.

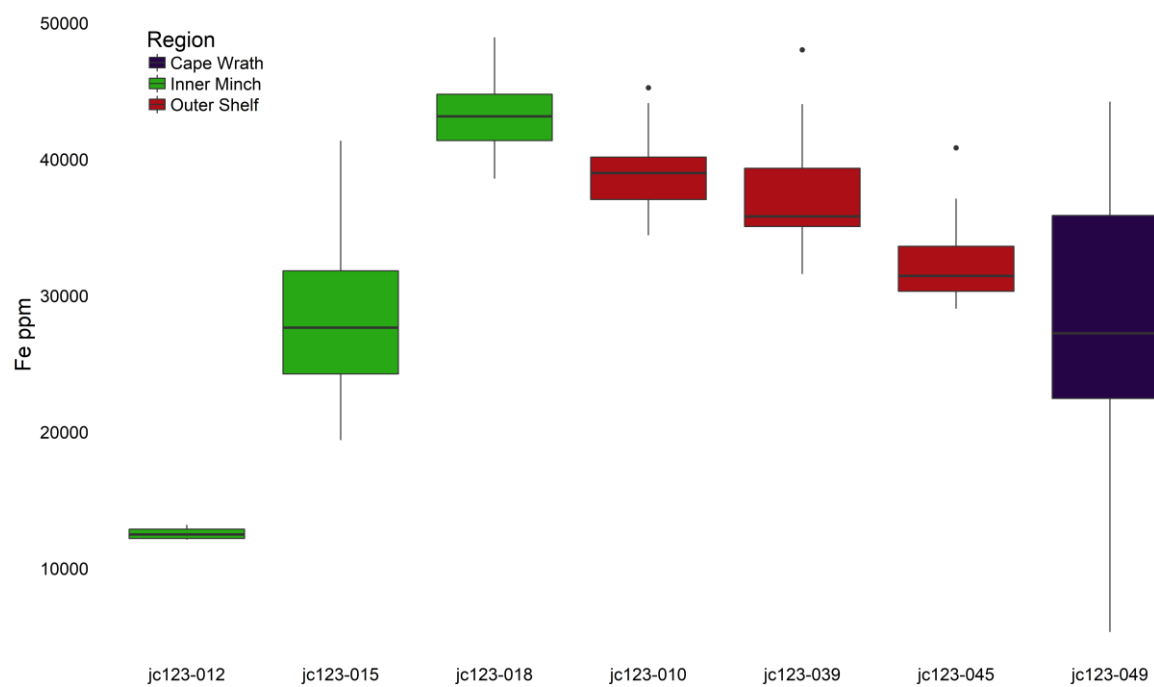


Figure 7.33 Boxplot displaying Fe concentrations of the seven sediment cores from the former Minch Ice Stream. The cores have been colour coded by region.

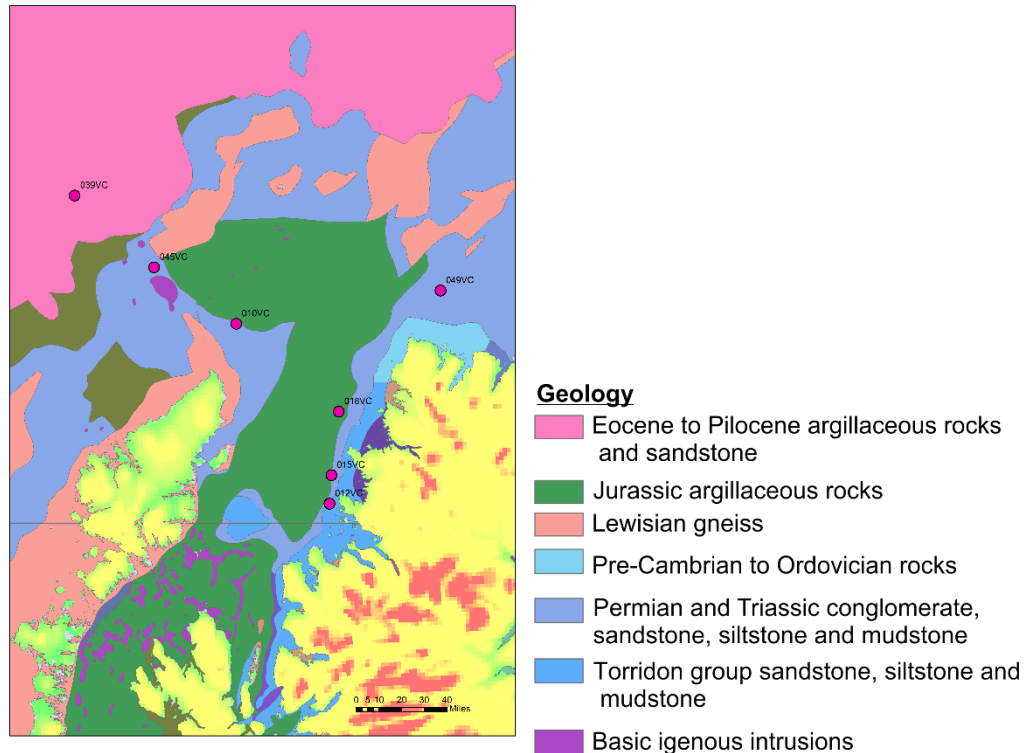


Figure 7.34 Geological map of the Minch and the Hebrides Shelf. The key illustrates the main formations present (British Geological Survey, 2008).

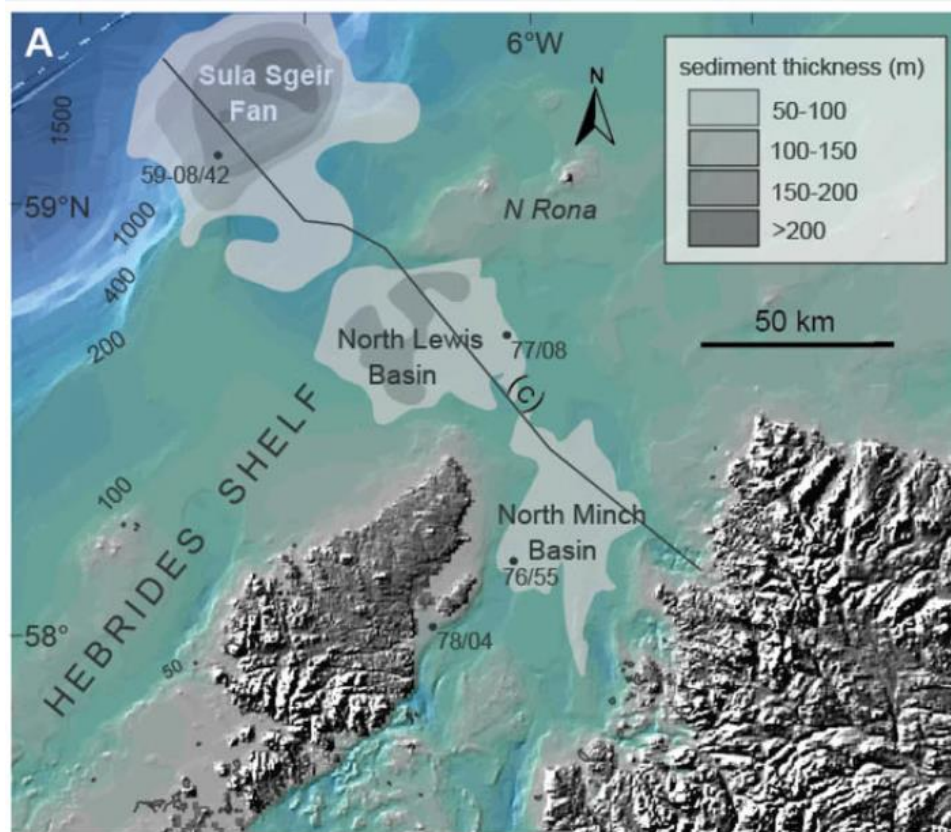


Figure 7.35 Sediment thickness map of the Minch and the Hebrides Shelf and the two main over-deepened basins (North Lewis Basin and North Minch Basin (Bradwell and Stoker, 2015).

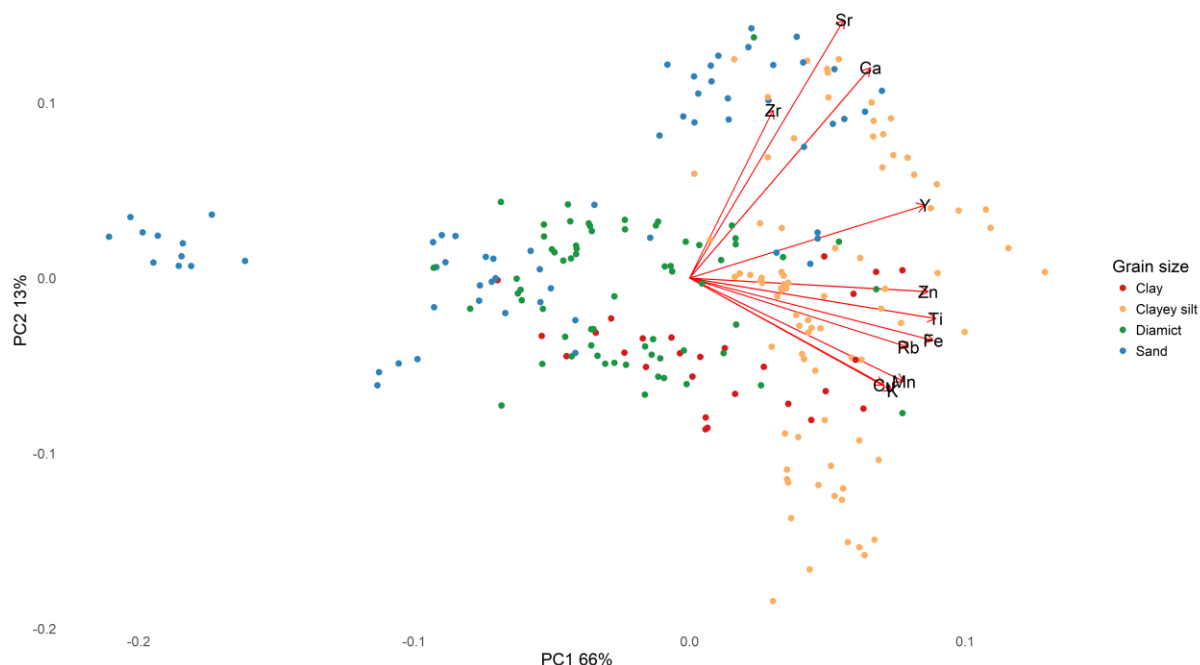


Figure 7.36 PCA biplot for the Minch Ice Stream sediment cores colour coded by grain size.

It is possible to conclude from these data that:

- There are subtle geochemical differences between the Minch regions, however there is also overlap which indicates these cores have similar catchment geology
- The geochemical signature reflects catchment geology foremost and not grain size on a catchment scale.
- Grain size influences the geochemical signature but this relationship varies between each individual sediment core.

### **7.3.2 Geochemical signature of MD04-2829CQ**

The PCA of MD04-2829CQ shows a subtle age/depth gradient (Figure 7.37). The 26-30 kyr BP group is enriched in Sr, Ca and Zr, whereas the 18-22 kyr BP group is depleted in Sr, Ca and Zr and enriched in Rb, K, Fe and Mn. Possible reasons could be a change in the predominant source of IRD. The 26-30 kyr BP interval most likely contains more detrital carbonate which could be sourced from the southerly terminating margins of the BIIS (Knutz *et al.* 2007).

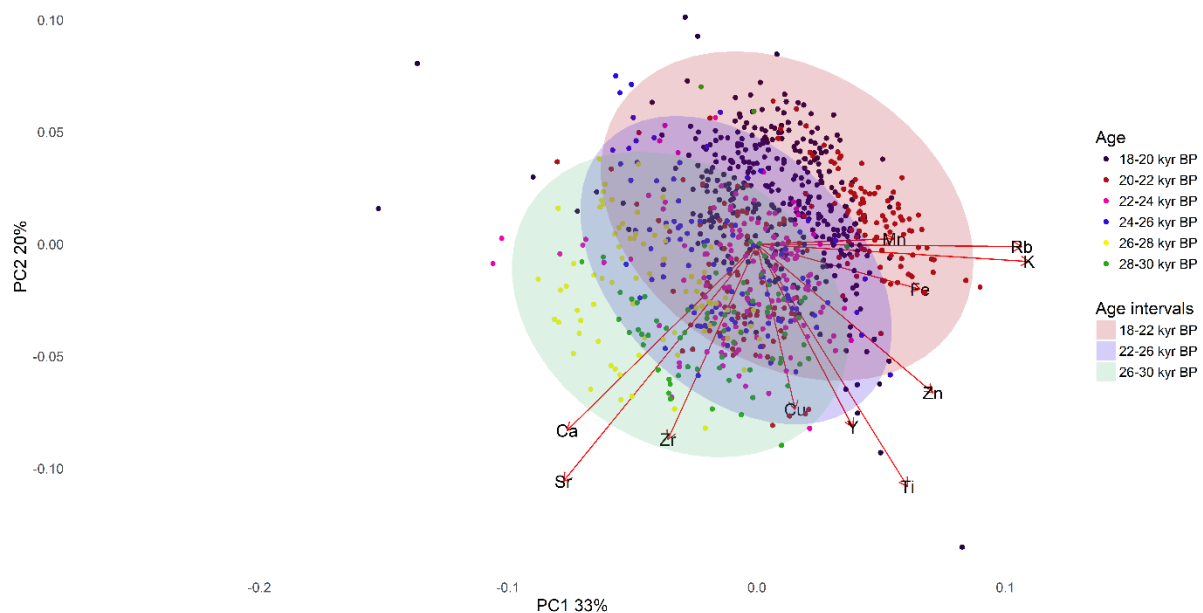


Figure 7.37 PCA biplot for MD04-2829CQ. PC 1 summarises 33% of the total variance in the dataset and PC 2 20%. The core has been colour coded by age intervals and further grouped into broader age intervals (18-22 kyr BP, 22-26 kyr BP and 26-30 kyr BP).

### **7.3.3 Exploring the geochemical relationship between MD04-2829CQ and the Minch sediment cores**

The PCA of the two datasets shows significant composition disparities between the shelf end members and the deep ocean core (Figure 7.38). The outer shelf cores and the Cape Wrath core show some geochemical overlap with MD04-2829CQ, especially the 26-30 kyr BP interval which plots closer to the shelf end members than the other age intervals. Overall, there is little similarity between the deep ocean core and the shelf sediments.



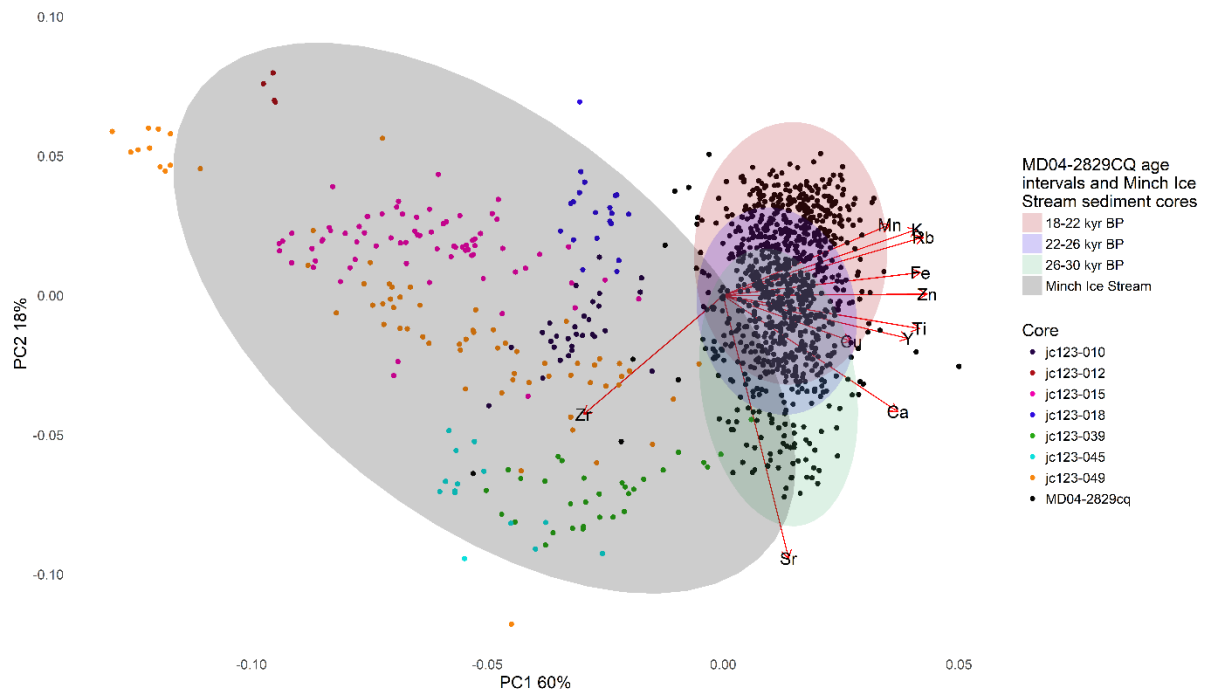


Figure 7.38 Biplot of the PCA results of MD04-2829CQ and Minch end members. PC 1 summarises 60% and PC 2 18%. The cores have been colour coded and further grouped by ellipses into broader age intervals (MD04-2829CQ) and Minch Ice Stream sediments.

It is possible to fingerprint depths within the deep ocean core to specific shelf end members. All seven cores were individually analysed by PCA with MD04-2829CQ. Data points for MD04-2829CQ were labelled by depth and, using the nearest neighbour approach, whichever depth plotted close to a shelf data point were allocated to specific end members as explained in Section 7.1.2. Figure 7.39 presents the results from this analysis. Fingerprinting analysis reveals that MD04-2829CQ can only be associated with the outer shelf and Cape Wrath cores. No geochemical similarities between the inner Minch cores and MD04-2829CQ could be identified. During the ~28 kyr BP and 26-28 kyr BP intervals MD04-2829CQ displays an outer shelf affinity (JC123-039VC). After this initial period, there is an absence of any Minch signature in the deep ocean core until ~21-22 kyr BP, (when there is a JC123-049VC affinity). After this there is another significant gap in the record until ~19 kyr BP. At ~19 kyr BP an outer shelf and Cape Wrath signature can be identified (JC123-010VC, JC123-045VC and JC123-049VC). An outer shelf signature identified at 19 kyr BP is unexpected because the Minch Ice Stream would have retreated to a near present day coastline position (Bradwell and Stoker, 2015). Consequently, because of the geochemical similarities of the Minch Ice Stream end members, this input is interpreted as reflecting a generic Minch Ice Stream IRD contribution (not specific to an outer shelf ice margin position).

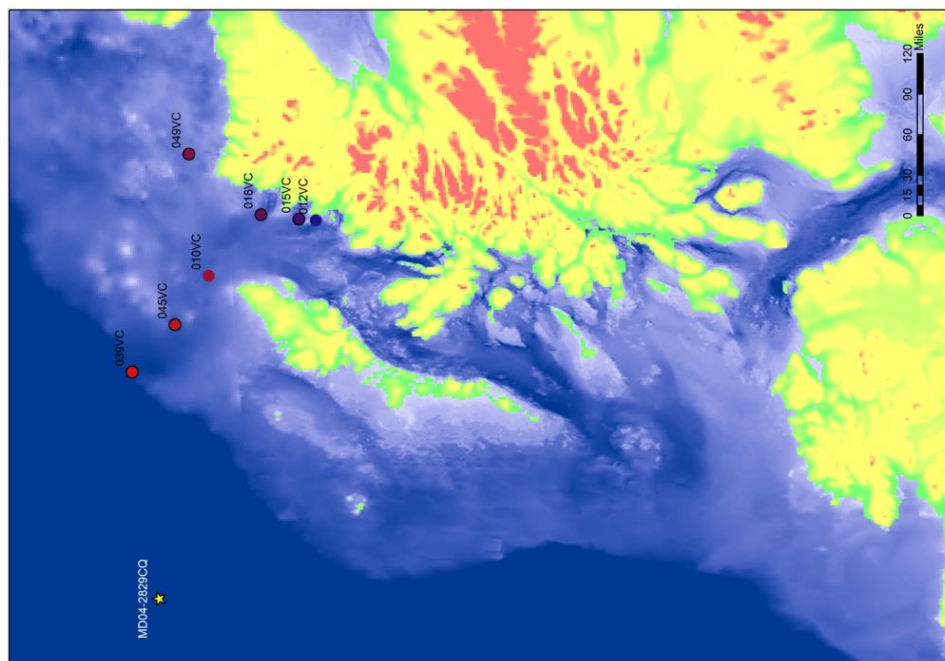
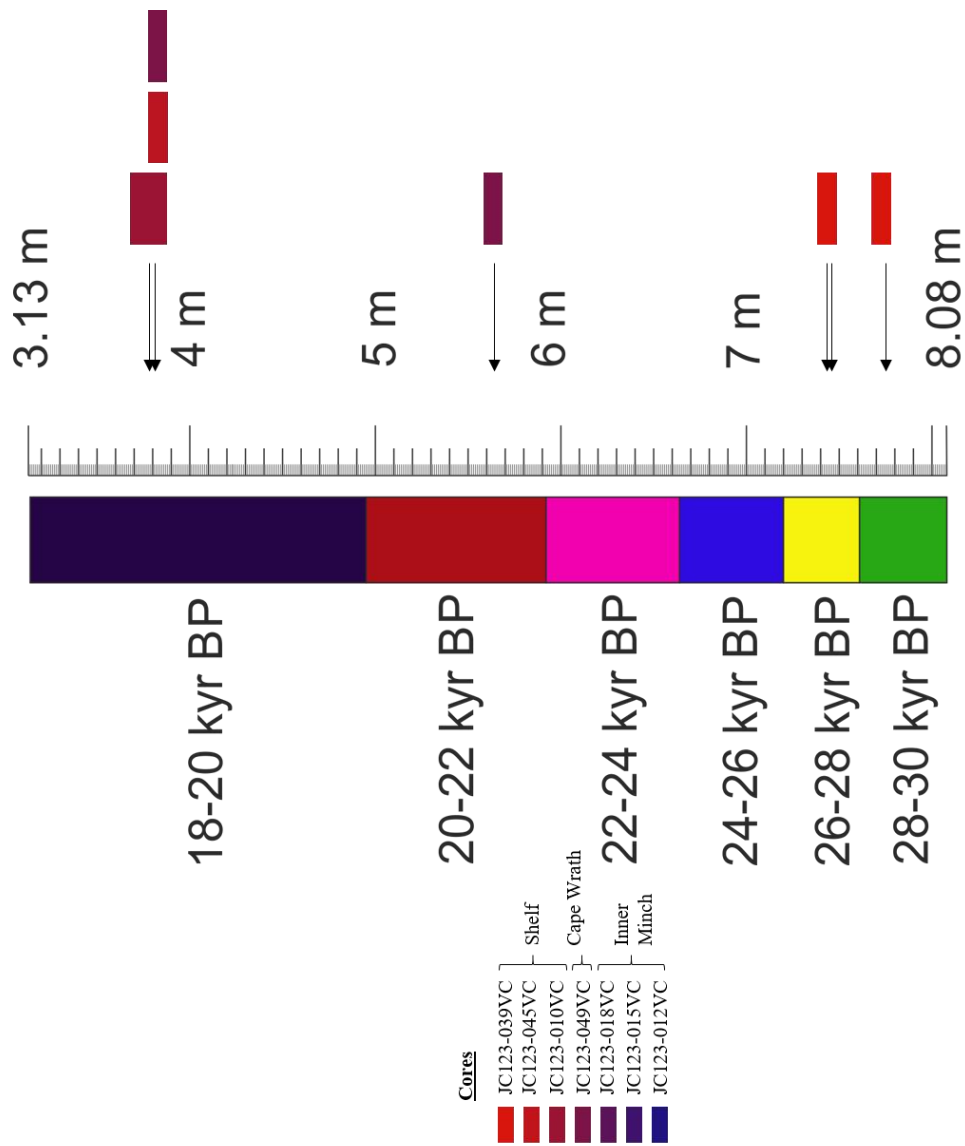


Figure 7.39 Schematic diagram displaying the location of the cores analysed and the colour that has been assigned to individual cores. Using the nearest neighbour approach, it has been possible to fingerprint depths within MD04-2829CQ to geochemically similar shelf end members.

In comparison to the other deep ocean cores and ice streams discussed in the two previous sections, this sector does not show a high degree of similarity between the deep ocean and the shelf end members. IRD has been documented at this core site previously; analysis of lithic grains indicated continuous IRD flux between 41 and 18 kyr BP (Hall *et al.* 2011). Hall *et al.* (2011) speculated that ice expansion in Western Scotland contributed to the IRD flux in the MD04-2829CQ record. From this analysis it is not possible to attribute the flux identified by Hall *et al.* (2011) to the Minch Ice Stream. Possible reasons include: 1) Minch IRD flux could be diluted by another IRD source; 2) The Minch icebergs may have deposited their load at the Sula Sgeir fan or 3) surface currents along the NW BIIS could have transported the main Minch Ice Stream contribution NE along the margin. If the Minch Ice Stream icebergs were entrained in the surface currents, it is possible that the Minch IRD contribution could have been transported and deposited in the Faroe-Shetland Channel or further NE towards the North Sea Fan (Figure 7.40).

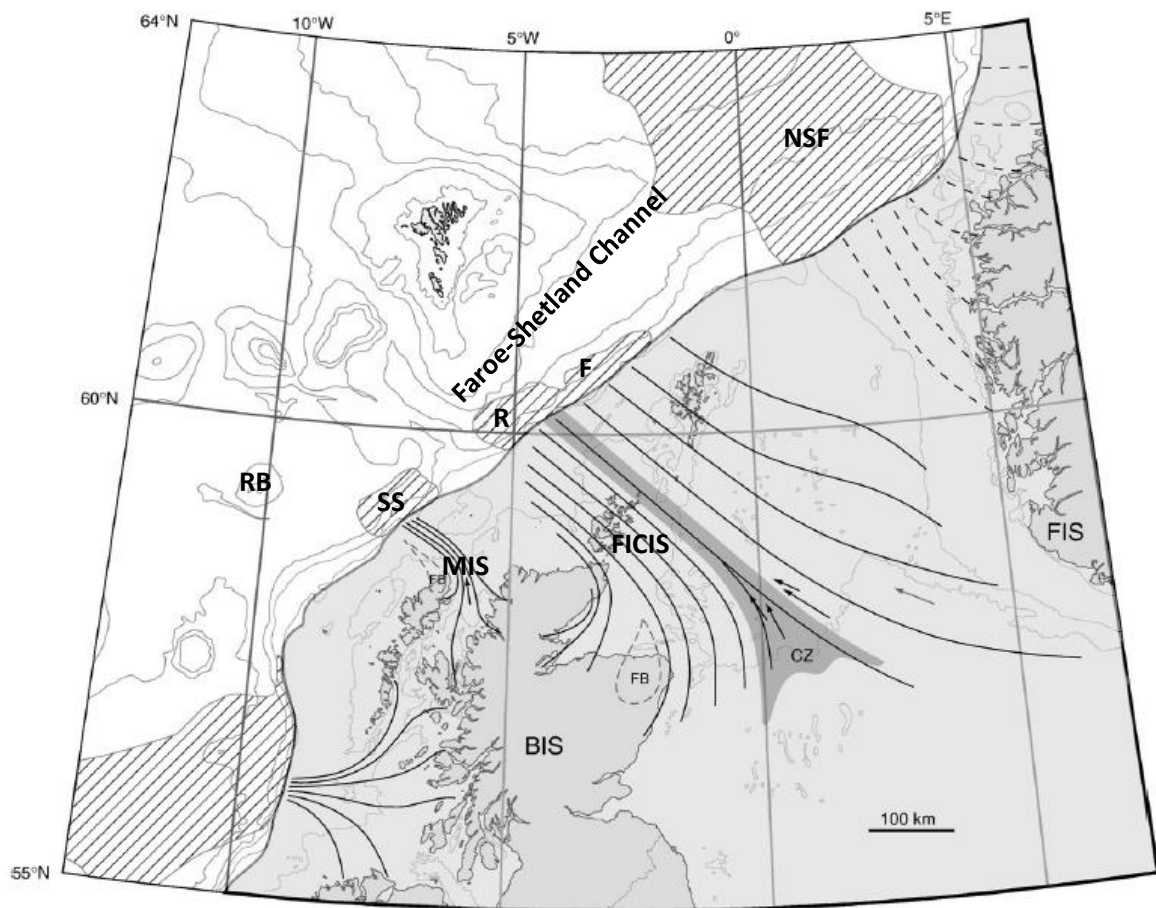


Figure 7.40 Reconstruction of the confluent British (BIS) and Fennoscandian Ice Sheets (FIS) at LGM (30–25 ka BP), with hypothesised flow lines from Bradwell *et al.* 2008. RB-Rosemary Bank; MIS-Minch Ice Stream; SS-Sula Sgeir Fan; R-Rona Wedge; F-Foula Wedge; NSF-North Sea Fan; FICIS-Fair Isle Channel Ice Stream.

Without more geochemical similarities, it is harder to relate the offshore record to the advance and retreat phases of the Minch Ice Stream. The initial period of Minch affinity sediments occurs ~28 and 26-28 kyr BP; given the ice sheet retreated from a mid-shelf position by ~25 kyr BP (Everest *et al.* 2013) this influx is interpreted as a possible ice margin advance and retreat from a more extensive shelf position. Bradwell and Stoker (2015) interpret the moraine complexes that occur in the coastal waters from Cape Wrath to Loch Ewe as evidence of a stillstand of the grounded ice sheet margin between 16-22 kyr BP. The Minch signature in MD04-2829CQ at 21-22 kyr BP could indicate the establishment of this grounded position. Iceberg calving has been associated with the rapid retreat of the Minch Ice Stream (Bradwell and Stoker, 2015) and iceberg scours have also been identified in the central Minch area (Inner Minch). These assertions demonstrate that the Minch Ice Stream produced icebergs but their flux is not clearly recorded geochemically in MD04-2829CQ. Possible reasons for this will be explored later. It is possible to conclude from these data that:

- Geochemical analysis established an age/depth gradient in MD04-2829CQ; the 26-30 kyr BP interval has higher Ca, Sr and Zr values which has been interpreted as representing an increase in detrital carbonate from a southerly BIIS terminating margin
- This sector does not show a high degree of similarity between the deep ocean and the Minch end members. Possible reasons include: 1) Minch IRD flux could be diluted by another IRD source; 2) The Minch icebergs may have deposited their load at the Sula Sgeir fan or 3) surface currents along the NW BIIS could have transported the main Minch Ice Stream contribution to other areas NE along the margin
- The 26-30 kyr BP interval of MD04-2829CQ plots closer to the shelf end members, particularly the outer shelf and Cape Wrath cores
- Nearest neighbour analysis reveals that:
  - The outer shelf and Cape Wrath cores are the main contributor to MD04-2829CQ
  - Minor contributions are interpreted as reflecting ice margin retreat from an outer shelf position
  - It is possible to fingerprint IRD flux in MD04-2829CQ to shelf end members

#### **7.4 Integration of all ice stream XRF data**

One of the aims of this study was to explore geochemical variation between the three ice streams. Analyses to address this aim will be presented in the following section.

The PCA plot examining the geochemical signature of the three ice streams demonstrate that there is significant overlap (Figure 7.41). When determining provenance of IRD, it is necessary that the sources can be discriminated geochemically (Andrews *et al.* 2014); some overlap is expected, but reliable provenance allocation requires a reasonable degree of discrimination. The PCA plot of the three ice streams does not display geochemically discriminant sources. Subdividing the data into key end members improves the delineation of the sources but there is still overlap (Figure 7.42). The ISIS has been subdivided into the Celtic Sea and Irish Sea end members; and the Hebrides Ice Stream and Donegal Bay Ice lobe has been subdivided into the Malin Sea and Donegal end members respectively. The Minch Ice Stream has not been subdivided, because there is little geochemical differentiation between the three regions (Inner Minch, Cape Wrath and Outer Shelf). Geochemical similarities between the end members within the BIIS may be due to similarities of the catchment geology. There is large geochemical variability between the two ISIS end members which most likely reflects the very geochemically distinct catchment geologies of the region (Upper Cretaceous chalk vs Permo-Triassic sandstone). The Celtic Sea is enriched in Ca and Sr and the Donegal end members also plot along the Ca and Sr vector; this supports the interpretation of Upper Cretaceous chalk and Carboniferous limestone influence on the geochemical signature of these end members. The Malin Sea end members have positive PC 1 scores, and share geochemical similarities with the Donegal, Irish Sea and Minch end members. This overlap is to be expected because ice flow into the Malin Sea would have originated in the Scottish Highlands (therefore similar catchment to the Minch Ice Stream), Northern Ireland (Tertiary Basalts) and the North Channel (Old Red Sandstone, as in the Irish Sea end member) (Dove *et al.* 2015). The PCA plot also displays geochemical similarities between the Minch end member and the Irish Sea end member (Figure 7.42). Similar elemental assemblages most likely reflect the similar mineralogy of the Permo-Triassic sandstone of the Irish Sea catchment and the Torridon group of the Minch catchment (British Geological Survey, 2008). These sandstones have different ages, however they would both be enriched in Fe.

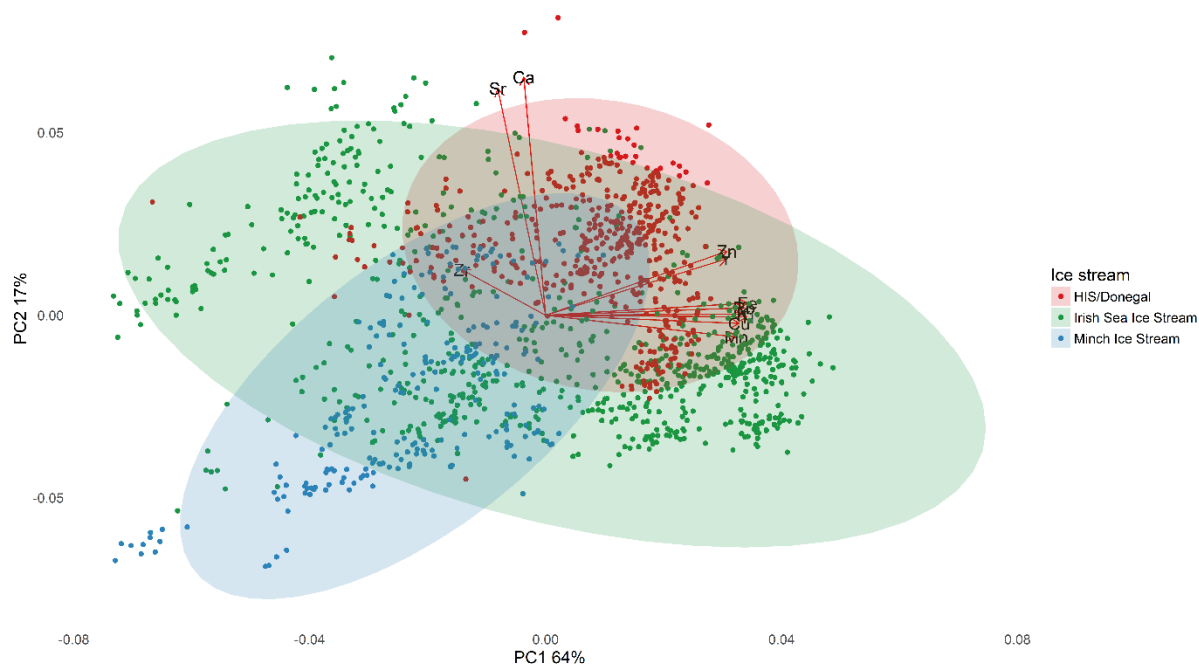


Figure 7.41 Biplot illustrating the PCA results obtained by integrating XRF data from each ice stream. PC 1 explains 64% of the variance and PC 2 17%. Each ice stream has been colour coded.

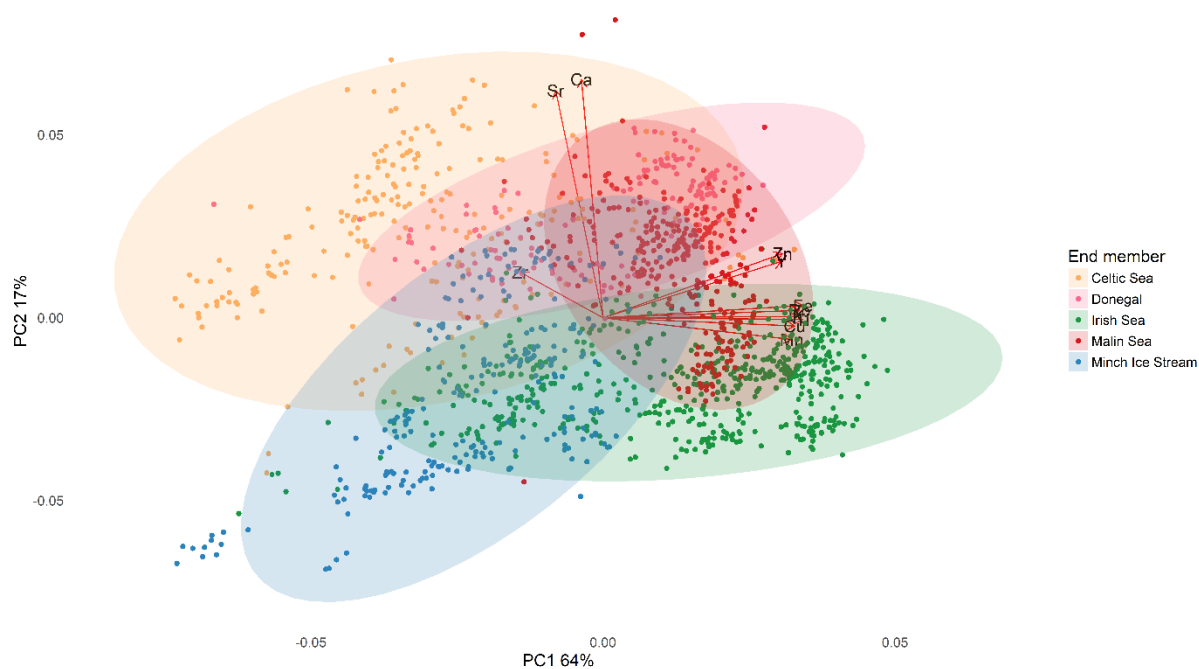


Figure 7.42 Biplot illustrating the PCA results obtained by integrating XRF data from each ice stream. PC 1 explains 64% of the variance and PC 2 17%. Each ice stream has been subdivided into end members. These end members have been colour coded.

## **Summary**

The use of XRF has determined the geochemical variation of the three ice streams and their end members. Comparisons of their geochemistry permits this study to assess their validity as sources. Subdivision into end members has demonstrated their provenance signatures, however, similar catchment geologies/mineralogy governed by ice stream flowpaths inhibit the identification of truly discriminant sources. Arosio *et al.* 2017 (in press) also encountered considerable geochemical overlap for the Hebrides Ice Stream, particularly when differentiating between the Moine and Torridonian rocks. Arosio *et al.* (2017) use discriminant function analysis (DFA) to improve differentiation between the two provenance groups, this technique does not allow complete separation however the DFA does improve distinction.

## **7.5 Integration of the XRF data from the three deep ocean cores**

One of the aims of this study was to determine the geochemical variability of the deep ocean cores. This largely relates to the internal variability of each core which has been previously demonstrated (Chapters 4, 5 and 6), however it is also important to address geochemical contrasts between the deep ocean cores.

The PCA of all three deep ocean cores demonstrates a tightly clustered relationship, excluding the two MD04-2820CQ arms (Figure 7.34). The PCA excludes the Heinrich events from MD04-2820CQ. The central cluster of the three cores demonstrates their similar geochemistry. During the 38-14 kyr BP interval, the geochemical signature of these cores will be chiefly determined by the lithic input generated by the expanding BIIS (Scourse *et al.* 2009) as well as the biogenic input from the water column. Minor compositional variations most likely reflect the degree of contribution from the various ice streams.

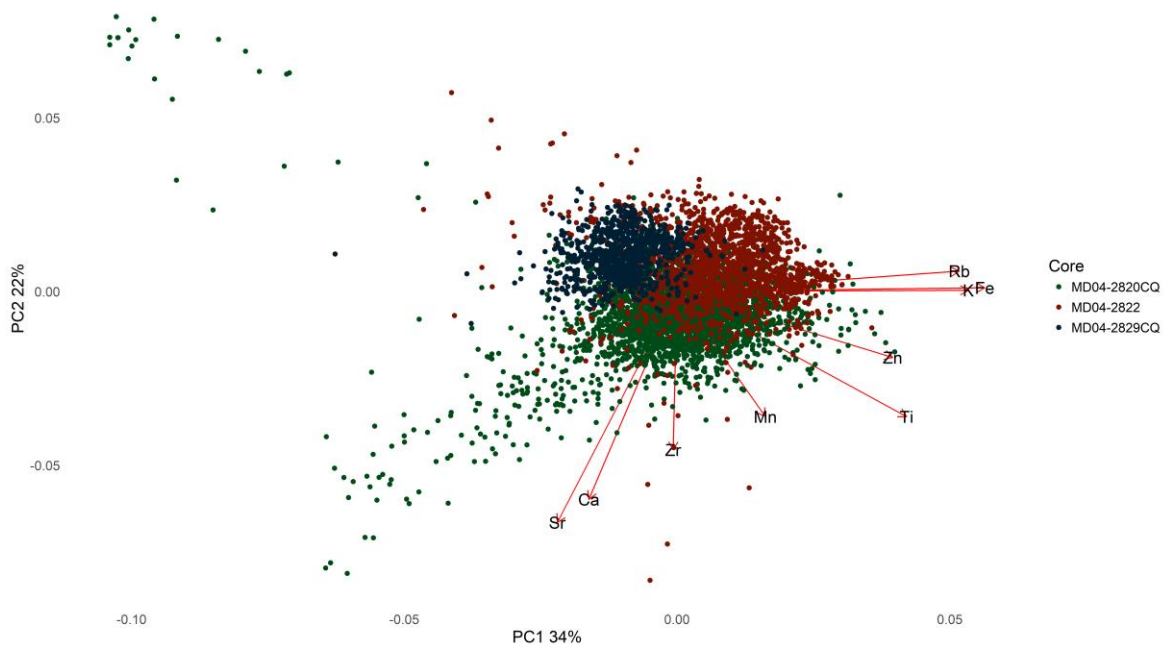


Figure 7.43 Biplot illustrating the PCA results obtained by integrating the XRF data from the three deep ocean cores excluding the Heinrich events in MD04-2820CQ. PC 1 summarises 34% of the variance and PC 2 22%. Each core has been colour coded.

## 7.6 Synthesis

One of the aims of this study was to determine whether the offshore IRD record can be attributed to the shelf glacigenic end members. Analysis thus far has focused on linking IRD flux in the deep ocean cores to the most proximal ice stream. This section addresses the contribution of non-adjacent ice streams to the IRD flux in the three deep ocean cores.

IRD flux in the deep ocean is governed by a number of factors: the presence of a marine margin; the rate of iceberg calving; iceberg sediment load; ocean and ice temperature and the strength and direction of wind/surface currents (Scourse *et al.* 2009; Hibbert *et al.* 2010). Using patterns of IRD deposition across the North Atlantic, Ruddiman (1977) and Grousset *et al.* (1993) determined that an anti-clockwise subpolar surface gyre was active during the LGM, consequently icebergs from the BIIS would have been entrained northwards (Scourse *et al.* 2009). This suggests that the deep ocean cores along the margin will receive flux from their proximal ice streams but there will also be a dilution of source material by other more southerly ice streams. In this scenario, MD04-2820CQ would receive IRD sourced from the ISIS, whereas MD04-2822 would receive IRD contribution from the Hebrides Ice Stream, Donegal Bay ice lobe and the ISIS; MD04-2829CQ on the other hand would contain IRD originating from the Hebrides Ice Stream, Donegal Bay lobe and the ISIS. These scenarios can be tested



by reviewing the contribution of the three ice streams to non-adjacent deep ocean cores using the fingerprinting analysis demonstrated in Sections 7.1.3, 7.2.3 and 7.3.3.

### **7.6.1 MD04-2820CQ and the Hebrides Ice Stream and Donegal Bay end members**

MD04-2820CQ was the most southerly deep ocean core analysed and is located somewhat north of the likely ISIS terminus (Figure 7.44). A northerly mean current flow suggests the ISIS would have been the main contributor to IRD flux, which was demonstrated by the fingerprinting analysis in Section 7.1.3. New analysis, fingerprinting MD04-2820CQ to the Hebrides Ice Stream and Donegal Bay sediment cores indicates there is also a Hebrides Ice Stream and Donegal Bay contribution to the Goban Spur (Figure 7.44). Analysis shows minor contribution from 5.24-3.14 m, however pre-H2 and post-H2 there is a significant contribution from both the Hebrides Ice Stream and Donegal Bay. Post-H2, Donegal Bay affinity is more abundant yet, from 1.85-1.72 m there is both a Donegal Bay and Hebrides Ice Stream signature before the cessation of both contributions. The apparent southward trajectory of these icebergs does not support a northerly mean current flow. This result however, does support the iceberg modelling by Bigg *et al.* (2012).

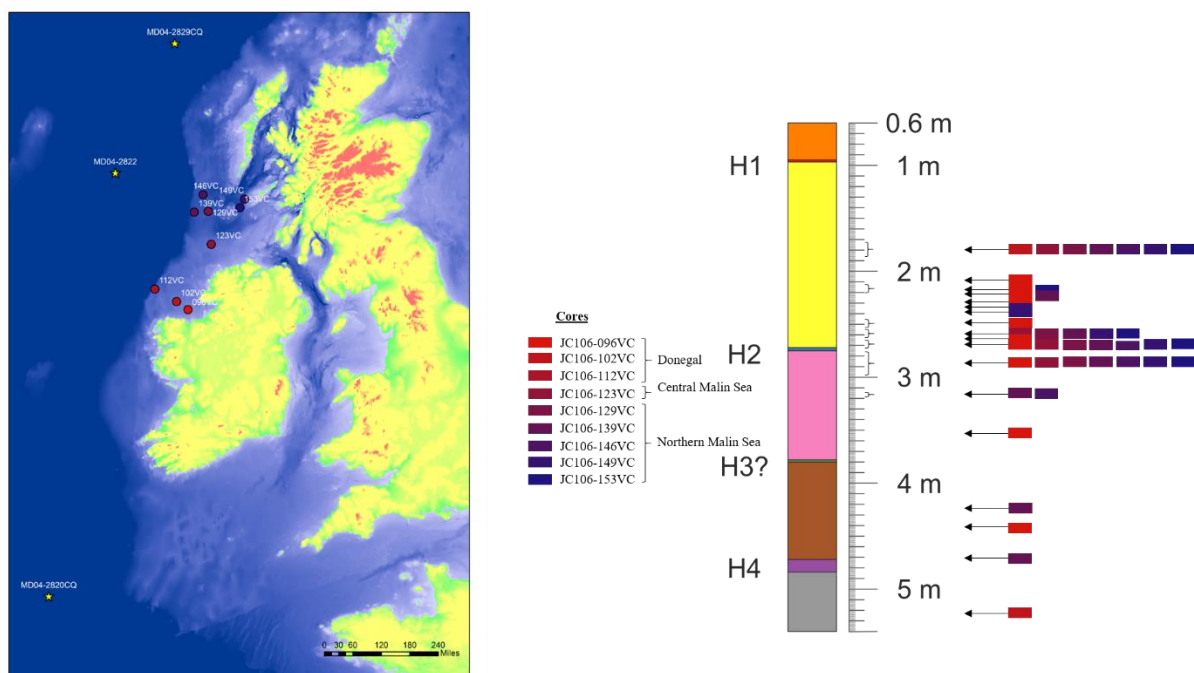


Figure 7.44 Schematic diagram displaying the location of the cores analysed and the colour that has been assigned to individual cores. Using the nearest neighbour approach, it has been possible to fingerprint depths within MD04-2820CQ to geochemically similar shelf end members from the Hebrides Ice Stream and Donegal Bay.

Bigg *et al.* (2012) use a coupled ocean-atmosphere-sea ice and iceberg model; this model has been updated to a higher resolution version for BRITICE CHRONO (Figures 7.45 and 7.46; Bigg pers. comm. 2017). This intermediate complexity climate model, Frugal (Fine ResolUtion Greenland And Labrador model) uses a curvilinear coordinate system with the North Pole placed in Greenland, thus improving the model resolution in the North Atlantic. The ocean model has a free surface and has 19 vertical levels (the upper two levels are ~15 m and ~45 m which represent the surface current flow). Temperature and salinity mixing have components in the horizontal, vertical and along isoneutral surfaces, values of mixing coefficients were taken from England (1993). Topography and sill depths were constructed from ETOPO (1986) and Thompson (1995), and were altered for the LGM (21-19 kyr BP) according to Peltier (1994) and with 120 m of sea level lowering (Fairbanks, 1989). The atmospheric part is a simple radiative-advective atmosphere that allows for the advection of water vapour and includes clouds, mountains, land-ice and land hydrology. The simulations use a monthly varying wind stress, which has no feedback from sea surface temperature (SST) field, with basic wind stress taken from present day climatological values but adjusted for the LGM by wind stress from atmospheric General Circulation Model (GCM) simulations by Dong and Valdes (1998). This study is focusing on the surface currents active during the LGM (see Bigg *et al.* 2012 for further information on the iceberg component of the model). The LGM control simulation was initiated with a uniformly cold ocean ( $-2^{\circ}\text{C}$ ) with global mean salinity 34.73 psu. An additional freshwater flux of 1.5 mm per day is added at a latitude band of  $60-75^{\circ}\text{N}$  over the Atlantic Ocean, to generate intermediate water formation in the North Atlantic. The control simulation discussed in Bigg *et al.* (2010) is consistent with palaeo-oceanographic evidence such as the distribution of IRD in the North Atlantic. The two figures used in this study (Figures 7.45 and 7.46) were generated at the end of a spin-up phase (year 1000) and includes the new BRITICE-CHRONO shelf configuration. The model indicates the mean flow is northward from Northern Ireland for both levels (level 1 ~15 m and level 2 ~45 m depth). Level 1 on the other hand, indicates southward flow along the Irish coast, which might explain the transport of Hebrides Ice Stream and Donegal Bay icebergs to the MD04-2820CQ core site. There are limitations that need to be considered when using palaeo-ocean-current modelling, these include uncertainties associated with our understanding of North Atlantic Ocean circulation during the LGM. The strength of the Atlantic Meridional Overturning Circulation (AMOC) is still contested in the literature (Lippold *et al.* 2012) as discussed in Section 1.7. The Bigg *et al.* model includes intermediate water formation and therefore makes assumptions on the strength of the AMOC during the LGM. The strength of the AMOC also effects the

positioning of the North Atlantic Current (NAC). Watkins *et al.* (2007) suggests that the NAC was displaced south of 42°N during the LGM and that North Atlantic circulation was dominated by a cyclonic central North Atlantic gyre. Surface current direction along the UK and Irish coast is controlled by the positioning of the bifurcation of the NAC. Scourse *et al.* (2009) proposed the meridional migration of the North Atlantic Polar Front (NAPF) during the last glacial period. The NAPF is positioned north of the sub-polar gyre, therefore the meridional migration of the NAPF will be coupled with the migration of the sub-polar gyre and the bifurcation. This migration will control the iceberg trajectories along the Irish coast, however it would be difficult for any model to capture the bifurcation of the NAC especially with possible meridional migration. The model is also limited by estimates of atmospheric forcing obtained from the atmospheric circulation models (Watkins *et al.* 2007). The Frugal model has been calibrated by evaluating its performance when compared to actual observations. The model has successfully modelled Present Day (Bigg *et al.* 2005) and LGM conditions (Bigg *et al.* 1998; Bigg *et al.* 2010; Bigg *et al.* 2012) and shows good agreement with palaeoceanographic evidence. For this reason, this thesis will include the model outcomes as a method of discussing and exploring possible trajectories of icebergs calving from the BIIS.

#### **7.6.2 MD04-2820CQ and the Minch Ice Stream end members**

Fingerprinting analysis of MD04-2820CQ and the Minch Ice Stream sediment cores indicates a very minor contribution to this deep ocean core (JC123-039VC and JC123-049VC; Figure 7.47). Minch Ice Stream icebergs surviving North Atlantic circulation to melt and deposit IRD at the Goban Spur core site is hard to explain by ocean circulation. The similarities of the geochemical signature of the Torridon sandstone and the Permo-Triassic sandstone of the Irish Sea means that it is possible that the depths in MD04-2820CQ that show a Minch affinity are actually sourced from the Irish Sea end member.

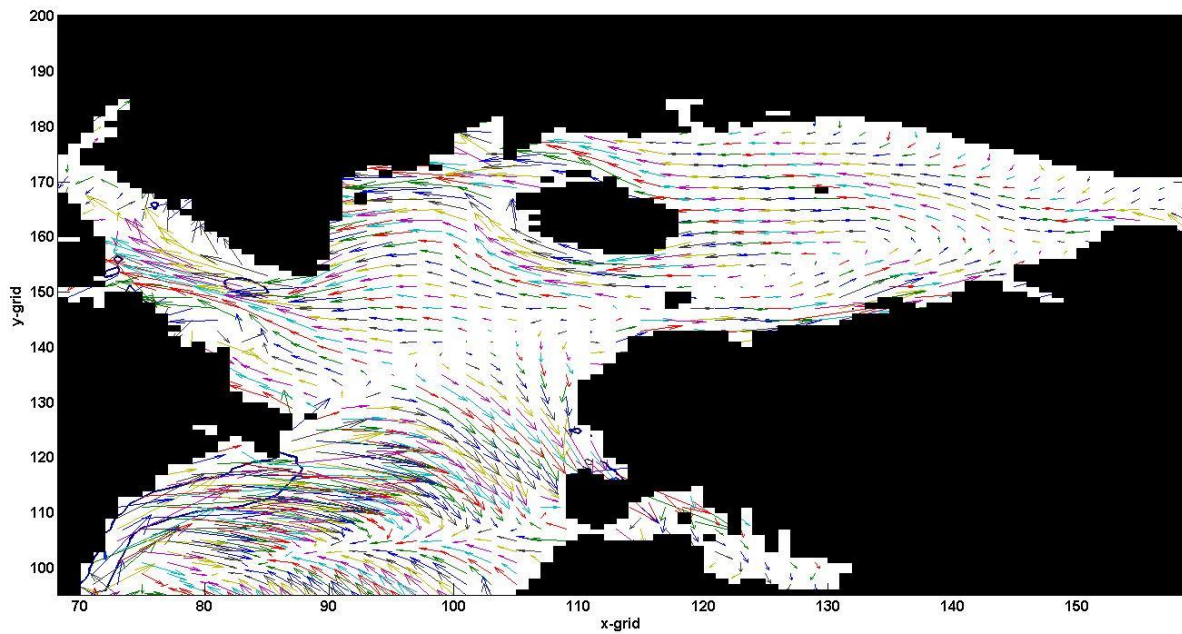


Figure 7.45 Annual mean surface currents for level 1 (~15 m depth). Note the currents and land masses have been interpolated onto a regular latitude-longitude grid for ease of presentation (Bigg 2017, pers. comm.).

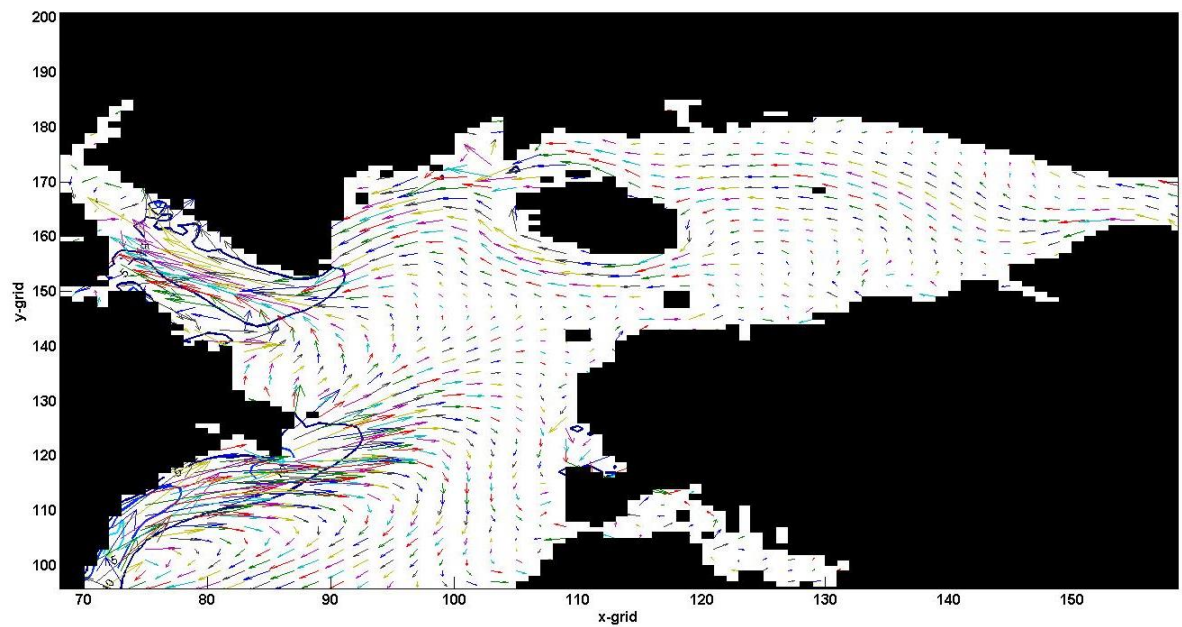


Figure 7.46 Annual mean surface currents for level 2 (~45 m depth). Note the currents and land masses have been interpolated onto a regular latitude-longitude grid for ease of presentation and the additional almost exposed land compared to Figure 7.45 is Rockall Bank (Bigg 2017, pers. comm.).

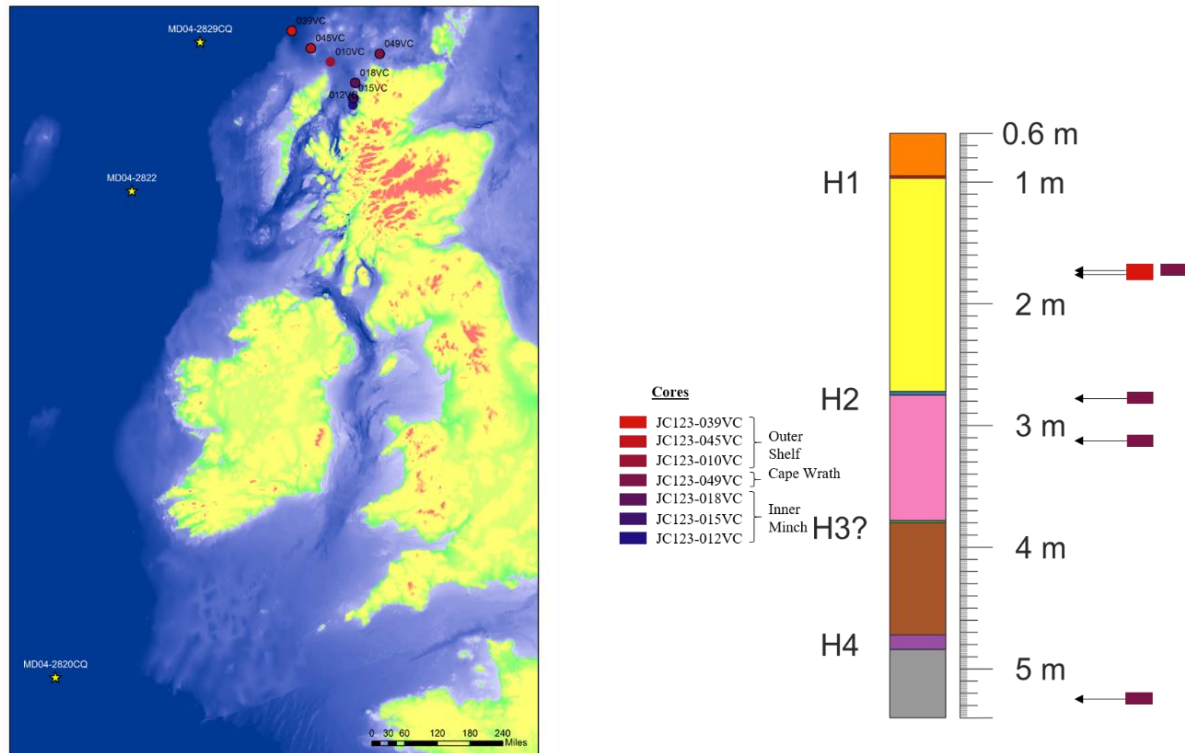


Figure 7.47 Schematic diagram displaying the location of the cores analysed and the colour that has been assigned to individual cores. Using the nearest neighbour approach, it has been possible to fingerprint depths within MD04-2820CQ to geochemically similar shelf end members from the Minch Ice Stream.

### 7.6.3 MD04-2822 and the Irish Sea Ice Stream end members

Analysis of MD04-2822 and the ISIS end members shows a sporadic ISIS affinity throughout the 14-30 kyr BP interval (Figure 7.48). From 17.65-10 m the ISIS contribution reflects the Celtic Sea end member, whereas from 8.09-5.18 m the Irish Sea end member is the main contributor. Most of the Celtic Sea affinity occurs within the 20-26 kyr BP interval and likely represents the advance of the ISIS into the Celtic Sea. This also supports the earlier interpretation of the high Ca and Sr in MD04-2822 representing detrital carbonate IRD from the BIIS (Section 7.2.2). The Celtic Sea input ~28 kyr BP is slightly earlier than expected, however new chronological data presented by Smedley *et al.* (2017), demonstrate ice advance onto the northern Isles of Scilly at ~26 kyr BP, which would account for this earlier influx. The Irish Sea end member contribution (15-18 kyr BP) is interpreted as representing the retreat of the ISIS into the northern Irish Sea region which is supported by the Chiverrell *et al.* (2013) Bayesian analysis. ISIS contribution to MD04-2822 contradicts the modelled level 1 iceberg trajectories (Figure 7.45). The reason for this northward trajectory of icebergs, most likely reflects the changing position of the bifurcation of the North Atlantic Current (Bigg 2017, pers. comm.). A more southerly bifurcation would result in the northward flow of icebergs from the ISIS. The timing of the migration of this bifurcation based on the flux to MD04-2822 suggests



a millennial migration. In the absence of an age model for MD04-2820CQ it is harder to constrain the timing of flux to MD04-2820CQ, however because of the millennial pattern illustrated in MD04-2822, it is reasonable to assume this millennial pattern will also affect MD04-2820CQ.

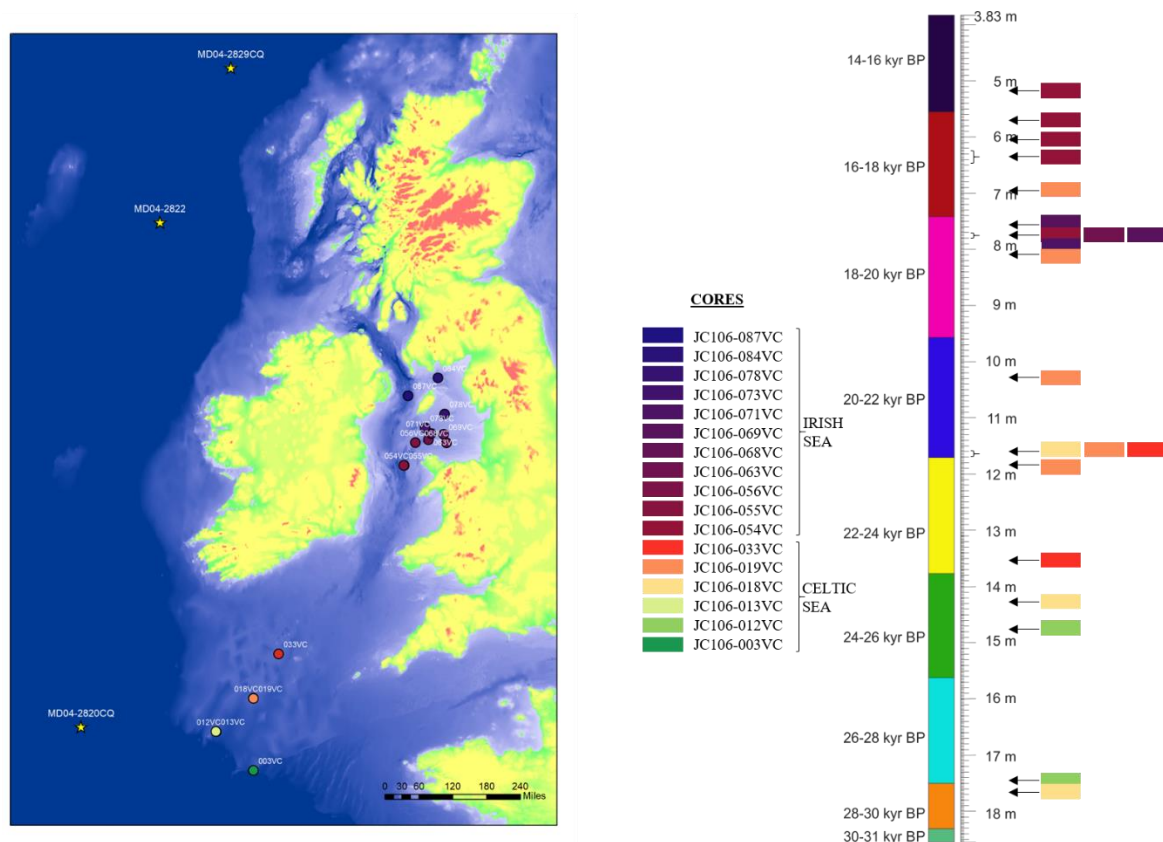


Figure 7.48 Schematic diagram displaying the location of the cores analysed and the colour that has been assigned to individual cores. Using the nearest neighbour approach, it has been possible to fingerprint depths within MD04-2822 to geochemically similar shelf end members from the ISIS.

#### **7.6.4 MD04-2822 and the Minch Ice Stream end members**

There is a limited contribution from the Minch Ice Stream to MD04-2822 (Figure 7.49). The Minch affinity occurs sporadically during the 24-14 kyr BP interval. From 24-18 kyr BP the flux is mainly from the Inner Minch and Cape Wrath regions and the 14 kyr BP contribution is from the Outer Shelf region. The 24-18 kyr BP input most likely reflects the retreat of the ice stream to coastal waters as supported by Bradwell and Stoker (2015). The origin of 14 kyr BP outer shelf input on the other hand is unknown, because at this stage the ice would have been less extensive, i.e. not positioned on the outer shelf (Ballantyne and Stone 2012). Previous analysis has not been able to geochemically differentiate between the Minch regions,

consequently this contribution is interpreted as generic Minch IRD flux. In Section 7.2.3, fingerprinting analysis of MD04-2822 to the Hebrides Ice Stream and Donegal Bay end members also identified a cluster ~14 kyr BP; this cluster had a Hebrides Ice Stream signature and was interpreted as IRD flux from a smaller regionalised marine terminating margin confined to the Inner Hebrides. Consequently, this Minch ~14 kyr BP contribution is also interpreted as indicating the flux of IRD from a smaller regionalised marine terminating margin confined to the Inner Hebrides. These data indicate that either Minch Ice Stream icebergs were occasionally entrained in the surface currents and melted over the MD04-2822 core site, or due to end member geochemical similarities these depths could be attributed to other sources such as the Malin Sea or Fe-rich Irish Sea end members.

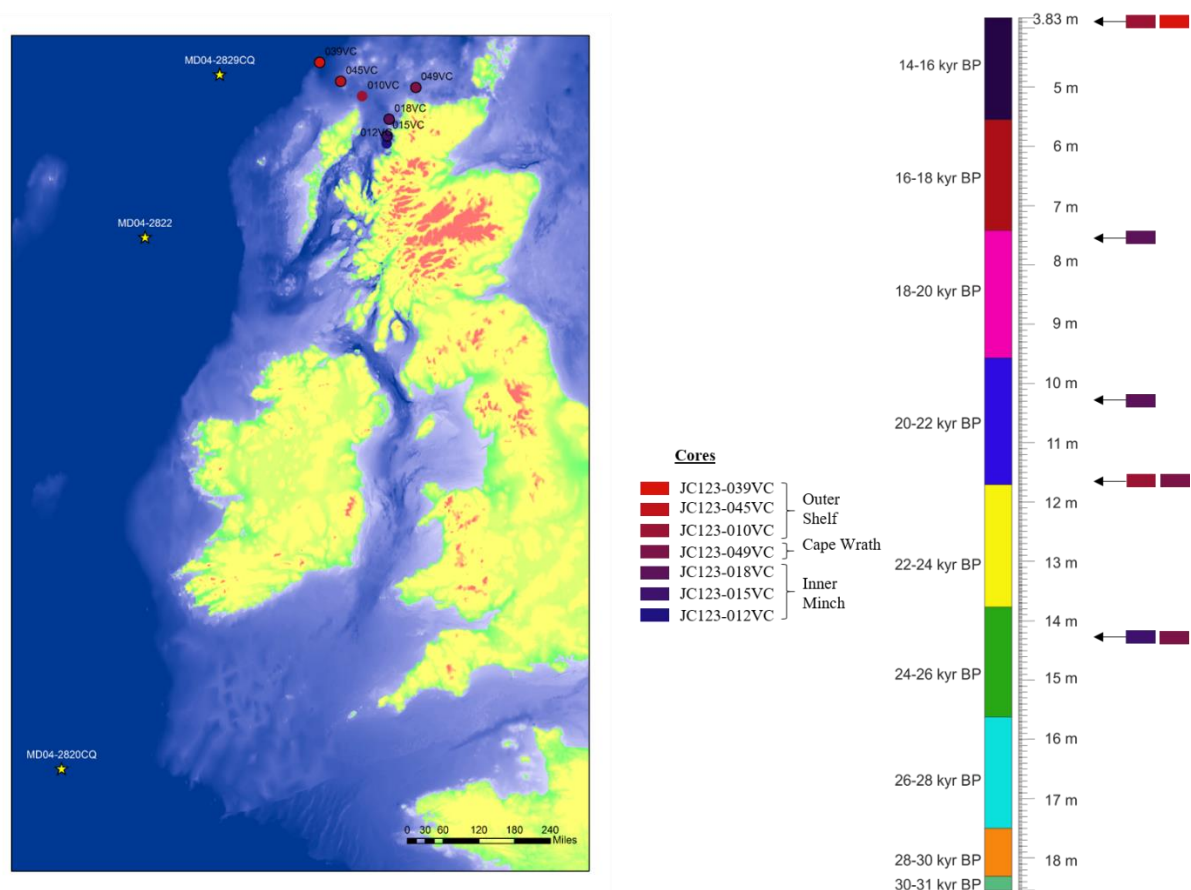


Figure 7.49 Schematic diagram displaying the location of the cores analysed and the colour that has been assigned to individual cores. Using the nearest neighbour approach, it has been possible to fingerprint depths within MD04-2822 to geochemically similar shelf end members from the Minch Ice Stream.

### **7.6.5 MD04-2829CQ and the Irish Sea Ice Stream end members**

Section 7.3.3 highlighted that the Minch Ice Stream was not the major source of IRD to MD04-2829CQ. Figure 7.45 suggests that the reason for this was probably because of the strong northward surface currents along the Scottish/Norwegian coast. These strong surface currents could have transported the icebergs along the Faroe-Shetland Channel as suggested in Section 7.3.3 thereby a likely sentinel for the Minch Ice Stream IRD would be further NE along the margin. This section interprets the ISIS contribution to the Rosemary Bank core site. The ISIS contribution to MD04-2829CQ is solely comprised of Celtic Sea affinity and no Irish Sea end members are identified (Figure 7.50). The Celtic Sea input occurs throughout the 19-30 kyr BP interval, and supports a mean northward current flow from the Goban Spur to Rosemary Bank, but contradicts the modelled iceberg trajectories (Figure 7.45 and 7.46). Identifying only a Celtic Sea affinity is unexpected because the advance into the Celtic Sea was short lived (Chiverrell *et al.* 2013; Smedley *et al.* 2017) but this could be because the analysis only addresses the 18-30 kyr BP interval. This interval would not reflect the retreat into the northern Irish Sea Basin which occurs ~20 kyr BP (Chiverrell *et al.* 2013; Smedley *et al.* 2017). The Celtic Sea affinity could indicate another source of IRD. The Celtic Sea end member is defined by its Upper Cretaceous chalk signature; however, chalk could also be sourced from the Fair Isle Channel Ice Stream (FICIS) (Graham *et al.* 2009; called the Witch Ground Ice Stream, cf. Graham *et al.* 2010; Figure 7.51) or the Norwegian Channel Ice Stream (NCIS) (Hebbeln and Wefer, 1997; Lekens *et al.* 2006, Figure 7.51). During the late Quaternary the BIIS and the Fennoscandian Ice Sheet (FIS) were conjoined in the North Sea Basin. The timing of maximum ice extent in this sector has been dated to 23-19 kyr BP (Sejrup *et al.* 2016). The FICIS drained NE Scotland and the North Sea Basin (Bradwell *et al.* 2008) and the NCIS drained a large part of the Scandinavian Ice Sheet over southern Norway and Sweden (Svendsen *et al.* 2015). The chalk signature associated with the FICIS could originate from the outcrop of Upper Cretaceous chalk exposed at the mouth of the Moray Firth or the north central North Sea Basin (Graham *et al.* 2009). However, chalk has also been used as a provenance indicator for the NCIS because of the Cretaceous deposits in the North Sea and the south Baltic areas (Hebbeln and Wefer, 1997; Lekens *et al.* 2006). Reconstruction of the FICIS indicated shelf edge extent at ~27 kyr BP and retreat from the shelf by ~18 kyr BP (Clark *et al.* 2012; Sejrup *et al.* 2016). Sejrup *et al.* (2016) interpret that ice sheet collapse in the North Sea Basin was triggered by the expansion of the NCIS between 20-19 kyr BP and by 18.5 kyr BP the NCIS had retreated by nearly 200 km with an ice free Norwegian channel by 17 kyr BP. Consequently, the Cretaceous chalk signature identified in MD04-2829CQ is interpreted to reflect input from the FICIS. The timing



of its maximum extent and subsequent retreat is consistent with the IRD input throughout the 19-30 kyr BP interval. The input could be from NCIS too however, because ice streaming has been interpreted to occur at a later stage, a FICIS source is preferred. Depending on prevalent surface current direction, it is possible that the FICIS iceberg drift pathway circulated counter-clockwise around Faroe Islands and melted at the MD04-2829CQ core site based on level 2 reconstruction (Figure 7.46).

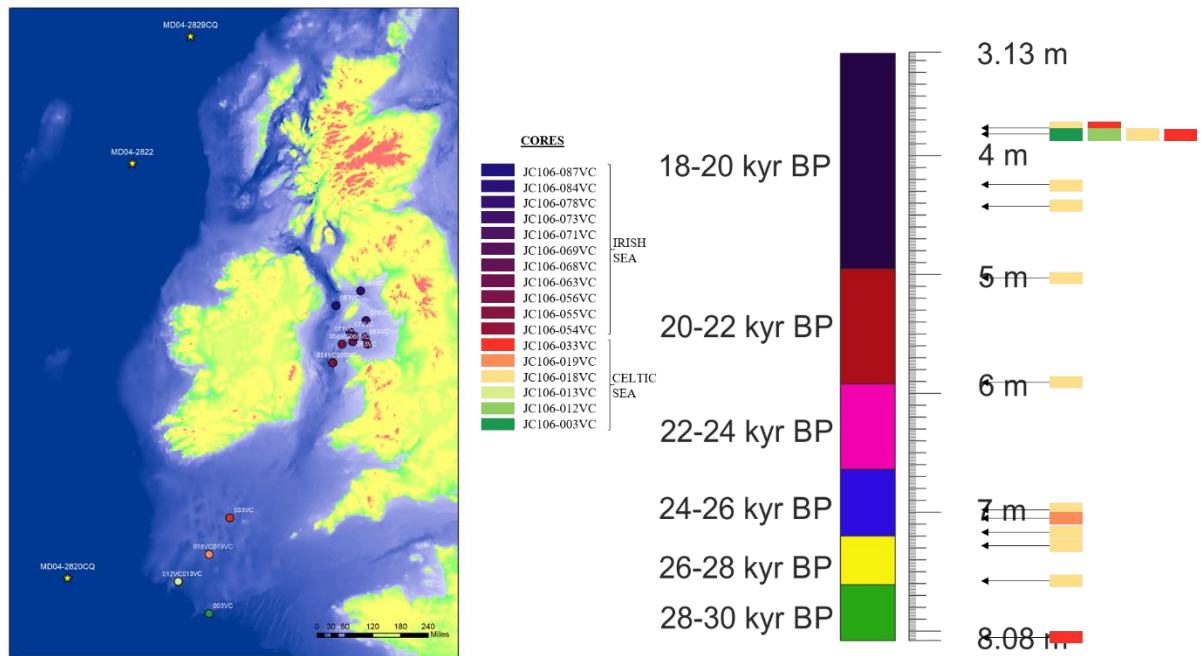


Figure 7.50 Schematic diagram displaying the location of the cores analysed and the colour that has been assigned to individual cores. Using the nearest neighbour approach, it has been possible to fingerprint depths within MD04-2829CQ to geochemically similar shelf end members from the ISIS.

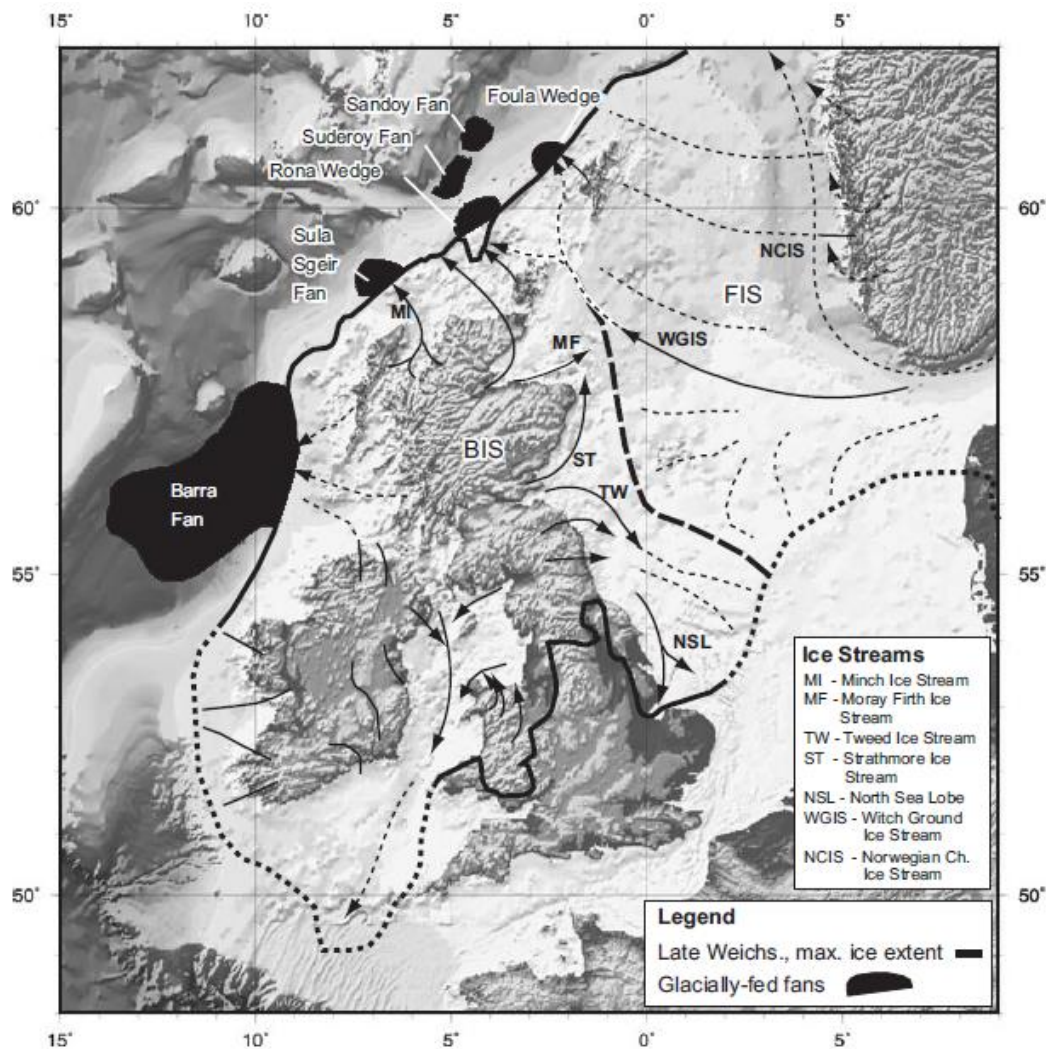


Figure 7.51 Reconstruction of ice-sheet extent and configuration for the Late Weichselian glacial maximum (MIS 3-2), in the North Sea Basin from Graham *et al.* 2011. The location of the Norwegian Channel Ice Stream is shown. This diagram separates the Moray Firth Ice Stream and the Witch Ground Basin Ice Stream, whereas this thesis refers to these ice streams collectively as the Fair Isle Channel Ice Stream.

#### **7.6.6 MD04-2829CQ and the Hebrides Ice Stream and Donegal Bay end members**

Analysis of MD04-2829CQ and the Hebrides Ice Stream and Donegal Bay sediment cores indicates that icebergs from this sector were a significant contributor of IRD to this core site (Figure 7.52). The analysis indicates that the Hebrides and Donegal affinity is much stronger in MD04-2829CQ than the adjacent Minch end members. Fingerprinting analysis indicates a Hebrides Ice Stream source throughout the 18-30 kyr BP interval and Donegal Bay IRD too (The Donegal Bay contribution is not as prominent as the Hebrides contribution). This pattern of IRD flux is consistent with the expansion of the Hebrides Ice Stream after 29 kyr BP and a shelf edge position ~25 kyr BP (Wilson and Austin 2002; Scourse *et al.* 2009; Hughes *et al.* 2016). The continued flux until 4.23 m is interpreted as the ongoing retreat of the ice sheet. After 4.23 m (~20 kyr BP) the Hebrides Ice Stream contribution reduces; this coincides with

the proposed ice stream cessation in the Northern Malin Sea ~20 kyr BP (Small *et al.* 2017). The Donegal Bay contribution on the other hand mainly occurs during the 22-28 kyr BP interval, radiocarbon dates from continental shelf cores obtained by Ó Cofaigh *et al.* (in press) show retreat from a shelf edge position between 26 and 24 kyr BP and a less extensive inner Donegal bay position between 20-19 kyr BP.

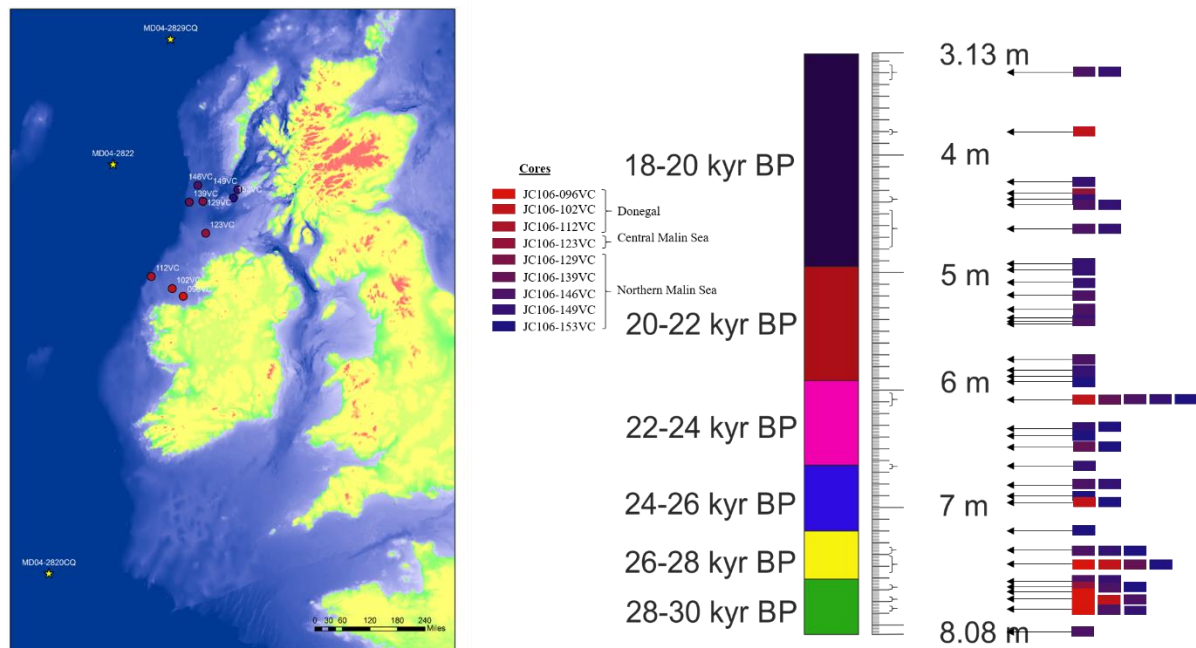


Figure 7.52 Schematic diagram displaying the location of the cores analysed and the colour that has been assigned to individual cores. Using the nearest neighbour approach, it has been possible to fingerprint depths within MD04-2829CQ to geochemically similar shelf end members from the Hebrides Ice Stream and Donegal Bay.

## **7.7 Summary**

This section has demonstrated that the offshore IRD record can be linked to the shelf glacigenic end members but, because of the homogenous nature of some of the end members, interpretation is complicated. The detrital carbonate input to MD04-2820CQ pre-H4 is interpreted as sourced from Ireland's Carboniferous limestone (Figure 7.53) and suggests that pre-H4 there was a less extensive BIIS which had a marine margin. From H4-31 kyr BP the minor Hebrides Ice Stream IRD input (Figure 7.53) could indicate the establishment of a marine margin in the catchment area of the Hebrides Ice Stream. Knutz *et al.* (2001) identify variable quantities of quartz-rich IRD input to the Barra fan between 45-30 kyr BP suggesting glacimarine conditions were intermittently established along the NW British margin. The Donegal Bay signature is characterised by detrital carbonate, therefore this input (Figure 7.53) is also interpreted as being sourced from a less extensive BIIS occupying Ireland. All ice streams are active between 31-27 kyr BP (Figure 7.54). The minor Celtic Sea input which occurs at ~28 kyr BP to MD04-2822 reflects either the advance of the ISIS into the northern part of the Celtic Sea or IRD sourced from Donegal Bay which has similar geochemical signature to the Celtic Sea end member. Transport of Celtic Sea IRD to MD04-2829CQ is possible but a FICIS source is assessed as more likely. According to independent chronologies most ice streams reach their maximum position and start their retreat in the 27-24 kyr BP time slice (Scourse *et al.* 2009; Clark *et al.* 2012; Chiverrell *et al.* 2013; Ó Cofaigh *et al.* in press). During this time (Figure 7.55) there is a minor contribution of IRD from the Celtic Sea sector of the BIIS to MD04-2820CQ which supports the advance of the ISIS into the Celtic Sea prior to H2. MD04-2820CQ also receives IRD from the Hebrides Ice Stream and Donegal Bay ice lobe which suggests a southward migration of icebergs from this sector of the BIIS. The Hebrides Ice Stream and Donegal Bay ice lobe also supply IRD to MD04-2822 and MD04-2829CQ. Figure 7.56 shows that from 24-20 kyr BP there is a stronger input from the Celtic Sea region to MD04-2820CQ and MD04-2822 which likely represents the rapid retreat of the ISIS from the shelf edge. Figure 7.56 also shows that the Donegal contribution to MD04-2829CQ lessens in comparison to the Hebrides Ice Stream. During the 20-15 kyr BP interval the pattern of IRD distribution suggests only a northward surface current is active along the Irish coast (Figure 7.57). MD04-2822 registers an Irish Sea contribution and minor input for the Donegal Bay ice lobe. The Hebrides Ice Stream is still active supplying IRD to MD04-2822 and MD04-2829CQ. MD04-2829CQ also suggests input from the Minch Ice Stream during this interval. From 15-14 kyr BP, both MD04-2820CQ and MD04-2822 register IRD flux from the BIIS (Figure 7.58). This input is interpreted as reflecting a smaller BIIS, which has some

marine terminating margins still present during the ongoing retreat such as in Ireland (as indicated by the Celtic Sea end member); northern Irish Sea catchment (as indicated by the Irish Sea end member) and the Inner Hebrides (as indicated by the Minch and Malin Sea end members).

The direction of surface currents has important implications for iceberg trajectories and determining the most likely source of the IRD. From this analysis, it is possible to infer that along the coast of Ireland surface currents shifted between a southerly and northerly direction (Figure 7.53-7.58) because of the migration of the bifurcation between the sub-polar and sub-tropical gyres. It has been suggested that the bifurcation migrated millennially, however without an age model for MD04-2820CQ this cannot be confirmed. Scourse *et al.* (2009) proposed the millennial meridional migration of the North Atlantic Polar Front (NAPF) during the last glacial period. The NAPF is positioned north of the sub-polar gyre, therefore the meridional migration of the NAPF will be coupled with the migration of the sub-polar gyre and the bifurcation. This migration will control the iceberg trajectories along the Irish coast.

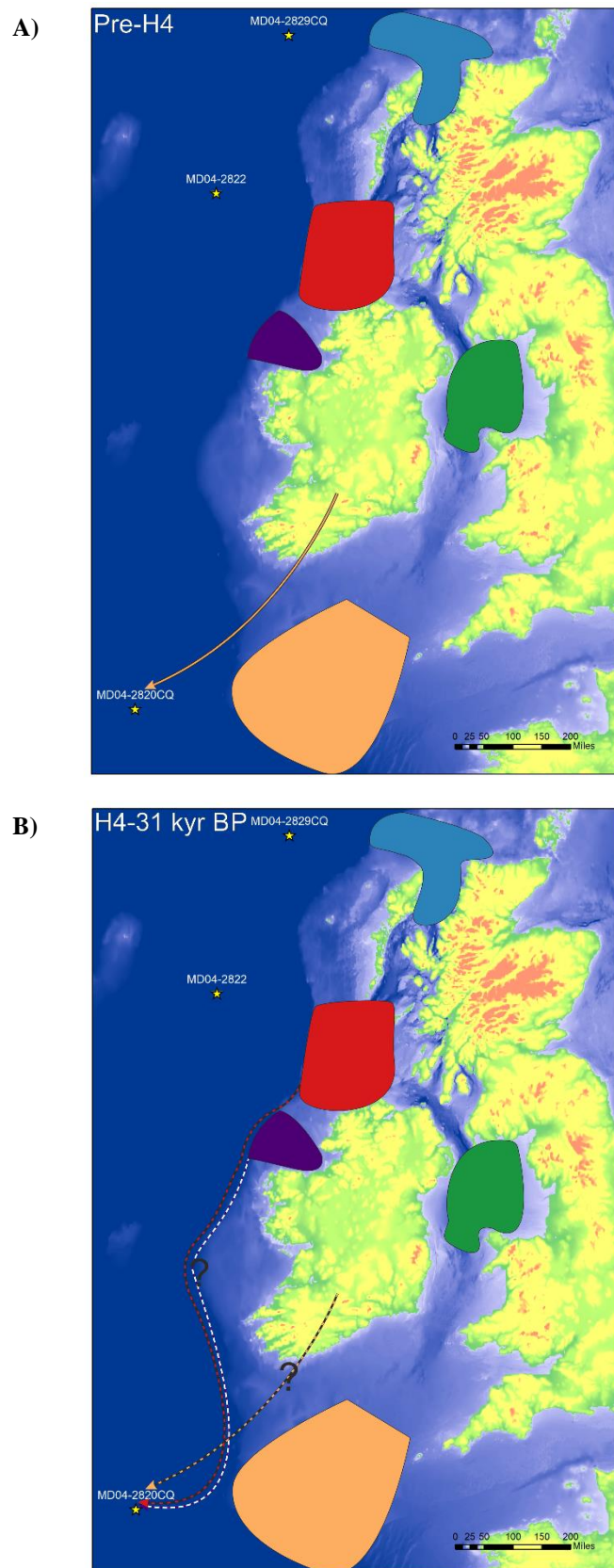


Figure 7.53 Schematic diagram summarising the trajectories and fates of icebergs/IRD from the five end members. A) Pre-H4; B) H4-31 kyr BP. The figure displays the location of three deep ocean cores analysed and the five end members colour coded (Green-Irish Sea, Beige-Celtic Sea, Purple-Donegal Bay, Red-Malin Sea and Blue-Minch Ice Stream). Dashed lines-minor input, solid lines-significant input, question marks-possible/questionable trajectories.



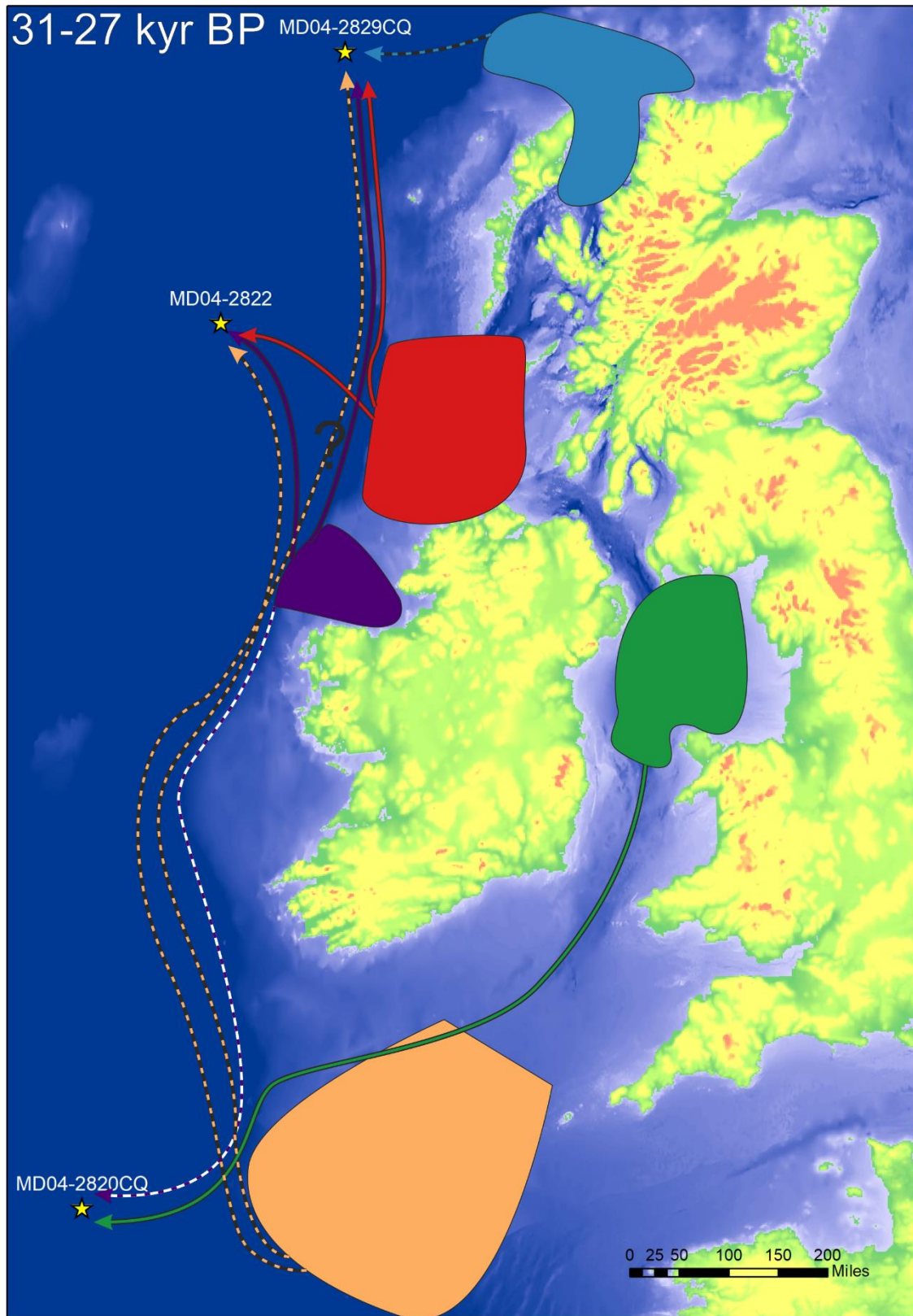


Figure 7.54 Schematic diagram summarising the trajectories and fates of icebergs/IRD from the five end members; 31-27 kyr BP. The figure displays the location of three deep ocean cores analysed and the five end members colour coded (Green-Irish Sea, Beige-Celtic Sea, Purple-Donegal Bay, Red-Malin Sea and Blue-Minch Ice Stream). Dashed lines-minor input, solid lines-significant input, question marks-possible/questionable trajectories.

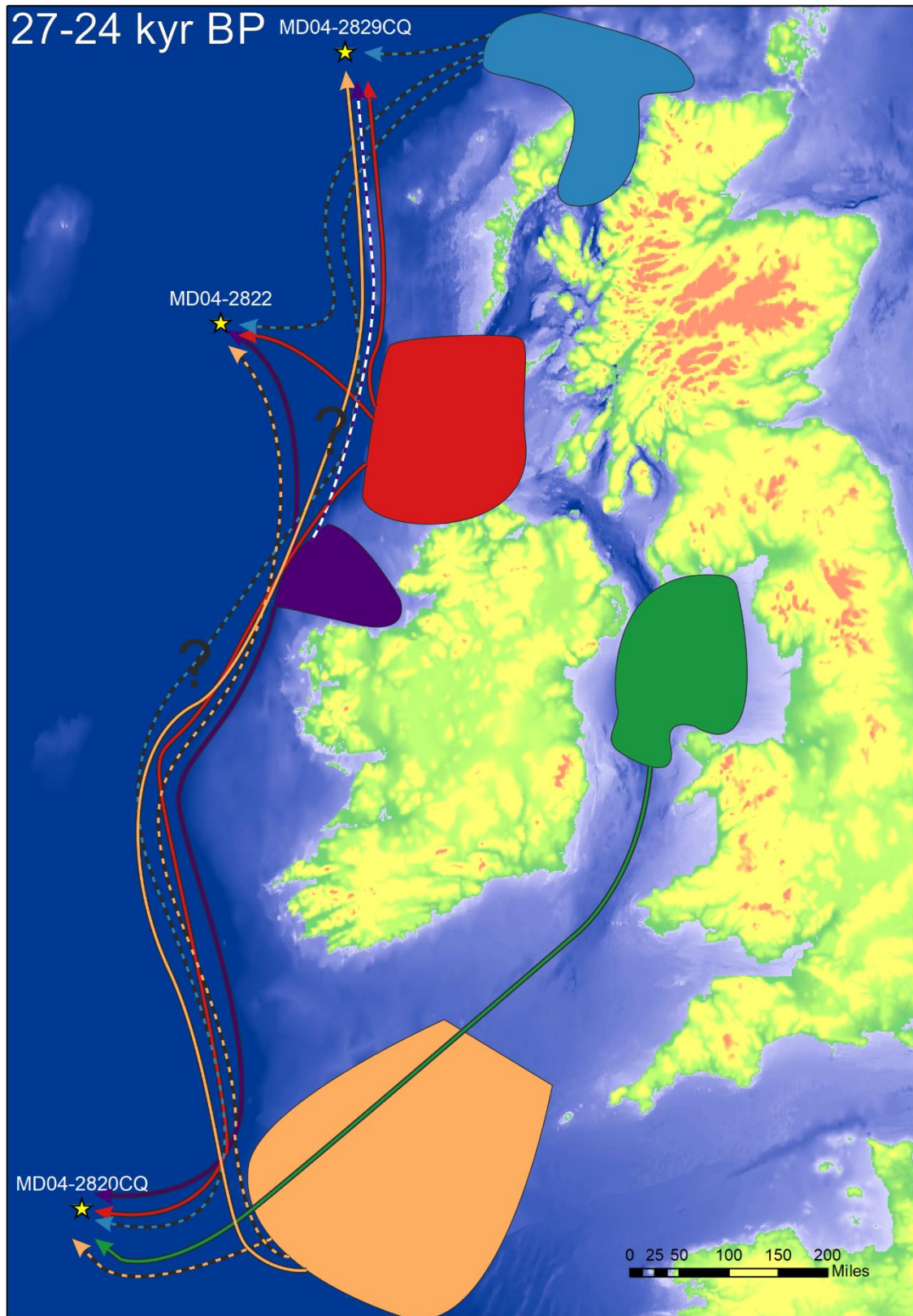


Figure 7.55 Schematic diagram summarising the trajectories and fates of icebergs/IRD from the five end members; 27-24 kyr BP. The figure displays the location of three deep ocean cores analysed and the five end members colour coded (Green-Irish Sea, Beige-Celtic Sea, Purple-Donegal Bay, Red-Malin Sea and Blue-Minch Ice Stream). Dashed lines-minor input, solid lines-significant input, question marks-possible/questionable trajectories.



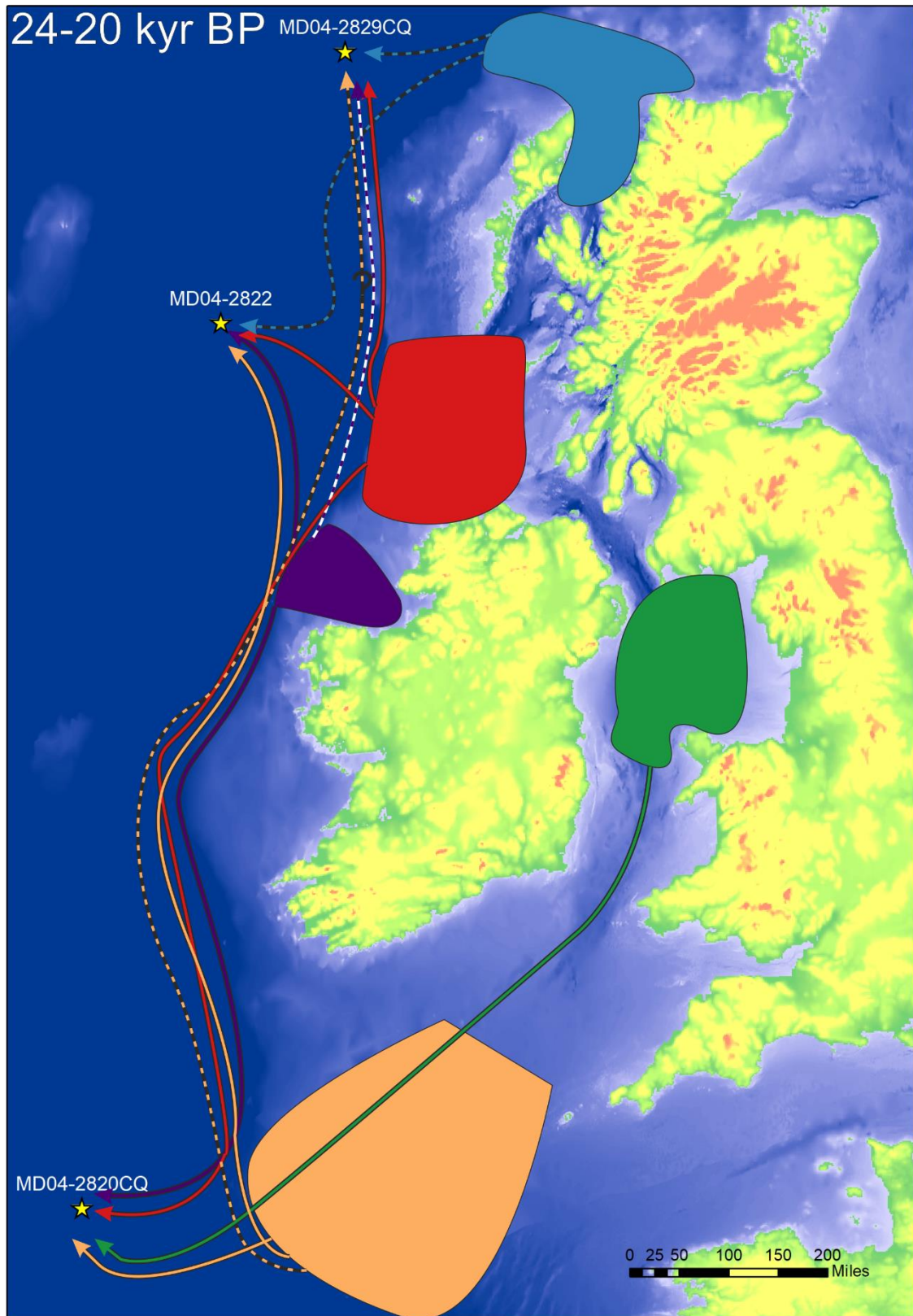


Figure 7.56 Schematic diagram summarising the trajectories and fates of icebergs/IRD from the five end members; 24-20 kyr BP. The figure displays the location of three deep ocean cores analysed and the five end members colour coded (Green-Irish Sea, Beige-Celtic Sea, Purple-Donegal Bay, Red-Malin Sea and Blue-Minch Ice Stream). Dashed lines-minor input, solid lines-significant input, question marks-possible/questionable trajectories.

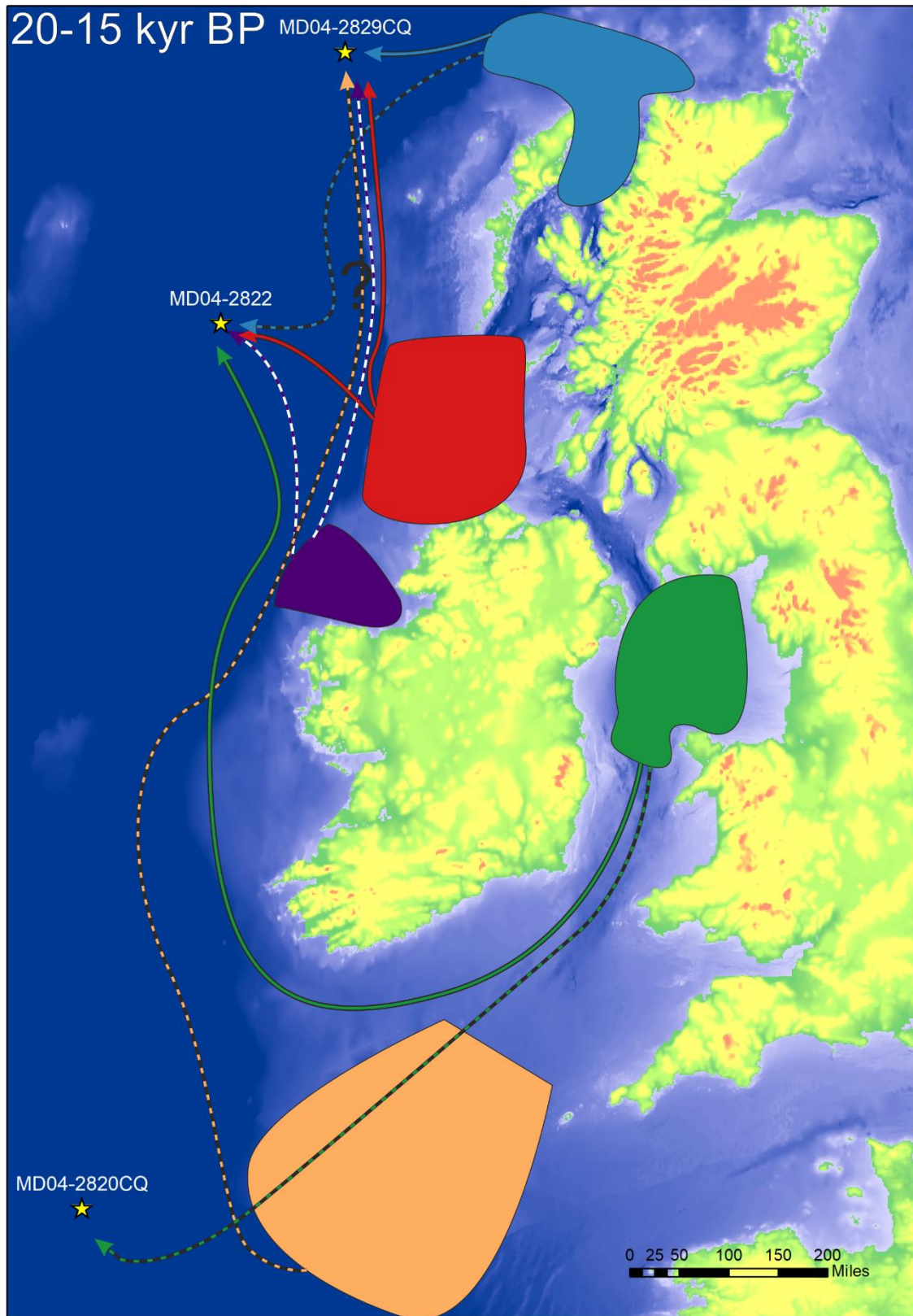


Figure 7.57 Schematic diagram summarising the trajectories and fates of icebergs/IRD from the five end members; 20-15 kyr BP. The figure displays the location of three deep ocean cores analysed and the five end members colour coded (Green-Irish Sea, Beige-Celtic Sea, Purple-Donegal Bay, Red-Malin Sea and Blue-Minch Ice Stream). Dashed lines-minor input, solid lines-significant input, question marks-possible/questionable trajectories.



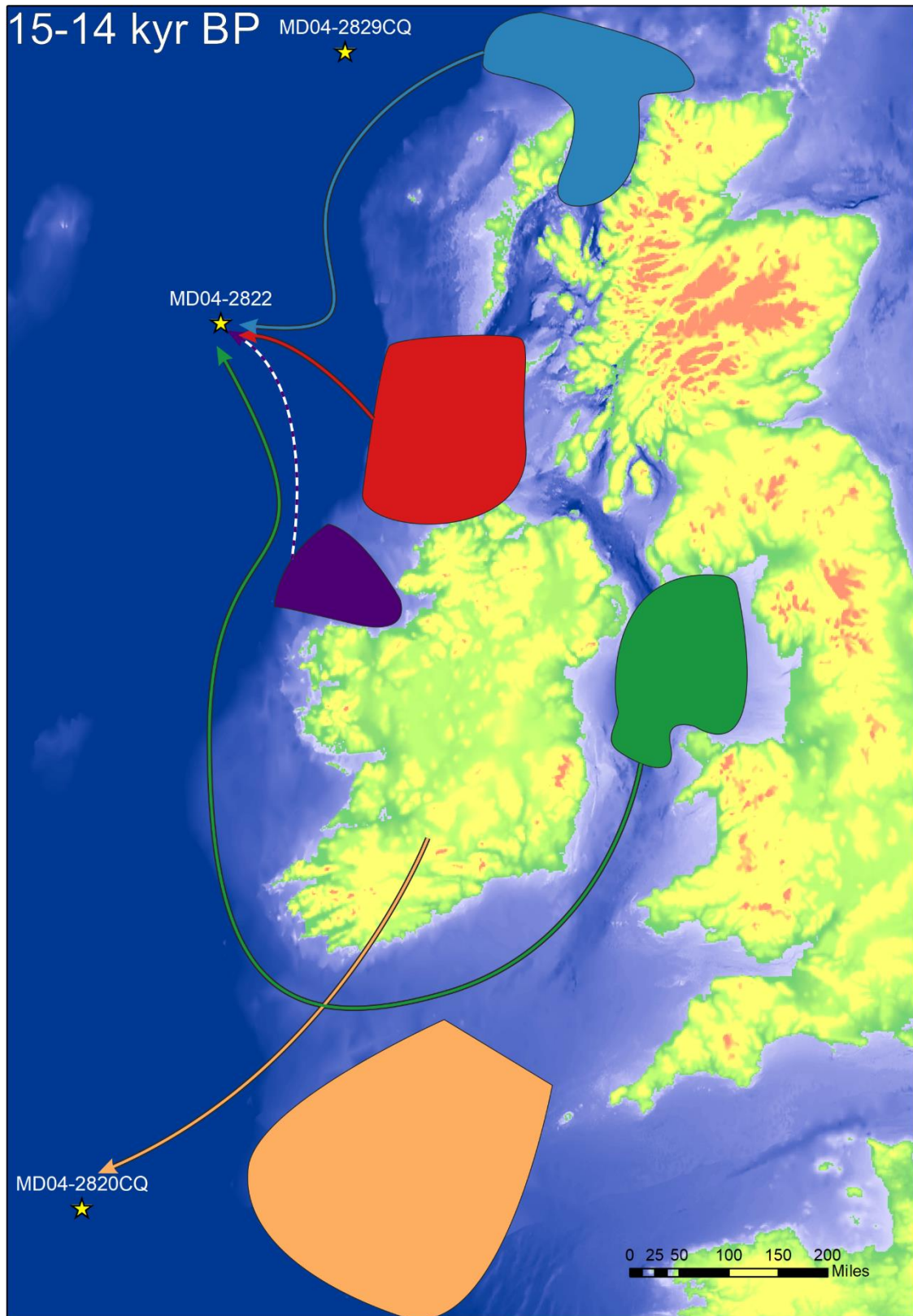


Figure 7.58 Schematic diagram summarising the trajectories and fates of icebergs/IRD from the five end members; 15-14 kyr BP. The figure displays the location of three deep ocean cores analysed and the five end members colour coded (Green-Irish Sea, Beige-Celtic Sea, Purple-Donegal Bay, Red-Malin Sea and Blue-Minch Ice Stream). Dashed lines-minor input, solid lines-significant input, question marks-possible/questionable trajectories.

# 8 Conclusion

This thesis analyses 38 marine sediment cores from the NE Atlantic with the aim to investigate the indicative meaning of the IRD record in the deep ocean. Analysis focused on determining the geochemistry of the glaciogenic sediments from across the continental shelf (which formerly drained the BIIS) and within the three deep ocean cores. The principal findings are summarised and discussed below, followed by suggestions for future work and wider implications.

## **8.1 The indicative meaning of the ice-rafted detritus record in the deep ocean**

IRD has been used extensively as a proxy for ice sheet dynamics, but significant uncertainty remains on how IRD flux relates to mass balance (negative or positive). Scourse *et al.* (2009) proposed a hybrid model whereby IRD is a function of ice sheet advance and ice sheet collapse; the aim of this thesis was to test this model, to determine the indicative meaning of the IRD record. To address this aim it is important to determine the most likely source of IRD. IRD provenance is usually determined by analysing lithic grains (>150  $\mu\text{m}$  fraction) using a light microscope which is time consuming; this study used XRF as a quick, high resolution method for generating elemental assemblages of marine sediment cores (incorporating all grain sizes). The adjacent deep ocean cores to the BIIS have been analysed extensively (Scourse *et al.* 2000; Knutz *et al.* 2001; Peck *et al.* 2006; Peck *et al.* 2007; Walden *et al.* 2007; Peters *et al.* 2008; Hibbert *et al.* 2010; Scourse *et al.* 2009; Haapaniemi *et al.* 2010), but to date the geochemical compositional data does not allow the identification of specific ice stream sources. Using XRF,

one of the key objectives outlined by this thesis was to assign a geochemical signature to three ice streams draining the western sector of the BIIS.

The geochemical signature of sediments can be strongly influenced by grain size (Bloemsma *et al.* 2012; von Eynatten *et al.* 2012). This study determined that on an ice stream scale, the catchment geology is the primary driver of geochemistry and that this overprints grain size effects. The importance of catchment geology supports the findings of Farmer *et al.* (2003), whereby IRD and glacimarine sediments reflect the local geology of the calving margin. Therefore, within ice streams, the degree of geochemical variation between glacial end members is controlled by the catchment geology. In ice streams with very geochemically distinct catchment geology e.g. ISIS (Upper Cretaceous chalk vs Permo-Triassic sandstone), there will be geochemically distinct end members. Whereas the Minch Ice Stream, for instance, does not have significant within-ice stream variation because of similar catchment geology. Analysis determined five end members for the BIIS (Celtic Sea, Irish Sea, Donegal, Malin Sea and the Minch), all of which showed a degree of similar geochemistry because of similar catchment geologies/mineralogy. Even though the end member signatures are geochemically similar, the fingerprinting analysis does support current understanding of ice sheet advance to the shelf edge and subsequent deglaciation (which will be discussed below); thereby we can link IRD flux to the deglaciation of individual ice streams of the BIIS. But it is important to consider surface current circulation and possible influence of other sources of IRD.

## **8.2 Iceberg trajectories**

The dispersal of IRD to distal core sites is interpreted to represent the dominant direction of surface currents. Patterns of dispersal which show bilateral transport pathways (e.g. along the Irish coast) most likely indicate changes in surface current direction, governed by the meridional migration of the bifurcation of the North Atlantic Current.

## **8.3 Ice-rafted detritus record and implications for the dynamics and collapse of the British-Irish Ice Sheet**

MD04-2820CQ is the only deep ocean record used in this study that extends earlier than 30-31 kyr BP. IRD analysis indicates a BIIS contribution pre-H4 in MD04-2820CQ. This finding is supported by Peck *et al.* (2007) and Ó Cofaigh *et al.* (2012) and demonstrates the presence of a marine terminating margin. Between H4 and H3, only a Hebrides Ice Stream flux is recorded and is interpreted as evidence of a smaller regionalised Scottish marine terminating margin.

This interpretation is supported by the lithic grains identified by Peck *et al.* (2007) prior to H3, which are ‘tentatively’ interpreted as sourced from the Dalradian Supergroup of Scotland. These findings are significant because they demonstrate a BIIS with a marine terminating margin prior to the onset of ice streaming associated with the LGM; this supports previous suggestions by Knutz *et al.* (2001), Peck *et al.* (2007) and Peters *et al.* (2008). After 31 kyr BP (after H3), there is an increase in the BIIS flux recorded in the deep ocean cores. The ISIS, the Hebrides Ice Stream and the Donegal Bay ice lobe are all active; with quasi-stable ice marginal positions in the Irish Sea Sector and the Donegal and Malin Sea sector. Fingerprinting evidence supports the extension of the Hebrides Ice Stream to the shelf edge ~27 kyr BP and ice stream cessation ~20 kyr BP; and the advance of the ISIS into the Celtic Sea circa H2 and its subsequent collapse following H2. The offshore record from the Minch Ice Stream indicates it was active from ~28-18 kyr BP. These findings are supported by other independent evidence on the dynamics and collapse of the BIIS (Scourse *et al.* 2009; Chiverrell *et al.* 2013; Bradwell and Stoker 2015; Praeg *et al.* 2015; Hughes *et al.* 2016; Small *et al.* 2017; Smedley *et al.* 2017; Ó Cofaigh *et al.* in press).

This thesis has also shown the presence of BIIS-sourced IRD in MD04-2822 ~14 kyr BP. This is a significant finding because it suggests a smaller regionalised marine terminating margin ~14 kyr BP. This margin is most likely located within the coastal fjords of the Inner Hebrides. The IRD input is interpreted as indicating the retreat of the ice sheet from the Wester Ross Readvance limits.

From the fingerprinting analysis, it has also been possible to disentangle flux from adjacent sources, for example Donegal Bay ice lobe and the Hebrides Ice Stream. Through this approach, it has been possible to make some inferences on the pattern of ice retreat within sectors of the BIIS. The Donegal Bay signature only had a minor contribution after 22 kyr BP, which suggests a less extensive position. This has been corroborated by the chronological control established on the continental shelf by Ó Cofaigh *et al.* (in press).

The iceberg turbate in JC106-139VC has a Hebrides Ice Stream geochemical signature. This indicates that the icebergs did not come from a distal source. The radiocarbon date of 12.6 kyr BP obtained from the turbated diamict indicates the reworking of shells by icebergs after 12.6 kyr BP. This suggests that there was a marine ice margin in Western Scotland during the Younger Dryas Stadial.

#### **8.4 Geochemical signature of Heinrich events**

MD04-2820CCQ is the only deep ocean core analysed in this study which has a strong Heinrich event signature. H1, H2 and H4 all have high values of Ca, Sr and Mn. In contrast, H3 plots within the central cluster of the ambient MD04-2820CQ sediment. This supports previous interpretation of H3 as a predominantly non-Laurentide source, because of the absence of the characteristic dolomitic carbonate signature (e.g., Grousset *et al.* 1993; Bond and Lotti 1995; Gwiazda *et al.* 1996; Snoeckx *et al.* 1999; Peck *et al.* 2007). H3 in MD04-2820CQ as stated previously, plots within the central cluster of the ambient sediment, suggesting geochemical similarities. Due to the proximity of the core site to the BIIS, it is reasonable to assume that the BIIS will be the main contributor to MD04-2820CQ. On this basis, the likely source for H3 is the BIIS. A European origin for H3 has been hypothesised (Peck *et al.* 2007; Scourse *et al.* 2009; Hal *et al.* 2011) and Bigg *et al.* 2011 suggest that the northern Fennoscandian Ice Sheet is the main source of iceberg release for H3. Further analysis is required to determine the origin of H3, but from this analysis it can be drawn that the geochemical signature of H3 is similar to the ambient sediment of MD04-2820CQ, suggesting a local source.

#### **8.5 Future work**

##### **British Irish Ice Sheet advance and the ice-rafted detritus record**

The analysis presented in thesis cannot definitively determine the indicative meaning of the IRD record. This is because the results mostly indicate the onset of deglaciation rather than the advance of the ice sheet. Excluding MD04-2820CQ, the other deep ocean cores only extend to 30/31 kyr BP; at this stage the ice streams were already almost at their furthest extent (excluding the ISIS). The hypothetical synthetic stratigraphy proposed in Chapter 1 cannot be supported by the data. The detailed retreat stages of the ice streams cannot be determined solely by the geochemistry of the deep ocean cores. This is because the spatial geochemical discrimination along the former flowpaths cannot be sufficiently highly resolved, the ideal context for this form of analysis would be an ice catchment which has more variable bedrock geology. To understand ice dynamics using this approach, it is necessary to have spatially variable geology which will reflect ice marginal position, temporally and spatially. This is true no matter what technique is used, since without geochemically discriminant sources only broad provenance affinities can be assigned. The UK and Ireland has a variable geology however there are too many similarities between the main ice dispersal centres to provide more meaningful results. This has also been investigated by Arosio *et al.* 2017 (in press) for the

Hebrides Ice Stream, where considerable geochemical overlap exists between the Moine and Torridonian rocks. The authors use discriminant function analysis (DFA) to improve differentiation between provenance groups. Application of DFA to the data generated in this thesis could improve the geochemical separation of the end members/ice streams and would be worth investigating.

### **X-ray fluorescence**

It has been shown that XRF is a useful tool for investigating IRD provenance, and the simple regression equation method for converting wet scan data to dry mass concentration is broadly successful. Further analysis should include more subsamples to better characterise the relationship between dry mass and wet scanned concentrations. Further studies would also benefit from analysing all cores on the same XRF scanner; this would limit inconsistencies between machine measurements and would permit the analysis of more elements (MD04-2822 and MD04-2820CQ datasets do not include some elements).

### **Grain size**

Further geochemical analysis of the marine sediment cores should incorporate grain size analysis to quantitatively determine the impact of grain size on the geochemical signature of the glacial sediments. Analysis could then investigate how/if provenance changes when only certain grain sizes are included in analysis.

### **Additional end members and deep ocean cores**

In Chapter 7, it was discussed that the FICIS or the NCIS may have contributed to the inferred chalk signature in MD04-2829CQ. For this reason, it would be beneficial to incorporate the FICIS and the NCIS as end members in further analysis. It is suggested that the FICIS is the most likely source of the chalk signature, however geochemical analysis would enable this theory to be tested.

The contribution of the ISIS, the Hebrides Ice Stream and Donegal Bay ice lobe are well reflected in the deep ocean cores selected for this thesis, however the Minch Ice Stream contribution is not. Consequently, incorporating an additional deep ocean core, north east of the Minch Ice Stream perhaps from the Faroe-Shetland channel/south-eastern Nordic Seas would most likely record a Minch contribution. Becker *et al.* (2017) analysed two giant CALYPSO cores from this region (MD99-2283, MD99-2284), within their analysis they



established a BIIS contribution. Therefore, if these cores were re-analysed using the approach adopted in this thesis, a Minch Ice Stream contribution might be established. An offshore record of Minch Ice Stream activity would help support the chronology being established for ice stream deglaciation across the continental shelf.

## **8.6 Implications for BRITICE-CHRONO**

As stated in Chapter 1, this PhD contributes to the NERC-funded BRITICE-CHRONO project, therefore it is important to review what implications the results outlined previously have for the BRITICE-CHRONO project. BRITICE-CHRONO aims to reconstruct the retreat stages of the BIIS from its maximum extent during the Last Glacial Maximum (LGM) until it backstepped onto land. The analysis presented in this thesis cannot be linked to the detailed retreat stages of individual ice streams, but it can link IRD flux to end members which can support the pattern of retreat for individual ice streams and provide evidence for the initiation of the marine sector of the BIIS and its transition to a land-based ice sheet.

This work provides evidence for an early establishment of a marine margin for BIIS prior to H4. Evidence for ice sheet initiation and growth is important for BRITICE-CHRONO reconstructions, because sedimentary evidence for ice sheet initiation are usually removed by ice sheet growth.

The data will be used to underpin the geochronological data relating to ice stream collapse generated by the BRITICE-CHRONO consortium. The evidence already supports the pattern of advance and retreat of the ISIS and the short lived advanced into the Celtic Sea. The analysis also provides evidence for the cessation of the Hebrides Ice Stream at 20 kyr BP.

These data can also be used to assess the accuracy of the iceberg trajectory modelling by providing observational constraints. As stated in Chapter 7 the Frugal model is calibrated by evaluating its performance when compared to actual observations. The Frugal model will be used by BRITICE-CHRONO to plot the course and melting of icebergs calved from the BIIS. This thesis however, has demonstrated the bilateral pathway of icebergs along the coast of the UK and Ireland, which would be difficult to capture in the Frugal model and would need to be considered when interpreting results generated.

One of the key remits of BRITICE-CHRONO is to determine when the BIIS backstepped onto land. Identifying IRD sourced from Scotland is evidence for a marine terminating margin until ~14 kyr BP. This study has also established the reworking of marine

shells by icebergs with a Western Scotland signature which has been interpreted as evidence for a marine terminating margin during the Younger Dryas stadial. Both interpretations are an important for ice sheet reconstruction. Changes to our understanding of the timing of deglaciation, ice sheet extent and thickness impact the ice sheet model experiments.

BRITICE-CHRONO aims to fit ice sheet experiment models onto key time slices during deglaciation to yield ice sheet thickness. Ice sheet thickness data will be critical for improved glacial isostatic adjustment (GIA) model simulations for sea level reconstructions during deglaciation.

## **References**

- Abbott, P. M., Austin, W. E. N., Davies, S. M., Pearce, N. J. & Hibbert, F. D. 2013: Cryptotephrochronology of the Eemian and the last interglacial–glacial transition in the North East Atlantic. *Journal of Quaternary Science* 28, 501-514.
- Alley, R.B, 2000: The Younger Dryas cold interval as viewed from central Greenland. *Quaternary Science Reviews* 19, 213-226.
- Andrews, J.T. 2000: Icebergs and iceberg rafted detritus (IRD) in the North Atlantic: facts and assumptions. *Oceanography* 13, 100-108.
- Andrews, J. T. & Eberl, D. D. 2011: Surface (sea floor) and near-surface (box cores) sediment mineralogy in Baffin Bay as a key to sediment provenance and ice sheet variations. *Canadian Journal of Earth Sciences* 48, 1307-1328.
- Andrews, J. T., Gibb, O. T., Jennings, A. E. & Simon, Q. 2014: Variations in the provenance of sediment from ice sheets surrounding Baffin Bay during MIS 2 and 3 and export to the Labrador Shelf Sea: site HU2008029-0008 Davis Strait. *Journal of Quaternary Science* 29, 3-13.
- Arosio, R., Crocket, K. C., Nowell, G. M., Callard, S. L., Howe, J. A., Benetti, S., Fabel, D., Moreton, S. & Clark, C. D. 2017: Weathering fluxes and sediment provenance on the SW Scottish shelf during the last deglaciation. *Marine Geology*, in press.
- Austin, W. E. N. & Hibbert, F. D. 2012: Tracing time in the ocean: a brief review of chronological constraints (60–8 kyr) on North Atlantic marine event-based stratigraphies. *Quaternary Science Reviews* 36, 28-37.
- Ballantyne, C. K. & Stone, J. O. 2012: Did large ice caps persist on low ground in north-west Scotland during the Lateglacial Interstade? *Journal of Quaternary Science* 27, 297-306.
- Bamber, J. L. & Aspinall, W. P. 2013: An expert judgement assessment of future sea level rise from the ice sheets. *Nature Climate Change* 3, 424-427.
- Bauch, H. A., Erlenkeuser, H., Spielhagen, R. F., Struck, U., Matthiessen, J., Thiede, J. & Heinemeier, J. 2001: A multiproxy reconstruction of the evolution of deep and surface waters in the subarctic Nordic seas over the last 30,000 yr. *Quaternary Science Reviews* 20, 659-678.

- Becker, L.W., Sejrup, H.P., Hjelstuen, B.O., Haflidason, H. and Dokken, T.M. 2017: Ocean-ice sheet interaction along the SE Nordic Seas margin from 35 to 15 ka BP. *Marine Geology*, in press.
- Bigg, G. R., Wadley, M. R., Stevens, D. P. & Johnson, J. A. 1997: Modelling the dynamics and thermodynamics of icebergs. *Cold Regions Science and Technology* 26, 113-135.
- Bigg, G.R., Wadley, M.R., Stevens, D.P. and Johnson, J.A. 1998: Simulations of two last glacial maximum ocean states. *Paleoceanography*, 13, 340-351.
- Bigg, G.R., Dye, S.R. and Wadley, M.R. 2005: Interannual variability in the 1990s in the northern Atlantic and Nordic Seas. *Journal of Atmospheric & Ocean Science*, 10, 123-143.
- Bigg, G.R., Levine, R.C., Clark, C.D., Greenwood, S.L., Haflidason, H., Hughes, A.L., Nygård, A. and Sejrup, H.P. 2010: Last glacial ice-rafted debris off southwestern Europe: the role of the British-Irish Ice Sheet. *Journal of Quaternary Science*, 25, 689-699.
- Bigg, G. R., Clark, C. D., Greenwood, S. L., Haflidason, H., Hughes, A. L., Levine, R. C., Nygård, A. & Sejrup, H. P. 2012: Sensitivity of the North Atlantic circulation to break-up of the marine sectors of the NW European ice sheets during the last Glacial: A synthesis of modelling and palaeoceanography. *Global and Planetary Change* 98, 153-165.
- Bloemsma, M. R., Zabel, M., Stuut, J. B. W., Tjallingii, R., Collins, J. A. & Weltje, G. J. 2012: Modelling the joint variability of grain size and chemical composition in sediments. *Sedimentary Geology* 280, 135-148.
- Bond, G., Broecker, W., Johnsen, S., McManus, J., Labeyrie, L., Jouzel, J. & Bonani, G. 1993: Correlations between climate records from North Atlantic sediments and Greenland ice. *Nature* 365, 143-147.
- Bond, G. C. & Lotti, R. 1995: Iceberg discharges into the North Atlantic on millennial time scales during the last glaciation. *Science* 267, 1005-1010.
- Boyle, J. F. 2000: Rapid elemental analysis of sediment samples by isotope source XRF. *Journal of Paleolimnology* 23, 213-221.
- Boyle, J. F., Chiverrell, R. C. & Schillereff, D. 2015: Approaches to water content correction and calibration for  $\mu$ XRF core scanning: comparing X-ray scattering with simple regression of elemental concentrations. In Croudace, I. W. & Rothwell, R. G. (eds.): *Micro-XRF Studies of Sediment Cores*, 373-390, Springer, Netherlands.

Bradley, S.L., Milne, G.A., Shennan, I. and Edwards, R. 2011: An improved glacial isostatic adjustment model for the British Isles. *Journal of Quaternary Science*, 26, 541-552.

Bradwell, T., Stoker, M. and Larter, R. 2007: Geomorphological signature and flow dynamics of The Minch palaeo-ice stream, northwest Scotland. *Journal of Quaternary Science*, 22, 609-617.

Bradwell, T., Stoker, M.S., Golledge, N.R., Wilson, C.K., Merritt, J.W., Long, D., Everest, J.D., Hestvik, O.B., Stevenson, A.G., Hubbard, A.L. and Finlayson, A.G. 2008: The northern sector of the last British Ice Sheet: maximum extent and demise. *Earth-Science Reviews*, 88, 207-226.

Bradwell, T., Fabel, D., Stoker, M., Mathers, H., McHargue, L. & Howe, J. 2008: Ice caps existed throughout the Lateglacial Interstadial in northern Scotland. *Journal of Quaternary Science* 23, 401-407.

Bradwell, T., Stoker, M. & Krabbendam, M. 2008: Megagrooves and streamlined bedrock in NW Scotland: the role of ice streams in landscape evolution. *Geomorphology* 97, 135-156.

Bradwell, T. & Stoker, M. S. 2015: Submarine sediment and landform record of a palaeo-ice stream within the British– Irish Ice Sheet. *Boreas* 44, 255-276.

British Geological Survey. 2008. Digital Geological Map of Great Britain 1:25 000 scale (DiGMapGB-25) data. Version 2.18. Keyworth, Nottingham: British Geological Survey. Tile SN82. Release date 25-11-2008.

Broecker, W.S. 1994: Massive iceberg discharges as triggers for global climate change. *Nature* 372, 421-424.

Brooks, A.J., Bradley, S.L., Edwards, R.J., Milne, G.A., Horton, B. and Shennan, I. 2008: Postglacial relative sea-level observations from Ireland and their role in glacial rebound modelling. *Journal of Quaternary Science*, 23, 175-192.

Buckley, M. W. & Marshall, J. 2016: Observations, inferences, and mechanisms of the Atlantic Meridional Overturning Circulation: A review. *Reviews of Geophysics* 54, 5-63.

Channell, J. E. T., Harrison, R. J., Lascu, I., McCave, I. N., Hibbert, F. D. & Austin, W. E. N. 2016: Magnetic record of deglaciation using FORC-PCA, sortable-silt grain size, and magnetic excursion at 26 ka, from the Rockall Trough (NE Atlantic). *Geochemistry, Geophysics, Geosystems* 17, 1823-1841.

- Chiverrell, R. C., Thrasher, I. M., Thomas, G. S., Lang, A., Scourse, J. D., van Landeghem, K. J., Mccarroll, D., Clark, C. D., Ó Cofaigh, C., Evans, D. J. & Ballantyne, C. K. 2013: Bayesian modelling the retreat of the Irish Sea Ice Stream. *Journal of Quaternary Science* 28, 200-209.
- Clark, C. D., Hughes, A. L., Greenwood, S. L., Jordan, C. & Sejrup, H. P. 2012: Pattern and timing of retreat of the last British-Irish Ice Sheet. *Quaternary Science Reviews* 44, 112-146.
- Cooke, F. 2008: Ice ocean climate interaction in the NE Atlantic: The study of Heinrich events and D/O cycles during the past 120,000 years. MSc Thesis, Bangor University.
- Croudace, I. W., Rindby, A. & Rothwell, R. G. 2006: ITRAX: description and evaluation of a new multi-function X-ray core scanner. *Geological Society, London, Special Publications* 267, 51-63.
- Croudace, I. W. & Rothwell, R. G. (eds.) 2015: *Micro-XRF Studies of Sediment Cores: Applications of a non-destructive tool for the environmental sciences* 17, Springer.
- Dong, B. and Valdes, P.J. 1998: Simulations of the Last Glacial Maximum climates using a general circulation model: prescribed versus computed sea surface temperatures. *Climate Dynamics*, 14, 571-591.
- Dove, D., Arosio, R., Finlayson, A., Bradwell, T. & Howe, J. A. 2015: Submarine glacial landforms record Late Pleistocene ice-sheet dynamics, Inner Hebrides, Scotland. *Quaternary Science Reviews* 123, 76-90.
- Dowdeswell, J. A., Canals, M., Jakobsson, M., Todd, B. J., Dowdeswell, E. K. & Hogan, K. A. (eds.) 2016: Atlas of Submarine Glacial Landforms: Modern, Quaternary and Ancient. *Geological Society of London Memoir* 46, 611 pp.
- Dunlop, P., Shannon, R., McCabe, M., Quinn, R. & Doyle, E. 2010: Marine geophysical evidence for ice sheet extension and recession on the Malin Shelf: New evidence for the western limits of the British Irish Ice Sheet. *Marine Geology* 276, 86-99.
- Edwards, J. W. F., Briant, M. & Arthur, M.J. 1991: Proposed Mesozoic dykes in the Celtic Sea. *Proceedings of the Ussher Society* 7, 344-349.
- England, M.H. 1993: Representing the global-scale water masses in ocean general circulation models. *Journal of Physical Oceanography*, 23, 1523-1552.

ETOPO. 1986: Global 5'T' depth and elevation. Available from National Geophysical Data Centre, NOAA, US Department of Commerce, Code E/GC3, Boulder, CO.

Everest, J. D., Bradwell, T., Stoker, M. & Dewey, S. 2013: New age constraints for the maximum extent of the last British–Irish Ice Sheet (NW sector). *Journal of Quaternary Science* 28, 2-7.

Fabel, D., Ballantyne, C.K. and Xu, S. 2012: Trimlines, blockfields, mountain-top erratics and the vertical dimensions of the last British–Irish Ice Sheet in NW Scotland. *Quaternary Science Reviews*, 55, 91-102.

Fairbanks, R.G. 1989: A 17,000-year glacio-eustatic sea level record: influence of glacial melting rates on the Younger Dryas event and deep-ocean circulation. *Nature*, 342, 637.

Farmer, G. L., Barber, D. & Andrews, J. 2003: Provenance of Late Quaternary ice-proximal sediments in the North Atlantic: Nd, Sr and Pb isotopic evidence. *Earth and Planetary Science Letters* 209, 227-243.

Farmer, G. L., Licht, K., Swope, R. J. & Andrews, J. 2006: Isotopic constraints on the provenance of fine-grained sediment in LGM tills from the Ross Embayment, Antarctica. *Earth and Planetary Science Letters* 249, 90-107.

Fyfe, J. A., Long, D. & Evans, D. 1993: *United Kingdom Offshore Regional Report: the Geology of the Malin–Hebrides Sea Area*. HMSO for the British Geological Survey, London.

Geological Survey of Ireland, 2014: Bedrock Geology of Ireland, 1:1,000,000 Scale (map).

Graham, A.G., Lonergan, L. and Stoker, M.S. 2009: Seafloor glacial features reveal the extent and decay of the last British Ice Sheet, east of Scotland. *Journal of Quaternary Science*, 24, 117-138.

Graham, A.G., Lonergan, L. and Stoker, M.S. 2010: Depositional environments and chronology of Late Weichselian glaciation and deglaciation in the central North Sea. *Boreas*, 39, 471-491.

Graham, A.G., Stoker, M.S., Lonergan, L., Bradwell, T. and Stewart, M.A. 2011: The Pleistocene glaciations of the North Sea basin. In Ehlers, J., Gibbard, P.L., Hughes, P.D. (eds.): *Quaternary glaciations – extent and chronology: a closer look. Developments in Quaternary Sciences*, 261-278, Elsevier, Amsterdam.

- Greenwood, S. L. & Clark, C. D. 2009: Reconstructing the last Irish Ice Sheet 1: changing flow geometries and ice flow dynamics deciphered from the glacial landform record. *Quaternary Science Reviews* 28, 3085-3100.
- Grousset, F. E., Labeyrie, L., Sinko, J. A., Cremer, M., Bond, G., Duprat, J., Cortijo, E. & Huon, S. 1993: Patterns of ice-rafted detritus in the glacial North Atlantic (40–55 N). *Paleoceanography* 8, 175-192.
- Gwiazda, R. H., Hemming, S. R. & Broecker, W. S. 1996: Provenance of icebergs during Heinrich event 3 and the contrast to their sources during other Heinrich episodes. *Paleoceanography* 11, 371-378.
- Haapaniemi, A. I. 2006: Palaeoceanography of the NE Atlantic during late MIS4 and early MIS3 – correlation of foraminiferal abundance changes in the Goban Spur with Greenland ice-core records. MSc thesis, University of Wales, Bangor.
- Haapaniemi, A. I., Scourse, J. D., Peck, V. L., Kennedy, H., Kennedy, P., Hemming, S. R., Furze, M. F. A., Pieńkowski, A. J., Austin, W. E. N., Walden, J., Wadsworth, E. & Hall, I. R. 2010: Source, timing, frequency and flux of ice-rafted detritus to the Northeast Atlantic margin, 30-12 ka: testing the Heinrich precursor hypothesis. *Boreas* 39, 576-591.
- Hall, I. R., Colmenero-Hidalgo, E., Zahn, R., Peck, V. L. & Hemming, S. R. 2011: Centennial-to millennial-scale ice-ocean interactions in the subpolar northeast Atlantic 18–41 kyr ago. *Paleoceanography* 26, PA2224.
- Hebbeln, D. and Wefer, G. 1997: Late Quaternary paleoceanography in the Fram Strait. *Paleoceanography*, 12, 65-78.
- Hebbeln, D., Henrich, R. & Baumann, K. H. 1998: Paleoceanography of the last interglacial/glacial cycle in the Polar North Atlantic. *Quaternary Science Reviews* 17, 125-153.
- Heinrich, H. 1988: Origin and consequences of cyclic ice rafting in the northeast Atlantic Ocean during the past 130,000 years. *Quaternary research* 29, 142-152.
- Hemming, S. R. 2004: Heinrich events: Massive late Pleistocene detritus layers of the North Atlantic and their global climate imprint. *Reviews of Geophysics* 42, RG1005.
- Hennekam, R. & de Lange, G. 2012: X-ray fluorescence core scanning of wet marine sediments: methods to improve quality and reproducibility of high-resolution paleoenvironmental records. *Limnology and Oceanography: Methods* 10, 991-1003.



- Hesse, T., Butzin, M., Bickert, T. & Lohmann, G. 2011: A model-data comparison of  $\delta^{13}\text{C}$  in the glacial Atlantic Ocean. *Paleoceanography* 26, PA3220.
- Hewitt, C., Stouffer, R., Broccoli, A., Mitchell, J. & Valdes, P. J. 2003: The effect of ocean dynamics in a coupled GCM simulation of the Last Glacial Maximum. *Climate Dynamics* 20, 203-218.
- Hibbert, F. D., Austin, W. E. N., Leng, M. J. & Gatliff, R. W. 2010: British Ice Sheet dynamics inferred from North Atlantic ice-rafted debris records spanning the last 175 000 years. *Journal of Quaternary Science* 25, 461-482.
- Hodell, D. A., Channell, J. E., Curtis, J. H., Romero, O. E. & Röhl, U. 2008: Onset of “Hudson Strait” Heinrich events in the eastern North Atlantic at the end of the middle Pleistocene transition ( $\sim 640$  ka)? *Paleoceanography* 23, PA4218.
- Howe, J. A., Dove, D., Bradwell, T. & Gafeira, J. 2012: Submarine geomorphology and glacial history of the Sea of the Hebrides, UK. *Marine Geology* 315, 64-76.
- Hughes, A. L., Gyllencreutz, R., Lohne, Ø. S., Mangerud, J. & Svendsen, J. I. 2016: The last Eurasian ice sheets—a chronological database and time-slice reconstruction, DATED-1. *Boreas* 45, 1-45.
- Jansen, J. H. F., Van der Gaast, S. J., Koster, B. & Vaars, A. J. 1998: CORTEX, a shipboard XRF-scanner for element analyses in split sediment cores. *Marine Geology* 151, 143-153.
- Jonkers, L., Moros, M., Prins, M. A., Dokken, T., Dahl, C. A., Dijkstra, N., Perner, K. & Brummer, G. J. A. 2010: A reconstruction of sea surface warming in the northern North Atlantic during MIS 3 ice-rafting events. *Quaternary Science Reviews* 29, 1791-1800.
- Joughin, I. & Alley, R. B. 2011: Stability of the West Antarctic ice sheet in a warming world. *Nature Geoscience* 4, 506-513.
- Joughin, I., Smith, B.E. and Medley, B. 2014: Marine ice sheet collapse potentially under way for the Thwaites Glacier Basin, West Antarctica. *Science*, 344, 735-738.
- Kido, Y., Koshikawa, T. & Tada, R. 2006: Rapid and quantitative major element analysis method for wet fine-grained sediments using an XRF microscanner. *Marine Geology* 229, 209-225.

- Kilfeather, A. A., Ó Cofaigh, C., Lloyd, J. M., Dowdeswell, J. A., Xu, S. & Moreton, S. G. 2011: Ice-stream retreat and ice-shelf history in Marguerite Trough, Antarctic Peninsula: Sedimentological and foraminiferal signatures. *Geological Society of America Bulletin* 123, 997-1015.
- Knutz, P. C., Austin, W. E. N. & Jones, E. J. W. 2001: Millennial-scale depositional cycles related to British Ice Sheet variability and North Atlantic paleocirculation since 45 kyr BP, Barra Fan, UK margin. *Paleoceanography* 16, 53-64.
- Kuijpers, A., Troelstra, S. R., Prins, M. A., Linthout, K., Akhmetzhanov, A., Bouryak, S., Bachmann, M. F., Lassen, S., Rasmussen, S. & Jensen, J. B. 2003: Late Quaternary sedimentary processes and ocean circulation changes at the Southeast Greenland margin. *Marine Geology* 195, 109-129.
- Kylander, M. E., Ampel, L., Wohlfarth, B. & Veres, D. 2011: High-resolution X-ray fluorescence core scanning analysis of Les Echets (France) sedimentary sequence: new insights from chemical proxies. *Journal of Quaternary Science* 26, 109-117.
- Lekens, W.A.H., Sejrup, H.P., Haflidason, H., Knies, J. and Richter, T. 2006: Meltwater and ice rafting in the southern Norwegian Sea between 20 and 40 calendar kyr BP: Implications for Fennoscandian Heinrich events. *Paleoceanography*, 21, PA3013.
- Licht, K. J. & Hemming, S. R. 2017: Analysis of Antarctic glacigenic sediment provenance through geochemical and petrologic applications. *Quaternary Science Reviews* 164, 1-24.
- Lippold, J., Luo, Y., Francois, R., Allen, S. E., Gherardi, J., Pichat, S., Hickey, B. & Schulz, H. 2012: Strength and geometry of the glacial Atlantic Meridional Overturning Circulation. *Nature Geoscience* 5, 813-816.
- Lopez, M. 2004: CASQ and giant CALYPSO piston cores from the Goban Spur: Under/over sampling and preliminary age model. MSc thesis, University of Wales, Bangor.
- Lowe, J. J., Rasmussen, S. O., Björck, S., Hoek, W. Z., Steffensen, J. P., Walker, M. J., Yu, Z. C. & Intimate Group, 2008: Synchronisation of palaeoenvironmental events in the North Atlantic region during the Last Termination: a revised protocol recommended by the INTIMATE group. *Quaternary Science Reviews* 27, 6-17.
- Löwemark, L., Chen, H. F., Yang, T. N., Kylander, M., Yu, E. F., Hsu, Y. W., Lee, T. Q., Song, S. R. & Jarvis, S. 2011: Normalizing XRF-scanner data: a cautionary note on the

interpretation of high-resolution records from organic-rich lakes. *Journal of Asian Earth Sciences* 40, 1250-1256.

Lynch-Stieglitz, J., Adkins, J. F., Curry, W. B., Dokken, T., Hall, I. R., Herguera, J. C., Hirschi, J. J. M., Ivanova, E. V., Kissel, C., Marchal, O. & Marchitto, T. M. 2007: Atlantic meridional overturning circulation during the Last Glacial Maximum. *Science* 316, 66-69.

Mao, L., Piper, D. J., Saint-Ange, F., Andrews, J. T. & Kienast, M. 2014: Provenance of sediment in the Labrador Current: a record of hinterland glaciation over the past 125 ka. *Journal of Quaternary Science* 29, 650-660.

Marchitto, T. M. & Broecker, W. S. 2006: Deep water mass geometry in the glacial Atlantic Ocean: A review of constraints from the paleonutrient proxy Cd/Ca. *Geochemistry, Geophysics, Geosystems* 7, Q12003.

Mouginot, J., Rignot, E., Scheuchl, B., Fenty, I., Khazendar, A., Morlighem, M., Buzzi, A. and Paden, J. 2015: Fast retreat of Zachariæ Isstrøm, northeast Greenland. *Science*, 350, 1357-1361.

Ó Cofaigh, C. & Evans, D. J. 2007: Radiocarbon constraints on the age of the maximum advance of the British–Irish Ice Sheet in the Celtic Sea. *Quaternary Science Reviews* 26, 1197-1203.

Ó Cofaigh, C., Dunlop, P. & Benetti, S. 2012: Marine geophysical evidence for Late Pleistocene ice sheet extent and recession off northwest Ireland. *Quaternary Science Reviews* 44, 147-159.

Ó Cofaigh, C., Telfer, M. W., Bailey, R. M. & Evans, D. J. 2012: Late Pleistocene chronostratigraphy and ice sheet limits, southern Ireland. *Quaternary Science Reviews* 44, 160-179.

Ó Cofaigh, C., Dowdeswell, J. A., Jennings, A. E., Hogan, K. A., Kilfeather, A., Hiemstra, J. F., Noormets, R., Evans, J., McCarthy, D. J., Andrews, J. T. & Lloyd, J. M. 2013: An extensive and dynamic ice sheet on the West Greenland shelf during the last glacial cycle. *Geology* 41, 219-222.

Ó Cofaigh, C. 2014: Britice-Chrono: constraining rates and styles of marine-influenced ice sheet retreat, 16<sup>th</sup> July- 25<sup>th</sup> August 2014 RRS JAMES COOK Cruise Report-JC106 106 pp unpublished.

Ó Cofaigh, C. 2015: Britice-Chrono: constraining rates and styles of marine-influenced ice sheet retreat, 3<sup>rd</sup> July- 2<sup>nd</sup> August 2015 RRS JAMES COOK Cruise Report-JC123 34 pp unpublished.

Ó Cofaigh, C., Weilbach, K., Lloyd, J. M., Benetti, S., Louise, S. L., Purcell, C., Chiverrell, R. C., Dunlop, P., Saher, M., Livingstone, S. J., Van Landeghem, K. J. J., Moreton, S. G., Clark, C. D., & Fabel, D. Early deglaciation of the British Irish Ice Sheet on the Atlantic shelf northwest of Ireland driven by glacioisostatic depression and high relative sea level. *Quaternary Science Reviews*, in press.

Patton, H., Hubbard, A., Bradwell, T., Glasser, N. F., Hambrey, M. J. & Clark, C. D. 2013: Rapid marine deglaciation: asynchronous retreat dynamics between the Irish Sea Ice Stream and terrestrial outlet glaciers. *Earth Surface Dynamics* 1, 53-65.

Payne, A. J., Vieli, A., Shepherd, A. P., Wingham, D. J. & Rignot, E. 2004: Recent dramatic thinning of largest West Antarctic ice stream triggered by oceans. *Geophysical Research Letters* 31, L23401.

Peck, V. L., Hall, I. R., Zahn, R., Elderfield, H., Grousset, F., Hemming, S. R. & Scourse, J. D. 2006: High resolution evidence for linkages between NW European ice sheet instability and Atlantic Meridional Overturning Circulation. *Earth and Planetary Science Letters* 243, 476-488.

Peck, V. L., Hall, I. R., Zahn, R., Grousset, F., Hemming, S. R. & Scourse, J. D. 2007: The relationship of Heinrich events and their European precursors over the past 60ka BP: a multi-proxy ice-rafted debris provenance study in the North East Atlantic. *Quaternary Science Reviews* 26, 862-875.

Peltier, W.R. 1994: Ice age paleotopography. *Science*, 265, 195-201.

Peters, C., Walden, J. & Austin, W. E. N. 2008: Magnetic signature of European margin sediments: Provenance of ice-rafted debris and the climatic response of the British ice sheet during Marine Isotope Stages 2 and 3. *Journal of Geophysical Research: Earth Surface* 113, F03007.

Peters, J. L., Benetti, S., Dunlop, P. & Ó Cofaigh, C. 2015: Maximum extent and dynamic behaviour of the last British–Irish Ice Sheet west of Ireland. *Quaternary Science Reviews* 128, 48-68.

- Plaza-Morlote, M., Rey, D., Santos, J. F., Ribeiro, S., Heslop, D., Bernabeu, A., Mohamed, K. J., Rubio, B. & Martíns, V. 2017: Southernmost evidence of large European Ice Sheet-derived freshwater discharges during the Heinrich Stadials of the Last Glacial Period (Galician Interior Basin, Northwest Iberian Continental Margin). *Earth and Planetary Science Letters* 457, 213-226.
- Pope, E. L., Talling, P. J., Hunt, J. E., Dowdeswell, J. A., Allin, J. R., Cartigny, M. J., Long, D., Mozzato, A., Stanford, J.D., Tappin, D.R. & Watts, M. 2016: Long-term record of Barents Sea Ice Sheet advance to the shelf edge from a 140,000 year record. *Quaternary Science Reviews* 150, 55-66.
- Powell, R. D. 1981: A model for sedimentation by tidewater glaciers. *Annals of Glaciology* 2, 129-134.
- Praeg, D., McCarron, S., Dove, D., Ó Cofaigh, C., Scott, G., Monteys, X., Facchin, L., Romeo, R. & Coxon, P. 2015: Ice sheet extension to the Celtic Sea shelf edge at the Last Glacial Maximum. *Quaternary Science Reviews* 111, 107-112.
- Prins, M. A., Troelstra, S. R., Kruk, R. W., Van Der Borg, K., De Jong, A. F. M. & Weltje, G. J. 2001: The late Quaternary sedimentary record of Reykjanes Ridge, north Atlantic. *Radiocarbon* 43, 939-947.
- Purcell, C., 2014: Late Quaternary glaciation of the continental shelf offshore of NW Ireland. MSc thesis, Durham University.
- Richter, T. O., Van der Gaast, S., Koster, B., Vaars, A., Gieles, R., de Stigter, H. C., De Haas, H. & van Weering, T. C. 2006: The Avaatech XRF Core Scanner: technical description and applications to NE Atlantic sediments. *Geological Society, London, Special Publications* 267, 39-50.
- Rignot, E., Velicogna, I., van den Broeke, M. R., Monaghan, A. & Lenaerts, J. T. 2011: Acceleration of the contribution of the Greenland and Antarctic ice sheets to sea level rise. *Geophysical Research Letters* 38, L05503.
- Rothwell, R. G., Hoogakker, B., Thomson, J., Croudace, I. W. & Frenz, M. 2006: Turbidite emplacement on the southern Balearic Abyssal Plain (western Mediterranean Sea) during Marine Isotope Stages 1–3: an application of ITRAX XRF scanning of sediment cores to lithostratigraphic analysis. *Geological Society, London, Special Publications*, 267, 79-98.

- Ruddiman, W. F. 1977: Late Quaternary deposition of ice-rafted sand in the subpolar North Atlantic (lat 40 to 65 N). *Geological Society of America Bulletin* 88, 1813-1827.
- Scourse, J. D., Austin, W. E. N., Bateman, R. M., Catt, J. A., Evans, C. D. R., Robinson, J. E. & Young, J. R. 1990: Sedimentology and micropalaeontology of glacial marine sediments from the central and southwestern Celtic Sea. *Geological Society, London, Special Publications* 53, 329-347.
- Scourse, J. D., 1991: Late Pleistocene stratigraphy and palaeobotany of the Isles of Scilly. *Philosophical Transactions of the Royal Society of London B* 334, 405-448.
- Scourse, J. D., Hall, I. R., McCave, I. N., Young, J. R. & Sugdon, C. 2000: The origin of Heinrich layers: evidence from H2 for European precursor events. *Earth and Planetary Science Letters* 182, 187-195.
- Scourse, J. D., Haapaniemi, A. I., Colmenero-Hidalgo, E., Peck, V. L., Hall, I. R., Austin, W. E., Knutz, P. C. & Zahn, R. 2009: Growth, dynamics and deglaciation of the last British-Irish ice sheet: the deep-sea ice-rafted detritus record. *Quaternary Science Reviews* 28, 3066-3084.
- Sejrup, H. P., Hjelstuen, B. O., Dahlgren, K. T., Haflidason, H., Kuijpers, A., Nygård, A., Praeg, D., Stoker, M. S. & Vorren, T. O. 2005: Pleistocene glacial history of the NW European continental margin. *Marine and Petroleum Geology* 22, 1111-1129.
- Sejrup, H.P., Clark, C.D. and Hjelstuen, B.O. 2016: Rapid ice sheet retreat triggered by ice stream debudding: Evidence from the North Sea. *Geology*, 44, 355-358.
- Sheldon, C., Jennings, A., Andrews, J. T., Ó Cofaigh, C., Hogan, K., Dowdeswell, J. A. & Seidenkrantz, M. S. 2016: Ice stream retreat following the LGM and onset of the west Greenland current in Uummannaq Trough, west Greenland. *Quaternary Science Reviews* 147, 27-46.
- Shennan, I., Bradley, S., Milne, G., Brooks, A., Bassett, S. and Hamilton, S. 2006: Relative sea-level changes, glacial isostatic modelling and ice-sheet reconstructions from the British Isles since the Last Glacial Maximum. *Journal of Quaternary Science*, 216, 585-599.
- Small, D., Parrish, R.R., Austin, W.E., Cawood, P.A. and Rinterknecht, V. 2013a: Provenance of North Atlantic ice-rafted debris during the last deglaciation—A new application of U-Pb rutile and zircon geochronology. *Geology* 41, 155-158.

Small, D., Austin, W. & Rinterknecht, V. 2013b: Freshwater influx, hydrographic reorganization and the dispersal of ice-rafted detritus in the sub-polar North Atlantic Ocean during the last deglaciation. *Journal of Quaternary Science* 28, 527-535.

Small, D., Rinterknecht, V., Austin, W. E. N., Bates, R., Benn, D. I., Scourse, J. D., Bourlès, D. L., Hibbert, F. D. & ASTER Team. 2016: Implications of 36 Cl exposure ages from Skye, northwest Scotland for the timing of ice stream deglaciation and deglacial ice dynamics. *Quaternary Science Reviews* 150, 130-145.

Small, D., Benetti, S., Dove, D., Ballantyne, C. K., Fabel, D., Clark, C. D., Gheorghiu, D. M., Newall, J. & Xu, S. 2017: Cosmogenic exposure age constraints on deglaciation and flow behaviour of a marine-based ice stream in western Scotland, 21–16 ka. *Quaternary Science Reviews* 167, 30-46.

Smedley, R. K., Scourse, J. D., Small, D., Hiemstra, J. F., Duller, G. A. T., Bateman, M. D., Burke, M. J., Chiverrell, R. C., Clark, C. D., Davies, S. M. & Fabel, D. 2017: New age constraints for the limit of the British–Irish Ice Sheet on the Isles of Scilly. *Journal of Quaternary Science* 32, 48-62.

Snoeckx, H., Grousset, F., Revel, M. & Boelaert, A. 1999: European contribution of ice-rafted sand to Heinrich layers H3 and H4. *Marine Geology* 158, 197-208.

Stanford, J. D., Rohling, E. J., Bacon, S. & Holliday, N. P. 2011: A review of the deep and surface currents around Eirik Drift, south of Greenland: Comparison of the past with the present. *Global and Planetary Change* 79, 244-254.

Stewart, H. A. 2004: MD 141/ALIENOR cruise report: first leg Lisbon-Cardiff. Nottingham, UK, British Geological Survey, 32 pp. (IR/04/126) unpublished.

Stoker, M. S., Bradwell, T., Howe, J. A., Wilkinson, I. P. & McIntyre, K. 2009: Lateglacial ice-cap dynamics in NW Scotland: evidence from the fjords of the Summer Isles region. *Quaternary Science Reviews* 28, 3161-3184.

Stokes, C. R. & Clark, C. D. 2001: Palaeo-ice streams. *Quaternary Science Reviews* 20, 1437-1457.

Stokes, C. R., Tarasov, L., Blomdin, R., Cronin, T.M., Fisher, T.G., Gyllencreutz, R., Hättestrand, C., Heyman, J., Hindmarsh, R.C., Hughes, A.L. & Jakobsson, M. 2015: On the

reconstruction of palaeo-ice sheets: recent advances and future challenges. *Quaternary Science Reviews* 125, 15-49.

Svendsen, J.I., Briner, J.P., Mangerud, J. and Young, N.E. 2015: Early break-up of the Norwegian channel ice stream during the last glacial maximum. *Quaternary Science Reviews*, 107, 231-242.

Syms, C. 2008: *Principal components analysis*. In Jorgensen, S. E. & Fath, B. D. (eds.): *Encyclopedia of Ecology*, 2940-2949, Elsevier, Oxford.

Syvitski, J.P. 1991: Towards an understanding of sediment deposition on glaciated continental shelves. *Continental Shelf Research* 11, 897-937.

Thompson, S.R. 1995: Sills of the global ocean: a compilation. *Ocean Modelling*, 109, 7-9.

Tjallingii, R., Röhl, U., Kölling, M. & Bickert, T. 2007: Influence of the water content on X-ray fluorescence core-scanning measurements in soft marine sediments. *Geochemistry, Geophysics, Geosystems* 8, Q02004.

Van Rooij, D., Blamart, D., Richter, T., Wheeler, A., Kozachenko, M. & Henriët, J. P. 2007: Quaternary sediment dynamics in the Belgica mound province, Porcupine Seabight: ice-rafting events and contour current processes. *International Journal of Earth Sciences* 96, 121-140.

Voelker, A. H., Grootes, P. M., Nadeau, M. J. & Sarnthein, M. 2000: Radiocarbon levels in the Iceland Sea from 25–53 kyr and their link to the Earth's magnetic field intensity. *Radiocarbon* 42, 437-452.

von Eynatten, H., Tolosana-Delgado, R. & Karius, V. 2012: Sediment generation in modern glacial settings: grain-size and source-rock control on sediment composition. *Sedimentary Geology* 280, 80-92.

Wanamaker Jr, A. D., Butler, P. G., Scourse, J. D., Heinemeier, J., Eiríksson, J., Knudsen, K. L. & Richardson, C. A. 2012: Surface changes in the North Atlantic meridional overturning circulation during the last millennium. *Nature communications* 3, 899.

Walden, J., Wadsworth, E., Austin, W. E. N., Peters, C., Scourse, J. D. & Hall, I. R. 2007: Compositional variability of ice-rafted debris in Heinrich layers 1 and 2 on the northwest European continental slope identified by environmental magnetic analyses. *Journal of Quaternary Science* 22, 163-172.



- Watkins, S. J., Maher, B. A. & Bigg, G. R. 2007: Ocean circulation at the Last Glacial Maximum: A combined modeling and magnetic proxy-based study. *Paleoceanography* 22, PA2204.
- Weltje, G. J. & Tjallingii, R. 2008: Calibration of XRF core scanners for quantitative geochemical logging of sediment cores: theory and application. *Earth and Planetary Science Letters* 274, 423-438.
- White, L. F., Bailey, I., Foster, G. L., Allen, G., Kelley, S. P., Andrews, J. T., Hogan, K., Dowdeswell, J. A. & Storey, C. D. 2016: Tracking the provenance of Greenland-sourced, Holocene aged, individual sand-sized ice-rafted debris using the Pb-isotope compositions of feldspars and  $^{40}\text{Ar}/^{39}\text{Ar}$  ages of hornblendes. *Earth and Planetary Science Letters* 433, 192-203.
- Wilson, L. J. & Austin, W. E. N. 2002: Millennial and sub-millennial-scale variability in sediment colour from the Barra Fan, NW Scotland: implications for British ice sheet dynamics. *Geological Society, London, Special Publications* 203, 349-365.
- Wittmeier, H. E., Bakke, J., Vasskog, K. & Trachsel, M. 2015: Reconstructing Holocene glacier activity at Langfjordjøkelen, Arctic Norway, using multi-proxy fingerprinting of distal glacier-fed lake sediments. *Quaternary Science Reviews* 114, 78-99.

## Appendices

### Appendix 1

Table A1. Summary table of radiocarbon dates obtained by the BRITICE-CHRONO consortium used in this thesis. \* Warning date most likely out of range

Core name	Publication Code	Sample depth (cm)	Conventional Radiocarbon Age (years BP $\pm 1\sigma$ )	Calibrated Age (cal yrs BP $\pm 1\sigma$ ) R = 0 years	Calibrated Age (cal yrs BP $\pm 1\sigma$ ) R = 300 years	Calibrated Age (cal yrs BP $\pm 1\sigma$ ) R = 700 years
JC106-012VC	SUERC-61838	62-63	23272 $\pm$ 81	27233 $\pm$ 216	26889 $\pm$ 323	26374 $\pm$ 274
JC106-013VC	SUERC-58296	288-289	55394 $\pm$ 2454 *			
JC106-018VC	SUERC-66648	137.5-140	Indistinguishable from background	infinite age		
JC106-018VC	SUERC-61842	177-178	Indistinguishable from background	infinite age		
JC106-019VC	SUERC-58301	122-123	Indistinguishable from background	infinite age		
JC106-051PC	SUERC-58309	463	Indistinguishable from background	infinite age		
JC106-068VC	SUERC-62458	207-209.5	>54229	infinite age		
JC106-068VC	SUERC-58320	230-232.5	42507 $\pm$ 505	45472 $\pm$ 904	45218 $\pm$ 888	44879 $\pm$ 900
JC106-087VC	SUERC-58330	187.5 cm	8500 $\pm$ 37	9123 $\pm$ 129	8704 $\pm$ 153	8265 $\pm$ 92
JC106-087VC	SUERC-68238	205-206	9200 $\pm$ 36	10010 $\pm$ 147	9550 $\pm$ 90	9123 $\pm$ 127
JC106-087VC	SUERC-68239	467.5	44075 $\pm$ 623	47006 $\pm$ 1411	46707 $\pm$ 1360	46317 $\pm$ 1286
JC106-102VC	SUERC-59510	72	16692 $\pm$ 45	19669 $\pm$ 186	19300 $\pm$ 190	18835 $\pm$ 106
JC106-102VC	UCIAMS-164437	247	21000 $\pm$ 110	24804 $\pm$ 388	24387 $\pm$ 339	23939 $\pm$ 300
JC106-112VC	SUERC-63584	51	22582 $\pm$ 67	26382 $\pm$ 257	26082 $\pm$ 178	25791 $\pm$ 153
JC106-112VC	SUERC-63585	59.5	22572 $\pm$ 71	26372 $\pm$ 259	26074 $\pm$ 180	25783 $\pm$ 159
JC106-139VC	UCIAMS-176381	151-154cm	18920 $\pm$ 80	22389 $\pm$ 184	22082 $\pm$ 249	21583 $\pm$ 269
JC106-139VC	SUERC-59488	172	52943 $\pm$ 1855 *			
JC106-139VC	SUERC-59489	208	11160 $\pm$ 39	12662 $\pm$ 88	12379 $\pm$ 206	11591 $\pm$ 267

JC106-139VC	SUERC-58379	305.5	13017 ± 39	14978 ± 221	14276 ± 253	13789 ± 137
JC106-139VC	SUERC-59483	312	Indistinguishable from	infinite age		
JC106-139VC	SUERC-59490	331.5	13048 ± 38	15031 ± 204	14345 ± 284	13825 ± 133
JC106-139VC	SUERC-59491	332.5	11280 ± 38	12749 ± 114	12542 ± 104	11866 ± 202
JC106-139VC	SUERC-59486	339	12729 ± 37	14299 ± 263	13910 ± 131	13467 ± 120
JC106-139VC	SUERC-59487	348.5	20519 ± 61	24179 ± 212	23850 ± 225	23371 ± 265
JC106-139VC	SUERC-58382	Shoe	13023 ± 38	14989 ± 216	14287 ± 259	13796 ± 135
JC106-146VC	UCIAMS-176382	223-225	20200 ± 80	23828 ± 251	23478 ± 288	23007 ± 290
JC106-146VC	UCIAMS-176383	369-372	22030 ± 100	25897 ± 178	25662 ± 225	25265 ± 302
JC106-146VC	UCIAMS-164440	389-392	20730 ± 100	24424 ± 331	24089 ± 270	23646 ± 300
JC106-149VC	UBA-29958	40	9873 ± 40	10824 ± 165	10441 ± 133	9972 ± 172
JC106-149VC	UBA-29138	51	12951 ± 48	14843 ± 321	14158 ± 196	13708 ± 161
JC106-149VC	UBA-29959	220	9501 ± 46	10352 ± 139	10005 ± 167	9464 ± 80
JC106-149VC	UBA-29960	420	18441 ± 94	21854 ± 290	21470 ± 319	20918 ± 292
JC106-149VC	SUERC-59509	421	17155 ± 47	20204 ± 190	19846 ± 202	19375 ± 180
JC106-153VC	UCIAMS-164432	277-279	19210 ± 110	22679 ± 270	22365 ± 261	21956 ± 321
JC123-010VC	UCIAMS-176373	526-536	15270 ± 45	18071 ± 171	17749 ± 176	17250 ± 198
JC123-012VC	SUERC-64114	170	11101 ± 38	12628 ± 80	12282 ± 218	11487 ± 249
JC123-012VC	SUERC-67432	178	11138 ± 38	12649 ± 84	12343 ± 212	11551 ± 257
JC123-015VC	SUERC-67433	200	13704 ± 40	15991 ± 178	15547 ± 220	14956 ± 229
JC123-018VC	SUERC-67434	451	13851 ± 41	16178 ± 169	15796 ± 186	15187 ± 145
JC123-039VC	SUERC-68228	231-234	18080 ± 52	21384 ± 239	20964 ± 212	20470 ± 186
JC123-039VC	SUERC-71557	390-395	18291 ± 50	21677 ± 202	21252 ± 233	20729 ± 184
JC123-045VC	SUERC-67451	424	14375 ± 43	16947 ± 220	16487 ± 221	15953 ± 180
JC123-045VC	SUERC-67452	445	14196 ± 41	16679 ± 235	16241 ± 180	15704 ± 208
JC123-045VC	SUERC-66654	491-494	15501 ± 42	18346 ± 165	17996 ± 155	17546 ± 171
JC123-049VC	UCIAMS-176376	65-74	16345 ± 50	19230 ± 204	18880 ± 118	18510 ± 147

## Appendix 2

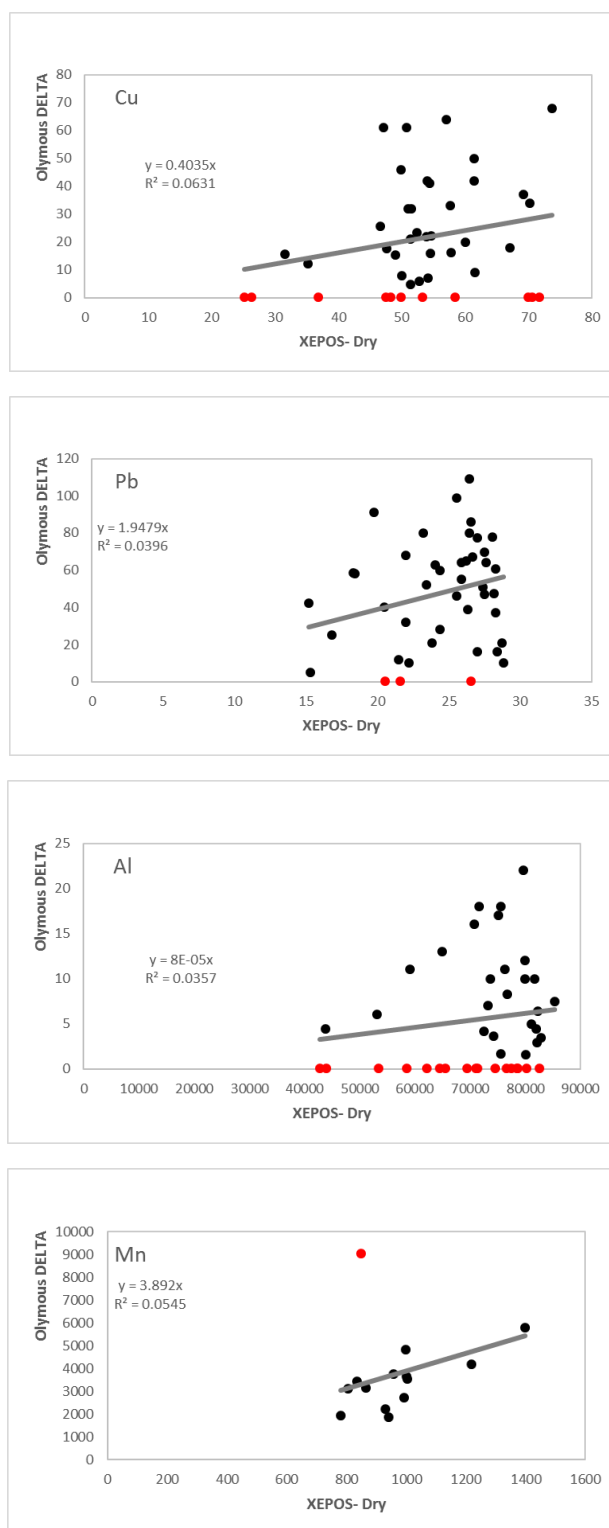
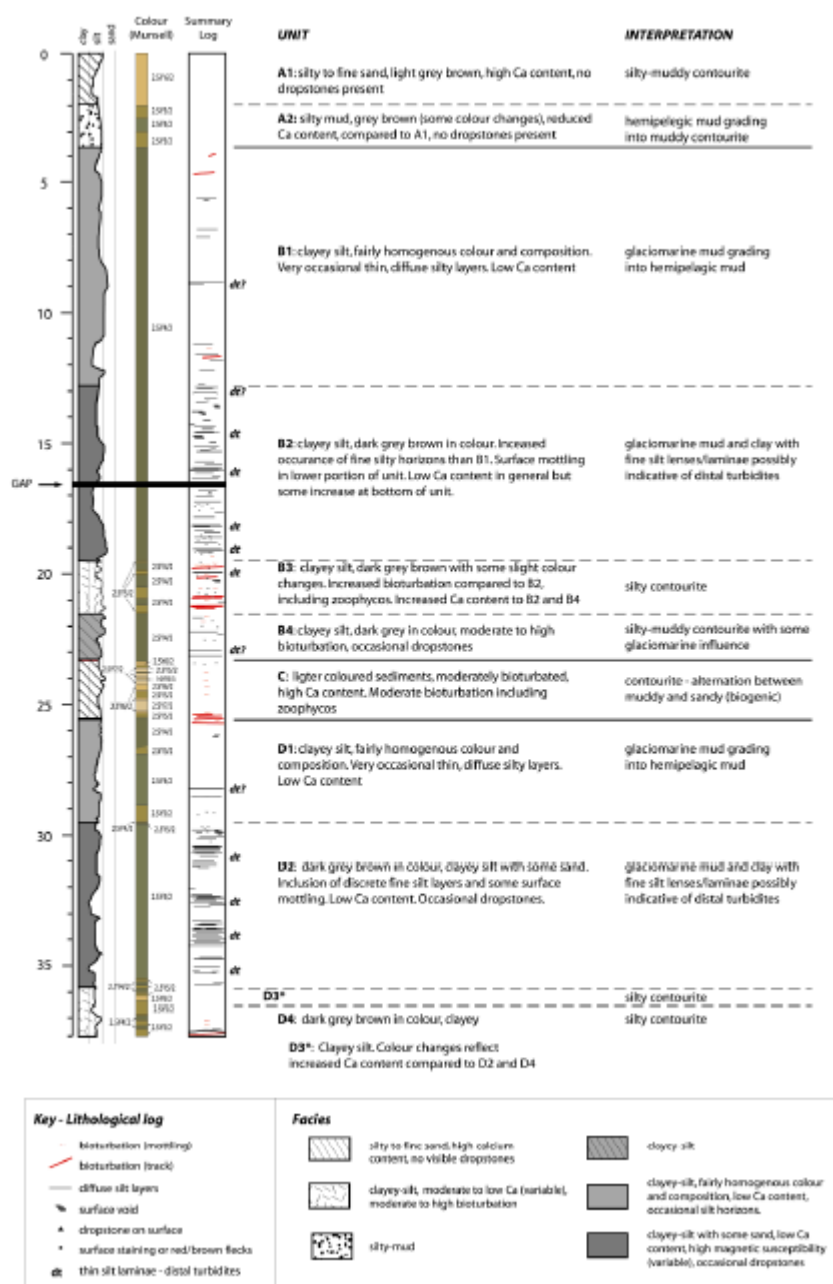


Figure A1. Correlations for the element concentrations of Cu, Pb, and Al for MD04-2820CQ and Mn for MD04-2822. Wet scan data measured by the Olympos DELTA (ppm) and dry subsamples measured by the SPECTRO XEPOS (ppm). Red data points are the deleted outliers or zeros.

## Appendix 3

Figure A.3. MD04-2822 lithological log, unit, facies and depositional interpretation from Hibbert 2016, pers. comm.



# Establishing reliable age models for the North Atlantic deep ocean cores

Establishing reliable age models are critical for all aspects of marine sediment core analysis. Significant issues arise for North Atlantic age models because of the large marine reservoir fluctuations in the glacial North Atlantic (Voelker *et al.* 2000; Peck *et al.* 2006). Consequently, there has been a proliferation in age models which are tuned to Greenland ice core records. This tuning approach ‘phase-locks’ the two records and assumes synchronicity, which therefore inhibits analysis of phasing within abrupt climate transitions (Austin and Hibbert 2012). The following chapter presents the analysis of tephra horizons in a marine sediment core from the North Atlantic, within a high resolution climostratigraphic framework. The aim of this analysis is to establish a time-synchronous marker horizon within the North Atlantic and therefore enable the construction of an independent age model.

Purcell, C.S contribution: The generation of a high resolution *Nps* and IRD concentrations between 450-550 cm depth to help constrain the tephra deposits within a climatic framework.

This chapter was submitted and accepted by Quaternary Geochronology:

Abbott, P.M., Bourne, A.J., Purcell, C.S., Davies, S.M., Scourse, J.D. and Pearce, N.J.G., 2016: Last glacial period cryptotephra deposits in an eastern North Atlantic marine sequence: exploring linkages to the Greenland ice-cores. *Quaternary Geochronology*, **31**, 62-76. Supplementary data is included on the Appendix data CD.

**Last Glacial Period Cryptotephra Deposits in an Eastern North Atlantic Marine  
Sequence: Exploring Linkages to the Greenland Ice-Cores**

**Abstract**

The establishment of a tephra framework for the Greenland ice-cores spanning the last glacial period, particularly between 25-45 ka b2k, provides strong potential for precisely correlating other palaeoclimatic records to these key archives. Tephra-based synchronisation allows the relative timing of past climatic changes recorded within different depositional environments and potential causal mechanisms to be assessed. Recent studies of North Atlantic marine records have demonstrated the potential of tracing cryptotephra horizons in these sequences and the development of protocols now allows a careful assessment of the isochronous nature of such horizons. Here we report on tephrochronological investigations of a marine sequence retrieved from the Goban Spur, Eastern North Atlantic, covering ~25-60 ka b2k. Density and magnetic separation techniques and an assessment of potential transport and depositional mechanisms have identified three previously unknown isochronous tephra horizons along with deposits of the widespread North Atlantic Ash Zone II and Faroe Marine Ash Zone III. Correlations between the new horizons and the Greenland ice-core tephra framework are explored and despite no tie-lines being identified the key roles that high-resolution climatostratigraphy and shard-specific trace element analysis can play within the assessment of correlations is demonstrated. The previously unknown horizons are new additions to the overall North Atlantic tephra framework for the last glacial period and could be key horizons for future correlations.

**1 Introduction**

The tracing of isochronous horizons of volcanic ash between different depositional realms (tephrochronology) has considerable potential for the independent correlation and synchronisation of disparate palaeoclimatic sequences and for assessing the relative timing of past climatic events (Lowe, 2011). The potential of tephrochronology to assess these relative timings is especially pertinent for the last glacial period as there is evidence for several abrupt climatic changes preserved within ice-cores from Greenland (e.g. GRIP Members, 1993; Johnsen et al., 2001; NGRIP Members, 2004) and numerous North Atlantic marine cores (e.g.

Bond et al., 1993, 1997; Van Kreveld et al., 2000; Martrat et al., 2007; Hall et al., 2011; Zumaque et al., 2012).

A large number of tephra horizons have been identified within multiple Greenland ice-cores spanning the last glacial period (Abbott and Davies, 2012; Bourne et al., 2013, 2015b; Davies et al., 2014). Bourne et al. (2015b) in particular increased the number of horizons identified in the NGRIP, NEEM, GRIP and DYE-3 ice-cores and, in combination with past studies, a framework of 99 geochemically characterised tephra deposits has now been defined for the 25-45 ka b2k period. Developing a framework of geochemically characterised horizons with strong stratigraphic and chronological control is an essential first step towards the synchronisation of these records to other palaeoclimatic sequences in a range of environments. A notable feature of the ice-core framework is the dominance of deposits, closely spaced in time, that have similar major element compositions relating to single sources, e.g. the Icelandic Grímsvötn volcanic system. Subtle major element differences can be used to discriminate between some deposits, but others have major element compositions which are indistinguishable (e.g. Bourne et al., 2013).

This compositional similarity presents a challenge when attempting to correlate tephra horizons from sequences with limited chronological and/or stratigraphic control. In these instances it has been widely advocated that any available climatostratigraphic evidence can be used alongside the compositional data to narrow down potential correlatives (e.g. Newnham and Lowe, 1999; Newnham et al., 2004; Pearce et al., 2008; Housley et al., 2012; MacLeod et al., 2015) and that trace element analysis of the tephra deposits may provide a useful secondary compositional fingerprint for testing and assessing the robustness of correlations (e.g. Allan et al., 2008; Abbott et al., 2012, 2014; Albert et al., 2012; Lane et al., 2012; Bramham-Law et al., 2013; Pearce et al., 2014; Bourne et al., 2015a).

Overall, there is an order of magnitude difference between the number of tephra horizons identified in the Greenland ice-cores and North Atlantic marine sequences between 25-60 ka b2k. Only a few marine records have been investigated for their tephra content and there is a tendency to focus on visible horizons or on the coarse-grained components (>150  $\mu\text{m}$ ) (e.g. Lackschewitz and Wallrabe-Adams, 1997; Wastegård and Rasmussen, 2014). As a result, only two ice-marine tie-lines have been defined within the last glacial period. Firstly, the rhyolitic component of the widespread North Atlantic Ash Zone (NAAZ) II ( $55,380 \pm 1184$  a b2k; Svensson et al., 2008) has been traced within multiple ice and marine cores (e.g. Kvamme et al., 1989; Grönvold et al., 1995; Lacasse et al., 1996; Zielinski et al., 1997; Haflidason et al., 2000; Austin et al., 2004). Secondly, Faroe Marine Ash Zone (FMAZ) II, a



visible horizon identified in a number of marine cores from the Faroe Islands region (Wastegård et al., 2006), was traced into the NGRIP ice-core by Davies et al. (2008) (NGRIP 1848 m;  $26,740 \pm 390$  a b2k). A third ice-marine correlation was also proposed between the NGRIP 2066.95 m horizon ( $38,122 \pm 723$  a b2k) and FMAZ III, a thick and relatively scattered zone of glass shards traced between a number of the Faroe Islands region cores (Wastegård et al., 2006; Davies et al., 2010). However, Bourne et al. (2013) later highlighted the complexity of this period and identified a series of closely spaced tephra horizons with similar glass compositions in the NGRIP and NEEM ice-cores. Their compositions all fall within the broad compositional envelope of FMAZ III and the marine deposit has been interpreted as resulting from the amalgamation of primary tephra-fall from a number of volcanic events as a consequence of low sedimentation rates at the marine core sites (Bourne et al., 2013; Griggs et al., 2014). Therefore, the prior correlation between FMAZ III and a single tephra layer in the ice-cores is no longer valid and should not be used as an ice-marine tie-line. However, the tephra layers in the ice may still act as tie-lines if individual homogenous horizons from those single events can be found in marine records. This particular example highlights some of the complexities involved with defining correlations between the records.

In recent years, there has been a shift towards the investigation of the cryptotephra record preserved within marine sediments. Density and magnetic separation techniques, previously applied to terrestrial sequences, have recently been successfully used to extract fine-grained cryptotephtras, preserved as discrete deposits of glass shards, from a number of cores around the North Atlantic (e.g. Abbott et al., 2011, 2013, 2014; Griggs et al., 2014; Davies et al., 2014). Magnetic separation techniques are particularly important for the identification of basaltic cryptotephtras in North Atlantic marine records because of the dominance of basaltic tephra deposits within the Greenland tephra framework (Abbott and Davies, 2012; Bourne et al., 2013, 2015b). In addition to these methodological advances, Griggs et al. (2014) outlined a protocol which uses a range of indicators to determine the potential influence of transportation and depositional processes on the stratigraphic and temporal integrity of marine tephra deposits. To date, these methods and approaches have not been utilised to isolate cryptotephtras in North Atlantic marine sequences covering the 25-60 ka b2k period. The Greenland tephra framework in particular, now demonstrates the potential for tephrochronological synchronisation if common horizons can be identified.

Here we report on tephrochronological investigations of the 25-60 ka b2k period within a marine core retrieved from the Goban Spur area in the eastern North Atlantic (MD04-2820CQ). Potential correlations to the Greenland tephra framework are explored with new

high-resolution proxy data from MD04-2820CQ used to help determine the stratigraphic position of the tephra horizons and trace element analysis is utilised as a secondary compositional fingerprint.

## **2 Materials and Methods**

### **2.1 MD04-2820CQ**

MD04-2820CQ was retrieved from the Goban Spur area (49°05.29'N; 13°25.90'W; Figure 1) and is a reoccupation of the OMEX-2K core site (see Hall and McCave, 1998a,b; Scourse et al., 2000; Haapaniemi et al., 2010). A Ca XRF record and a low-resolution record of the percentage abundance of the polar foraminiferal species *Neogloboquadrina pachyderma* (sinistral) (*Np(s)*) have been used to define a preliminary stratigraphy for the sequence between MIS 3-2. A number of Dansgaard-Oeschger events related to the Greenland Interstadial (GI) events in the Greenland ice-cores are recognised within this record (Figure 2; Rasmussen et al., 2014). Between 450-550 cm depth, high-resolution (up to 1 cm) records of *Np(s)* and ice rafted debris (IRD) concentrations (150 µm-1 mm fraction) were generated to provide a more detailed stratigraphy between DO-12 and DO-8 to help constrain the tephra deposits within a climatic framework (Figure 6).

The tephra content of the core was initially investigated at a low-resolution (5 cm contiguous samples) between 250-650 cm depth. Intervals with distinct peaks in glass shard content above background levels were subsequently re-investigated at 1 cm resolution to refine their stratigraphic position (Figure 2).

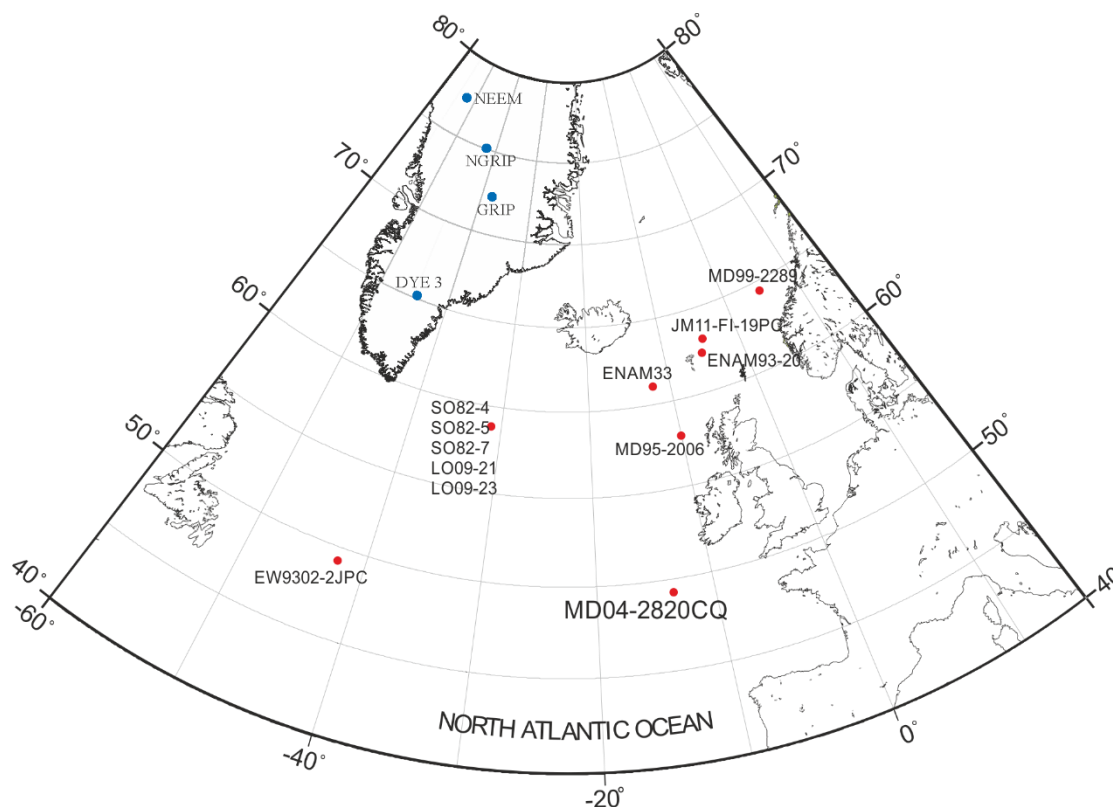


Figure 1 Location map of the MD04-2820CQ core site and other cores referred to within the text.

## 2.2 Extraction of tephra-derived glass shards from marine sequences

From the 5 and 1 cm samples, 0.5 g sub-samples of freeze-dried marine sediments were immersed in 10% HCl overnight to remove carbonate material. Samples were then wet sieved using 125 and 80  $\mu\text{m}$  test sieves and 25  $\mu\text{m}$  nylon mesh. The 25-80  $\mu\text{m}$  fraction was then density separated using sodium polytungstate prepared to the specific gravities of 2.3 and 2.5  $\text{g}/\text{cm}^3$  to split the material into the density fractions of  $<2.3 \text{ g}/\text{cm}^3$ , to remove biogenic material, 2.3-2.5  $\text{g}/\text{cm}^3$ , to isolate rhyolitic material, and  $>2.5 \text{ g}/\text{cm}^3$  to isolate basaltic material (Turney, 1998). To further purify the  $>2.5 \text{ g}/\text{cm}^3$  fraction it was magnetically separated using a Frantz Isodynamic Magnetic Separator. The methodology and conditions for magnetic separation are outlined in Griggs et al. (2014) and allow the separation of non-magnetic quartz material from any paramagnetic basaltic material. The  $>125 \mu\text{m}$  and 80-125  $\mu\text{m}$  grain-size fractions, and the 2.3-2.5  $\text{g}/\text{cm}^3$  and magnetic  $>2.5 \text{ g}/\text{cm}^3$  density fractions, were mounted on microscope slides in Canada Balsam for optical microscopy to quantify their glass shard content.

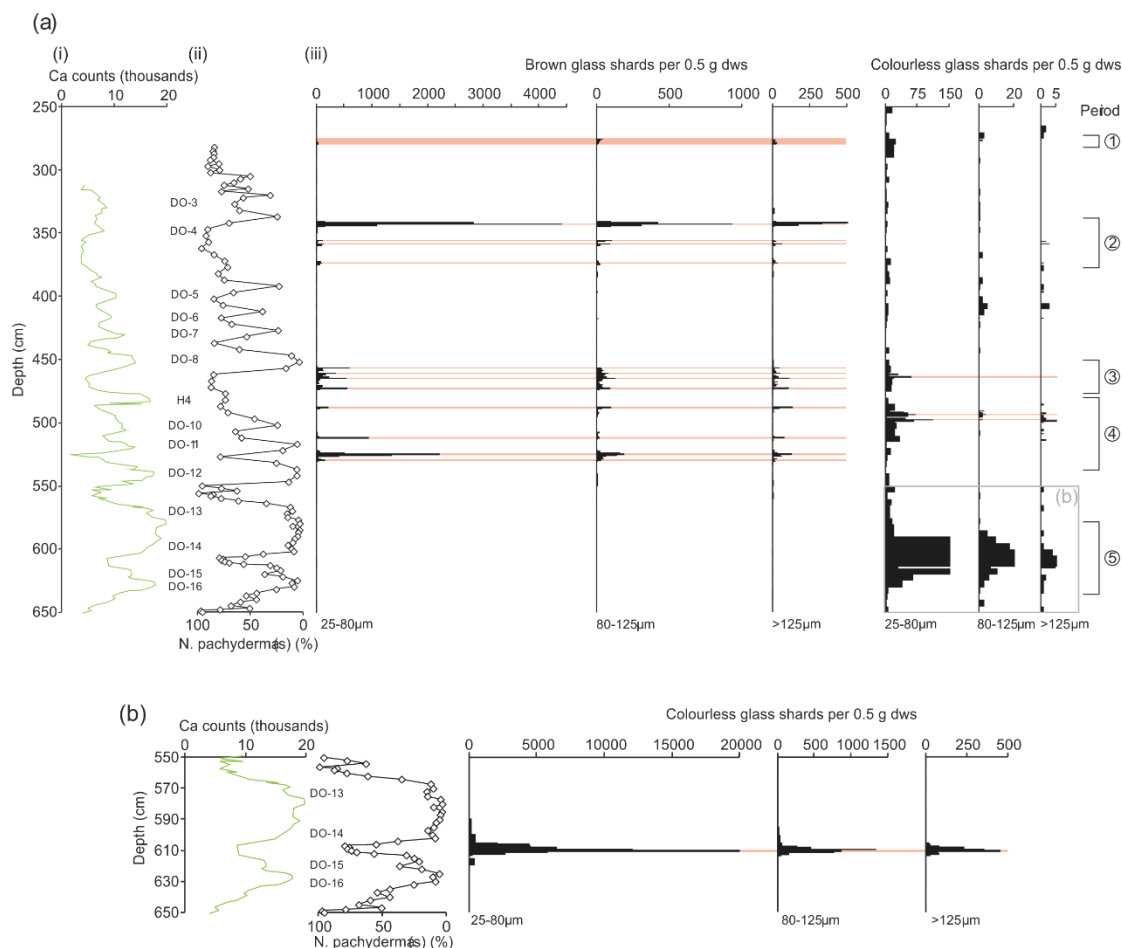


Figure 2 (a) Climate and tepthrostratigraphy of the last glacial period within the MD04-2820CQ core.

(i) XRF (ITRAX core scanning) Ca count rates (ii) percentage abundance of *Neogloboquadrina pachyderma* (sinistral) (iii) tepthrostratigraphy incorporating 5 and 1 cm resolution shard counts. (b) Inset of climate and tepthrostratigraphy of colourless shards between 550-650 cm depth. This figure is an expansion of the colourless shard counts that were truncated on Figure 2a. Red bars denote depth intervals from which glass shards were extracted for geochemical analysis.

### 2.3 Geochemical analysis of individual glass shards

Samples for geochemical analysis were prepared using the procedure outlined in Section 2.2. The fraction of interest was then mounted in epoxy resin on a 28 × 48 mm frosted microscope slide to prepare thin sections of the glass shards. This was achieved by grinding the material using decreasing grades of silicon carbide paper and then polishing the surface using 9, 6 and 1 µm diamond suspension.

Major element compositions of individual shards were determined using electron-probe micro-analysis (EPMA) at the Tephra Analytical Unit, University of Edinburgh, using a Cameca SX100 with five wavelength dispersive spectrometers. The operating conditions followed those outlined in Hayward (2012). Calibration was carried out using pure metals,

synthetic oxides and silicate standards and the secondary standards of Cannetto Lami Lava, Lipari and BCR2g were analysed at regular intervals to monitor for instrumental drift and assess the precision and accuracy of analysed samples (see Table S18). For data comparison all analyses were normalised to an anhydrous basis, i.e. 100 % total oxides, but all raw data analyses are provided in the supplementary information (Tables S1-S17). Statistical comparisons between tephra horizons have been made using the statistical distance test ( $D^2$ ) of Perkins et al. (1995, 1998) and the similarity coefficient function (SC) of Borchardt et al. (1972).

Trace element compositions of single shards from one marine and one ice-core horizon were analysed using laser ablation inductively coupled plasma mass spectrometry (LA-ICP-MS) at Aberystwyth University. A Coherent GeoLas 193 nm Excimer laser coupled with a Thermo Finnigan Element 2 high-resolution sector field mass spectrometer was utilised (Pearce et al., 2011). Due to the small grain size of the shards making up the ice-core horizon, a laser with a beam diameter of 10  $\mu\text{m}$  and a fluence of 10  $\text{J}/\text{cm}^2$  was pulsed at 5 Hz with a flash duration of  $\sim 10$  ns. Despite the larger grain size of shards in the marine horizon, a 10  $\mu\text{m}$  laser beam diameter was used for all analyses to limit any differential impact of fractionation effects. As a potential correlation was being tested, the samples were analysed ‘side-by-side’ to limit any potential influence of instrumental differences between analytical periods (Pearce et al., 2014). Trace element concentrations were calculated using methods outlined in Pearce et al. (2007), with  $^{29}\text{Si}$  previously determined through EPMA used as the internal standard and NIST 612 used as the calibration standard, taking concentrations from Pearce et al. (1997). A correction factor was used to remove bias in analyses caused by fractional effects (Pearce et al., 2011). Trace element concentrations for individual shards are provided in Table S19 and analyses of the secondary standards BCR2g and BHVO-2g are provided in Table S20.

### 3 Results

Of the 80 intervals investigated at low-resolution, 21 were selected for high-resolution analysis resulting in the processing of 105 1 cm samples. Figure 2 integrates low-resolution counts from intervals that were not reanalysed with the high-resolution counts. These overall shard profiles were employed to select 17 samples for geochemical analysis (Figure 2). Overall, the record contains a number of distinct concentrations of brown glass shards and this type of shard is also present as a low background. There is a more consistent background of rhyolitic shards throughout the whole of the studied interval. Given the tephrostratigraphical record, the deposits are grouped into five periods and used as a basis to present results below. To determine

the source of the glass shards, compositions are compared to glass and whole rock analyses to allow material to be assigned to Icelandic rock suites and specific volcanic systems.

### **3.1 Period 1 - Post DO-3**

Between 275-279 cm a dispersed zone of shards with a low concentration of basaltic shards and no discernible peak was identified. Geochemical characterisation shows that the glass in this zone has a highly heterogeneous composition with shards of both transitional alkali and tholeiitic composition present (Figure 3a). Similar heterogeneity is observed in shards from both the less-than and greater-than 80  $\mu\text{m}$  grain-size fractions (Figure 3). This characterisation shows that the deposit is an amalgamation of material from a number of volcanic eruptions from multiple volcanic centres.

According to the stratigraphy for MD04-2820CQ, this zone of ash was deposited during the stadial period following DO-3. In the NGRIP ice-core, FMAZ II was deposited within Greenland Stadial (GS) 3 approximately 1000 years after the cooling transition at the end of GI-3 (Davies et al., 2008). The composition of MD04-2820CQ 275-279 cm demonstrates that this deposit does not directly relate to the homogenous transitional alkali basaltic FMAZ II horizon found within ice and marine sequences (Figure 3b). Some shard analyses fall within the compositional envelopes of the homogenous VZ 1x and the heterogeneous VZ 1 ash zones from cores on the Reykjanes Ridge, but the greater heterogeneity of the 275-279 cm deposit suggests they are unrelated (Figure 3b).

The compositional heterogeneity and lack of a distinct peak in the shard concentration profile strongly suggests that this deposit represents a minor input of material, potentially through iceberg rafting or secondary transportation processes such as bottom currents, and cannot be regarded as isochronous.

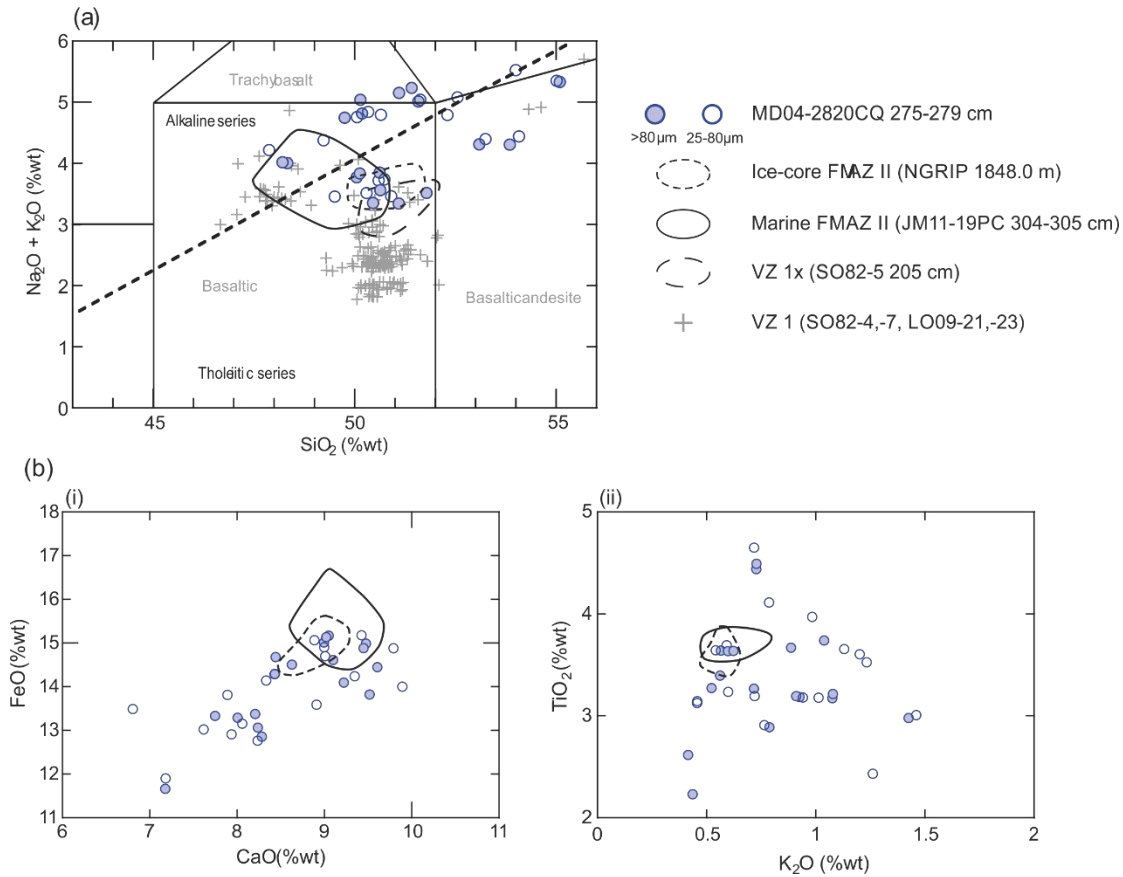


Figure 3 Comparison of glass compositions from MD04-2820CQ 275-279 cm to that from FMAZ II, VZ 1x and VZ 1 characterisations from Davies et al. (2008), Griggs et al. (2014) and Lackschewitz and Wallrabe-Adams (1997). (a) Inset of total alkalis versus silica plot. Division line to separate alkaline and sub-alkaline material from MacDonald and Katsura (1964). Chemical classification and nomenclature after Le Maitre et al. (1989). (b) (i) CaO vs FeO and (ii)  $\text{K}_2\text{O}$  vs  $\text{TiO}_2$  biplot comparisons. NGRIP data from Davies et al. (2008), JM11-19PC data from Griggs et al. (2014) and VZ 1x and VZ 1 data from Lackschewitz and Wallrabe-Adams (1997). All plots on a normalised anhydrous basis.

### 3.2 Period 2 – DO-5 to DO-3

The highest glass shard concentration peak in the 25-80  $\mu\text{m}$  fraction is observed within period 2 at 342-343 cm (Figure 2). The maximum peak in the >125  $\mu\text{m}$  size fraction is between 341-342 cm. Two narrow zones of ash below this high peak between 355-360 cm and 370-375 cm depth were found in low-resolution counts, but no distinct peaks in concentration were observed in the high-resolution counts.

Shards from the main peak and the two underlying ash zones have a basaltic composition (Figure 4a). With the exception of a shard population >80  $\mu\text{m}$  in size in the 373-374 cm sample, and a few outlying analyses that have affinities to the Icelandic transitional alkali rock suite, these deposits have a tholeiitic composition sourced from the Kverkfjöll volcanic system (Figure 4a). Although the analysed glass shards are from four different depths,

it is clear that the majority of shards from each interval occupy the same compositional space on geochemical plots and hence are related to one another. The relatively homogenous dominant population has SiO<sub>2</sub> concentrations between 48.5-51.0 %wt, CaO concentrations between 8.9-9.9 %wt and FeO concentrations of ~15 %wt (Figure 4). Slight geochemical bimodality can be observed, most notably within the TiO<sub>2</sub> concentrations and FeO/MgO ratios (Figure 4bi). This bimodality is present within the main shard peak at 342-343 cm and the underlying zones of low shard concentration. However, the deposit at 373-374 cm has proportionally more shards with high TiO<sub>2</sub> values than the other two deposits (Figure 4bi).

Determining potential correlatives, the isochronous nature and likely transport mechanisms for these deposits is complex. Bourne et al. (2015b) identified a number of tholeiitic basaltic tephra horizons with a Kverkfjöll source in the Greenland ice-cores between GI-5.2 and GS-4. The composition of all 10 of these ice-core horizons fall within the compositional field of the main population of the 342-343 cm and underlying deposits (Figure 4b), hampering their correlation to individual ice-core horizons. Some of these eruptives, however, have greater compositional heterogeneity, such as GRIP 2064.35 m, NGRIP 1931.60 m and NGRIP 1950.50 m, and cover the full compositional range observed in the marine deposit (Figure 4c). The peak input of ash at 342-343 cm may represent a single primary tephra-fall event related to one of these eruptions with the underlying deposits, between 355-360 and 370-375 cm, possibly representing downward movement of tephra within the sediment column via bioturbation. This scenario seems unlikely, however, due to the lack of a distinct background of basaltic shards between the deposits. An alternative scenario is that the geochemical similarities are a consequence of the marine deposits being composed of an amalgamation of glass shards from a number of eruptions. Shards could be amalgamated during protracted input of material via primary fall and post-depositional reworking, akin to the proposed depositional mechanism for FMAZ III (see Section 3.1). This proposition is, however, not supported by the relatively discrete nature of the peak input of ash to the site between 342-343 cm and the underlying deposits, which implies that tephra delivery occurred as short-lived pulses of material.



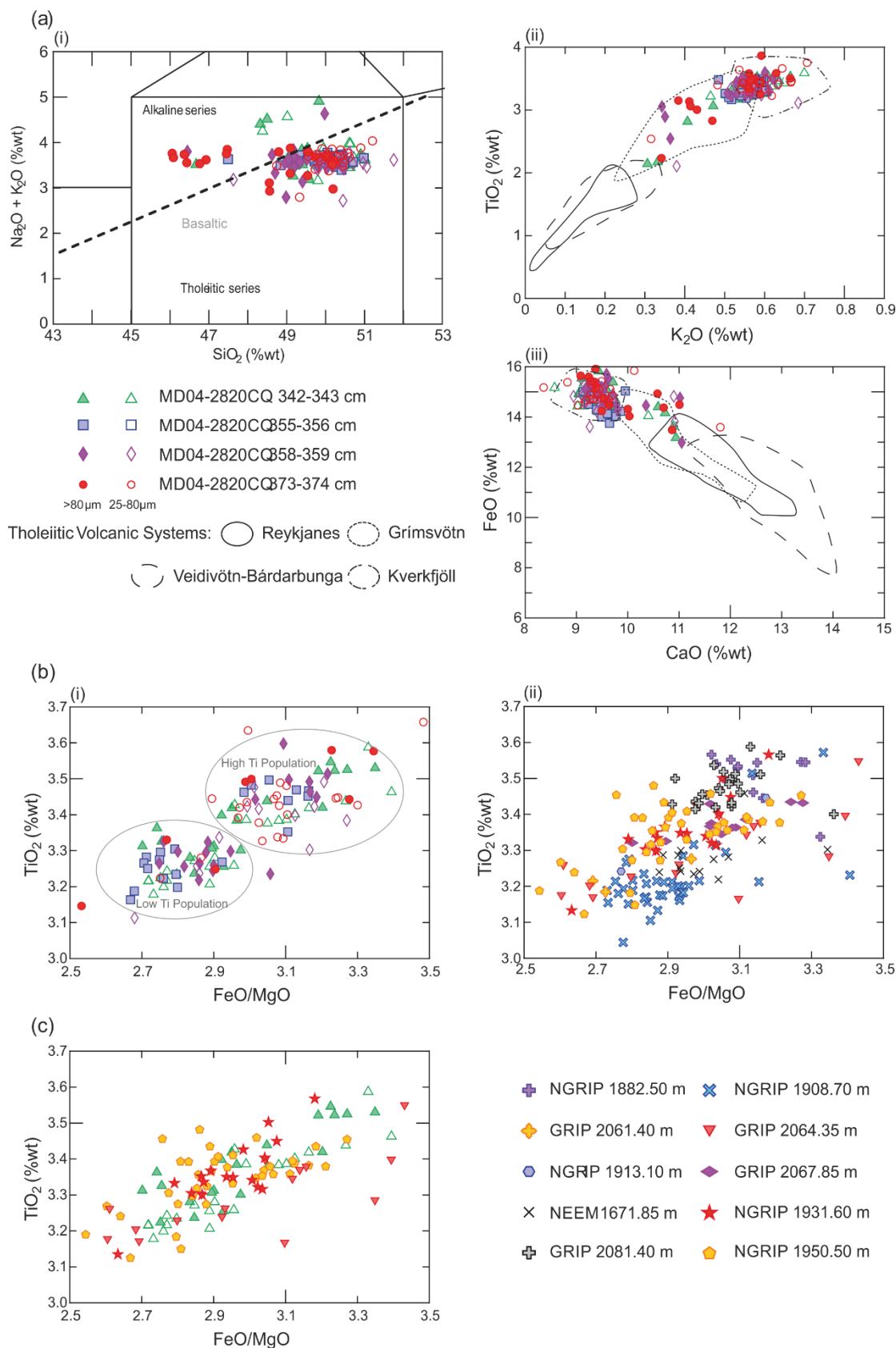


Figure 4 Compositional characterisation of MD04-2820CQ glass shard deposits between 340-380 cm depth, comparisons to proximal Icelandic deposits and comparisons with horizons with a Kverkfjöll volcanic source in the Greenland tephra framework. (a) (i) inset of total alkalis versus silica plot. Division line to separate alkaline and sub-alkaline material from MacDonald and Katsura (1964). Chemical classification and nomenclature after Le Maitre et al. (1989).

Figure 4 caption continued (ii and iii) Compositional variation diagrams comparing analyses to deposits proximal to four tholeiitic Icelandic volcanic systems. Compositional fields defined using glass and whole rock analyses from Jakobsson et al. (2008) (Reykjanes), Höskuldsson et al. (2006) and Óladóttir et al. (2011) (Kverkfjöll) and Jakobsson (1979), Haflidason et al. (2000) and Óladóttir et al. (2011) (Grímsvötn and Veidivötn-Bardabunga). (b) (i) Compositional variation diagram of glass between 340-380 cm depth in MD04-2820CQ (ii) Compositional variation diagram of glass from ice-core horizons from the framework of Bourne et al. (2015b). (c) Compositional variation diagram of glass from MD04-2820CQ 342-343 cm and glass from three heterogeneous Kverkfjöll eruptives identified between GI-5.2 and GS-4 in the Greenland tephra framework of Bourne et al. (2015b). Ice-core horizons in bold are identified in multiple cores. All plots on a normalised anhydrous basis.

Delivery via repeated iceberg rafting events could create deposits of this nature. The greater heterogeneity of the material at 373-374 cm depth, with a transitional alkali composition similar to those of Katla eruptives in the Greenland tephra framework between GI-5.2 and GS-4 (Figure 4ai), and an additional tholeiitic population from Grímsvötn (Figure 4aaii), may indicate that this material, with a slightly different compositional signature, is derived from a prior iceberg rafting event. We cannot fully test this proposition because an IRD record has currently not been established over this period. However, the high concentration of coarse-grained shards ( $>125\ \mu\text{m}$ ) (Figure 2), in a relatively distal location to Iceland, supports iceberg rafting as the transport process. Overall, this likelihood prevents the deposits in period 2 from being useful regional isochrons but they could be used for local core correlations (Brendryen et al., 2010).

### 3.3 Period 3 – DO-9 to DO-8

Period 3 is characterised by an approximately 20 cm thick zone of elevated basaltic glass concentrations within which four small peaks in concentration can be observed. Peaks at 456-457 cm, 460-461 cm, 464-465 cm and 472-473 cm depth are observed in the 25-80  $\mu\text{m}$  and  $>125\ \mu\text{m}$  grain size fractions and three can be clearly observed in the 80-125  $\mu\text{m}$  fraction. Each peak contains shards with affinities to either the transitional alkali or tholeiitic rock suites of Iceland, with the material from each of these rock suites displaying distinct heterogeneity (Figure 5a). Compositional similarities between the deposits and the continuous nature of the ash deposition allow the whole of the deposit between 455-475 cm to be interpreted as a single entity.

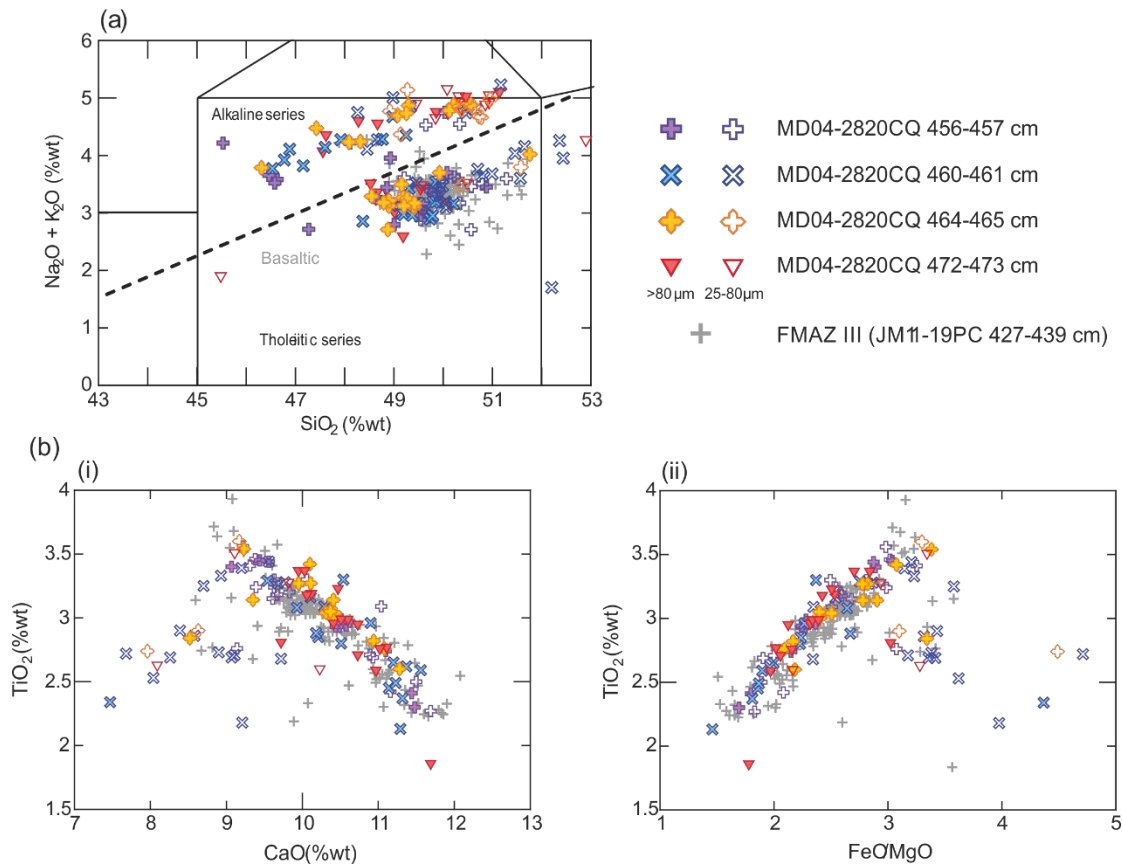


Figure 5 Compositional characterisation of glass from MD04-2820CQ tephra deposits between 455-475 cm depth and comparison to the glass characterised for FMAZ III. (a) inset of total alkali vs. silica plot. Division line to separate alkaline and sub-alkaline material from MacDonald and Katsura (1964). Chemical classification and nomenclature after Le Maitre et al. (1989). (b) Compositional variation diagrams for tholeiitic glass. FMAZ III data from JM11-19PC core outlined in Griggs et al. (2014). All plots on a normalised anhydrous basis.

According to the MD04-2820CQ stratigraphy, this deposit spans the warming transition related to DO-8 (Figure 2 and 6), akin to the FMAZ III deposit identified in other North Atlantic marine records. Distinct similarities are evident between the heterogeneous Grímsvötn-sourced material of FMAZ III characterised from a record in the SE Norwegian Sea (Griggs et al., 2014) and the tholeiitic material present in this ash zone (Figure 5). Homogenous Grímsvötn-sourced populations identified in the Greenland tephra framework between GI-8c and GS-9 cannot be identified at any depth in MD04-2820CQ (Figure 7a). The geochemical range of the tholeiitic material in MD04-2820CQ encompasses that of glass in all the ice-core horizons (Figure 7a). Despite the failure to correlate to an ice-core deposit, the MD04-2820CQ deposit can be correlated to the marine FMAZ III due to the stratigraphic similarities and geochemical affinity of the tholeiitic basaltic material. None of the Faroes Islands region occurrences of FMAZ III contain a population of transitional alkali material as observed in the MD04-2820CQ deposit (Figure 5; Wastegård et al., 2006; Griggs et al., 2014). Two transitional alkali basaltic horizons

from Katla were identified in early GS-9 by Bourne et al. (2013, 2015b) and also fall within the range of the MD04-2820CQ analyses, but the heterogeneity is far greater in the marine deposits and no potential correlations can be suggested (Figure 7b).

Griggs et al. (2014) interpreted FMAZ III in the Faroe Islands region as resulting from the amalgamation of primary fall material from closely timed Grímsvötn eruptions. Sediment accumulation rates are considered to be insufficient to allow the events to be separated and secondary processes such as bioturbation and bottom currents may have caused mixing of shards between depths. An ice-rafting transport and deposition mechanism was ruled out by Griggs et al. (2014) due to a lack of a coeval IRD signal. Within MD04-2820CQ, IRD concentrations are declining between 455-475 cm and there is no direct co-variance with glass shard concentrations (Figure 6). This lack of correlation could imply that the transport, deposition and post-deposition mechanisms are common between the MD04-2820CQ and JM11-FI-19PC core sites. The incorporation of transitional alkali material at the MD04-2820CQ site could result from more southerly transport of material from these eruptions. This would also account for the relative lack of transitional alkali eruptions in the Greenland tephra framework during this interval. As highlighted earlier, the FMAZ III cannot be used as a precise ice-marine tie-line (Bourne et al., 2013). However, the correlation of MD04-2820CQ 455-475 cm to FMAZ III extends the geographical distribution of this deposit and it can be used as a marine-marine tie-line.

A small peak in colourless shards occurs at 463-464 cm and major element analysis shows that the glass has a rhyolitic composition and an affinity to the Icelandic transitional alkali rock suite (Figure 8a). Two populations are apparent, one with affinities to material from the rhyolitic component of NAAZ II and one with affinities to a number of Katla-sourced rhyolitic horizons deposited during the last glacial-interglacial transition and an underlying horizon in MD04-2820CQ at a depth of 497-498 cm (Figure 8b and c). These compositional affinities and the low shard concentration suggests that this material is not from a distinct volcanic event but may relate to a background of reworked colourless shards in the sequence.

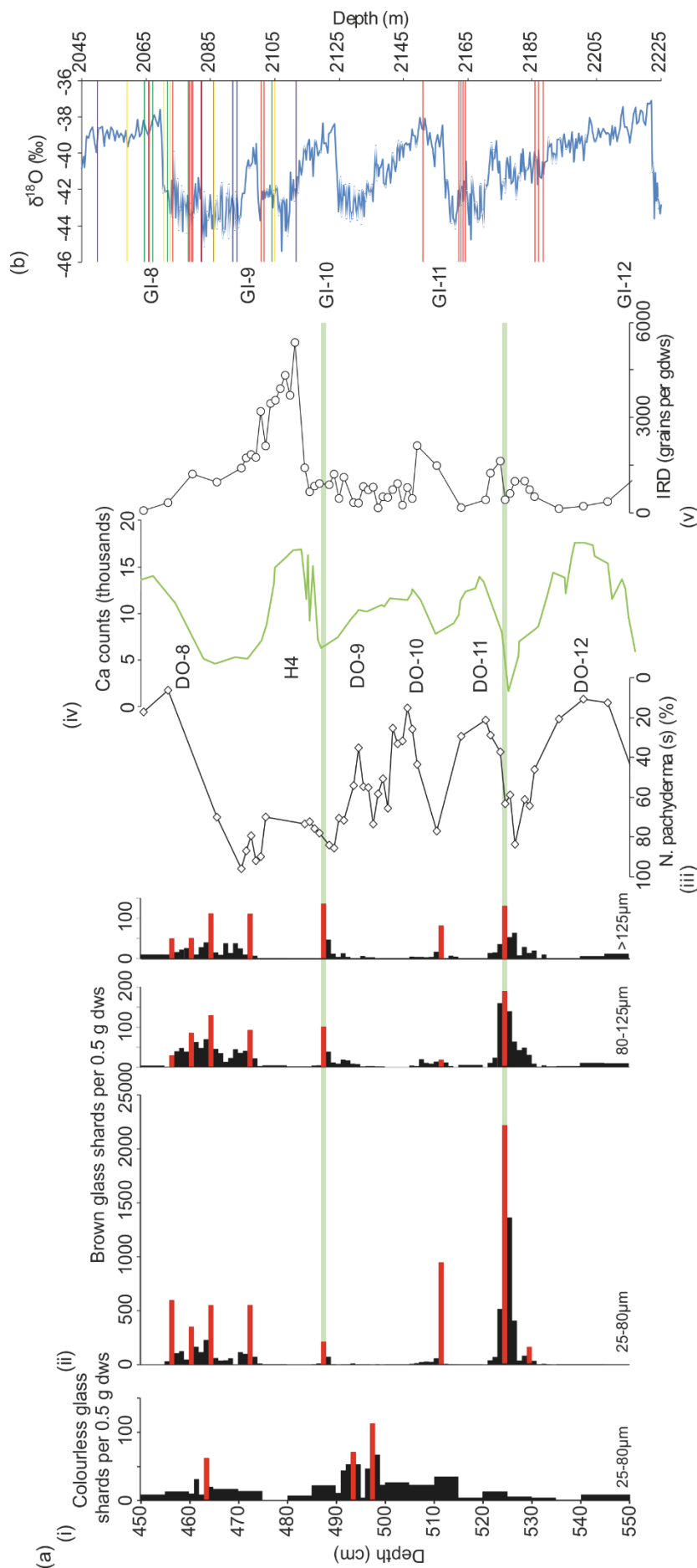


Figure 6 (a) High-resolution stratigraphy of the 450-550 cm interval within MD04-2820CQ. (i) Stratigraphy of colourless glass shard concentrations. (ii) Stratigraphy of brown glass shard concentrations. Red bars denote samples from which shards were extracted for compositional analysis. (iii) High-resolution percentage abundance of Neogloboquadrina pachyderma (sinistral). (iv) XRF (ITRAX core scanning) Ca count rates. (v) High-resolution IRD counts. Light green bars highlight glass shard peaks with homogenous compositions. (b) Greenland tephra framework between GI-8 and GI-12 (Bourne et al., 2015b and references within) plotted on the NGRIP oxygen isotope stratigraphy (NGRIP Members, 2004). Green lines denote horizons that can be traced in multiple cores. Other horizons are only present in NGRIP (red), NEEEM (purple), GRIP (yellow) and DYE-3 (blue).

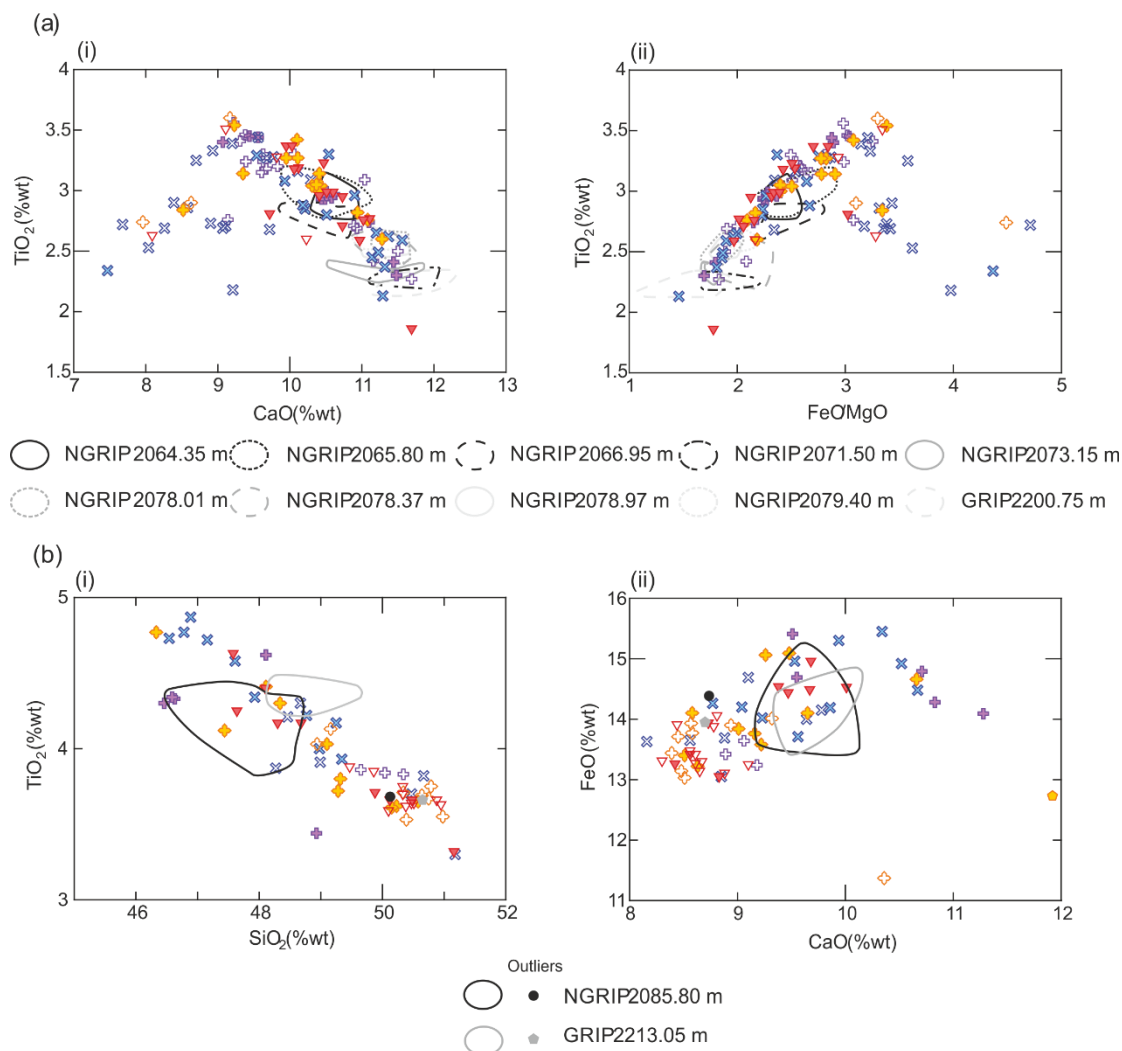


Figure 7 (a) Compositional comparisons of tholeiitic glass from MD04-2820CQ Period 3 deposits and GI-8c and GS-9 tephra in the Greenland tephra framework of Bourne et al. (2013, 2015b). (b) Compositional comparisons of transitional alkali glass from MD04-2820CQ Period 3 deposits and GS-9 tephra in the Greenland tephra framework. Ice-core data from Bourne et al. (2015b). Ice-core horizons in bold can be traced in multiple cores and only data from the NGRIP occurrence have been used for those horizons. All plots on a normalised anhydrous basis. The key for analyses from MD04-2820CQ is the same as Figure 5.

### 3.4 Period 4 – DO-12 to DO-9

During this period a series of three relatively discrete peaks (~1-3 cm) in brown glass shards can be identified (Figure 2 and 6). The peaks in brown shards at 487-488 cm and 524-525 cm depth are distinct across all grain-size fractions, whereas the peak at 511-512 cm is only evident within the 25-80 and >125  $\mu$ m grain-size fractions. A broad increase in colourless shards between 490-500 cm displays a double peak in concentration within the 25-80  $\mu$ m grain-size fraction at 493-494 cm and 497-498 cm.

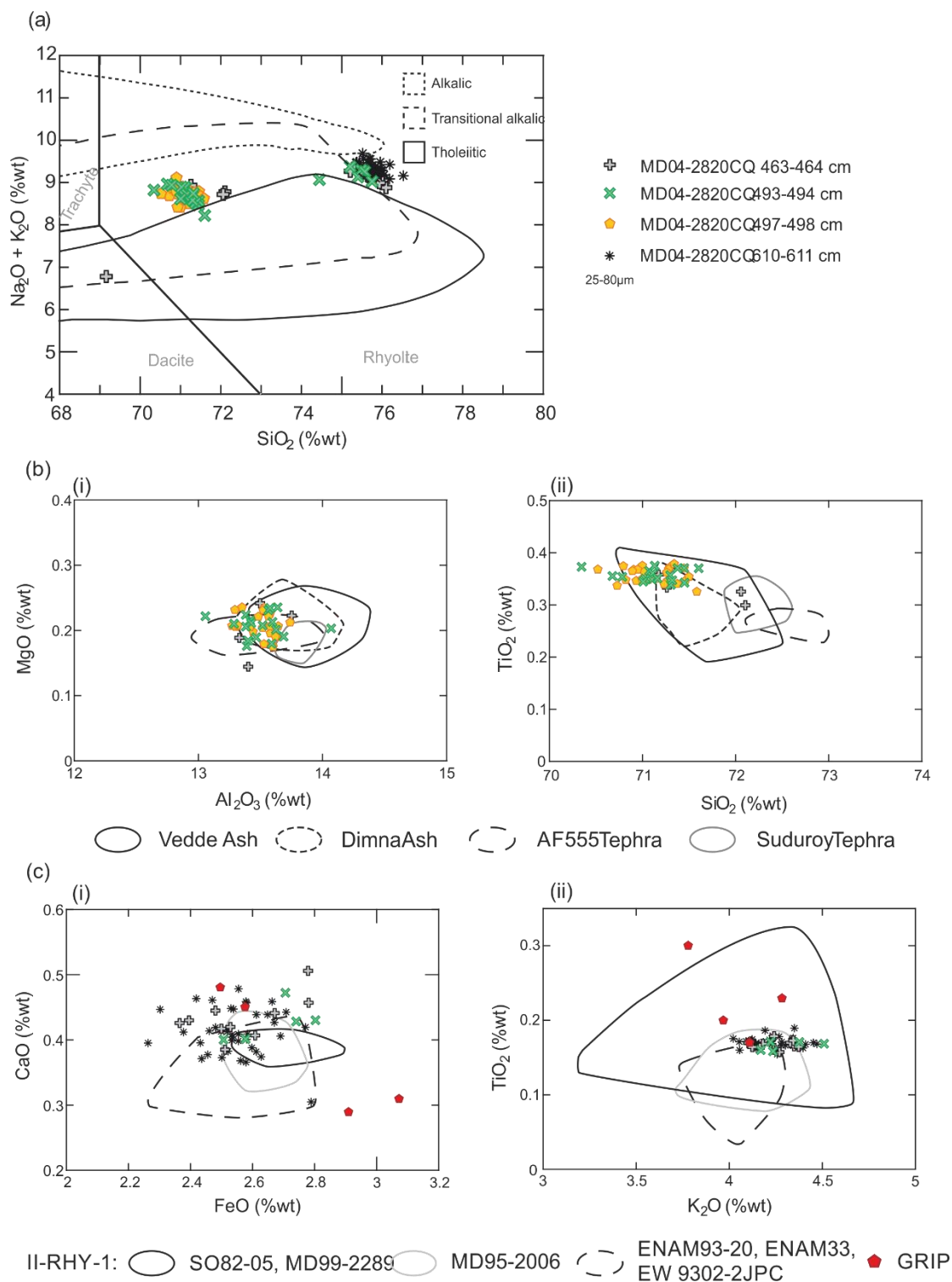


Figure 8 (a) Inset of total alkali vs. silica plot focusing on rhyolitic material from the MD04-2820CQ core. Normalised compositional fields for the Icelandic rock suites derived from whole rock analyses in Jakobsson et al. (2008). Chemical classification and nomenclature after Le Maitre et al. (1989). (b) Compositional variation diagrams comparing low  $\text{SiO}_2$  rhyolitic glass from MD04-2820CQ to geochemical fields for a number of Katla-derived tephra horizons. Glass compositions from Lane et al. (2012) (Vedde Ash and Dimna Ash), Matthews et al. (2011) (AF555; Abernethy Tephra (MacLeod et al., 2015)) and Pilcher et al. (2005) (Suduroy). (c) Compositional variation diagrams comparing high  $\text{SiO}_2$  rhyolitic glass from MD04-2820CQ to fields for marine and ice occurrences of the NAAZ II rhyolitic component. Glass data from Austin et al. (2004) (MD95-2006), Wastegård et al. (2006) (ENAM93-20, ENAM33, EW9302-2JPC).

Figure 8 caption continued. Brendryen et al. (2011) (SO82-05, MD99-2289) and Grönvold et al. (1995). All plots on a normalised anhydrous basis.

### 3.4.1 MD04-2820CQ 487-488 cm

All shards in the 487-488 cm deposit are basaltic in composition with one dominant and homogenous tholeiitic population (Figure 9). Some outliers with a transitional alkali composition are also observed, but are primarily restricted to the  $>80\ \mu\text{m}$  fraction (Figure 9a). The main population is characterised by  $\text{SiO}_2$  concentrations of  $\sim 49.5\ \%\text{wt}$ ,  $\text{TiO}_2$  concentrations between 2.6-3.2  $\%\text{wt}$ ,  $\text{CaO}$  concentrations between 10.1 and 10.9  $\%\text{wt}$  and  $\text{FeO}$  concentrations of  $\sim 13.8\ \%\text{wt}$ , showing affinities to the Grímsvötn volcanic system (Figure 9).

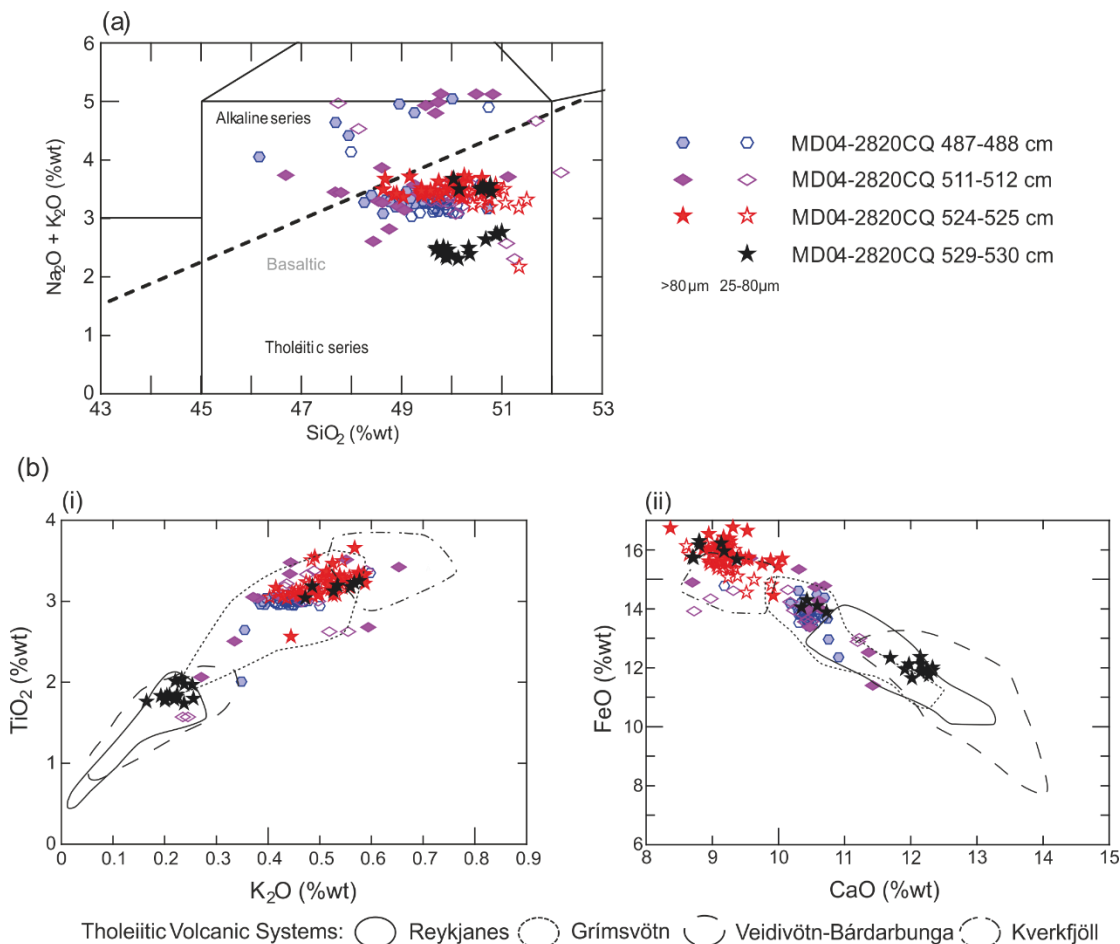


Figure 9 Compositional characterisation of basaltic glass from deposits between 485 and 530 cm in MD04-2820CQ and comparisons with Icelandic proximal material. (a) inset of inset of total alkali vs. silica plot. Division line to separate alkaline and sub-alkaline material from MacDonald and Katsura (1964). Chemical classification and nomenclature after Le Maitre et al. (1989). (b) Compositional variation diagrams comparing analyses with material proximal to four tholeiitic Icelandic volcanic systems. Compositional fields defined using glass and whole rock analyses from Jakobsson et al. (2008) (Reykjanes), Höskuldsson et al. (2006) and Óladóttir et al. (2011) (Kverkfjöll) and Jakobsson (1979), Haflidason et al. (2000) and Óladóttir et al. (2011) (Grímsvötn and Veidivötn-Bardabunga). All plots on a normalised anhydrous basis.



A large number of Grímsvötn eruptives are found within the Greenland tephra framework between 25-45 ka b2k with several showing compositional similarities to the main population of MD04-2820CQ 487-488 cm (Bourne et al., 2015b). Stratigraphic information from MD04-2820CQ is thus employed to provide a broad constraint on the timing of this eruption relative to the main climato-stratigraphic framework for the North Atlantic. Further discussion of this approach is provided in Section 3.4. MD04-2820CQ 487-488 cm was deposited just prior to Heinrich event 4 (Figure 6), which is widely regarded to have occurred in GS-9 and between DO-9 and DO-8 (Sanchez Goñi and Harrison, 2010). The high-resolution  $Np(s)$  record for this interval shows that MD04-2820CQ 487-488 cm falls within a cold period above two distinct decreases in  $Np(s)$  percentages, between 490-510 cm depth, and thought to be related to warming over the DO-9 and DO-10 events (Figure 6iii). These events were not apparent within the original low resolution  $Np(s)$  record or the Ca XRF record (Figure 2ii and 6iv). These stratigraphic constraints suggest deposition during the cold period following DO-9, which is equivalent to GS-9 within the Greenland stratigraphic framework (Rasmussen et al., 2014). The GS-9 interval has been fully sampled in all the ice-cores that contribute to the Greenland tephra framework (see Bourne et al., 2015b). In total, 10 Grímsvötn-sourced tephra horizons have been identified in one or more of the Greenland cores (Figure 6b). Geochemical comparisons show that no horizons provide a clear major element match to 487-488 cm. Therefore, a potential correlative to the marine horizon cannot be proposed (Figure 10a).

The transport mechanism for this deposit is unlikely to be iceberg rafting because of the relatively homogenous geochemical signature of the material and a lack of co-variance with IRD (Figure 6). Other potential mechanisms, sea-ice rafting and primary airfall, would not impart a temporal delay and the deposit can be assumed to be isochronous. The relative proportion of larger grains in the 80-125  $\mu\text{m}$  and >125  $\mu\text{m}$  fractions compared to other deposits, e.g. 524-525 cm, could be indicative of transportation via sea-ice rafting. This deposit is considered to have strong stratigraphic integrity as the peak in shard concentration is relatively discrete with only a restricted downward tail in concentration, most likely due to post-depositional bioturbation. Although not present in Greenland, if it was widely dispersed over the North Atlantic, this volcanic deposit may be a useful isochron for linking this sequence to other marine records.

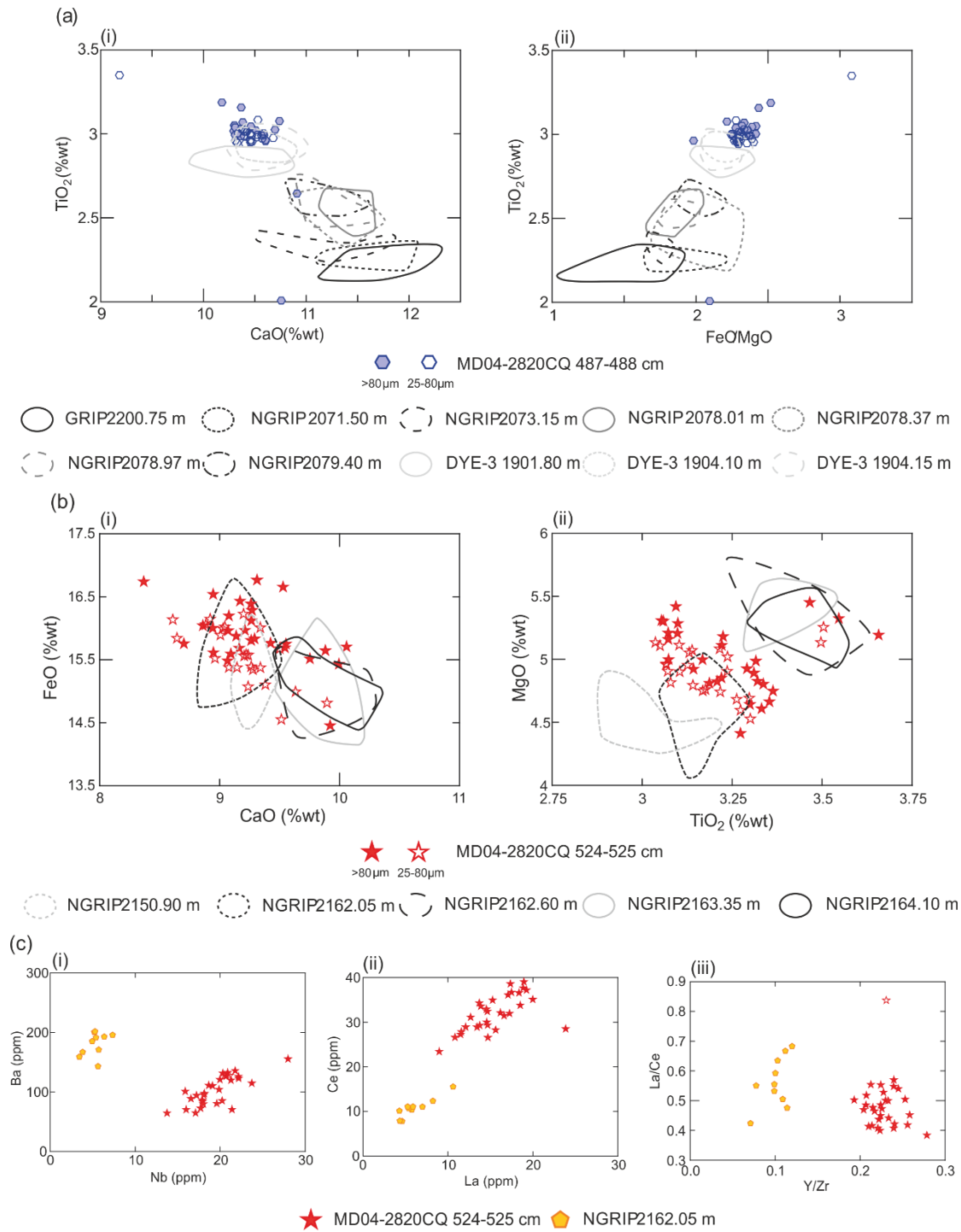


Figure 10 (a) Comparison of the main tholeiitic glass population of MD04-2820CQ 487-488 cm with glass compositional fields for GS-9 tephra horizons sourced from Grímsvötn in the Greenland tephra framework of Bourne et al. (2015b). Horizons in bold have been identified in multiple ice-cores. (b) Comparison of MD04-2820CQ 524-525 cm glass with characterisations of glass from tephra horizons in the Greenland tephra framework of Bourne et al. (2015b). (c) Comparison of trace element characterisations of individual shards from MD04-2820CQ 524-525 cm and NGRIP 2162.05 m. All plots on a normalised anhydrous basis.

### 3.4.2 MD04-2820CQ 493-494 cm and 497-498 cm

According to the stratigraphy for MD04-2820CQ, the slight increase in colourless shards between 490-500 cm occurred during the short-lived cold period between DO-10 and DO-9, based on an increase in *Np(s)* percentages (Figure 2 and 6). Shards from both peaks have a rhyolitic composition (Figure 8). The material from the larger peak at 497-498 cm has affinities to the transitional alkali rock suite of Iceland and forms a single homogenous population with SiO<sub>2</sub> concentrations between 70.5 and 71.5 %wt, Al<sub>2</sub>O<sub>3</sub> concentrations of ~13.5 %wt, K<sub>2</sub>O concentrations of ~3.6 %wt and CaO concentrations between 1.44 and 1.65 %wt (Figure 8). A source for these glass shards could not be determined through comparisons to characterisations of proximal whole rock rhyolites from Iceland, which may be due to the presence of other mineral phases within whole rock analyses. However, compositional similarities to glass shards from last glacial-interglacial transition rhyolitic tephra horizons sourced from the Katla volcanic system (Figure 8b) strongly indicate that this is the volcanic source. Shards in the overlying smaller peak at 493-494 cm fall into two populations, one with affinities to the Katla material 4 cm below and one with strong overlap with shards from 610-611 cm in the core from NAAZ II (Figure 8b and c). No rhyolitic horizons have been isolated within the Greenland ice-core records between GI-9 and GI-11 (Bourne et al., 2015b).

The homogeneity of the 25 shards from the 497-498 cm peak and the predominance of material in the 25-80 µm grain size fraction suggests that this represents primary fall deposition. The upward tail in shard concentrations could be related to secondary redistribution of material by bottom currents and the compositional bimodality in this tail (493-494 cm sample) suggests reworking of the underlying Katla-sourced material and NAAZ II input. Shards from NAAZ II (see Section 3.5) are present within overlying sediments and are the likely primary constituent of the reworked background of fine-grained rhyolitic material.

### 3.4.3 MD04-2820 CQ 511-512 cm

Brown shards from the peak at 511-512 cm are basaltic in composition with both tholeiitic and transitional alkali material present. Distinct heterogeneity can be observed in a number of components, e.g. Na<sub>2</sub>O, K<sub>2</sub>O, TiO<sub>2</sub> and FeO, and the analyses cannot be grouped into clear populations (Figure 9). The glass peak is directly associated with a peak in IRD, which combined with the geochemical signature strongly suggests it is an ice-rafted deposit and cannot be assumed to be isochronous.

### 3.4.4 MD04-2820 CQ 524-525 cm and 529-530 cm

The highest shard concentration in this period is found at 524-525 cm and exhibits a broader rise in shard concentrations including a small shard peak 4 cm below the main peak at 529-530 cm (Figure 2 and 6). The stratigraphy of MD04-2820CQ shows that the tephra horizon falls on the decrease in  $Np(s)$  percentage and increase in Ca content of the sediment that has been related to warming at the onset of DO-11 (Figure 2 and 6). Shards from both the main peak and underlying peak have a tholeiitic basaltic composition (Figure 9a). Shards from 524-525 cm form a homogenous population characterised by distinctly high FeO concentrations between 14.5 and 16.7 %wt, low CaO concentrations of ~9.25 %wt, TiO<sub>2</sub> concentrations of ~3.2 %wt and MgO concentrations between 4.5 and 5.5 %wt (Figure 9). Comparison with proximal deposits highlights similarities to the products of both the Kverkfjöll and Grímsvötn volcanic systems (Figure 9b).

Four Grímsvötn-sourced deposits are found within the GS-12 climatic period and one within GI-11 in the Greenland tephra framework (Bourne et al., 2015b). Statistical comparisons show that none of these horizons are statistically different from 524-525 cm and all SC values exceed 0.95, due to the common source (Table 1). There is a clear affinity between the main population of MD04-2820CQ 524-525 cm and NGRIP 2162.05 m with a low  $D^2$  value and the highest similarity coefficient of 0.977; this assessment is corroborated by major element biplot comparisons (Table 1; Figure 9b). To test this affinity, the trace element composition of both horizons was determined. Distinct differences can be observed in these characterisations, both in absolute concentrations and trace element ratios (Figure 10c). These demonstrate that the two horizons were not produced during the same volcanic event and cannot be correlated between the archives. The differences in trace element composition could be due to a number of factors, which will be discussed in Section 4.2.

Assessing this deposit according to the protocol of Griggs et al. (2014) is problematic as key indicators are contradictory. The homogenous composition of the deposit suggests that this deposit was unlikely to be iceberg rafted, but it was deposited during a period of increased IRD concentrations (Figure 6). It is possible that primary fall deposition is superimposed on a period dominated by iceberg rafting. What is more, iceberg rafting is typically thought to transport heterogeneous tephra deposits from an amalgamation of tephra from a number of eruptions. Tracing this horizon in the same stratigraphic position in another marine sequence would provide supporting evidence for this interpretation.

<b>Ice core horizon</b>	<b>D<sup>2</sup></b>	<b>SC</b>
NGRIP 2150.90 m	10.042	0.959
NGRIP 2162.05 m	1.740	0.977
NGRIP 2162.60 m	8.349	0.959
NGRIP 2163.35 m	9.709	0.953
NGRIP 2164.10 m	8.239	0.952

Table 1. Statistical comparisons of the main tholeiitic population of glass from MD04-2820CQ 524-525 cm with glass from GI-11 and GS-12 tephra horizons within the Greenland tephra framework. Some outliers were removed from the ice-core characterisations. Critical value of 23.21 for statistical distance comparisons (10 degrees of freedom; 99 % confidence interval).

Glass shards from the small peak at 529-530 cm were additionally geochemically analysed to assess its relationship to the main overlying peak at 524-525 cm. All of the shards have a tholeiitic basaltic composition (Figure 9a), with three distinct major element populations present based on major oxides including FeO, CaO, MgO and Al<sub>2</sub>O<sub>3</sub> (Figure 8bii). Half of the shards from this deposit make up the main population and indicate a source from either the Veidivötn-Bárdabunga or Reykjanes volcanic systems (Figure 9b). One population is sourced from Grímsvötn or Kverkfjöll and has compositional affinities to MD04-2820CQ 524-525 cm and the final population is sourced from Grímsvötn and has affinities to MD04-2820CQ 487-488 cm (Figure 9b). The only known tephra horizon in the Greenland ice-core framework between 25-45 ka b2k with a composition similar to the dominant population was deposited during GS-5 and thus is not a correlative to this deposit. The similarity in geochemistry between the sub-population and MD04-2820CQ 487-488 cm is likely to be coincidental, with the Greenland tephra framework showing that Grímsvötn produced many eruptives with similar compositions throughout this period (Bourne et al., 2015b). The heterogeneity of this material could be linked to some iceberg rafting of earlier events combined with downward reworking of material from the 524-525 cm peak.

### 3.5 Period 5 – DO-15 to DO-14

The highest concentration of colourless shards was observed at 610-611 cm with ~19,500 shards per 0.5 g dry weight sediment (dws) in the 25-80 µm fraction and ~450 shards in the >125 µm fraction in this cryptotephra (Figure 2b). A peak in shards 80-125 µm in diameter associated with this deposit occurs 1 cm above this depth between 609-610 cm (Figure 2b). Within the proposed MD04-2820CQ stratigraphy, the shard concentration peak falls on the cooling transition at the end of DO-15 as shown by the rise in the *Np(s)* percentage (Figure 2b).

These colourless shards have a rhyolitic composition with affinities to the Icelandic transitional alkali rock suite (Figure 8a) and are characterised by SiO<sub>2</sub> concentrations of ~75.8 % wt, Al<sub>2</sub>O<sub>3</sub> concentrations of ~11.7 % wt, FeO concentrations between 2.25 and 2.8 % wt and K<sub>2</sub>O concentrations of ~4.2 % wt. Geochemical similarities are highlighted between the MD04-2820CQ 610-611 cm deposit and other occurrences of the rhyolitic component of NAAZ II (II-RHY-1) in North Atlantic marine sequences and the GRIP ice-core (Figure 8c). There are some slight offsets between the MD04-2820CQ characterisations and the older analyses, e.g. the MD04-2820CQ shards have higher Na<sub>2</sub>O and lower Al<sub>2</sub>O<sub>3</sub> and SiO<sub>2</sub> concentrations, and these differences can be attributed to the effect of sodium loss during the older analyses (Hunt and Hill, 2001; Kuehn et al., 2011; Hayward, 2012). Therefore, these newer analyses represent a more up-to-date characterisation of the II-RHY-1 component of NAAZ II and should be utilised in future comparisons.

Identification of this horizon provides a direct ice-marine tie-line, a basal stratigraphic constraint for the core, and a test of the proposed stratigraphy for MD04-2820CQ because this horizon has been identified in the Greenland ice-cores and other marine sequences on the cooling transition at the end of GI-15 (Grönvold et al., 1995; Austin et al., 2004).

## **4 Discussion**

### **4.1 Tephrostratigraphy of MD04-2820CQ between ~25-60 ka b2k and implications for the regional tephra framework**

This work represents one of the first studies to employ density and magnetic separation techniques to isolate and identify cryptotephra within North Atlantic marine sediments between 25-60 ka b2k. Here, the identification of basaltic tephra deposits has been improved when compared with previous studies, e.g. Abbott et al. (2014), as magnetic separation of basaltic shards from the host sediment produced purer samples for optical microscopy work and geochemical analysis preparation.

Overall, the tephrostratigraphy of MD04-2820CQ is complex and differing transport and deposition processes have given rise to a range of contrasting deposits. For example, the geochemical heterogeneity of the MD04-2820CQ 275-279 cm and 511-512 cm deposits and to a certain extent the deposits between 340-380 cm depth suggests they were deposited via iceberg rafting. Whilst three of the deposits, the basaltic 487-488 cm and 524-525 cm and the rhyolitic 497-498 cm, have isochronous characteristics and have the potential to act as tie-lines between records, however none of these horizons were found to have correlatives within the current Greenland tephra framework (Table 2; see section 4.2 for further discussion).

Depth Interval	Timing	Composition	Potential Source	Correlations
456-473 cm	DO-8 warming	Heterogenous Tholeiitic Basaltic	Grímsvötn, Iceland	FMAZ III*
487-488 cm	Between DO-10 and DO-9	Tholeiitic Basaltic	Grímsvötn, Iceland	New horizon
497-498 cm	DO-11	Transitional alkali Rhyolitic	Katla, Iceland	New horizon
524-525 cm	DO-11 warming	Tholeiitic Basaltic	Grímsvötn, Iceland	New horizon
610-611 cm	DO-15 cooling	Transitional alkali Rhyolitic	Tindfjallajökull, Iceland	NAAZ II

Table 2. Summary of tephra horizons in MD04-2820CQ with the potential to act as widespread tie-lines to other palaeoclimatic sequences in the North Atlantic region. The timing of events is based on the stratigraphy for the MD04-2820CQ record. \*Only to be used as a marine-marine tie-point.

Two of the deposits in MD04-2820CQ have been correlated to previously known tephra horizons (Table 2). MD04-2820CQ 610-611 cm correlates to NAAZ II and permits a direct link to the Greenland ice-cores and other marine sequences while MD04-2820CQ 455-475 cm can be correlated to FMAZ III, a broad marine-marine link around DO-8 to sequences in the Faroe Island region. The MD04-2820CQ 455-475 cm deposit differs from FMAZ III occurrences in the Faroe Islands region as it contains transitional alkali basaltic glass in addition to the tholeiitic basaltic glass characteristic of the original deposit (Griggs et al., 2014). Further work on tracing the FMAZ III at sites between the Goban Spur area and the Faroe Islands region may help isolate the transportation and depositional processes controlling this contrast. At present the MD04-2820CQ core site on the Goban Spur is the furthest south that FMAZ III has been identified; this increase in geographical range of the deposit suggests that it could be a key stratigraphic marker for the DO-8 event in widespread marine records.

The identification of horizons that do not at present have correlatives in other palaeoarchives adds three further volcanic events into the regional framework for the 25-60 ka b2k period (Table 2). Tracing these horizons within other sequences would test our assertion

that these are atmospherically-derived and potentially validate their use as isochronous tie-lines. This is most relevant for the MD04-2820CQ 497-498 cm deposit which has a broader shard count profile relative to the two basaltic deposits. The timing of emplacement of the three deposits can be inferred from their relationship to the high-resolution stratigraphy for MD04-2820CQ shown in Figure 6, which can act as a guide for tracing these deposits in other records (Table 2).

The two basaltic deposits are thought to be sourced from the Grímsvötn and/or Kverkfjöll volcanic systems, providing further support for the high productivity of these systems during the last glacial period (cf. Bourne et al., 2015b). These results also demonstrate that their eruptive products were transported south of Iceland, most likely via direct atmospheric transport. Katla is thought to be the most likely source of MD04-2820CQ 497-498 cm and a correlative could not be identified in the Greenland ice-cores (Section 3.4.2; Bourne et al., 2015b). Indeed, no rhyolitic tephra horizons from this source and very few Icelandic rhyolitic horizons are present throughout the last glacial period in the Greenland ice-cores (Davies et al., 2014; Bourne et al., 2015b). The identification of this Katla horizon within the cool interval between DO-10 and DO-9 thus demonstrates that older rhyolitic eruptions from this source did occur prior to the last glacial-interglacial transition (Lane et al., 2012).

#### **4.2 Testing correlations using stratigraphy and trace element analysis**

The stratigraphy of MD04-2820CQ and its likely relationship to the Greenland climatic record was used throughout to assess the timing of the emplacement of the tephra deposits. This climatostratigraphic approach was particularly crucial for assessing potential correlatives for the MD04-2820CQ 487-488 cm and 524-525 cm horizons and high-resolution records of  $Np(s)$  and IRD were available for these purposes.

The correlation of tephtras solely based on geochemical matches between horizons, relies on every eruption having a unique geochemical signature. For the North Atlantic region, however, the new Greenland tephra framework demonstrates that multiple basaltic horizons with overlapping geochemical signatures were erupted within relatively short time-intervals (Bourne et al., 2013, 2015b). Therefore, as is required for many other tephrochronological studies, stratigraphic control was used alongside the compositional data to guide the testing of correlations. This approach does introduce an element of circularity if the tephra correlations are to be used as climatically independent tools to test stratigraphic comparisons and the relative timing of past climatic changes (see discussion in Matthews et al., 2015). However, in this instance the approach is valid as the overall stratigraphy of MD04-2820CQ is supported



by distinct event markers such as Heinrich Event 4 and NAAZ II and there is a strong relationship to the sequence of well-defined Greenland Interstadial events recorded in the ice-cores. This relationship is especially apparent over the section where high-resolution proxy data has been acquired. In addition, the stratigraphic comparisons used to test correlations were broad and on a millennial-scale, and not centennial or decadal-scale which is the potential magnitude of climatic phasing between the environments.

The use of stratigraphy to guide correlations will be limited or problematic when correlations are being assessed between the Greenland records and marine sequences that have a less well-resolved stratigraphic framework, due to core location and/or sedimentation rate differences. However, due to the high frequency of Icelandic basaltic eruptions, particularly from Grímsvötn, some form of stratigraphic constraint is essential for exploring potential tie-lines. We recommend that, when possible, high-resolution stratigraphic information is gained over key intervals of interest to aid correlation testing.

The potential correlation between MD04-2820CQ and NGRIP 2162.05 m was tested using grain-specific trace element analysis, due to strong major element similarities (Figure 10b). This analysis showed that the two horizons were not produced during the same volcanic event (Figure 10c). The use of trace element analysis to test and add robustness to correlations has been encouraged previously and its use is steadily increasing within tephrochronological studies (see Section 1). Our work provides further support for the use of this technique for testing correlations and for providing a key insight into geochemical variability between Icelandic eruptions, specifically those sourced from the Grímsvötn volcanic system. As basaltic magmas have undergone relatively limited compositional evolution, intra-eruption variability in trace elements from a single evolving system could be limited as significant fractional crystallisation may not have occurred, this being the process which dominantly controls trace element evolution (see Pearce et al., 2008). Therefore, it is of interest to see clear trace element differences between two Grímsvötn-sourced eruptions with highly similar major element compositions. In this instance, the differences could result from magmatic evolution within a single, fractionating magma chamber between eruptions or the eruptions tapped magma from different fissures within the overall Grímsvötn system with similar major element but differing trace element compositions. Trace element analysis of proximal deposits could provide an insight into the intra-eruption variability of Grímsvötn basalts.

## 5 Conclusions

The potential for using density and magnetic separation techniques to identify tephra deposits within North Atlantic marine sequences spanning ~25-60 ka b2k has been clearly demonstrated. Applying these techniques to MD04-2820CQ has unearthed a complex tephrostratigraphical record with differing transportation and depositional processes operating at different times, but the identification of isochronous deposits highlights the potential for using tephrochronology to link marine sequences. One of the biggest challenges for establishing correlations is the high number of compositionally similar eruptives preserved in the ice-cores within short time-intervals. We have outlined how stratigraphic constraints can help reduce the number of potential candidates and the need for high-resolution proxy data to constrain key intervals. The use of stratigraphic constraints from proxy data could ultimately be limited by the resolution of marine records. In addition, it has been shown that trace element comparisons provide a secondary fingerprint that can test the robustness of correlations suggested by major element geochemical similarities. Exploration of further records in this region will help assess the isochronous nature of the key deposits in MD04-2820CQ and represent a major step towards synchronisation of regional marine archives using cryptotephra deposits.

## References

- Abbott, P.M., Austin, W.E.N., Davies, S.M., Pearce, N.J.G., Hibbert, F.D., 2013: Cryptotephrochronology of a North East Atlantic marine sequence over Termination II, the Eemian and the last interglacial-glacial transition. *Journal of Quaternary Science* 28, 501-514.
- Abbott, P.M., Austin, W.E.N., Davies, S.M., Pearce, N.J.G., Rasmussen, T.L., Wastegård, S., Brendryen, J., 2014: Re-evaluation and extension of the MIS 5 tephrostratigraphy of the Faroe Islands Region: the cryptotephra record. *Palaeogeography, Palaeoclimatology, Palaeoecology* 409, 153-168.
- Abbott, P.M., Davies, S.M., 2012: Volcanism and the Greenland ice-cores: the tephra record. *Earth-Science Reviews* 115, 173-191.
- Abbott, P.M., Davies, S.M., Austin, W.E.N., Pearce, N.J.G., Hibbert, F.D., 2011: Identification of cryptotephra horizons in a North East Atlantic marine record spanning

marine isotope stages 4 and 5a (~60,000-82,000 a b2k). *Quaternary International* 246, 177-189.

Albert, P.G., Tomlinson, E.L., Smith, V.C., Di Roberto, A., Todman, A., Rosi, M., Marini, M., Muller, W., Menzies, M., 2012: Marine-continental tephra correlations: Volcanic glass geochemistry from the Marsili Basin and the Aeolian Islands, Southern Tyrrhenian Sea, Italy. *Journal of Volcanology and Geothermal Research* 229-230, 74-94.

Allan, A.S.R., Baker, J.A., Carter, L., Wysoczanski, R.J., 2008: Reconstructing the Quaternary evolution of the world's most active silicic volcanic system: insights from an ~1.65 Ma deep ocean tephra record sourced from Taupo Volcanic Zone, New Zealand. *Quaternary Science Reviews* 27, 2341-2360.

Austin, W.E.N., Wilson, L.J., Hunt, J.B., 2004: The age and chronostratigraphical significance of North Atlantic Ash Zone II. *Journal of Quaternary Science* 19, 137-146.

Bond, G., Broecker, W., Johnsen, S., McManus, J., Labeyrie, L., Jouzel, J., Bonani, G., 1993: Correlations between climate records from North Atlantic sediments and Greenland ice. *Nature* 365, 143-147.

Bond, G., Showers, W., Cheseby, M., Lotti, R., Almasi, P., deMenocal, P., Priore, P., Cullen, H., Hajdas, I., Bonani, G., 1997: A Pervasive Millennial-Scale Cycle in North Atlantic Holocene and Glacial Climates. *Science* 278, 1257-1266.

Borchardt, G.A., Aruscavage, P.J., Millard, H., 1972: Correlation of the Bishop ash, a Pleistocene marker bed, using instrumental neutron activation analysis. *Journal of Sedimentary Petrology* 42, 201-206.

Bourne, A., Albert, P.G., Matthews, I.P., Trincardi, F., Wulf, S., Asioli, A., Blockley, S.P.E., Keller, J., Lowe, J.J., 2015a: Tephrochronology of core PRAD 1-2 from the Adriatic Sea: insights into Italian explosive volcanism for the period 200-80 ka. *Quaternary Science Reviews* 116, 28-43.

Bourne, A.J., Cook, E., Abbott, P.M., Seierstad, I.K., Steffensen, J.P., Svensson, A., Fischer, H., Schupbach, S., Davies, S.M., 2015b: A tephra lattice for Greenland and a reconstruction of volcanic events spanning 25-45 ka b2k. *Quaternary Science Reviews* 118, 122-141.

Bourne, A.J., Davies, S.M., Abbott, P.M., Rasmussen, S.O., Steffensen, J.P., Svensson, A., 2013: Revisiting the Faroe Marine Ash Zone III in two Greenland ice cores: implications for marine-ice correlations. *Journal of Quaternary Science* 28, 641-646.

Bramham-Law, C.W.F., Theuerkauf, M., Lane, C.S., Mangerud, J., 2013: New findings regarding the Saksunarvatn Ash in Germany. *Journal of Quaternary Science* 28, 248-257.

Brendryen, J., Haflidason, H., Sejrup, H.P., 2010: Norwegian Sea tephrostratigraphy of marine isotope stages 4 and 5: Prospects and problems for tephrochronology in the North Atlantic region. *Quaternary Science Reviews* 29, 847-864.

Brendryen, J., Haflidason, H., Sejrup, H.P., 2011: Non-synchronous deposition of North Atlantic Ash Zone II in Greenland ice cores, and North Atlantic and Norwegian Sea sediments: an example of complex glacial-stage tephra transport. *Journal of Quaternary Science* 26, 739-745.

Davies, S.M., Abbott, P.M., Meara, Rh. H., Pearce, N.J.G., Austin, W.E.N., Chapman, M. R., Svensson, A., Bigler, M., Rasmussen, T.L., Rasmussen, S.O., Farmer, E.J., 2014: A North Atlantic tephrostratigraphical framework for 130-60 ka b2k: new tephra discoveries, marine-based correlations, and future challenges. *Quaternary Science Reviews* 106, 101-121.

Davies, S.M., Wastegård, S., Abbott, P.M., Barbante, C., Bigler, M., Johnsen, S.J., Rasmussen, T.L., Steffensen, J.P., Svensson, A., 2010: Tracing volcanic events in the NGRIP ice-core and synchronising North Atlantic marine records during the last glacial period. *Earth and Planetary Science Letters* 294, 69-79.

Davies, S.M., Wastegård, S., Rasmussen, T.L., Svensson, A., Johnsen, S.J., Steffensen, J.P., Andersen, K.K., 2008: Identification of the Fugloyarbanki tephra in the NGRIP ice core: a key tie-point for marine and ice-core sequences during the last glacial period. *Journal of Quaternary Science* 23, 409-414.

Greenland Ice-core Project (GRIP) Members, 1993: Climate instability during the last interglacial period recorded in the GRIP ice core. *Nature* 364, 203-207.

Griggs, A.J., Davies, S.M., Abbott, P.M., Rasmussen, T.L., Palmer, A.P., 2014: Optimising the use of marine tephrochronology in the North Atlantic: A detailed investigation of the Faroe Marine Ash Zones II, III and IV. *Quaternary Science Reviews* 106, 122-139.

- Grönvold K., Óskarsson N., Johnsen S.J., Clausen H.B., Hammer C.U., Bond G., Bard E., 1995: Ash layers from Iceland in the Greenland GRIP ice core correlated with oceanic and land sediments. *Earth and Planetary Science Letters* 135, 149-155.
- Haapaniemi, A.I., Scourse, J.D., Peck, V.L., Kennedy, H., Kennedy, P., Hemming, S.R., Furze, M.F.A., Pieńkowski, A.J., Austin, W.E.N., Walden, J., Wadsworth, E., Hall, I.R., 2010: Source, timing, frequency and flux of ice-rafted detritus to the Northeast Atlantic margin, 30-12 ka: testing the Heinrich precursor hypothesis. *Boreas* 39, 576-591.
- Haflidason H., Eiriksson J., Van Kreveld S., 2000: The tephrochronology of Iceland and the North Atlantic region during the Middle and Late Quaternary: a review. *Journal of Quaternary Science* 15, 3-22.
- Hall, I.R., Colmenero-Hidalgo, E., Zahn, R., Peck, V.L., Hemming, S.R., 2011: Centennial-to millennial-scale ice-ocean interactions in the subpolar northeast Atlantic 18-41 kyr ago. *Paleoceanography* 26, PA2224, doi:10.1029/2010PA002084.
- Hall, I.R., McCave, I.N., 1998a: Late Glacial to recent accumulation fluxes of sediments at the shelf edge and slope of NW Europe, 48-50°N. *Special Publications of the Geological Society of London* 129, 339-350.
- Hall, I.R., McCave, I.N., 1998b: Glacial-interglacial variation in organic carbon burial on the slope of the NW European continental margin (40°-50°N). *Progress in Oceanography* 42, 37-60.
- Hayward, C., 2012: High spatial resolution electron probe microanalysis of tephras and melt inclusions without beam-induced chemical modification. *The Holocene* 22, 119-125.
- Höskuldsson, Á., Sparks, R.S.J., Carroll, M.R., 2006: Constraints on the dynamics of subglacial basalt eruptions from geological and geochemical observations at Kverkfjöll, NE-Iceland. *Bulletin of Volcanology* 68, 689-701.
- Housley, R.A., Lane, C.S., Cullen, V.L., Weber, M.-J., Riede, F., Gamble, C.S., Brock, F., 2012: Icelandic volcanic ash from the Late-glacial open-air archaeological site of Ahrenshöft LA 58 D, North Germany. *Journal of Archaeological Science* 39, 708-716.
- Hunt, J.B., Hill, P.G., 2001: Tephrological implications of beam size-sample-size effects in electron microprobe analysis of glass shards. *Journal of Quaternary Science* 16, 105-117.

- Jakobsson, S.P., 1979: Petrology of recent basalts of the Eastern Volcanic Zone, Iceland. *Acta Naturalia Islandia* 26, 1-103.
- Jakobsson, S.P., Jónasson, K., Sigurdsson, I.A., 2008: The three igneous rock suites of Iceland. *Jökull* 58, 117-138.
- Johnsen, S.J., Dahl-Jensen, D., Gundestrup, N., Steffensen, J.P., Clausen, H.B., Miller, H., Masson-Delmotte, V., Sveinbjörnsdóttir, A.E., White, J., 2001: Oxygen isotope and palaeotemperature records from six Greenland ice-core stations: Camp Century, Dye-3, GRIP, GISP2, Renland and NorthGRIP. *Journal of Quaternary Science* 16, 299-307.
- Kuehn, S.C., Froese, D.G., Shane, P.A.R., INTAV Intercomparison Participants (2011) “The INTAV intercomparison of electron-beam microanalysis of glass by tephrochronology laboratories: Results and recommendations”, *Quaternary International* 246, 19-47.
- Kvamme T., Mangerud J., Furnes H., Ruddiman W., 1989: Geochemistry of Pleistocene ash zones in cores from the North Atlantic. *Norsk Geologisk Tidsskrift* 69, 251-272.
- Lacasse C., Sigurdsson H., Carey S., Paterne M., Guichard F., 1996: North Atlantic deep-sea sedimentation of Late Quaternary tephra from the Iceland hotspot. *Marine Geology* 129, 207-235.
- Lackschewitz, K.S., Wallrabe-Adams, H.J., 1997: Composition and origin of volcanic ash zones in Late Quaternary sediments from the Reykjanes Ridge: evidence for ash fallout and ice-rafting. *Marine Geology* 136, 209-224.
- Lane, C.S., Blockley, S.P.E., Mangerud, J., Smith, V.C., Lohne, Ø.S., Tomlinson, E.L., Matthews, I.P., Lotter, A.F., 2012: Was the 12.1 ka Icelandic Vedde Ash one of a kind? *Quaternary Science Reviews* 33, 87-99.
- Le Maitre, R.W., Bateman, P., Dudek, A., Keller, J., Lameyre, Le Bas, M.J., Sabine, P.A., Schmid, R., Sorensen, H., Streckeisen, A., Woolley, A.R., Zanettin, B., 1989: A Classification of Igneous Rocks and Glossary of Terms. Blackwell, Oxford.
- Lowe, D.J., 2011: Tephrochronology and its application: A review. *Quaternary Geochronology* 6, 107-153.
- MacDonald, G.A., Katsura, T. 1964: Chemical composition of Hawaiian lavas. *Journal of Petrology* 5, 83-133.

MacLeod, A., Matthews, I.P., Lowe, J.J., Palmer, A.P., Albert, P.G., 2015: A second tephra isochron for the Younger Dryas period in northern Europe: The Abernethy Tephra.

*Quaternary Geochronology* 28, 1-11.

Martrat, B., Grimalt, J.O., Shackleton, N.J., de Abreu, L., Hutterli, M.A. and Stocker, T.F., 2007: Four climate cycles of recurring deep and surface water destabilizations on the Iberian Margin. *Science* 317, 502-507.

Matthews, I.P., Birks, H.H., Bourne, A.J., Brooks, S.J., Lowe, J.J., MacLeod, A., Pyne-O'Donnell, S.D.F., 2011: New age estimates and climatostratigraphic correlations for the Borrobol and Penifiler Tephra: evidence from Abernethy Forest, Scotland. *Journal of Quaternary Science* 26, 247-252.

Matthews, I.P., Trincardi, F., Lowe, J.J., Bourne, A.J., Macleod, A., Abbott, P.M., Andersen, N., Asioli, A., Blockley, S.P.E., Lane, C.S., Oh, Y.A., Satow, C.S., Staff, R.A., Wulf, S., 2015: Developing a robust tephrochronological framework for Late Quaternary marine records in the Southern Adriatic Sea: new data from core station SA03-11. *Quaternary Science Reviews* 118, 84-104.

Newnham, R.M., Lowe, D.J., 1999: Testing the synchronicity of pollen signals using tephrostratigraphy. *Global and Planetary Change* 21, 113-128.

Newnham, R.M., Lowe, D.J., Green, J.D., Turner, G.M., Harper, M.A., McGlone, M.S., Stout, S.L., Horie, S., Froggatt, P.C., 2004: A discontinuous ca. 80 ka record of Late Quaternary environmental change from Lake Omapere, Northland, New Zealand. *Palaeogeography, Palaeoclimatology, Palaeoecology* 207, 165-198.

North Greenland Ice Core Project Members, 2004: High-resolution record of Northern Hemisphere climate extending into the last interglacial period. *Nature* 431, 147-151.

Óladóttir, B.A., Sigmarsson, O., Larsen, G., Devidal, J.-L., 2011: Provenance of basaltic tephra from Vatnajökull volcanoes, Iceland, as determined by major- and trace-element analyses. *The Holocene* 21, 1037-1048.

Pearce, N.J.G., Abbott, P.M., Martin-Jones, C., 2014: Microbeam methods for the analysis of glass in fine grained tephra deposits: a SMART perspective on current and future trends. In Austin, W.E.N., Abbott, P.M., Davies, S.M., Pearce, N.J.G., Wastegård, S., (eds) *Marine Tephrochronology*, Geological Society of London Special Publication 398, 29-46.

- Pearce, N.J.G., Bendall, C.A., Westgate, J.A., 2008: Comment on “Some numerical considerations in the geochemical analysis of distal microtephra” by A.M. Pollard, S.P.E. Blockley and C.S. Lane. *Applied Geochemistry* 23, 1353-1364.
- Pearce, N.J.G., Denton, J.S., Perkins, W.T., Westgate, J.A., Alloway, B.V., 2007: Correlation and characterisation of individual glass shards from tephra deposits using trace element laser ablation ICP-MS analyses: current status and future potential. *Journal of Quaternary Science* 22, 721-736.
- Pearce N.J.G., Perkins W.T., Westgate J.A., Gorton M.P., Jackson S.E., Neal C.R., Chenery S.P., 1997: A compilation of new and published major and trace element data for NIST SRM 610 and NIST SRM 612 glass reference materials. *Geostandards Newsletter* 21, 115-144.
- Pearce N.J.G., Perkins W.T., Westgate J.A., Wade S.C., 2011: Trace-element microanalysis by LA-ICP-MS: the quest for comprehensive chemical characterisation of single, sub-10 µm volcanic glass shards. *Quaternary International* 246, 57-81.
- Perkins M.E., Brown F.H., Nash W.P., McIntosh W., Williams S.K., 1998: Sequence, age, and source of silicic fallout tuffs in middle to late Miocene basins of the northern Basin and Range province. *Bulletin of the Geological Society of America* 110, 344-360.
- Perkins M.E., Nash W.P., Brown F.H., Fleck R.J., 1995: Fallout tuffs of Trapper Creek, Idaho – a record of Miocene explosive volcanism in the Snake River Plain volcanic province. *Bulletin of the Geological Society of America* 107, 1484-1506.
- Pilcher, J., Bradley, R.S., Francus, P., Anderson, L., 2005: A Holocene tephra record from the Lofoten Islands, Arctic Norway. *Boreas* 34, 136-156.
- Rasmussen, S.O., Bigler, M., Blockley, S.P., Blunier, T., Buchardt, S.L., Clausen, H.B., Cvijanovic, I., Dahl-Jensen, D., Johnsen, S.J., Fischer, H., Gkinis, V., Guillevic, M., Hoek, W.Z., Lowe, J.J., Pedro, J.B., Popp, T., Seierstad, I.K., Steffensen, J.P., Svensson, A.M., Vallelonga, P., Vinther, B.M., Walker, M.J., Wheatley, J.J., Winstrup, M., 2014: A stratigraphic framework for abrupt climatic changes during the Last Glacial period based on three synchronized Greenland ice-core records. *Quaternary Science Reviews* 106, 14-28.
- Sanchez Goñi, M.F., Harrison, S.P., 2010: Millennial-scale climate variability and vegetation changes during the Last Glacial: Concepts and terminology. *Quaternary Science Reviews* 29, 2823-2827.



- Scourse, J.D., Hall, I.R., McCave, I.N., Young, J.R., Sugdon, C., 2000: The origin of Heinrich layers: evidence from H2 for European precursor events. *Earth and Planetary Science Letters* 182, 187-195.
- Svensson, A., Andersen, K.K., Bigler, M., Clausen, H.B., Dahl-Jensen, D., Davies, S.M., Johnsen, S.J., Muscheler, R., Parrenin, F., Rasmussen, S.O., Röthlisberger, R., Seierstad, I., Steffensen, J.P., Vinther, B.M., 2008: A 60 000 year Greenland stratigraphic ice core chronology. *Climate of the Past* 4, 47-57.
- Turney, C.S.M., 1998: Extraction of rhyolitic component of Vedde microtephra from minerogenic lake sediments. *Journal of Palaeolimnology* 19, 199-206.
- Van Kreveld, S., Sarnthein, M., Erlenkeuser, H., Grootes, P., Jung, S., Nadeau, M.J., Pflaumann, U., Voelker, A., 2000: Potential links between surging ice sheets, circulation changes, and the Dansgaard-Oeschger cycles in the Irminger Sea, 60-18 kyr. *Paleoceanography* 15, 425-442.
- Wastegård, S., Rasmussen, T.L., 2014: Faroe Marine Ash Zone IV: a new MIS 3 ash zone on the Faroe Islands margin. In Austin, W.E.N., Abbott, P.M., Davies, S.M., Pearce, N.J.G., Wastegård, S., (eds) Marine Tephrochronology, Geological Society of London Special Publication 398, 81-93.
- Wastegård, S., Rasmussen, T.L., Kuijpers, A., Nielsen, T., van Weering, T.C.E., 2006: Composition and origin of ash zones from Marine Isotope Stages 3 and 2 in the North Atlantic. *Quaternary Science Reviews* 25, 2409-2419.
- Zielinski G.A., Mayewski P.A., Meeker L.D., Gronvöld K., Germani M.S., Whitlow S., Twickler M.S., Taylor K., 1997: Volcanic aerosol records and tephrochronology of the Summit, Greenland, ice cores. *Journal of Geophysical Research* 102, 26625-26640.
- Zumaque, J., Eynaud, F., Zaragosi, S., Marret, F., Matsuzaki, K.M., Kissel, C., Roche, D.M., Malaize, B., Michel, E., Billy, I., Richter, T., Palis, E., 2012: An ocean-ice coupled response during the last glacial: a view from a marine isotope stage 3 record south of the Faeroe Shetland Gateway. *Climate of the Past* 8, 1997-2017.